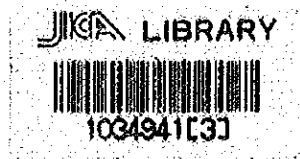


REPUBLIC OF PERU
REPORT ON GEOLOGICAL SURVEY
OF
THE YAURI AREA, SOUTHERN PERU

PHASE II
(VOL. 5)



June 1973

METALLIC MINERALS EXPLORATION AGENCY
OVERSEAS TECHNICAL COOPERATION AGENCY
GOVERNMENT OF JAPAN

国際協力事業団

〒100 東京都千代田区千代田 1-1-1

TEL

03-3581-1111

FAX

03-3581-1112

国際協力事業団	
受入 月日 '84. 4. -6	709
登録No. 03074	55
	MP

〒100 東京都千代田区千代田 1-1-1

TEL 03-3581-1111

FAX 03-3581-1112

PREFACE

The Government of Japan, in response to a request by the Government of the Republic of Peru decided to investigate the potential of mineral resources in the Yauri area, southern Peru and entrusted the survey works to the Overseas Technical Cooperation Agency. The Agency, considering the importance of technical nature of the survey work, in turn sought the cooperation of the Metallic Minerals Exploration Agency (MMEA) to accomplish the task.

The survey works are expected to be carried out over a period of three years, beginning in 1971. MMEA organized a 27-man survey team headed by Mr. Shigeaki Yoshikawa, Director of Mitsui Kinzoku Engineering Service Co., Ltd., and sent to the Republic of Peru, from September 24 to December 6, 1972. During this period, the team, with the help of the Government of the Republic of Peru and its various agencies, was able to complete survey works on schedule for the current year.

This report summarizes the results of the survey, and will form a portion of the final survey reports that will be prepared with regard to the results obtained in 1971 and 1973.

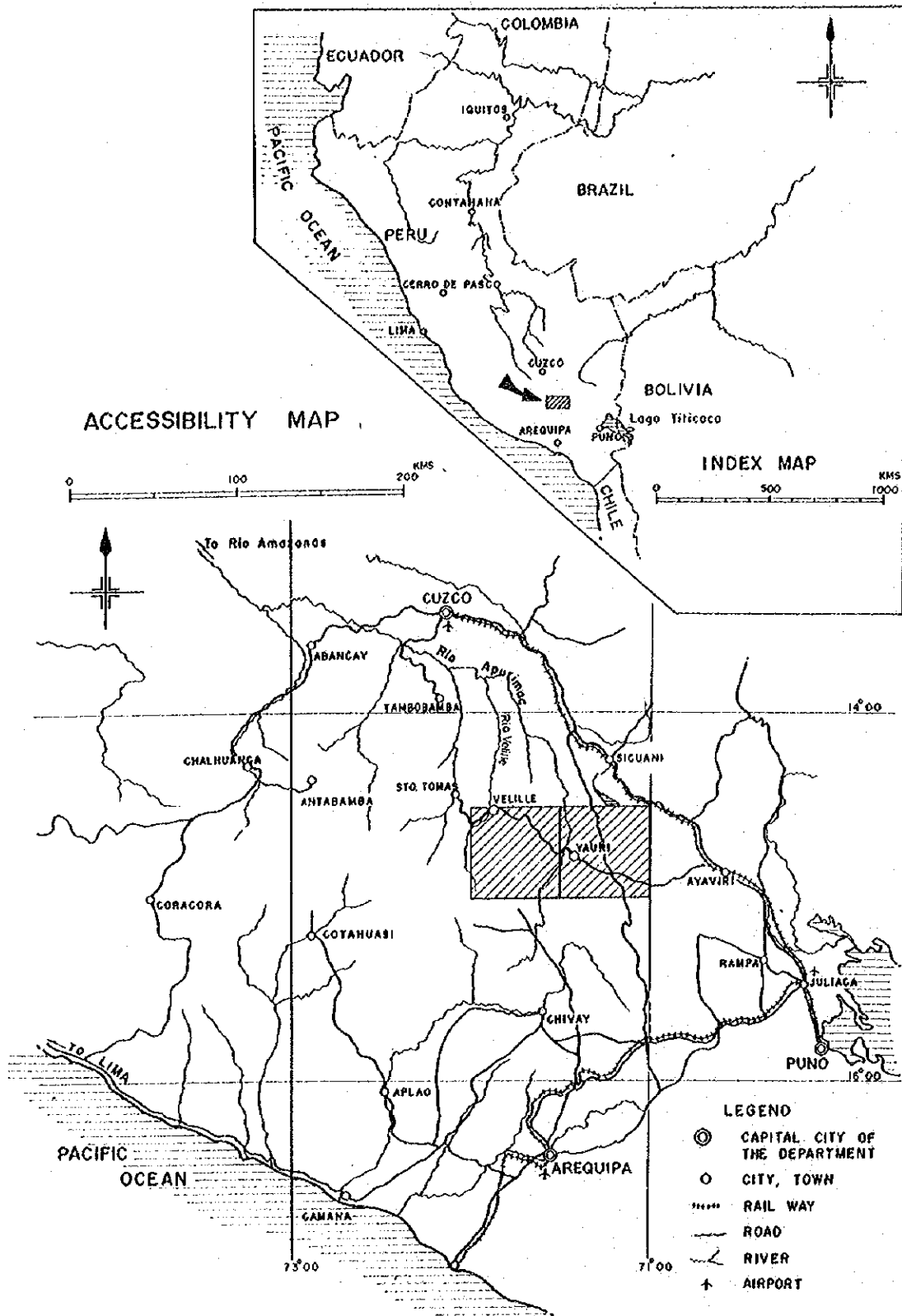
Finally I wish to take this opportunity to express my heartfelt gratitude to the officials of the Government of the Republic of Peru for their wholehearted cooperation and support extended to the Japanese survey team.

June, 1973



Keiichi Tatsuke
Director General
Overseas Technical Cooperation
Agency

Fig. 1. Location Map of the Yauri Area



GENERAL CONTENTS

PREFACE	i
Location Map of the Yauri Area	ii
SUMMARY	iv
GENERAL	- i -

PARTICULARS

PART. I	GEOLOGICAL SURVEY	I-1 ~ I-100
PART. II	GEOPHYSICAL SURVEY	II-1 ~ II-86

APPENDICES

GEOLOGICAL DATA	A-1 ~ A-108
GEOPHYSICAL DATA	A-109 ~ A-124

ATTACHED MAPS (IN POCKET)

GEOLOGICAL MAPS

GEOPHYSICAL MAPS

SUMMARY

Geological and geophysical surveys were conducted as the second-phase works of the Yauri Area Project in the Republic of Peru, for the purpose to clarify the modes of occurrence of the mineral resources and also the geologic environments of the mineralization, on both Yauri and Velille Quadrangles which had been selected as the potential area by the first-phase aerial survey in 1971.

The field works were carried out during the period from October to November, 1972. They are mostly a geological and geochemical reconnaissance of the entire project (approx. 5,950 km²) and a gravity survey for the Yauri Basin and its periphery (approx. 2,500 km²). In addition, a geological and geochemical detailed survey was made at Coroccohuayco and Huaccollo where the attractive copper showings were newly discovered. A vertical electrical sounding (Schulumberger's method) was also taken up to supplement the gravity survey on these limited area.

Present survey has revealed several minor corrections on the results of the first-phase survey. However, the first-phase survey had forecasted almost precisely the fundamental geologic environments regarding the occurrences of the mineral resources, and thereby were led to the discovery of mineralized zones of porphyry copper type in the said districts and also the confirmation of petroleum seepage at Islaicocha in the present survey.

The rocks covering the area are mainly composed of limestone, and marine and nonmarine clastics of the Late Mesozoic; intrusives of possibly between Late Mesozoic and Tertiary; terrestrial and lake deposits and volcanics of Tertiary; and volcanics and glacial deposits of the Quaternary.

The east and west sides of the present Yauri Basin remarkably differ both stratigraphically and lithologically from each other. Their discrepancies do not appear so clearly in the sequence of Mesozoic sediments, but lithologically they differ distinctly. However, with the earlier intrusive activity (intrusion of batholiths) having occurred only in the "Western Region" as a momentum, both Regions, "Eastern" and "Western", are inferred to have set up independent geotectonic units respectively. The Eastern Region experienced a sedimentation of thick continental red clastics during the period from the end of the Cretaceous to the Early Tertiary; whereas the Western Region had a thick accumulation of lava flows and pyroclastics owing to intermittently repeated volcanism between Early Tertiary and Early Quaternary time. Further, along the boundary-zone between both of them, the formation of the Yauri Lake Basin, one of taphrogeosynclinal type, appears to have begun in the Early Tertiary (?), and there a series of lake sediments have deposited possibly until the end of the Pliocene.

The age determination on the intrusives and volcanics by the K-Ar method has revealed some ages different from those previously estimated, and hence re-investigation especially for the ages of the early intrusives and invaded Mesozoic sediments has become inevitable.

General trend line of the area is in the direction of NNW-SSE to NW-SE; and folding, faulting and igneous intrusion as well are all strongly controlled by this trend. Also, weak structural controls of the NE-SW and E-W trends are observed.

Metalliferous mineralizations in the area are considered to have been accompanied by all of intrusive activities and the volcanisms of earlier stage up to the Medial Tacaza, and so far 36 mineral indications have been confirmed. However,

as the mineral resources, economically significant mineralization seems to be limited the copper alone which is related with the later igneous activity of monzonite porphyries.

Tintaya Mine and its vicinity make an important cupriferous region due to concentrated intrusions of monzonite porphyries. Monzonite porphyries in the "Tintaya Region" are inferred to have invaded as stocks or as large dykes along the three tectonic lines (?) all running in parallel with the NNW-SSE direction. Along the "West Line", Ataraya Mine (skarn-copper deposits) is known to exist, and along the "Central Line" Tintaya Mine (skarn-copper deposits and indication of porphyry copper type) and Quechua mineralized zone (porphyry copper type) are also known. Along the "East Line", the said mineralized zones of Coroccohuayco and Huaccollo have been found in the present survey. Further, eight geophysical anomalous zones suggesting a probability of latent ore deposits have been detected in and around the Tintaya Region. Five out of eight are presumed to be particularly attractive as lying on the NNW extension of the above three tectonic lines.

An oil seepage has been confirmed at Islaicocha near the border between the Yauri Basin and the Laramani Massif. The reservoir rock is considered as the Mesozoic Ayabacas limestone. The region where latency of oil deposits seem possible, is from the eastern Yauri Basin to the western flank of the Laramani Massif. Judging from general criteria of the petroleum geology, probable size of the oil deposits may be rather small because of somewhat complicated geostructure in the region. However, the economical estimation should not be done at the present stage by reason of very short information on the oil resources of the area.

The present survey has revealed, as mentioned above, the fundamental con-

ditions of mineral localization both geologically and geophysically, and some attractive mineral indications and geophysical anomalies have also been found. But their economical significances are still left for the future problems. Also, problems of rock ages remain unsettled.

We believe therefore that the following investigations should be pushed forward henceforth:

- 1) Basic investigation on the subsurface structure and mineralization at Coroccohuayco and Huaccollo.
- 2) Fundamental survey on the petroleum resources.
- 3) Re-examination for the chronologic problems newly proposed from dating.
- 4) Confirmation of promising districts detected by geophysical survey.

Recommendable methods of the above investigations are respectively: as for 1) information drilling and geophysical prospecting by IP and magnetic methods, as for 2) geological and geochemical (in respect of hydrocarbon) reconnaissance, as for 3) additional age determination of igneous rocks and fossil study on the Mesozoic beds, and as for 4) geophysical prospecting by IP and magnetic methods.

The Yauri Area Project should be finished within the next year (1973 fiscal year) under the present agreement, and hence it seems impossible to execute all of them completely. It is therefore desirable to carry out the investigations of Item 1) to 3) in the next fiscal year. Survey of Item 4) can not but be left as a future problem, as this alone requires at least one year to cover all of eight promising districts.

GENERAL

CONTENTS

GENERAL

1.	Introduction	1
1-1	Purpose of Survey	1
1-2	Outline of Survey	1
2.	General Discussion on Results	5
2-1	Comparison with Results of First-Phase Survey	5
2-2	Discussion on Geology	6
2-3	Discussion on Metallic Mineral Resources	11
2-4	Discussion on Petroleum Resources	15
3.	Conclusion and Future Prospects	17
3-1	Conclusion	17
3-2	Future Prospects	18

1 INTRODUCTION

1-1 Purpose of Survey

The purpose of the present survey, the second-phase work in the Yauri Area Project, was to make clear the modes of occurrence of the mineral resources and also the geological environments of the mineralization, by means of geological and geophysical ground-surveys, on the potential area of the mineral resources which was selected from the results of the first-phase survey conducted mainly by air-borne methods in 1971.

1-2 Outline of Survey

1-2-1 Scope of Survey

1) Area of Geological Survey (Fig. 1)

The project area covers a sphere measuring about 5,950 km² which is demarcated by the following latitude and longitude lines:

Lat. 14°30'S (northern limit), lat. 15°00'S (southern limit),
long. 71°00'W (eastern limit), long. 72°00'W (western limit).

This area coincides with the combined area of both Yauri and Velille Quadrangles, according to the division of the topographic maps on the scale of 1:100,000 in the Republic of Peru.

2) Area of Geophysical Survey

The project area covers a sphere measuring about 2,500 km² within Yauri Quadrangle, the eastern half of geological survey area.

1-2-2 Method and Period of Survey

1) Geological Survey

The geological survey, involved in the contract, included a geological and geochemical (stream sediment) reconnaissance and a geological and geochemical (rock/soil) detailed survey for the mineralized zones at Coroccohuayco and Huacollo. 49 days from 4th October to 21st November, 1972 were required for the field work.

2) . Geophysical Survey

The geophysical survey consisted of a gravity survey for the entire project area and a vertical electrical sounding (Schulunberger's method) of 25.5 km long, and 50 days from 4th October to 22nd November, 1972 were spent.

3) Comprehensive Study

A series of processings and analyses on the various data obtained from the above field works, and a comprehensive interpretation were attempted regarding mineral resources and geology. Some 5 months from December, 1972 to April, 1973 were required for the study.

1-2-3 Constitution of Survey Team

The survey was undertaken by Japanese survey team in collaboration with Peruvian counterparts.

Participants of the survey are listed as follows:

1) General Supervision and liaison

Head	Shigeaki	Yoshikawa	Mitsui Kinzoku Engineering Service Co., Ltd., Japan
	Yoshio	Matsukawa	Metallic Minerals Exploration Agency of Japan
	Michihisa	Shimoda	Overseas Technical Cooperation Agency of Japan

Hiroshi Sato Mitsui Kinzoku Engineering Service Co. , Ltd. ,
Japan
2) Geological Survey

Team No. 1

Jorge Galdos Servicio de Geología y Minería del Perú
Junnosuke Oikawa Mitsui Kinzoku Engineering Service Co. , Ltd. ,
Japan
Kiyohisa Shibata - do. -
Tsuyoshi Yamada - do. -

Team No. 2

Julian Baca Servicio de Geología y Minería del Perú
Masao Saito Mitsui Kinzoku Engineering Service Co. , Ltd. ,
Japan
Eigo Futamura - do. -

Team No. 3

Jurío Acevedo Servicio de Geología y Minería del Perú
Yutaka Kikuchi Mitsui Kinzoku Engineering Service Co. , Ltd. ,
Japan
Koichi Shinoda - do. -
Akira Takigawa - do. -

Team No. 4

Hugo Ferro Servicio de Geología y Minería del Perú
Toshio Kuwahara Mitsui Kinzoku Engineering Service Co. , Ltd. ,
Japan
Ken Obara - do. -
Yuya Furukawa - do. -
Kotaro Tomita - do. -

3) Geophysical Survey

Shigezo	Inuzuka	Mitsui Kinzoku Engineering Service Co., Ltd., Japan	
Tooru	Tsuchiya		- do. -
Fukujiro	Miyoshi		- do. -
Takashi	Aoyama		- do. -
Akira	Egawa		- do. -
Susumu	Abumi		- do. -
Kunihiro	Hotta		- do. -
Hisayoshi	Sato		- do. -
Kazuhiko	Kinoshita		- do. -
Shigeji	Asaoka		- do. -
Kazuhisa	Nishio		- do. -

2 GENERAL DISCUSSION ON RESULTS

2-1 Comparison with Results of First-Phase Survey

Informations regarding the geology and mineral resources in the area have been considerably increased by the present survey, and a number of new data have been added to the results of the first-phase survey, which was mainly conducted by the airborne methods. Also, some revisions to the results were done.

Many interpretations or presumptions in the first-phase survey have been practically checked up and confirmed which was the main progress in the present survey.

The improvement against the result of the first-phase survey is mainly as follows:

- 1) The geology and structure of Laramani Mountains have now been clarified, which defied satisfactory interpretation in the first-phase survey due to the lack of the ground survey data.
- 2) The relationship between igneous activities and mineralizations has become more precise.
- 3) It has been found that most of volcanics in the area are of the Tertiary Tacaza and Senna, which were interpreted mainly as the Quaternary Barroso volcanics in the last survey.
- 4) The subsurface structure of Yauri Basin has become much more clarified by the gravity survey and vertical electrical sounding. The distribution and shape of the subsurface intrusives, which were surmised last time only by the airborne magnetic survey, have also been confirmed and partially modified by combined analysis of all geophysical data.

Concerning the occurrence of mineral resources, however, the first-phase survey grasped almost precisely the fundamental geologic environments, hence having brought to the discovery of attractive mineralizations of porphyry copper type at Coroccohuayco and Huaccollo and also the confirmation of the oil seepage at Islaicocha in the present survey.

2-2 Discussion on Geology

The stratigraphic relations and lithologic characteristics of respective rock units exposed within the area have been roughly worked out through the present survey. However, the results of K-Ar dating for the intrusives and volcanics have shown some dates contradictory to those previously estimated. In this respect, the present geological survey is still incomplete, and re-investigation on geological age has become necessary.

Definitely dated Palaeozoic formations have not been represented within the area. But a sequence of red sandstone and conglomerate, which makes three isolated outcrops around the Coporaque village in the southeastern Velille Quadrangle, may be of the Upper Permian Mitsu group judging from their lithologic similarity.

The clear record of sedimentations and volcanic activities in the area can be traced down since the Late Mesozoic, but from its beginning, lithologic and stratigraphic discrepancies are marked between both the sides, east and west, of the Yauri Basin.

The Mesozoic sequence to the east of Yauri Basin (Laramani Mountains) consists of the Huancané formation (red sandstones intercalated with conglomerates), the Moho formation (mainly Ayabacas limestone), and the Muñani-Cotacucho formations (shale and sandstone) in ascending order. Whereas, the Mesozoic section

from the western Yauri Basin to the Western Cordillera is made up of the Hualhuani quartzite of Yura group, the Murco formation (an alternation of shales and sandstone), and the Ferrobamba limestone. Both Hualhuani and Murco formations of "Western Region" may be approximately correlated with the Huancané formation of the "Eastern Region", and the Ferrobamba formation is also considered as the correlative of the Moho formation. But these correlatives distinctly differ in lithofacies and biofacies, thereby making it possible to presume that the marine transgression at the age progressed from the west to the east in the area. For instance, the fossil fauna of the Ayabacas limestone is very possibly of a coral or littoral nature, whereas that of the Ferrobamba limestone suggests an origin of deeper sea, although both are inferred to have deposited in an age between Late Jurassic and Early Cretaceous from fossil evidences.

No definite ages of each of the formations above mentioned are settled, although they have been agreed of Late Mesozoic sediments. According to published papers and stratigraphic informations, three formations of Hualhuani, Murco and Huancané are generally correlated with the Lower cretaceous, and both Ferrobamba and Moho formations are believed to be of the Lower or Middle Cretaceous. Also, the Muñani-Cotacucho formations are regarded as the Upper Cretaceous. However, a gabbro sample taken from the Tintaya batholith, which clearly penetrates the Ferrobamba limestone, has shown the K-Ar age of 144 m. y. (Late Jurassic). According to this result, the age of Ferrobamba limestone should be dated back at least to the Late Jurassic.

Anyway, an orogeny occurred after the said geosynclinal sedimentation, and a series of intrusions of dioritic to granodioritic batholiths followed.

The ages of respective batholiths measured by the K-Ar method are as follows:

- 1) Tintaya batholith in the southwestern Yauri Basin is 144 m. y.
- 2) Velille batholith in the northwestern Velille Quadrangle is 105 m. y. (Medial Cretaceous).
- 3) Pichigua batholith near the western boundary of Yauri Quadrangle is 86 to 74 m. y. (Medial to Late Cretaceous).

The above results suggest that the intrusion of batholiths occurred intermittently through Late Mesozoic age.

These batholiths are presumed to have been derived from a parental magma, but they differ somewhat from each other in chemical composition and lithology according to their ages of intrusion. The oldest Tintaya batholith is a perfect pluton and predominantly includes pyroxene diorite or gabbroic diorite. The medial Velille batholith is also a pluton and mostly composed of quartz diorite and granodiorite. The youngest Pichigua batholith is of a hypabyssal nature though its chemical composition is very similar to those of older batholiths.

All of them are restricted within the said "Western Region" and appear to have intruded along the trends of NW-SE and NE-SW. Neither of geological nor geophysical indication of the intrusives has been detected to the east of the central Yauri Basin. These spatial and structural features may implicate a preceeded tectogenesis which controlled their emplacements. Regional upheaval and erosion also appear to have predominated throughout the age of intrusions, and the erosion is likely to have considerably progressed at the time of the intrusion of hypabyssal Pichigua batholith.

With the above-stated orogeny as a momentum, both Regions, "Western" and

"Eastern" seem to have become completely independent geotectonic units respectively.

In the Eastern Region, enormous red clastics of the Puno group deposited probably during rather short time from the close of Cretaceous (?) to the beginning of the Tertiary. The Puno group consists of two formations, Lower and Upper, and a clear unconformity is marked between both of them. The Lower Puno formation is mostly composed of coarse-grained conglomerates, whereas the Upper Puno is an alternation of sandstones and conglomerates with intercalation of thin shaly beds in its upper part.

The Puno rocks are not represented in the Western Region. Instead, a series of monzonitic porphyries seem to have intruded and brought an important copper mineralization during Lower Puno time. A monzonite sample has been dated as 57 m. y. (Latest Paleocene) by the K-Ar method, but its actual age may be a little older than the measured one, since the sample has been weakly affected by later alteration. At the upper Puno time, too, the first volcanic activity possibly occurred in the Western Region, and acidic pyroclastics (Lower Tacaza formation) were deposited. This volcanism also seems responsible for the considerable predominance of tuffaceous sandstones and the partial intercalation of acidic tuff and lava flow in the Upper Puno formation.

Next, a prominent tectonic movement and subsequent uplift occurred. The tectogenesis is considered to have formed the main structures of NNW-SSE to NW-SE trending and the subordinate ones of the NE-SW and E-W. The upheaval appears to have caused the regional superficial erosion shown as the post-Puno or post-Lower Tacaza truncation. Further, the Yauri Basin of a taphrogeosynclinal

type after the definition of M. Key (1951) seems to have begun its setting along the boundary-zone between the East and West Regions, thereby establishing the present three geomorphic-structural units; the eastern Laramani Massif, the central Yauri Basin, and the Western Cordillera.

Subsequently, the Western Cordillera experienced repetitive volcanisms, whereas the Yauri Basin had a series of lake sedimentation. In the Laramani Massif, the superficial erosion seems to have generally predominated except small-scale effusion of the Middle Tacaza volcanics in Eocene time (55 m. y. in a K-Ar dating).

The volcanic rocks of Western Cordillera consist of the Early Tertiary Tacaza, the Pliocene Sencca, and the Plio-Pleistocene Barroso. The Tacaza volcanics are considerably rich in alkali. They may be classified into two formations; the older belongs to the Eocene (?), consisting mainly of lava flows of olivine basalt and trachy andesite (the Middle Tacaza formation), the younger occurred during the age from the end of the Eocene to the beginning of the Miocene (40 ± 2 m. y. to 28 m. y. in K-Ar age), being chiefly composed of trachyte, alkalic dacite, and trachy andesite (the Upper Tacaza formation). The Sencca volcanics consist of rhyolitic or dacitic pyroclastics and lavas, and a dacite sample has been dated as 7 m. y. by the K-Ar method. The Barroso volcanics are composed of lava flows of basalt and andesite, and andesitic pyroclastics.

The geophysical survey has detected a large graben structure of NNW-SSE trend occupying approximately the eastern half of Yauri Basin. The eastern boundary of the graben nearly coincides with that of the Basin itself, and its western boundary is almost in contact with the eastern boundary of Tintaya and Pichigua batholiths.

Both boundaries make a clear fault-like structure on each side. The gravitational basement (probably Lower Puno formation or Mesozoic sediments) also dips gently to the west, and the vertical movement of the western "fault" seems to be larger than that of the eastern "fault".

The lake sediments of Yauri Basin can be separated into three units; the Lower Descanso, the Upper Descanso, and the Yauri formations in ascending order. The Lower Descanso formation is an alternation of sandstones and conglomerates, and the Upper Descanso is mostly massive tuffs of white and salmon colours. The Yauri formation consists of tuff, tuffaceous siltstone, and calcareous siltstone. The Lower Descanso formation is restricted within the graben, whereas both the Upper Descanso and Yauri formations are widely distributed over the west side of the graben, thereby suggesting that the Yauri Basin made step-like expansions westwards from the graben. The deposition of lake sediments appears to have continued intermittently since the formation of the graben (the close of Paleocene?) until the Pliocene. A sample of massive biotite-bearing tuff taken from the upper part of the Upper Descanso formation has been dated as 5 m. y. (Medial Pliocene time) by the K-Ar method. The pollen analysis has also suggested that the Yauri formation deposited in a temperate, shallow and stagnant lake possibly during the Pliocene.

The regional and absolute uplifting, however, so continued after the post-Puno tectogenesis that glaciers were formed various places of both west and east high lands in Pleistocene age and some outwashes reached to the fringe of the Yauri Basin.

2-3 Discussion on Metallic Mineral Resources

Metalliferous mineralizations in the area have the close spatial and, possibly, genetic relationship with all of intrusive activities and the earlier volcanisms up to the Medial Tacaza, as pointed out in the report of the first-phase survey and so far 36 of mineral showings and ore deposits have been confirmed. However, economically important mineralization is most probably limited the copper alone which is related with the intrusive activity of monzonite porphyries, the later stage of intrusive activity, whereas all the mineralizations associated with the Tacaza volcanics and earlier intrusives, batholiths, seem too small and/or weak to be available.

The monzonite porphyries concentrate in and around the Tintaya batholith, were the known mines and large mineralized zone such as Tintaya, Ataraya and Quechua are located in close association with monzonite porphyries. Two attractive mineralizations newly discovered at Coroccohuayco and Huaccollo in the eastern Tintaya Region are of a porphyry copper type, being accompanied with monzonite porphyries, too.

At Coroccohuayco a NNW-SSE trending stock or large dyke intrudes into the dioritic batholith, where a hydrothermally altered zone measuring about 800 m wide in the E-W direction and more than 2.5 km long in the N-S direction is formed. The altered zone includes geochemical anomalies of remarkably high copper and also disseminations of copper oxides at places. Ore samples taken from various mineralized outcrops contain poor but universal molybdenum.

The Huaccollo showing lies at 2.5 km on the northern extension of the Coroccohuayco. The mineralization here is marked in the porphyritic monzonite and invaded diorite limittedly exposed along the valley bottom. The outcrop of porphyritic monzonite is only some 350 m wide, but chalcopyrite and pyrite with

minor amount of molybdenite are disseminated throughout the monzonite. Total copper content of monzonite samples taken by the channel sampling for 350 m span, has averaged 0.55% in assay. In diorite, ore dissemination is generally weak, but pyrite veins and veinlets rather pervade and some veins are accompanied with remarkable copper ore (max. copper content 5.18% for the sampled width of 1.2 m).

Important copper mineralizations, as mentioned above, are all accompanied with monzonite porphyries in the Tintaya Region. These monzonite porphyries are inferred to have invaded as stocks or large dykes along the three hypothetical tectonic lines all running in parallel with the NNW-SSE direction; the eastern Coroccohuayco-Huaccollo line, the central Quechua-Tintaya line, and the western Ataraya line. This hypothesis appears to agree with the geophysical interpretation as mentioned below, and thus may become an available indicator for future prospecting of the area.

The geophysical survey has revealed some geophysical environments of ore localization. Their main features and geological interpretations are as follows:

- 1) Tintaya Region, an important cupriferous zone, is considered to make a large high gravity anomaly zone from the macroscopic point of view, but the anomaly is conspicuously heterogeneous and may also be interpreted as a congregation of many local high gravity anomalies. Most of these local high gravity anomalies also overlap the shallow high magnetic anomalies detected by the airborne survey. Further, known ore deposits and large mineralized zones are all restricted around the local high gravity and magnetic anomalies (or low anomalous zones sandwiched by local high anomalies in other words).
- 2) Physical property test on the rocks constituting the Tintaya Region has made

it clear that the high density as well as high magnetic rocks most possibly correspond to the intrusives such as diorite and granodiorite, whereas the Mesozoic sediments and the acidic intrusives such as monzonitic porphyries are less magnetic and a little less dense than diorite and granodiorite.

- 3) The fact that Tintaya Region forms a large high gravity zone may, therefore, implicate a large diorite and/or granodiorite mass, i. e., batholith. The distinct heterogeneity of the anomaly or the gathering of local high anomalies may also agree with the geological evidence that the batholith is often invaded by monzonitic porphyries and is overlaid by the roof pendants of the Mesozoic sediments, too. Thus, the localization of geophysical anomalies as related to the known mineralized zones as described in Item 1) seems to mean geologically that mineralized zones occur in monzonitic porphyries penetrating the batholith or in the roof pendants of the Mesozoic sediments.
- 4) Consequently, attention should be paid to the local "low" anomalies of gravity and magnetism within a large high anomalous zone of them or to the "peripheries" of the local high anomalies for locating geophysically possible sites of ore deposits.
- 5) Tintaya Region includes 8 attractive districts shown by the local high gravity anomalies of H₄, H₅, H₆, H₇, H₈, H₉, H₁₅ and H₁₆. They also appear to be arranged in the NNW-SSE direction, and 5 out of them are located on the above-stated tectonic lines; H₈ and H₇ on the Ataraya line, H₅ on the Quechua-Tintaya line, and H₄ and H₁₅ on the Corrocohuayco-Huaccollo line.
- 6) High gravity anomalies H₁ and H₂, which are overlapped by the shallow high magnetic anomalies, have been detected at the Pichigua batholith. The

anomaly of Pichigua is remarkably homogeneous in comparison to that of Tintaya, and is interpreted as showing of an essentially same intrusive mass though having some differences of physical property. The Pichigua batholith is of a hypabyssal type as previously mentioned, and its chemical composition is mostly equivalents of diorite and granodiorite. But the degree of porphyritic texture distinctly varies locally, probably reflecting its consolidation conditions, and further disseminations of pyrite and masses of magmatic magnetite are often present in the distinctly porphyritic ones. These partial differences may be responsible for the said geophysical variations. Furthermore, as this iron mineralization seems to be accompanied by rather universal but generally weak copper mineralization, some supplementary survey may be necessary on the copper mineralization.

2-4 Discussion on Petroleum Resources

The possibility of fuel resources, which was forecasted in the first-phase survey, has been proven by the confirmation of Islaicocha oil seepage. This seepage lies just the east side of a large fault which separates the Yauri Basin and the Laramani Massif. There a small quantity of oil is seeping from the alluvium covering the west wing of Ayabacas limestone which crops out as a small inlier in the Puno group and form a small and gentle anticline.

The crude oil is of a low-sulphur and excellent paraffinbased property, but its gasoline and asphalt contents are extremely lower than those of other general crude oils. This peculiarity of the crude oil is considered to indicate that the oil has traveled fairly far.

The reservoir rock in the area is considered as the Ayabacas limestone

judging from the records of oil wells and seepages in the Pirin oil field of the Titicaca area and also from its spacial relationship with the Islaicocha oil seepage.

The rather complicated geologic structure makes it difficult to expect the formation of large-scale anticlinal trap in the area, and, therefore, the size of oil deposits seems rather small from the general viewpoint of petroleum geology. Also, the greater part of the Laramani Massif becomes an unfavourable region of oil retaining due to the exposing of presumed reservoir rock, the Ayabacas limestone. The region to the west of the central Yauri Basin, too, is not likely to permit the deposition of petroleum because of the distinct igneous activity.

However, the region from the eastern part of the Yauri Basin (the graben zone) to the western slope of the Laramani Massif keeps some possibilities of oil occurrence. The Ayabacas limestone here is thickly overlain by the Puno group and the lake sediments, and also no intrusive activity has been detected geologically as well as geophysically. In addition, the formation of some traps such as fault type and small anticlinal one can be anticipated in this region.

Anyway, the information on the oil resources of the area is too short for its immediate evaluation without further investigation.

3 CONCLUSION AND FUTURE PROSPECTS

3-1 Conclusion

The forecasts on mineral occurrences and the selection of the potential areas in the first-phase survey were mostly correct.

The copper mineralization related to the monzonite porphyries (later intrusives of the area) is considered to be very important economically. The Tintaya Region is, in this sense, regarded as an important cupriferous region, and in fact known large copper deposits and attractive showings are all restricted within the Region.

Both Coroccohuayco and Huaccollo mineralized zones discovered in the eastern Tintaya Region show some attractive features of porphyry copper type, and further investigations are indispensable for them.

The peripheries of eight local hi-gravity anomalies which have been detected in and around the Tintaya Region have a possibility of occurrence of ore deposits as well. Five out of them; H₄, H₅, H₇, H₈ and H₁₅ are particularly interesting because they lie on the three tectonic lines presumably having relation with the intrusion of monzonite porphyries.

Mineralizations occur also in the batholiths (earlier intrusives) and the Tacaza volcanics, but they are generally very weak and seem unavailable in economic sense. However, some attention may be required to the mineralization of the Pichigua batholith as this batholith is of a hypabyssal nature and includes, in contrast to other plutonic batholiths, fairly wide pyrite disseminations and magnetite masses which are generally accompanied by a little copper ores.

Oil deposits may lie latent in the region from the eastern part of the Yauri

Basin to the western part of the Laramani Massif. It is difficult to expect the large oil field in the region judging from the geostructural condition, but there is some possibility on the existence of economical deposit. Anyhow, further careful investigation is required in order to evaluate its economic significance.

The general geology of the area has been mostly worked out. However, the age determination on the intrusives and volcanics by the K-Ar method has presented some ages different from those previously estimated. Therefore, further investigation is necessary on this problem.

3-2 Future Prospects

The present survey has revealed many attractive indications of the mineral resources and also has brought a new problem regarding geological ages as mentioned at Clause 3-1. Considering the object of the project all these problems should be investigated, but it is impossible to execute all of them completely as the contract shall be terminated within the next year (1973 fiscal year). So, the following sequence of the survey is tentatively proposed:

- 1) First, it would be desirable to complete the fundamental investigation of both Coroccohuayco and Huaccollo mineralized zones to decide whether the full-scale prospecting is necessary for them or not. This investigation if being fortunately crowned with success, will be able to contribute most quickly to the regional development of the Yauri. The geological and geochemical ground-surveys of both the districts have been mostly worked out. Therefore, future survey should be directed towards clarifying the underground geostructure and mineralization. For this purpose, it would be most effective to conduct the geophysical prospecting by a combination of IP and magnetic methods

and subsequent information frilling. The geological and geochemical ground-survey would be, of course, necessary for the peripheries of the known mineralized zones.

- 2) Secondly, it would be desirable to conduct the preliminary survey on the petroleum resources in order to obtain its fundamental informations. If any economical deposits of oil is found in the area, they would, even small in scale, make a great contribution to the regional development of the Yauri. As for the petroleum prospecting, seismic prospecting by the reflection method and test drilling are well known as the indispensable ones. But they are very expensive and the present area seems unfavourable to expect the presence of large oil field, and therefore more basic surveys should carefully be conducted before taking up such methods. Thus, it is recommended first to conduct geostatigraphic investigation and geochemical survey by hydrocarbon in order to clarify the source and reservoir rocks of oil. It is also important to surmise, if possible, the underground geostructure of the eastern Yauri Basin which is tentatively considered as most hopeful region of oil occurrence.
- 3) Thirdly, the chronologic investigation would be desirable for the igneous rocks and the Mesozoic sediments. This problem has no direct bearing on the mineral resources, but, without clarifying this problem, it would be impossible to achieve completely another large objective, namely, the preparation of the geological map of the survey area. First, it would be necessary to re-examine the ages of intrusive rocks which have originally presented the problem in the present age determination by the K-Ar method. Also, every

effort should be made to find index fossils from the Mesozoic sediments and, if possible, from the undated Coporaque formation. The expert in paleontology is necessary for this survey.

- 4) Fourthly, it would be desirable to examine the eight promising districts of metallic mineral occurrence which have been detected by the present geophysical survey. For this examination, the geophysical prospecting by a combination of IP and magnetic methods is most recommendable, since most of them are possibly of a latent nature.
- 5) The investigation of mineralization of the Pichigua batholith comes to the last in the sequence of the survey, as is not so important.

The execution of the investigations from Item 1) to Item 3) is desirable as the next and final survey of the Yauri Area Project. It is desirable to conduct the survey of Item 4) as well, but this alone requires at least another one year to cover all of eight districts.

PARTICULARS

PART I. GEOLOGICAL SURVEY

CONTENTS

PART I. GEOLOGICAL SURVEY

1.	Outline of Survey Work	I- 1
1-1	Field Work	I- 1
1-2	Laboratory Work	I- 3
2.	Geomorphology	I- 6
2-1	Classification of Landform	I- 6
2-2	Western Cordillera	I- 6
2-3	Yauri Basin	I- 8
2-4	Laramani Massif	I- 9
3.	Geology	I-11
3-1	Stratigraphic Summary	I-11
3-2	Coporaque Formation	I-14
3-3	Hualhuani Formation of Yura Group	I-16
3-4	Huancané Formation	I-18
3-5	Murco Formation	I-20
3-6	Moho Formation	I-22
3-7	Perrobamba Limestone	I-25
3-8	Muñani-Cotacucho Formations	I-28
3-9	Puno Group	I-29
3-10	Tacaza Group	I-37
3-11	Sencca Formation	I-46

3-12	Lake Sediments (Descanso Group and Yauri Formation)	I-48
3-13	Barroso Group	I-52
3-14	Glacial Deposit	I-54
3-15	Recent Deposit	I-55
4.	Intusive Rocks	I-56
4-1	General Remarks	I-56
4-2	Tintaya Region	I-57
4-3	Velille Town and its Periphery	I-61
4-4	Periphery of Coporaque Village	I-62
4-5	Periphery of Santa Lucia de Pichigua Town	I-63
4-6	Upper Stream of Rio Paychuma	I-65
5.	Geological Structure	I-66
5-1	Folding	I-66
5-2	Faulting	I-68
6.	Geologic History	I-70
7.	Economic Geology	I-76
7-1	General Remarks	I-77
7-2	Geochemical Reconnaissance for Stream Sediments	I-77
7-3	Metallic Resources	I-81
7-4	Petroleum Resources	I-89
	References	I-98

LIST OF ILLUSTRATIONS

		Page
Fig. 1.	Location Map of the Yauri Area	ii
Fig. 2.	Division of the Surveyed Area and Members	I-1
Fig. 3.	Geomorphic Division of the Yauri Area by Summit Level	I-7
Fig. 4.	Histogram and Frequency Curve of Cu (Stream Sediment)	I-79
Fig. 5.	Histogram and Frequency Curve of Cu at Coroccohuayco	I-84

LIST OF TABLES

Table I-1.	Generalized Columnar of the Yauri Area	I-12
Table I-2.	Mineral Showings of the Yauri Area	A-2
Table I-3.	Flow Sheet of Geochemical Analysis on Copper	A-3
Table I-4.	Flow Sheet of Geochemical Analysis on Molybdenum	A-5

LIST OF APPENDICES

Table I-1	Generalized Columnar of the Yauri Area	I-12
Table I-2	Mineral Showings of the Yauri Area	A- 2
Table I-3	Flow Sheet of Geochemical Analysis on Copper	A- 3
Table I-4	Flow Sheet of Geochemical Analysis on Molybdenum	A- 5
Table I-5	Property Test of Crude Oil from Islaicocha	A- 7
Table I-6	Qualitative Analysis of the "mixed" Water from Islaicocha Oil Seepage	A- 8
Table I-7	List of Rock Samples	A- 9
Table I-8	Microscopic Observations	A-30
Table I-9	Microphotographs	A-60
Table I-10	Chemical Analysis of Rocks	A-74
Table I-11	Alkali-Lime Index of Volcanic Rocks from the Yauri Area	A-82
Table I-12	Triangular Diagram Showing the Ratio Normative Orthoclase (Or), Albite (Ab and Anorthite (An) of Volcanic Rocks from the Yauri Area	A-83
Table I-13	AFM Diagram of Volcanic Rocks from the Yauri Area	A-84
Table I-14	Classification of Intrusive Rocks by Normative Quartz and Feldspars	A-85
Table I-15	Geochemical Analysis of Stream Sediments	A-86
Table I-16	Chemical Analysis of Ores	A-92
Table I-17	Chart of X-ray Diffractive Analysis	A-93
Table I-18	K-Ar Ages of Igneous Rocks from the Yauri Area	A-96
Table I-19	Fossils	A-97
Table I-20	Pollen Analysis	A-100
Table I-21	Photographs	A-102

LIST OF PLATES (are in Pocket)

PL. I-1-1.	Geological Map of the Vellie Quadrangle	1:100,000
PL. I-1-2.	Geological Map of the Yauri Quadrangle	1:100,000
PL. I-2.	Geological Profile of the Surveyed Area	1:100,000
PL. I-3.	Route and Rock Sample Map (8 sheets)	1: 50,000
PL. I-4.	Geological Map of the Coroccohuayco and the Huaccollo Area	1: 4,000
PL. I-5.	Geochemical Map by Stream Sediment (2 sheets)	1:100,000
PL. I-6	Geochemical Map of the Coroccohuayco and the Huaccollo Areas	1: 4,000

CHAPTER 1 OUTLINE OF SURVEY WORK

1-1 Field Work

1-1-1 Geological Reconnaissance Work

The present work covered both Yauri and Velille Quadrangles (approx. 5,950 sq. km.) as stated previously.

The area was divided into eight blocks and the four teams took charge each two blocks as shown in Fig. 2.

Fig. 2. Division of the Surveyed Area and Members

VELILLE		YAURI	
(BLOCK I)	(BLOCK II)	(BLOCK V)	(BLOCK VI)
Team 1	Team 2	Team 4	Team 2
(BLOCK III)	(BLOCK IV)	(BLOCK VII)	(BLOCK VIII)
Team 4	Team 3	Team 1	Team 3

72°00
71°20
7°00
14°30
15°00

<p>Team 1 : Junnosuke Okawa Kiyohisa Shibata Tsuyoshi Yamada Jorge Galdos</p>	<p>Team 3 : Yutaka Kikuchi Koichi Shinoda Akira Tokigawa Julio Acevedo</p>
<p>Team 2 : Masao Saito Eigo Futamura Julian Boca</p>	<p>Team 4 : Toshio Kuwahara Yuya Furukawa Ken Obara Kotaro Tomita Hugo Ferro</p>

Topographic maps of 1:25,000 were prepared through the courtesies of El Instituto Geografico Militar del Peru for the purpose of the route mapping.

The traffic situation of the present area is not satisfactory except the pampa spreading broadly around the Yauri city. Especially, most of the Velille Quadrangle and the eastern border of the Yauri Quadrangle, make high mountainous regions of more than 4,500 m. S. L., and few auto-roads are available there. Therefore, the survey of such regions was conducted by the caravan system using horses or llamas, and sometimes the survey had to be done on foot due to the unavailability of horses.

The present work was over without heavy troubles after 41 days, although hampered by intermittent but daily-like rains, snows or hailstones.

1-1-2 Geochemical Reconnaissance Work

The geochemical reconnaissance was attempted for the purpose of a quick examination of the mineral localizations in the wide area by means of tracing elements of stream sediments.

Both copper and molybdenum were adopted as the tracer in the present survey by reason that the most predominant ore element was considered as the copper from the known data, and also that the large-scale ore deposits like the porphyry copper was aimed from the economical point of view.

Stream sediments were sampled from rivers and valleys at their intersections with mapping routes of the geological reconnaissance. Samples were preferentially taken from the river bottom rich in the fine sands or from the sand bar. In case such locations were unavailable, sampling was made at the river side where the soil contamination was scarcely considered. However, it was fairly difficult to obtain ideal samples from the small valleys, since most of them would be dried up in the dry

season.

Each sample was about 200 gr. of fine silty sediments under 80-mesh screened at each site as a rule.

608 samples were collected from the whole area, with an average ratio of 0.1 sample/km². However, the density was raised up to an average of 0.25 sample/km² in the Mesozoics-intrusives region where the mineralization was considered particularly intense.

1-1-3 Detailed Work at Coroccohuayco and Huaccollo Showings

A geological and geochemical detailed survey was conducted during eight days all the four teams for both Coroccohuayco and Huaccollo showings of the porphyry copper type discovered through the said reconnaissance survey.

At Coroccohuayco, the survey covered an area of 800 m (1,000 m in part) in the E-W and 2.5 km in the N-S directions. 50 m-grid stations were first established on the project area by the transit compass-measuring tape method. Then, geological mapping of the scale 1:2,000 and geochemical sampling at each station were conducted. Channel sampling for assay was also carried out at markedly mineralized outcrops.

The survey of the Huaccollo district was restricted along the valley, as the mineralized zone is of a sub-latent nature and crops out only along the valley bottom. Survey method consisted of geological mapping on the scale of 1:2,000, geochemical sampling of 50 m-grid, and channel sampling for mineralized outcrops.

Geochemical samples collected in the detailed survey amounted to 916, and ore samples for assay totaled 67.

1-2 Laboratory Work

The following laboratory studies were conducted in order to examine the data

and samples obtained through the field work:

1-2-1 Geochemical Analysis

1,524 samples for geochemical survey (608 of the reconnaissance and 916 of the detailed) were analyzed on copper and molybdenum. The assay was done by Maria Lau, a skilled geochemical analyst in Peru, and the results after Maria Lau were further checked up by the Central Research Laboratory of Mitsui Mining and Smelting Co., Ltd., Tokyo.

1-2-2 Ore Assay

77 ore samples (67 of the detailed survey and 10 of the reconnaissance) were assayed. The work was entrusted to the C. H. Plenge Laboratory in Peru.

1-2-3 58 rock specimens (35 lavas, 10 intrusives, and 8 others) were analyzed in respect of 13 major chemical constituents as shown in the Appendices.

1-2-4 Age Determination of Igneous Rock

12 samples of igneous rocks (6 intrusives, 5 lavas and 1 tuff) were dated by the potassium-argon method.

1-2-5 Pollen Analysis

Pollen analyses of 4 samples taken from lake sediments were done by the KOH-HF-Acetylolysis method.

1-2-6 Property Test of Petroleum

A property test of the Islaicocha crude oil was done and the mixed water of oil was analyzed qualitatively.

1-2-7 Microscopic Observation

155 thin sections of various rock specimens and 14 polished sections of ore samples were examined microscopically.

1-2-8 X-ray Diffractive Analysis

18 specimens of minerals and rocks were investigated by the X-ray diffraction method for the purpose of mineral identification.

1-2-9 Fossil Identification

40 fossiliferous samples were studied, which were mainly taken from the Mesozoic limestone and the Tertiary lake sediments.

CHAPTER 2 GEOMORPHOLOGY

2-1 Classification of Landform

The present area may, as outlined in the last report, be divided geomorphologically into three units; the Western Cordillera, the Yauri Basin, and the Laramani Massif (Fig. 3).

They are considered to have been formed through their respective histories, not only geomorphologically but also geologically, as described below.

2-2 Western Cordillera

This region may be defined as the western plateau mostly at elevations of more than 4,500 m. S. L., being covered largely by the thick volcanics, and occupying the greater part of the Velille Quadrangle.

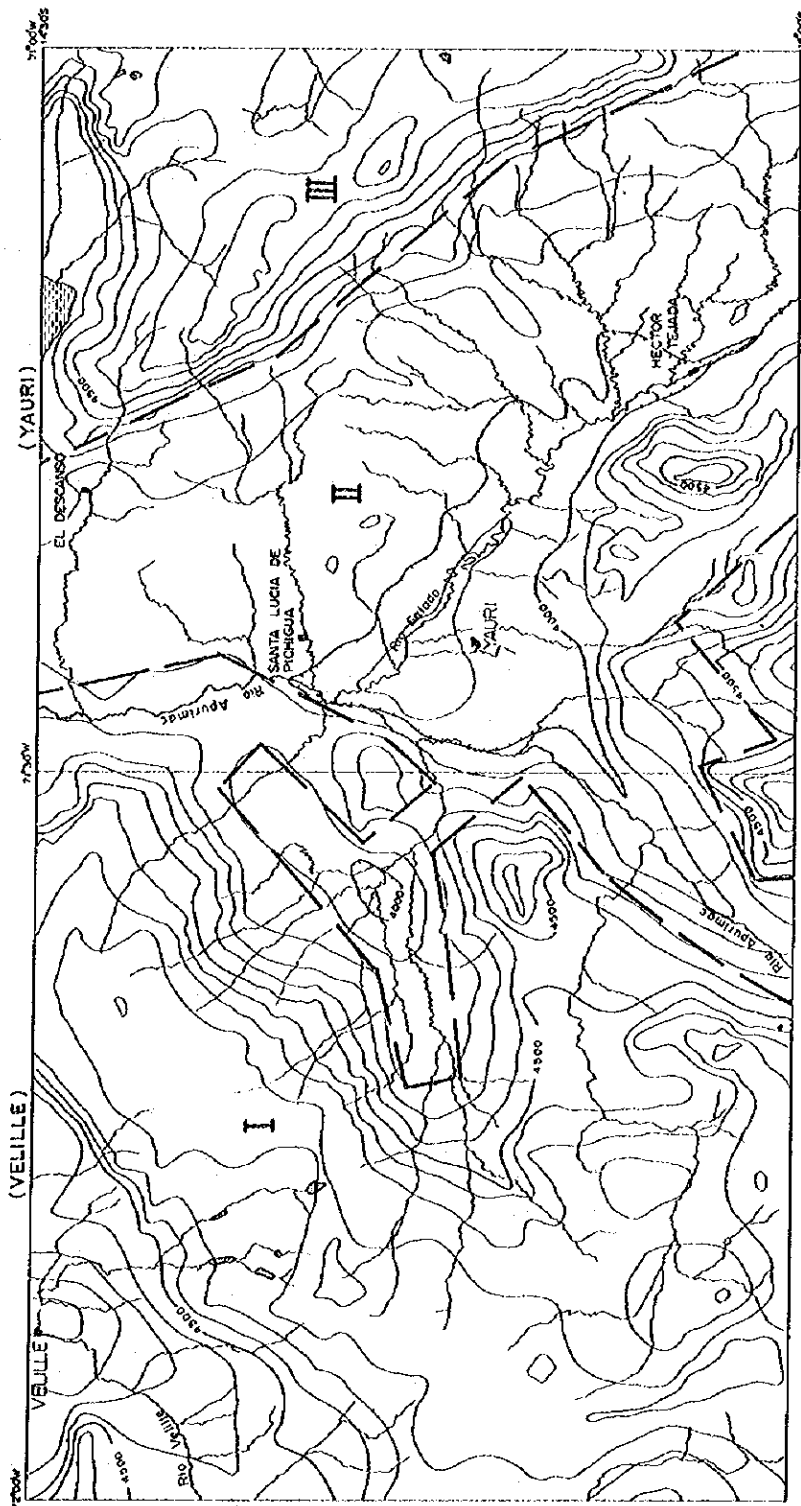
The volcanic activity of the region is considered to have been repeated intermittently since the Early Tertiary until the Pleistocene, and during its pauses, the erosion seems to have taken place. Among such activities, those which made the foundation of the present topography are considered as the erosion after the Tacaza volcanism and the subsequent deposition of the Sencca volcanics.

The post-Tacaza erosion may probably be correlated to the "Stage 1 of Puna erosion" after N. D. Newell (1949), and it appears to have made a gently undulated erosion surface at present elevations from 4,200 to 4,700 m. S. L.

This erosion surface has possibly been flattened further by the deposition of the Sencca volcanics, and formed into such a plateau of some 4,700 m. S. L. as seen in the central part of the present region.

The Plateau has been considerably modified by the subsequent local erosions

Fig. 3. Geomorphic Division of the Yauri Area by Summit Level



LEGEND

- | | |
|--------------------------|-----------------------------|
| Geomorphic regions | Summit level |
| I The Western Cordillera | By 4 kilometers square grid |
| II The Yauri Basin | Contour interval 100 meters |
| III The Laramani Massif | |

(Pleistocene glaciation and recent fluviraption) and also by the deposition of the Pleistocene Barroso volcanics.

The fluvial erosion is distinctly marked in the drainage of Rio Velille (a branch of Rio Apurimac) of the northern part of the region and along the contact with the Yauri Basin. Especially, the erosion by Rio Velille has reached up to a depth of 500 to 1,000 m., resulting in the wide exposure of Mesozoic sediments and intrusives which were the base of the volcanics.

The Barroso volcanics generally make the scattered high summits at elevations from 4,800 to near 5,000 m. S. L., but some of the lavas, as seen at the southwestern corner, might have flown down along the newly cut hollows, suggesting that the local erosion was already in progress at the Barroso time.

The evidences of glacial erosion mainly remain in the high part of more than 4,500 m. S. L., especially in the southern part of the region.

2-3 Yauri Basin

The Yauri Basin is a large pampa at an elevation of about 4,000 m. S. L. with some hills, stretching in most of the Yauri Quadrangle and the eastern part of the Velille.

The morphologic history of the Yauri Basin is probably as follows:

- 1) Peneplanation after the deposition of Puno group.
- 2) Construction of a large graben structure in the eastern part of the present Yauri Basin due to faulting of the NNW-SSE trend, and possible start of the lake sedimentation (Lower Descanso formation).
- 3) Westward expansion of the Basin due to down-faulting of the NE-SW trend and the rejuvenation of the NNW-SSE trending faults especially

to the west of the graben.

- 4) Deposition of the Pliocene lake sediments (Upper Descanso and Yauri formations).
- 5) Superficial modifications by fluvial erosion since the Pleistocene to the present time.

The post-Puno peneplanation may be correlated to the "Stage 1 of Puna erosion" by N. D. Newell (1949).

The Yauri Basin was evidently formed prior to the Sencca volcanism, because the Upper Descanso formation is of the same age as the Sencca volcanics according to the K-Ar age determination. Further, its first down-faulting (construction of the graben) have probably preceded the Medial Tacaza volcanism (a K-Ar age; 55 m. y.), since the field relation seems to suggest that the NNW-SSE trending fault bounding the eastern limit of the Yauri Basin is older than the Middle Tacaza volcanics.

The faults are not directly observed along the western border of the Basin, but the conspicuous morphologic trends surrounding the west side of the Basin suggest their presence. Moreover, a clear fault structure has been detected along the western margin of the graben by the present geophysical survey.

2-4 Laramani Massif

The Laramani Massif is a mountainous region at elevations from 4,200 to near 5,000 m. S. L. , occupying the eastern part of the Yauri Quadrangle. The highest peak, Cerro Laramani, has an elevation of 4,937 m. S. L.

This region lies between both subsided zones, Yauri Basin and Interandes Valleys, and its clear morphologic trend of the NNW-SSE to NW-SE seems due to the control of the well-developed faults.

Rocks constituting the region are mostly the Early Tertiary Puno group and the Mesozoic formations, and the volcanics here are, in contrast to the Western Cordillera, only of the Middle Tertiary which are poorly scattered along the faults.

The surface of the Laramian Massif is remarkably dissected in comparison to the other two regions. This suggests that the present region has been suffered from a long-range erosion since its uplift or the depression of the Yauri "graben" until today.

CHAPTER 3. GEOLOGY

3-1 Stratigraphic Summary

In the present survey, no time was available for visiting representative geological sites in the adjacent areas to ascertain their geological features. The present stratigraphic correlation and naming of the formations, therefore, were done only by referring to published papers, stratigraphic columns, and geological maps by Jenks (1948), Newell (1949), Marrocco and Del Pino (1966), Bellido (1969), Peralez (1970), Vargas (1970), and Audebaud and Pecho (1970).

Rock formations known within the area are given in Table 1-1.

The oldest rock found in the area surveyed may be the Coporaque red sandstone-conglomerate formation. It is covered by the Early Tertiary Tacaza volcanics unconformably, and lithologically similar to the Mitu group or the Ambo group of the Upper Palaeozoic. Its distribution, however, is very limited, and the stratigraphic correlation could not be fully worked out. Hence, the tentative name, "Coporaque formation", has been newly given to this red clastics after the "Coporaque village" in the vicinity of which it distributes.

The definite record of sedimentations and volcanic activities in this area is started from the later Mesozoic. But since the east and west sides of the Yauri Basin remarkably differ both stratigraphically and lithologically from each other, formations were arranged in two stratigraphic sequences (Table 1-1).

The followings are the stratigraphic sequences correlated mainly from their lithologic similarities on the basis of the above-mentioned literatures:

Table I-1 Generalized Columnar of the Yauri Area

Western side of Yauri basin					Eastern side of Yauri basin					
Geological age		Geological units		Columnar section	Description	Geological units		Columnar section	Description	
CENOZOIC	Quaternary	Recent	Alluvium, talus etc.		Gravel, sand & clay	Alluvium, talus etc.			Gravel, sand & clay	
		Pleistocene	Morain & fluvio-glacial deposits		Gravel, sand & clay deposits due to glaciations	Morain & fluvio-glacial deposits			Gravel, sand & clay deposits due to glaciations	
			Barroso Group 200m 150m			Andesite, basaltic andesite, tuff-agglomerate & tuff				
	Tertiary	Neogene	Pliocene	Yauri Formation (80m)		Tuffaceous sandstone, calcarenite & tuff with fossils	Yauri Formation (80m)			Tuffaceous sandstone, calcarenite & tuff with fossils
			Miocene	Sencca Volcanics (450m+)		Rhyolite, dacite, welded tuff & tuff	Upper (60m)			Light brown to white massive tuff & tuffaceous sandstone
		Upper (250m)		Stage 2 of Puno erosion	Lower (500m)			Tuffaceous sandstone & conglomerate		
		Palaeogene	Oligocene	Descenso Formation		Porphyritic trachyte, dacite, pyroclastic rocks with thin basalt flow at top	Descenso Group			
				Upper (400m)			Middle			
	Eocene		Middle (1500m+)		Upper part: Fine grained basalt & trachy andesite	Middle			Gray brown trachy andesitic lapilli tuff & basalt	
		Lower (250m)		Lower part: Porphyritic trachy andesite, pyroclastic rocks & tuff	Lower					
	Palaeocene	Tacaza Group	Upper (1000m)		Upper part: Pale green tuff breccia, lapilli tuff & tuff	Upper (3000m)			Reddish brown conglomerate, sandstone & shale with rhyolite flow & tuff near the top	
			Lower (1000m)		Lower part: Reddish brown sandstone with agglomerate	Lower (3000m)			Reddish brown conglomerate, sandstone & sandy shale	
		Puno Group							Reddish brown sandstone intercalated with shale	
	MESOZOIC	Cretaceous	Upper			Munõñi - Colacucho Formation (500m+)			Upper part: Gray shale intercalated with silicious sandstone	
			Lower		Gray to dark gray massive limestone with chert nodules & a little microfossils	Maha Formation (Ayabacas) (500m+)			Lower part: Red shale intercalated with Ayabacas Limestone with abundant fossils	
Murco Formation (600m+)			Red to greenish gray sandstone & shale	Huancaña Formation (400m+)			Red sandstone intercalated with conglomerate			
Jurassic		Upper	Yura Group	Hualhuani Formation (900m)	Pale gray quartzite intercalated with thin beds of black shale					
PALAEOZOIC	Permian?	Upper	Coporaque Formation		Reddish brown sandstone intercalated with conglomerate & rare brown shale					

The sequence of the eastern side of Yauri Basin consists of the Huancané red sandstone formation of the "Lower or Middle Cretaceous"; the Moho formation (mainly Ayabacas limestone) of the "Middle Cretaceous"; the Cotacucho - Muñani sandstone-shale formations of the "Upper Cretaceous"; the Puno red group of the "Early or Middle Tertiary"; and the volcanic Tacaza group of the "Middle or Late Tertiary". The Puno group is covered by the "Pleistocene" lake sediments in the Yauri Basin.

That of the western side of the Basin is composed of the Coporaque formation; Hualhuani quartzitic formation (the top of Yura group) of the "Upper Jurassic or Lower Cretaceous"; the Murco shaly formation of the "Lower Cretaceous"; the Tacaza volcanics; the volcanic Seneca formation of the "Late Tertiary"; and the volcanic Barroso group of the "Pleistocene". Lake sediments cover the Tacaza volcanics and older rocks in the Yauri Basin.

Although the stratigraphic columns of the area were, thus, established in reference to the geological literatures, there may still exist some chronological problems as shown by the results of age determination on the intrusive and volcanic rocks by means of the K-Ar method.

For instance, the gabbro sampled from the Tintaya batholith near the head of Quebrada Coroccohuayco in the southern part of Yauri Quadrangle was dated as 144 m. y. (the end of Jurassic age) and the quartz diorite sample from the Vellille batholith near the Vellille town gave a measured age of 105 m. y. (the end of Early Cretaceous) in spite of the fact that the both penetrate the Ferrobamba limestone which is correlated to the Arcurquina limestone of the Arequipa Quadr-

angle, being estimated to the Albian stage. If the above K-Ar ages correctly indicate the ages of the intrusives, the formation of the Ferrobamba limestone should be dated back at least to the "Upper Jurassic".

In the results of age determination for the volcanic rocks, the lavas of the Upper Tacaza volcanics indicated the ages from the Eocene to the beginning of the Miocene, and a lava sample of the Middle Tacaza was dated at the beginning of Eocene time.

The stratigraphy described in this report is, therefore, of a preliminary nature, and further examinations, especially on chronologic problems, are required.

3-2 Coporaque Formation

3-2-1 Name and Definition

A new name, the Coporaque formation, has been given to the red formation of an unknown age which is distributed only around the village of Coporaque in the southeastern Vellile Quadrangle.

3-2-2 Distribution

This formation is exposed as several small inliers isolated from one another near the village of Coporaque. The main exposures are found at three places; one at the Puente Oquero 4 km north, a second 2 km west, and a third 6 km southwest of Coporaque.

This is covered by the Tacaza group, Seneca and Descanso formations of the Tertiary unconformably, and is penetrated by a small stock of granodiorite and several porphyrite dykes.

3-2-3 Lithology and Structure

Of the said exposures, the ones at the Puente Oquero and the west of Coporaque are mainly composed of reddish-brown hard arkosic sandstone intercalated by thin conglomerate and shale layers of the same colour. The conglomerate contains pebbles, 2 to 4 cm in diameter, of white quartzite, pegmatite quartz, older red granite, and rare volcanics in a matrix consisting of reddish-brown sandstone. Some 90% of pebbles are quartzite and massive quartz. A synclinal structure with the axis of NW-SE direction is presumed between the two exposures.

The outcrop southwest of Coporaque is composed of an alternation of reddish-brown conglomerates and sandstones, the volume ratio of which is roughly 1 : 1. The rocks of this exposure are possibly lower in stratigraphic situation than those of the said exposures.

The thickness of this formation is more than 1,700 m according to the estimation from the geologic profile.

3-2-4 Age and Correlation

The Coporaque formation is definitely pre-granodiorite, and may probably be pre-Ferrobamba as no pebbles of the Ferrobamba limestone are found in it.

It is pretty similar to the Mitu red clastics lithologically, but there is no decisive evidence that they can be correlated each other. An impression fossil like Pteridophyta was recognized at the outcrop of Puente Oquero, but it could not be identified.

3 Hualhuani Formation of Yura Group

3-1 Definition

Jenks (1948) gave the name of "Yura formation" to the Upper Jurassic which was distributed in the vicinity of Yura of the Arequipa Quadrangle. Later, Wilson and Garcia (1962) subdivided it into two formations, lower shaly sequence of the Upper Jurassic and upper quartzitic sequence of the Lower Cretaceous(?), thereby established the "Yura group".

The Hualhuani formation, essentially consisting of massive quartzite and representing the uppermost section of the Yura group, can be easily distinguished by its characteristic lithology.

The Hualhuani formation under the present survey was established on the bases of its lithology and its stratigraphic relation with the Ferrobamba limestone described later.

3-3-2 Distribution

The formation is exposed in the Tintaya region of the southern Yauri Basin mainly in the form of roof pendants of the batholithic intrusive mass. It is covered partially by the Murco formation conformably and mostly by the Ferrobamba unconformably.

3-3-3 Lithology and Structure

The Hualhuani formation is made up of massive quartzite intercalated by thin layers, generally 5 to 10 m thick, of gray to black shale.

The quartzite consists of medium to fine grains of quartz with minor amount of magnetite and, occasionally, of feldspar grains. Its colour is light

brown to white where weathered, and light gray on the whole in the fresh part. The quartz grains are generally inlaid in a mosaic pattern by cementation of silica and later re-crystallization, forming characteristic massive and hard rock. However, sandy quartzite which shows under-developed re-crystallization still remains locally, often indicating cross-bedding.

The quartzite is hardly affected by contact metamorphism, but the shale generally becomes slaty and is locally metamorphosed into phyllite along its contact with the batholithic intrusives.

Monzonitic porphyries of the later intrusion often give this formation conspicuous hydrothermal alteration and copper mineralization of dissemination-type as seen at Quechua in the southern part of Tintaya region.

The formation is structurally controlled by the NNW-SSW to NW-SE trending folds, being exposed mainly along the crest of anticlines in the Mesozoic formations.

The thickness of this formation is hard to determine since it is known in the form of roof pendant only, but seems more than 900 m according to the estimation from the geologic profile.

3-3-4 Age and Correlation

This formation is very possibly correlative of Huancané formation in the eastern side of the Yauri Basin.

No fossil has been found from the formation in the present area. It is correlated to the Lowest Cretaceous by Wilson and Garcia (1962) et al., but it might have been formed at the Upper Jurassic or earlier as the gabbro taken

taken from the batholith invading it was dated as 144 m. y. by the K-Ar method.

3-4 Huancané Formation

3-4-1 Definition

According to Newell (1949), the features of the Huancané formation in the Titicaca area are as follows:

"This formation overlies the Muni formation and underlies the Moho formation conformably. Generally it consists of pink or buff, massive sandstones, locally "quartzitic", with little or no interbedded shales. Westward, the Huancané sandstone is coarser and more generally conglomeratic where it appears to be represented by coarse red conglomerates in the region of Languillas. Most of the coarse materials of conglomerate is derived from the erosion of underlying local Jurassic and Devonian rocks on which it rests, abounding in cobbles of quartzite. A single pebble of reddish andesite porphyry was discovered at the base of the formation near the village of Ayabacas."

The Huancané formation under the present survey was established by taking into account these lithologic features as well as its relation with the Moho formation.

3-4-2 Distribution

The Huancané formation crops out locally on the eastern side of Cerro Chuspine and on the southern shore of Lago Langui Layo in the Laramani Massif.

To the east of Cerro Chuspine, the formation is overlain by the Ayabacas limestone of the Moho formation and the conglomerate of the Lower Puno formation unconformably. This and the lower Puno formations are also in contact with a

fault along their west-side boundary.

On the southern shore of Lago Langui Layo, it is covered by the Lower Puno formation unconformably.

3-4-3 Lithology and Structure

The formation to the east of Cerro Chuspine is mainly composed of red to crimson sandstone intercalating a conglomerate layer of 8 m thick. The sandstone, medium to coarse-grained, is rich in quartz grains, and often contains rounded pebbles of quartzite and massive quartz (vein quartz or pegmatite?). The formation here shows an anticlinal structure with the NW-SE bearing axis.

Along the south margin of Lago Langui Layo, it consists of an alternation of reddish pebble-conglomerates and coarse to medium-grained sandstones, striking NW-SE to NNW-SSE, and dipping southwestward. The conglomerate is mainly composed of quartzite and limestones different from the Ayabacas, and can be easily distinguished from the overlying Puno conglomerate by the different rock types of the coarse materials.

The thickness of the formation is estimated for more than 600 m from the geologic profile.

3-4-4 Age and Correlation

This is lack of fossils, and what is known is only the fact that it is evidently pre-Moho.

It can be correlated with the Huancané formation of the Titicaca area from the lithologic similarity and the relationship to the Moho, but Newell (1949) too, mentions about its age only that "the general stratigraphic position

indicates Early or Medial Cretaceous Age".

3-5 Murco Formation

3-5-1 Definition

The Murco formation was established by Jenks (1948) in his investigation of the Arequipa Quadrangle, of which characteristics he has described as follows:

"This formation overlies the Yura clastics and underlies the Arcurquina limestone. It is a sequence of red, light to dark gray, and green shales and white, light tan, brown or reddish sandstones, with some thin conglomerates and gypsum beds. Shale beds form more than 50% of the Murco formation. Due to the rather high proportion of soft and friable shale, the formation as a whole is less resistant to erosion than the underlying Yura and the overlying Arcurquina rocks. Most of sandstone beds are cross-bedded, and in some beds cross-bedding is developed on a large scale. Ripple marks are abundant."

The Murco formation under the present survey has been established by taking into consideration of the above stratigraphic relation and lithologic characteristics.

3-5-2 Distribution

This formation crops out locally in the Tintaya region of the southwestern Yauri Quadrangle, and rather widely in the vicinity of the Velille town in the northwestern Velille Quadrangle.

In the Tintaya region, it rests on the Hualhuani quartzite conformably, and is covered by the Ferrobamba limestone, the relation between this and the Ferrobamba formations appears conformable wherever the both occur together,

but since the formation is often missing due to thinning, the actual relation may be in disconformity. Its distribution in this region is mostly omitted from the present geological map as it is too thin to be marked on.

In the Velille Quadrangle, the Murco formation occur at two localities 3 km and 10 km to the east of the town of Velille, where it is overlain by the Ferrobamba limestone and is intruded by the batholithic intrusive mass.

3-5-3 Lithology and Structure

It is mainly composed of red to greenish-gray shale in the Tintaya region, but makes an alternation of gray to greenish gray sandstones and shales on the top of the hill 6 km south of Tintaya Mine.

The formation exposed 3 km east of Velille is an alternation of sandstones and shales with gray, light green or blue colour. The shale, being generally gray to bluish-green, become slaty near the contact with the batholithic intrusive rock, and is locally metamorphosed into the sericite phyllite or schist. The sandstone, mainly forming the upper part of alternation, is gray to greenish-olive in colour, and fine to medium-grained in size. Here it is controlled by a synclinal structure having the NNW-SSE bearing axis.

The outcrop 10 km east of Velille is composed of reddish-brown shale lower, and gray siliceous sandstone upper. The upper sandstone is intercalated by thin layers of shale of the same colour. This outcrop too, is a roof pendant same as that cited afore, and the beds are changed into hornfels along their contact with the intrusives.

The thickness in the northwestern Velille Quadrangle is estimated for more than 600 m, but it is less than 100 m thick and often thins out in the

southern Yauri Quadrangle.

3-5-4 Age and Correlation

As no fossil is found in the formation, nothing can be said about its age except that it is pre-Hualhuani and post-Ferrobamba. Jenks (1948) and Bellido (1969) et al. have considered it as the Lower Cretaceous from its stratigraphic position.

No formation is found which can definitely be correlated with the Murco to the east of Yauri Basin, but the upper part of the Huancané may be a correlative of it judging from the stratigraphic position.

3-6 Moho Formation

3-6-1 Definition

Newell (1949) said: "the Moho formation overlies the Huancané formation (conformably?) and underlies the Cotacucho group unconformably. The lower part of this formation is an alternation of red shales and sandstones intercalating the Ayabacas limestone near the base, and the upper part consists mainly of an alternation of gray shales and gray to white siliceous sandstones. To the southwest of Lake Titicaca, it is the highest Cretaceous unit preserved after pre-Tertiary erosion. The Ayabacas limestone is exceedingly persistent and surprisingly uniform in its details. Relatively weak, or "incompetent", to compression, the Moho formation has yielded in the form of intricate isoclinal and recumbent folds and low-angle compression faults, whereas subjacent and superjacent strong formations are very much less profoundly affected."

The Moho formation under the present survey is established mainly

on the basis of lithological similarity from the characteristics mentioned above.

3-6-2 Distribution

This is widely distributed over the Laramani Massif in the eastern part of the Yauri Quadrangle, but it is not found to the west of the central Yauri Basin.

It overlies the Huancané formation conformably in aspect, and underlies the Lower Puno formation unconformably. It is also penetrated by the granite porphyry.

3-6-3 Lithology

The Moho formation of this area is mostly the lower part (especially the Ayabacas limestone) based on the Moho section by Newell (1949), and the rock having a possibility of the upper Moho is found only in one small exposure as the white to crimson siliceous sandstone near Hda. Soclla Grande at the northeastern corner of the area. As this siliceous sandstone too, however, is exposed only in a very small scale, less than 100 m², at the boundary between the Ayabacas limestone and intrusive rock, it is difficult to correlate definitely to the upper part of the Moho. Presumably, the upper part of the Moho formation in the area was largely truncated by "pre-Tertiary erosion".

Most of the Moho formation found in the area is the Ayabacas limestone, and somewhat large exposures of red shale are recognized only near the center of eastern bordering area.

The Ayabacas limestone is generally compact and massive with a wide range of colours from gray or grayish-yellow to light blue. One of the characteristics of this limestone is that it is rich in fossils which suggest coral or

littoral origin. Although collected fossils could not be identified thoroughly due to their poor preservation, they are largely composed of mollusca such as *Ampullina* sp., *Ostreidae* sp., *Neithea* sp., *Aptyxiella*(?) sp., *Leptochondria*(?) sp., *Belemnite*(?) sp. (see Table I-19). Especially *Aptyxiella*(?) sp. indicates its characteristic multiplication in the coral environment. Also many fossils which might be identified to be fragments of coral and spines of sea urchin have been found in the limestone. The littoral origin of the Ayabacas limestone have been suggested by Newell (1949) as well as Bellido (1969).

3-6-4 Structure

The formation is controlled by faults of the NW-SE direction, and foldings with the axes of same bearing.

Most of faults are steep and normal type, the west side of them being down-throw. No large thrust faults have been confirmed in the present survey.

As for folding, the said ones control the regional structure, but many small foldings with the NE-SW trending axes overlap them, causing locally rather complicated structures. However, such recumbent and isoclinal folds as Newell (1949) recognized in the Titicaca area (especially in the Putina synclinorium) have not been found out in the present area.

3-6-5 Age and Correlation

Although any definitive fossils have not been discovered to determine the age of the Ayabacas limestone, the following fossils suggest that it was very possibly formed during some time between Jurassic and (Early) Cretaceous ages:

- 1) Pectinidae: *Neithea* (s. l.) sp.

This specimen appears very close to *Neithea* (s. s.) which is indicative the Lower Cretaceous. However, it should be noted that in *Neithea* (s. s.) ribs on the right-side shell have different heights, whereas the ribs of this specimen are nearly even.

2) Naticidae: *Ampullina* s. p.

Ampullina occurs since the Triassic, but is mostly found in the later Mesozoic.

3) Nerineidae: *Aptyxiella*(?) s. p.

Aptyxiella is found from the Jurassic to the Cretaceous.

Newell (1949) considered the Moho as the Middle Cretaceous.

This is correlated with the Ferrobamba limestone lying in the east side of Yauri Basin, and with the Arcurquina limestone of the Arequipa Quadrangle.

3-6-6 Thickness of Ayabacas Limestone

The Moho formation of the area is composed mainly of the Ayabacas limestone as mentioned previously, and its thickness is estimated for more than 500 m from geologic section.

On the other hand, the thickness of the Ayabacas in the Titicaca area has been measured as 20 or 30 m only by Newell (1949) although the total thickness of the Moho formation has been estimated for some 800 m.

Such a difference in thickness of the Ayabacas can be well understood from the following explanation by Bellido (1969).

He says, "the Moho group of the Titicaca area becomes more calcareous

toward the west and possibly changes into the Arcuquina limestone of the Arequipa area, and northward into the limestone sequence of the Cuzco and Aprimac areas."

3-7 Ferrobamba Limestone

3-7-1 Definition

It is said that geologists of Cerro de Pasco Copper Corporation gave this name to the limestone which is distributed pretty widely over the Western Cordillera including the western part of the present area, and is correlated with the Ayabacas and Arcuquina limestones.

Since the limestone west of the Yauri Basin is lithologically different from the Ayabacas limestone, the Ferrobamba formation has been established to distinguish the two limestones.

3-7-2 Distribution

The Ferrobamba limestone, like as the Yura and Murco rocks, crops out mainly in the Tintaya region of the southwestern Yauri Quadrangle and in the vicinity of the Velille town of the northwestern Velille Quadrangle.

It overlies the Murco and Hualhuani formations unconformably, and underlies the Tacaza and younger beds. It is intruded by the batholithic intrusives, being usually exposed as roof pendants.

3-7-3 Lithology and Structure

This formation is composed of massive and compact limestone with little change of lithofacies throughout the distributed area. The colour is mainly gray, dark-gray and blueish-gray, but is changed from light-gray to white along

its contact zone with the intrusives. Mineralogically, it generally consists of re-crystallized xenomorphic calcite with minor amounts of dolomite and quartz.

The limestone often contains small nodules of chert, and is sometimes intercalated with thin layers of light-gray sandy limestone and black calcareous shale.

Fossils in this limestone are mainly contained in the cherty nodules, and they are quite different from the fossil fauna in the Ayabacas limestone, being composed of small foraminifera and planktons, etc. Judging from the contained fossil fauna as well as its lithologic features, this limestone may probably not be of the littoral origin such as the Ayabacas but of a deeper sea type.

In the Tintaya region, the formation repeats synclines and anticlines having axes of the NNW-SSE to NW-SE bearing, and is cut by two large faults of the NNW-SSE and NE-SW directions respectively.

Near Velille, it is mainly controlled by a comparatively large syncline with the N-S trending axis, but minor folding of the E-W direction overlap on this synclines diagonally, resultantly extending in the N-S direction on the whole with repeating small anticlines and synclines of the E-W trend. There is a N-S striking fault which cut the formation.

3-7-4 Age and Correlation

Fossils collected from this limestone in the last survey suggest the correctness of its correlation to the Ayabacas limestone in geologic time as reviewed below.

1) Foraminifera: Polymorphinidae

This occurs since the Triassic to the present.

2) Foraminifera: Oolininae

This is of the age from the Jurassic to the Cretaceous.

3) Tintinoids: Carponella sp.

This is a plankton belonging to Ciliatae which occurs characteristically in the Upper Jurassic and Lower Cretaceous of the European Alps mountains.

3-8 Muñani-Cotacucho Formations

3-8-1 Definition

An alternation of sandstones and shales is present at the northeastern corner of the Yauri Quadrangle, and any definite evidence for the correlation could not be obtained by the present survey due to its limited distribution within the area surveyed. In this respect this should be treated as unknown sequence. However as this continues to the "Muñani-Cotacucho formations" of the adjacent Sicuaní Quadrangle which were defined by Audebaud and Fecho (1970), this, too, has been considered as the Muñani-Cotacucho tentatively.

3-8-2 General Description

The formations are intruded by the granite porphyry and covered by the glacial and alluvium deposits.

They are essentially an alternation of grayish-buff to reddish-brown massive sandstones and gray to blueish-gray shales, and the shale is metamorphosed into hornfels along its contact zone with the intrusives.

They form a synclinal structure of the NNW-SSE axis.

The thickness of them is estimated for more than 500 m from the

geological profile.

3-9 Puno Group

3-9-1 Definition and Discussion Concerned

A thick section of reddish conglomerates, sandstones and minor shales is found from the Laramani Massif to the eastern fringe of the Yauri Basin. Evidently as most of these red clastics cover the Moho formation (especially the Ayabacas limestone) unconformably, they are correlated to the Tertiary Puno rocks lithologically as well as stratigraphically.

However, Audebaud and Pecho (1970) reported a wide distribution of the Upper Permian Mitu red clastics in the Sicuani Quadrangle, and Bellido, who inspected this area, pointed out the lithologic similarity of these rocks to the Mitu group. The followings are the reasons and bases for correlating these red clastics with the Puno group in the present survey:

1) Lithological Difference between Puno and Mitu (Basis 1)

The lithologic characteristics of the Puno group given by Newell (1949) can be summarized as follows:

"The Puno group in the Titicaca area consists mainly of conglomerates, tuffaceous and arkosic soft sandstones with subordinate beds of sandy shales. The colour is generally pink, chocolate-gray and, less commonly, greenish-gray or light-olive hues. Generally the rocks are distinctly more somber and darker than the red beds of the Cretaceous. The conglomerates contain abundant rounded and subangular pebbles and cobbles of andesite porphyry and basalt, except in areas where the Puno group rests directly on the Devonian. These

rocks, because of the contained volcanic materials, are readily distinguished from the red sandstones and shales of the Permian and Cretaceous, which are also somewhat arkosic, but are not known to contain appreciable quantities of volcanic materials near Lake Titicaca. Cobbles containing Jurassic and Cretaceous fossils are common in Puno conglomerates."

Bellido (1969) describes on the general characteristics of the Puno group, "the Puno group is of a continental origin, and consists of grayish-red arkosic and tuffaceous sandstones, intercalated by shales and thick conglomerates of very variable origins."

On the other hand, the lithological characteristics of the Mitu group by Bellido (1969) are as follows:

"The Mitu group is continental, and consists of reddish-brown and maroon conglomerates, sandstones and shales, intercalated by thick pyroclastics and lava flows of greenish, maroon and purplish colours."

Judging from the said lithologic descriptions, the following points may be important in order to define the red rocks of the area.

- i) The existence of volcanic materials can not be considered essential for the discrimination, but the presence of lava flows may imply the Mitu group.
- ii) The existence of gravels of Jurassic or Cretaceous rocks in conglomerates indicates the Puno group definitely.

2) Distributive Characteristics of Puno Group (Basis 2)

Newell's (1949) description on the distributive features and structural controls of the Puno group is as follows:

"The Tertiary Puno group broadly truncates Middle Cretaceous (Moho) and all older rocks, in places resting directly on the Devonian. More recent folding and faulting have resulted in widespread low-angle overthrusts and bedding plane thrusts at the base of the competent sandstone of the Tertiary. Displacement along thrust faults is most evident where strong Tertiary rocks overlie the structurally weak Moho group, and in such areas the contact between two series of rocks is commonly a thrust zone marked by profound trituration of the Cretaceous rocks. The character of the Puno group indicates a region of high relief at the beginning of Puno deposition, and during much of the time of deposition, with streams of high transporting competency."

Judging from the above characteristics of Puno deposition, the "contact relationship" can only be the basis of determination of the Puno, as the Puno rocks may lie in lower places topographically than where the Moho and older rocks crop out.

3) Reason for Correlation of Red Beds with Puno Group

The red conglomerates of the area are generally rich in volcanic materials, but also contain commonly the pebbles or cobbles of the Ayabacas limestone with characteristic fossil fauna except for a part of conglomerates as described below.

The conglomerate exposed some 5 km east of Descanso consists of subangular cobbles and pebbles of volcanic rocks only, but its southward extension, near Hda. Cassillo, contains cobbles and pebbles of the Ayabacas limestone.

In the southern part of the Laramani Massif, there is a thick conglomerate consisting of rounded to subangular pebbles and cobbles of volcanic materials only which underlies the definite Puno conglomerate and is in contact with the Ayabacas limestone by a fault. As there is neither unconformity nor fault between this and the definite conglomerate, this agglomerate-like conglomerate, too, is considered as the Puno group.

Although the Puno group of the area has been thus established by lithologic as well as stratigraphic examinations, the source of volcanic materials is still unknown. The Mitu group now distributed broadly in the north might be a source of the volcanics as Newell (1949) says that the pre-Puno truncation reached more than 2,500 m in the Putina synclorium.

3-9-2 Distribution, Lithology and Structure

As mentioned above, the Puno group is widely distributed from the Laramani Massif to the eastern part of the Yauri Basin, and consists of reddish conglomerate, sandstone and sandy shale.

It is classified into two formations: the Lower cobble-conglomerates, and the Upper consisting of an alternation of pebble-conglomerates, sandstones

and sandy shales. An inclined unconformity separates the Lower from the Upper formation.

The thickness of each of the two is estimated for more than 3,000 m maximum, totaling more than 6,000 m.

(1) Lower Puno Formation

This is widely distributed over the Laramani Massif, but is not exposed in the Yauri Basin. It covers the Moho formation (mainly the Ayabacas limestone) unconformably and is in contact with the Huancané formation by a fault.

It is overlain by the Tacaza volcanics and the Quarternary unconformably. In the northeastern part of the Laramani Massif, a stock of granite porphyry is present, being presumably overlain by the Puno clastics. But, since no sufficient investigation has been done on the contact relation of the two, nothing definite can be said about it.

The Lower formation consists mostly of reddish-brown or brown conglomerates containing a lot of cobbles and boulders, locally intercalated by thin layers or lenses of conglomeratic sandstone. Boulders reach nearly 1 m in diameter sometimes.

The conglomerate is generally polymictic, differing in the rock types and ratio of the component gravels. But the most predominant material is volcanic rocks mainly consisting of reddish-brown porphyritic andesite, monogenetic parts of agglomerate-looking being formed locally. Other rock types of coarse materials

are limestone (mostly Ayabacas limestone) and quartzite, both rather pervading throughout the formation, and, less commonly, red siliceous sandstone, gray quartz porphyry, rhyolite and diorite.

A pebble of limestone with the veinlets of lead and zinc ores has been discovered in the northeastern part of the Laramani Massif. The geological structure which controls this formation coincides with what controls the Moho formation, but the Moho formation is generally exposed in the anticlinal zones, while this is rather distributed in the synclinal ones.

A number of small inliers of the Ayabacas limestone crop out along the crests of the anticlines in the Puno group.

(2) Upper Puno Formation

The distribution of this is controlled by two normal faults of the NNW-SSE direction, dipping steeply to the west, and being divided into three zones.

In the eastern zone, it develops along the axis of the synclinorium which is formed in the eastern part of the Laramani Massif. Here the Upper Puno formation rests on the Lower Puno with clino-unconformity. It shows the variety of lithofacies in the upper, middle and lower parts as follows, each of them showing gradual transition into the annex; lower; an alternation of reddish-brown sandstone and pebble-conglomerate, middle; mostly sandstone, upper; sandstone and sandy shale.

The conglomerate is polymictic of which pebbles are mostly rounded. The sandstone is arkosic, and the shale is sandy with dark-

red or dark-brown color, forming thin layers or lenses of 5 to 30 cm. thick in the sandstone.

In the central zone sandwiched between two faults, it is distributed over the western flank of the Laramani Massif. Here this formation shows clear clino-unconformity against the Lower Puno. The dip shows monocline in the SWW direction in the southern part, but from the central to the northern parts, both the strike and dip are variable because of local synclines and anticlines.

In the central part, it undulates in an angle of less than 10° generally in the east or west direction controlled by the said foldings of which axes trend NNW-SSE. Along the crest of anticline, the Ayabacas limestone and the lower Puno formation are exposed as small inliers, and at Islaicocha which lies at its west wing, oil seepage is present. The Upper Puno here consists of an alternation of reddish-brown arkosic sandstone and pebble-conglomerates (see Photo 2.)

The western zone of the Upper Puno lies on the west side of the NNW-SSE fault which makes a boundary between the Laramani Massif and the Yauri Basin. The general strike here is in the NNW-SSE direction, and its general dip shows ESE, and the dip decreases as the zone proceeds from the east (stratigraphically lower) to the west (stratigraphically upper). At the northern end of this zone, local synclines and anticlines are developed. It is composed of an alternation of reddish-brown to brown conglomerates and sandstones. In its lower part, the conglomerate is dominant, whereas in the upper

part, the sandstone predominates. The conglomerate is polymictic mainly consisting of rounded pebbles and subordinate cobbles of limestone, quartzite and andesite. The size of pebbles tends to decrease from the lower part to the upper, and the conglomerates of the lower part often contain boulders (up to 30 cm in diameter). Pebbles are filled with arkosic coarse sands. The sandstone is composed of arkosic and tuffaceous sands. In the northern part of the zone, it is intercalated by thin layers (10 to 50 m thick) of massive pink lapilli tuff. Although the tuff appears to be three strata, it is presumed to be of a single one showing a repetition by folding. In the southern part, it is overlain by lake sediments, and at the boundary between the eastern and the central zones, pretty thick lava flow of rhyolite is observed. In the present survey, this rhyolitic lava flow is tentatively correlated to the tuff of the north, but there is also a possibility that the lava flow may be the post-Puno volcanic rock that has erupted along the fault, although nothing definite can be said about its age.

3-9-3 Age and Correlation

The Puno group is presumed by Jenks (1948) and Newell (1949) to be correlated with the Huanca red formation in the Arequipa area.

The Huanca has been correlated, by Jenks (1949), to the Early Tertiary, while the Puno group at Lago Titicaca is assumed by Newell (1949) to have been formed during sometime between from the Early Tertiary to the Miocene(?).

In this area, the conglomerate of the Lower Puno formation contains pebbles of diorite presumably derived from the earlier batholithic intrusives, and

limestone penetrated by veinlets of lead and zinc ores. According to the conventional age correlation, the Puno formation of the area is also considered to be Tertiary.

A fossil of *Dicotyledonea*(?) has been discovered from the white tuffaceous sandstone which occupies the middle part of the Upper Puno formation, and from the reddish-brown sandstone at the middle part of the Upper formation fossils of *Rissoacea*(?) s.p. of *Gastropoda* have been discovered.

On the other hand, the lava, which is considered as Middle formation of the Tacaza group and covers the Puno group, is dated at 55 m.y. (Early Eocene age) by the K-Ar method.

It is likely, therefore, that the Puno group was mainly deposited in the Paleocene, but the sedimentation of the Lower formation may have been started at the Late Cretaceous.

3-10 Tacaza Group

3-10-1 Definition

According to Newell (1949), the name "Tacaza" has been suggested by Jenks for the older volcanics in the vicinity of Tacaza Mine about 15 km northwest of Santa Lucfa (about 150 km southwest of Yauri). Jenks describes the type-site being introduced by Newell (1949) in the following way:

"The lower part of this group consists of lava flows of pyroxene basalt, flow - breccias, agglomerates and tuffs with thick intercalations of distinctly dull red conglomerates in which both boulders and matrix are volcanic origin. In the lower third are some andesitic porphyries. The upper part consists of white dacite tuff which rests on lower basaltic member with apparent conformity.

The thickness of the Tacaza group reaches at least 3,600 m just south of the Tacaza Mine. The thickness of the upper dacite tuff is highly variable, ranging up to 310 m at the maximum. The Tacaza group covers the Puno formation with angular unconformity."

In determining the Tacaza group, these descriptions have been mainly referred to, although some differences of rock facies of volcanics have been recognized. The Tacaza group of the area is roughly divided into three formations according to the lithologic and stratigraphic differences: 1) the Lower formation consisting mainly of sandstones of volcanic materials and trachy-andesitic pyroclastics, 2) the Middle formation mainly consisting of the fine-grained and compact lava flows of alkali basalt or trachy andesite, and 3) the Upper formation mainly consisting of porphyritic trachyte or dacite and its pyroclastic rocks. Among the three, the Lower formation should be correlated to the Upper Puno formation from the stratigraphical point. In the present survey, all the products of volcanic activities during the Early to Middle Tertiary in the area are arranged together into the Tacaza group.

3-10-2 Distribution and Lithology

The Tacaza group is distributed widely over the west of the Yauri Basin, and especially in the Velille Quadrangle. In the east side of the Yauri Basin, the Middle formation of the group is scattered only along the fault. The thickness of the group varies from place to place, but the maximum thickness is estimated for more than 3,000 m.

(1) Lower Tacaza Formation

This formation is exposed in the northwestern part of Velille

Quadrangle and near the western border of Yauri Quadrangle.

i) Northwestern Part of Vellile Quadrangle

The Lower formation in this region rests unconformably on the Ferrobamba formation and batholith of quartz diorite and granodiorite, and is unconformably overlain by the Middle formation of the same group. The unconformity between this formation and batholith can be confirmed by the facts that pebbles of quartz diorite and grandiorite possibly derived from the batholith, are contained in the formation near the contact, and that it is affected by neither contact metamorphism nor alteration. The unconformity between this and the Middle formation is also indicated by the difference in structures which control the each of them. For example, this forms a syncline with an axis of WNW-ESE direction, but this structure does not control the Middle formation. In addition, at the boundary, the structures shown by the two formations cross each other obliquely, clearly showing clino-unconformity.

The lower part of this formation mainly consists of reddish-brown or brown sandstone, locally accompanied by reddish-brown agglomerate. The sandstone is generally composed of rounded grains, 1 to 2 mm in diameter, of quartz and feldspar, and fine fragments of volcanic rocks. The Upper part of this formation consists of gray to light-green tuff breccia, lapilli tuff and tuff. According to optical determination,

these pyroclastics are considered mostly the derivative of trachy andesite, although trachytic and andesitic pyroclastics are locally intercalated. In the typical tuff breccia, crystal grains of plagioclase, potash feldspar, pyroxene, amphibole, biotite, apatite and iron ores, and rock fragments consisting mostly of trachy andesite are embedded in the fine-grained matrices of the same kinds of rocks.

The thickness is estimated for more than 1,000 m.

ii) Northwestern Part of Yauri Quadrangle

The Lower Tacaza formation is exposed along the Rio Aprimac which flows in the N-S direction near the western border of Yauri Quadrangle. Here also, the formation overlies intrusive rock unconformably and is overlain by the Middle and Upper formations of the group. At the bottom of the lower formation lies basal conglomerate which mainly consists of pebbles of intrusive rock (4 km north of Pichigua). This conglomerate consists of pebbles and cobbles of intrusive, poorly sorted and less than 50 cm in size, and is intercalated by yellowish-gray or grayish-green sandstones. Above the basal conglomerate lies an alternation of conglomerate and sandstone, which gradually changes into sandstone beds, being covered conformably by an alternation of grayish-white to reddish-brown tuff breccia, lapilli tuff and tuff.

On the west side of the Rio Aprimac, the upper pyroclastics are intercalated by the lavas of trachy andesite.

III) Southwestern Corner of Yauri Quadrangle

Here the Lower Tacaza formation overlies the Mesozoic rocks, and is covered by the Upper formation of the same group and younger sedimentary rocks.

It consists of an alternation of trachy andesitic to dacitic tuff breccia, lapilli tuff and tuff, and contains neither sandstone nor conglomerate as does in the said districts. The welded structure is locally found in the lapilli tuff of the upper part of the exposure.

(2) Middle Tacaza Formation

This formation as well is distributed mainly over the west side of the Yauri Basin in the same way as the Lower Tacaza formation, but its distribution is far wider than that of the Lower formation, showing its exposures at many localities except the southwestern part of the Vellile Quadrangle where the Tacaza Upper formation and subsequent volcanic rocks are thickly accumulated. In addition, the Middle formation is distributed, though in a small scale, in the Laramani Massif of the east side of the Yauri Basin. This formation unconformably overlies the Tacaza Lower formation and older rocks, being unconformably overlain by the Upper Tacaza formation and younger rocks. The lower part of Middle formation is represented by an alternation of thick lava flows and thin pyroclastics of porphyritic trachyte and trachy andesite, and the upper part generally consists of the thick lava flows of dark-coloured, fine-grained and compact alkali basalt and trachy

andesite. The thickness is very variable in places, and a little change in the rock facies too, is locally recognized.

This formation is most dominantly exposed from the central to the southern parts of the eastern Velille Quadrangle. In this region, the lower part of this formation is not exposed, but its upper part alone, which consists of basaltic lava flows with several thin intercalated layers of essential pyroclastics, is estimated to reach the thickness of more than 1,500 m maximum.

In the northwestern part of the Velille Quadrangle, however, the lower part consists of white to reddish-brown tuff 10 to 30 m thick only, and the upper part is the lava flows of alkali basalt and trachy andesite about 200 m thick.

West of the Huatilla Pass of the Yauri-Velille auto-road, the lower part of this formation is composed of porphyritic trachyte lavas and its pyroclastics of more than 250 m in thickness, and the upper part is made up of the lava flows of compact alkali basalt and trachy andesite. While, in the vicinity of Casanuma about 5 km to the north of the pass, this formation almost thins out.

In the northwestern part of the Yauri Quadrangle, thin lavas of trachybasalt intercalate in the alternation of trachy andesitic tuff breccias and white tuffs in the lower part. In the upper part, alkali-basaltic to trachy-andesitic lava flows are intercalated by thin beds, generally 2 to 6 m thick, of brownish-purple to grayish-brown essential volcanic tuff breccia, lapillituff and tuff.

The rocks occurring in the Laramant Massif are mostly composed of brownish-violet to grayish-brown trachy-andesitic volcanic breccias, but the lava flows of dark-grayish alkali basalt is distributed in the Cerro Chaspine.

As mentioned above, the Middle Tacaza formation shows local differences in rock facies, thickness and stratigraphy. These local differences may indicate that the Middle Tacaza volcanics was produced by the repeated eruptions from the separated "craters".

A large center of this volcanic activity may probably be the region from the central part to the southeast of Velille Quadrangle where lava flows of basalt are enormously accumulated. The fact that mineralization recognized in the Tacaza volcanic rocks is concentrated in this region would serve one of the good reasons for the said presumption.

(3) Upper Tacaza Formation

The main distributed area of this formation is the high land stretching from the northeastern part to the southwest of Velille Quadrangle.

This formation rests upon the Middle Tacaza formation unconformably, and also its volcanic vents cut the Middle formation.

Although the rock facies and thickness of the Upper formation rather vary from place to place as in the case of the Middle formation, the dominant rock types are lava flows of porphyritic trachyte or dacite, and essential pyroclastics. In the region from the southeastern part to the center of the Velille Quadrangle, thin flows and pyroclastics of alkali basalt, the youngest volcanics of the Upper Tacaza, rest sporadically

on the above volcanics.

Porphyritic to vitrophyric trachyte containing abundant large crystals of sanidine up to 3 cm in diameter, and subordinate essential to accessory pyroclastics consisting of volcanic breccia, tuff breccia and lapilli tuff occur at and around the northeastern corner of the Vellille Quadrangle. Trachyte is mostly lava flow and generally alternates with pyroclastics, but some trachyte, as volcanic vents, intrudes the Middle Tacaza formation.

In the vicinity of the central Vellille Quadrangle, it mostly consists of an alternation of porphyric trachyte and its pyroclastics with thin lava and pyroclastics including scoria of alkali basalt at the top, resting on the Middle Tacaza formation with apparent conformity. The thickness of the Upper Tacaza formation here is estimated for about 250 m.

In the vicinity of Casanuma near the northern border of the Vellille Quadrangle, trachytic to dacitic pyroclastics are dominant in the Upper Tacaza, and especially its lower section is composed of thick white tuff. The thickness here is estimated for about 400 m.

In the southeastern part of the Vellille, the Upper Tacaza formation is made up of the lower alternation of tuff breccia and lapilli tuff, the middle sandy tuff and the upper lavas and pyroclastics of alkali basalt. Basalt occurs in the form of small volcanic pipes, too, and essential agglomerate accompanies it.

From the said rock facies and modes of occurrence of the formation, it is presumed that the volcanic activity of the Upper Tacaza is

represented by the eruptions of trachyte mainly in the northeastern part of Velille Quadrangle, and closed with the small-scale eruption of alkali basalt in the southwestern part of the Velille.

3-10-3 Age and Correlation

The Lower Tacaza formation may probably be correlated with the Upper Puno formation, as it, likewise the Upper Puno, is suffered from pre-Middle Tacaza tectogenesis and erosion.

The results of K-Ar age determination for the Middle and Upper Tacaza volcanics are as follows (cf. Table I-18):

- 1) Alkali Basalt of Middle Tacaza Formation
Location of Sample: Cerro Chaspine of Laramani Massif
Measured Age : 55 m.y.
- 2) Trachyte of Lower Part of Upper Tacaza Formation
Location of Sample : (A) Quebrada Altar, and (B) 1 km
West of Hda. Palomani;
Northeastern Velille Quadrangle
Measured Age : (A) 41 m.y. and (B) 38 m.y.
- 3) Alkali Basalt Near Top of Upper Tacaza Formation
Location of Sample : Huatilla Pass of Yauri - Velille Road;
Velille Quadrangle
Measured Age : 28 m.y.

Abbsolute ages of the Tertiary period measured by the K-Ar and

Sr-Rb methods are as follows (excerpts from Geological Dictionary by Helbonsha, Tokyo):

Pliocene	:	12 ± 2 to 2	m.y.
Miocene	:	26 ± 2 to 12 ± 2	m.y.
Oligocene	:	25 ± 2 to 37 ± 2	m.y.
Eocene	:	37 ± 2 to 58 ± 4	m.y.
Paleocene	:	58 ± 4 to 67 ± 3	m.y.

It is considered, therefore, that the Middle Tacaza formation was formed at Early Eocene age, and the Upper Tacaza was produced from the Eocene to the end of Oligocene (or the beginning of Miocene) ages.

The Lower Tacaza formation may probably be of the Paleocene.

3-11 Sencca Formation

3-11-1 Definition

Mendivil (1965), who surveyed the Maure and Antajave Quadrangles, gave the name "Sencca volcanics" to the rhyolitic, dellenitic or rhyodacitic pyroclastics which were correlated to the Pliocene.

The Sencca formation established by the present survey consists of the rhyolitic to dacitic pyroclastics and lava flows, overlying the Tacaza group unconformably, and underlying the Barroso volcanics unconformably.

3-11-2 Distribution and Lithology

The Sencca formation is distributed to the east of Yauri Basin, especially wider in the southern part of Velille Quadrangle.

In the southeastern part of Velille Quadrangle, it is mainly composed of white to pink, hard and compact vitrophyric rhyolite and welded tuff with white and soft tuff at the lowermost. Rhyolite contains phenocrysts of quartz, plagioclase, sanidine and minor amount of biotite, up to 3 mm in diameter, in a glassy groundmass showing spherulitic texture. Welded tuff consists of grains of quartz, feldspar and biotite, and lithic fragments of andesite and basalt in a glassy matrix with welded texture. Soft tuff is generally of a lapilli tuff, and contains vitrified pumice and lithic fragments of andesite, basalt and rhyolite, up to 10 mm in diameter. It is nearly horizontal (dipping 1° to 2° to the west ?), resting mostly on the Middle Tacaza formation unconformably. Its thickness here is estimated for about 450 m.

In the southwestern part of Velille Quadrangle, the formation consists of an alternation of lava flows and pyroclastics of rhyolite, dacite and trachyte with massive tuff at the top. Here they often intrude in the forms of small stocks, dykes, and sills. Near Esquina in the northwestern part of Velille Quadrangle, four volcanic necks (?) of rhyolite intrude the Upper Tacaza volcanics, forming plug-like small hills (see Photo. 4).

In the northeastern part of the Velille, this formation is largely eroded, and thin layers of white lapilli tuff remain only on the summits.

Near Cerro Lanco at the boundary between the Yauri and Velille Quadrangles, there is a lava dome (?) of dacite, and also dykes and sills of dacite intrude the Tacaza volcanics on the east side of dome. The date of this dacite is not precisely known, but it may be correlated with the Sencca formation from its

lithologic similarity as well as its relation to the Tacaza group.

3-11-3 Age and Correlation

A dacite lava of this formation sampled near Callanca in the southwestern Vellile Quadrangle has been dated at 7 m.y. (Middle Pliocene time).

Mendivil (1965) estimated the date of the "Sencca volcanics" lying in the Maure and Antajave Quadrangles at Middle or Late Pliocene, and the result of dating is well in accord with his estimation, too.

3-12 Lake Sediments (Descanso Group and Yauri Formation)

3-12-1 Definition

A rather thick sequence of lake sediments lies in the Yauri Basin, being separated by clear unconformities into three units; lower alternation of sandstones and conglomerates, middle acidic tuffs or tuffaceous sandstones, and upper alternation of tuffaceous and calcareous siltstones and sandstones.

In the present survey, the upper unit has been given the name of Yauri formation, and the middle and lower units have been arranged as the Descanso group with reference to the stratigraphic column of "la Zona de Espinar" by Martinez and Huarta (1965).

3-12-2 Descanso group

This is distributed widely in the northern part of the Yauri Basin, and also crops out along the margin of the southern Basin. As mentioned above, this is subdivided into the Lower and Upper formations by their lithologic difference as well as the existence of unconformity between them.

1) Lower Descanso formation

This formation consists mainly of an alternation of tuffaceous sandstones and conglomerates of light-gray to buff or reddish brown, with local intercalation of white silty and sandy tuffs.

Conglomerate is polymictic and its materials are derived from the surrounding areas. It is fairly resistant to erosion, forming continuous small hills between the easily eroded sandstone and shale beds.

Cross beddings are fairly common in the sandstone and conglomerate, and especially a sandstone bed near the top of the formation is remarkably cross-bedded.

Although the strike of the formation is considerably variable locally, it trends NNW-SSE regionally. Generally, it dips 5° or less, though dipping more than 20° very locally, with variable direction due to several gentle foldings.

The Lower Descanso formation is restricted nearly within the eastern half of Yauri Basin, and it is never found to the west though the Upper Descanso is widely distributed there. This fact may probably suggest the progressive and westward expansion of Yauri Basin.

The formation covers, in the form of clino-unconformity, the Upper Puno formation in the east side, and the Mesozoic formations, intrusive rocks and Tacaza group in the west side of Yauri Basin.

The thickness of this formation is estimated for some 500 m.

2) Upper Descanso Formation

It is mainly composed of massive tuff, but its upper and lower parts show different colours each other and a disconformity exists between the two. It is mainly distributed in the southern Yauri Basin, especially in its central to western parts, and is not found in the northern Basin, overlying the Lower Descanso and older rocks unconformably.

The lower part of the formation consists mainly of white to light-pink massive tuff with local tuffaceous sandstone of light-brown colour and up to 10 m in thickness. This tuff contains mineral grains of quartz, feldspar and idiomorphic biotite commonly and lithic fragments of andesite and basalt frequently. The matrix is distinctly albitized and often forms axiolitic spherulite, suggesting recrystallization. This tuff is presumed, from its distribution, to have been supplied through the old inlet or old valley formed in the southeastern Velille Quadrangle into the Yauri Basin. The tuff is comparatively hard and rich in columnar joints, and its erosion is strongly controlled by these joints to form characteristic ragged surface.

The upper part of the formation is mostly composed of salmon-pink massive tuff, but there is a thin bed of stratified tuff at the base. This tuff contains pumices, vitreous fragments and minor amounts of mineral grains such as feldspar, quartz and biotite. Salmon colour of the tuff is probably responsible for minor amount of fine-grained hematite in it. This tuff is, in contrast to the lower tuff, shows little recrystallization, being softer and more sandy.

The Upper Descanzo formation is sub-horizontal, generally less than 5° in dip. The thickness is estimated to reach 250m maximum in the old inlet of the southeastern Vellille Quadrangle, but is 60 m maximum in the central part of the Basin.

3-12-3 Yauri Formation

This is essentially an alternation of white tuffs, grayish-white tuffaceous siltstones and sandstones, and calcareous siltstones and sandstones with local intercalations of conglomeratic sandstone and lignite.

Tuff and tuffaceous sediments are stratified with unit-thickness of several to ten meters, and furthermore fissilities are developed in them at the interval of 0.5 to several centimeters. Cyprinodontiforms (non-marine fish) and plant fossils have been discovered from the tuffaceous siltstone beds.

Calcareous beds lie mainly in the upper section, and at least nine of such beds, 0.5 to 2 m thick, have been ascertained. Calcareous siltstone often contains abundant fossils of plant stem.

According to the pollen analysis for the tuffaceous siltstone and lignite, the formation is presumed to have been deposited in shallow and stagnant waters under a temperate climate, and the age is almost definitely Neogene and probably Pliocene. The details of pollen analysis are shown in Table I-20.

The maximum thickness of the formation is 80m.

3-12-4 Age and Correlation

A white massive tuff of the lower part of the Upper Descanzo formation sampled at the upstream of Rio Apurimac in the southeastern Vellille Quadrangle

was dated as 5 m.y. (Middle Pliocene time). Likewise, the Yauri formation is probably of the Pliocene as mentioned above. The Lower Descanso formation, however, is overlain by the Upper Descanso with the clear unconformity, and its thickness is very much larger than those of younger ones, suggesting a possibility that the deposition of the Lower Descanso formation began from Miocene age or earlier.

The Yauri formation may be correlated to the lake sediments of the Rio Asangaro in the Titicaca Basin (Newell, 1949) and the Capillone formation of the Maure and Antajave Quadrangles (Mendivil, 1965). The Upper Descanso formation is considered to have been deposited at almost same age as the Sencca formation from the result of dating.

3-13 Barroso Group

3-13-1 Definition

Wilson (1962) gave the name "Barroso formation" to the volcanics constituting the Barroso volcanic belt, and subsequently Mendivil (1965) classified the Quaternary volcanics of the Maure and Antajave Quadrangles in the name of "Barroso group" into three formations.

In this survey, the name "Barroso group" has been given to the youngest volcanics of the surveyed area which have erupted presumably in the age from the close of the Pliocene to the Pleistocene.

3-13-2 Distribution and Lithology

It is distributed mainly on the summits of the high land in the southern

part of Velille Quadrangle, overlying the Sencca formation unconformably. In the northern part of the Velille, some remnants of the group rest mainly on the Sencca and rarely on the Tacaza volcanics.

In the southwestern part of Velille Quadrangle, it consists of an alternation of dark-gray to black and compact lava flows of andesite, basaltic andesite and basalt, andesitic agglomerates and tuffs. Basalt is of an olivine basalt type, and contains phenocrysts of olivine and minor amount of bytownite in a intergranular groundmass of laboradorite, olivine, augite, anorthoclase and minor amounts of analcite, suggesting that this basalt belongs to alkali rock series likewise the Tacaza volcanics.

At the middle of the southern boundary of Velille Quadrangle, it is composed of the lower lava flows of dark-gray to black and compact andesite and olivine basalt, and the upper alternation of andesitic lavas, lapilli tuffs and tuffs of andesitic to dacitic composition. The thickness of the lower lava flows is about 150 m, and the upper alternation is more than 200 m.

In the northern part of Velille Quadrangle, it is mostly eroded out as mentioned first, and only thin flows of basalt or andesite remain sporadically.

3-13-3 Age and Correlation

The Barroso group here erupted after the regional erosion of post-Sencca. It is also suffered from the Pleistocene glaciation fairly severely. Its age, therefore, is presumed as the close of the Pliocene or the beginning of the Pleistocene.

The Barroso volcanics of this area may be correlated to the Chilla for-

matlon, the lowest unit of the Barroso group in the Maure and Antajave Quadrangles. According to Mendivil (1965), the Chila volcanics is composed of an alternation of gray to black and fine-grained andesitic lava flows, volcanic breccias and agglomerates, and is strongly suffered from the Pleistocene glaciation. These features of the Chila volcanics are very similar to those of the Barroso volcanics of this area, hence both must have occurred by the volcanic activities of almost same age and similar nature.

3-14 Glacial Deposit

There are moraines and fluvio-glacial deposits. Although the ages of these glacial deposits can not be precisely decided, they have been tentatively regarded as the Pleistocene as many of them are affected by the later fluvial erosion.

Glacial deposits lie most abundantly on the high land of the southwestern part of Velille Quadrangle. In this region, many morains occur at altitude of more than 4,400 m.S.L., and fluvio-glacial deposits flowed down glacial trough to form small outwash plains near altitude of 4,200 m.S.L.

From the central part to the north of the Velille Quadrangle, small morains only are scattered at high places of more than 4,400 m.S.L., but traces of the glacial landform are still found at many localities, and glacial striae too, remain rarely (see Photo. 6).

In the Laramani Massif of the eastern Yauri Quadrangle, small-scale moraines are observed sporadically. Among those morains, that of north-

eastern corner of the Quadrangle is comparatively large. Moraines of this region lie more than 4,200 m.S.L. and fluvio-glacial deposits occur rarely in the Yauri Basin at about 4,000 m.S.L. Most of moraines form inverted-delta-shaped small hills with bowed ends.

Moraine is a "little-sorted mixture" of angular to sub-angular gravels and sandy rock fragments. The rock materials of moraines differ in different localities, reflecting strongly their local occurrence. For instance, they are mainly composed of the volcanics in the Velille Quadrangle, whereas they contain a great deal of granite porphyry at the northeastern corner of Yauri Quadrangle.

3-15 Recent Deposit

Recent deposits in the high lands are only gravel beds on the rivers and sandy muds of swampy places.

In the pampa covering most of the Yauri Basin, alluvial soil is distributed widely, forming arable land. On river beds here gravels are well developed.

Along the boundary between the Yauri Basin and the Laramani Massif, gravel terraces like alluvial fans are formed locally.

In the periphery of the Lago Langui Layo of the northern border of Yauri Basin, terraces, river gravels and alluvial soils are developed comparatively widely.

CHAPTER 4 INTRUSIVE ROCKS

4-1 General Remarks

Aside from the Tertiary volcanic rocks in forms of vents and dykes, etc., as stated before, there are a series of the intrusive igneous rocks. They penetrate the "Early Cretaceous" Ferrobamba Limestone, and have been believed to be of the Late Cretaceous or the Early Tertiary. The result of the age determination, however, has revealed a possibility that the intrusive activity occurred intermittently from Late Jurassic up to Early Tertiary. They may be divided into two groups; earlier and later.

The earlier intrusives mainly form batholiths or large stocks. They are presumed to have been derived from a parental magma, although there are some varieties in their chemical compositions and textures. These differences suggest that the intrusions of magma occurred at the different stage of its differentiation or under the different physicochemical environments during one cycle of the intrusive activity.

The earlier intrusive activity in the area is represented by three batholiths (or large stocks), the Tintaya, the Vellile, and the Pichigua batholiths. But petrographically they differ from each other according to their respective ages of intrusion.

Tintaya batholith occurs around Tintaya Mine in the southwestern Yauri Quadrangle. This includes predominantly pyroxene diorite or gabbroic diorite, and appear to be most basic among the three. A gabbro sample has shown the K-Ar age of 144 m. y., the oldest of all.

Velille batholith, which occupies the northwestern corner of the vellille, is mainly composed of quartz diorite and granodiorite, but the differentiation ranging from diorite to granite is also marked. A quartz diorite sample has been dated as 105 m. y.

Pichigua batholith, cropping out in the vicinity of Santa Lucia de Pichigua of the western Yauri Quadrangle, has mainly dioritic and granodioritic chemical compositions similar to the other two, but its petrographic texture is distinctly porphyritic, suggestive of the shallow intrusion, in contrast to the other typical plutons. K-Ar measurement of two samples from this batholith gave ages of 74 and 86 m. y. , the youngest of all.

The later intrusive rocks consist of porphyritic monzonite, quartz monzonite porphyry and granite porphyry. They largely invade in and around the earlier batholiths as stocks, dykes and rarely sills. They also seem to have intruded at several stages. At Quechua 10 km south of Tintaya Mine, for instance, a stock of porphyritic monzonite was emplaced first, followed by dyke swarms of quartz monzonite porphyry, and finally dykes of granite porphyry.

The metallic mineralization in the area, as described later, appears to have become conspicuous from the latest stage of earlier intrusive activity (intrusion of hypabyssal Pichigua batholith), and to have reached its climax in the later activity. The age of the later intrusive activity is considered as the Early Tertiary based on K-Ar dating which gave an age of 57 m. y. for the Quechua porphyritic monzonite.

4-2 Tintaya Region

The intrusives, as batholith, stock, dyke and sill, penetrate the Mesozoic formations consisting of the Hualhuanl quartzite, the Murco sandstone and shale,

and the Ferrobamba limestone.

4-2-1 Batholith

The present intrusive mass, although thinly overlain by the roof pendants of the Mesozoic sediments mainly on its central part, seems to have the dimensions of about 10 km by more than 20 km, showing a definite elongation in the NNW-SSE direction, parallel to the major tectonic axis of the Mesozoic formations.

The mass is essentially a complex of many rock types, varying from gabbro to granodiorite in composition, but the most predominant type is the gabbroic diorite or pyroxene diorite.

Petrographic characteristics of the representative facies of batholith are described below.

The gabbro is of an amphibole gabbro type, and consists mainly of medium-grained, hypidiomorphic and granular plagioclase and brown hornblende. Crystals of hornblende commonly include poikilitically minute and anhedral crystals of olivine, clinopyroxene and cummingtonite.

The diorite also shows a medium-grained, hypidiomorphic and granular texture, and is composed of plagioclase, clinopyroxene, green hornblende and biotite with minor K-feldspar, quartz and cummingtonite.

The granodiorite usually consists of medium-grained, hypidiomorphic and granular plagioclase, quartz, K-feldspar, green hornblende and biotite. Rarely, clinopyroxene and cummingtonite are included in hornblende crystals.

Gabbroic diorite predominates in the southern part of batholith, whereas granodiorite occurs abundantly in the north. They appear to change gradually each other.

The contact effect of the Mesozoic sediments around the batholith is generally very weak, and limestone is only suffered from recrystallization and very local magnetite skarnization.

A gabbro sample collected from the southeastern part of the batholith near the head of the Coroccohuayco valley was, as mentioned previously, dated as 144 m. y.

4-2-2 Stocks, Dykes and Sills

1) Monzonitic porphyry at Tintaya Mine

A stock of monzonite or quartz monzonite porphyry was emplaced at the northern part of the batholith, in a size of 2 km long by 1.5 km wide.

Roof pendants of limestone, arranged in a crescent shape along the southern border of the stock, are replaced by copper ore-bearing skarn to form excellent copper deposits.

The stock itself also is hydrothermally altered remarkably and produces the mineralization of porphyry copper type.

Small dykes and sills of monzonite porphyry as well give weak skarnization and propylitization to the invaded limestone and batholith along their contacts.

2) Quartz monzonite porphyry at Ataraya Mine

At Ataraya Mine, 10 km southeast of Tintaya Mine, a small stock of quartz monzonite porphyry intrudes the limestone.

The stock is mainly composed of phenocrysts of K-feldspar, plagioclase, green hornblende and green biotite in a microgranitic groundmass of K-feldspar, quartz, plagioclase and accessories. Some part of the stock is, however, characteristically accompanied by idiomorphic quartz phenocrysts. Such may be of a somewhat later stage.

Copper deposit of contact metasomatic type is formed around the stock, and local dissemination of copper and iron sulphides is also recognized in the stock.

3) Monzonitic rocks at Quechua

At Quechua, about 10 km south of Tintaya Mine, a series of monzonitic rocks intrude the Mesozoic quartzite, shale and limestone.

Here, a NNW-SSE trending monzonite stock (or large dyke) with distinct porphyritic texture was first emplaced. Under the microscope, it contains phenocrysts of K-feldspar, and plagioclase (less than K-feldspar in quantity), with minor amount of brown biotite. The groundmass consists of a microgranitic aggregate of K-feldspar, plagioclase and minor quartz.

Next, narrow dyke swarms penetrated the stock. They are more porphyritic than the stock, and characteristically contain quartz phenocrysts although the constituent minerals are essentially same as those of the stock.

Last of all, thin dykes of granite porphyry intruded. They generally contain phenocrysts of K-feldspar, minor amount of plagioclase and trace biotite in a microgranitic ground mass of quartz, K-feldspar, plagioclase and accessories.

These porphyritic intrusives, and peripheral quartzite and shale are markedly altered hydrothermally, and the dissemination of pyrite and chalcopyrite commonly occur there. Limestone and calcareous shale are, too, locally mineralized by the copper-bearing contact metasomatism.

A sample of porphyritic monzonite has been dated as 57 m. y. But as the sample is slightly affected by the supergene alteration, the dating result may

show somewhat younger than actual.

4) Monzonitic rocks at Corocchohuayco and Huacollo

Monzonitic intrusives invade the batholith at Corocchohuayco, 9 km southeast of Tintaya Mine, and at Huacollo, 6 km southeast of Tintaya.

At Corocchohuayco, a porphyritic monzonite stock, about 500 m wide by more than 2.5 km long in plan, intrudes the gabbroic diorite in the NNW-SSE direction, roughly parallel to the trend of batholith. Further, a few dykes of quartz monzonite porphyry cut both the said intrusives in the direction of NW-SE. Porphyritic monzonite consists chiefly of K-feldspar, plagioclase (less than K-feldspar in amount), green biotite, green hornblende and quartz. Megascopically, its porphyritic texture is indistinct, but is clearly observable under the microscope. Quartz monzonite porphyry is mainly composed of phenocrysts of K-feldspar, plagioclase, green hornblende and a little quartz, and a microgranitic groundmass of K-feldspar, plagioclase, quartz and probably secondary biotite. Here occurs mineralization and alteration of porphyry copper type in and around the monzonite stock.

At Huacollo, an exposure of porphyritic monzonite, cutting the batholith, is observed along the valley stream. This one too, is altered hydrothermally and disseminated by iron and copper sulphides.

4-3 Velille Town and its Periphery

A batholith is exposed from the northwestern part of Velille Quadrangle to the adjacent Livitaca and Santo Tomas Quadrangles.

This intrudes the Mesozoic Ferrobamba limestone and Murco formation, and is overlain by the Tertiary Tacazá volcanics.

Petrographically, the present batholith is a complex varying from diorite to granite, although the granodiorite facies is most predominant and the quartz diorite follows.

Granodiorite is mainly composed of medium to coarse-grained, hypidiomorphic and granular plagioclase, K-feldspar, quartz, hornblende and minor amount of biotite.

Quartz diorite generally shows a medium-grained, hypidiomorphic and granular texture, and consists largely of plagioclase, hornblende, quartz and biotite. Clinopyroxene often remains in nuclei of hornblendes, and anhedral K-feldspar occurs as the interstitial to other minerals.

This batholith locally gives thermal metamorphism to the Mesozoic sandstone and shale along its contact zone. Limestone is recrystallized and occasionally reacts with it to form a "hibrid rock".

A few veins of lead and zinc, and several small bodies of magnetite skarn are found in the batholith. Magnetite bodies about 4 km south of the Velille town, are presumably of replacement of the limestone roof pendants, and spatially have close relation to the "locally altered" batholith. The batholith, however, is mostly very fresh, and such neither bears any mineralization, nor gives mineralization to the intruded Mesozoic rocks.

A quartz diorite sample taken near the Huancané village about 5 km south of Velille has been dated as 105 m. y.

4-4 Periphery of Coporaque Village

Granodiorite is exposed as an inlier of about 2 km by 3 km in plan at 2 km south of the Coporaque village. At about 6 km west of the village, another small outcrop of granodiorite intruding the Coporaque formation is present.

The "south" granodiorite consists of plagioclase, green hornblende, brown biotite, microcline, orthoclase, quartz and accessories. Its texture is generally medium-grained, hypidiomorphic and granular, but becomes much finer-grained and porphyritic locally. This granodiorite is intruded by an andestitic dyke, and a hydrothermal alteration zone is formed along their contact, which includes a thin copper-lead-zinc vein.

The "west" granodiorite is medium-grained, hypidiomorphic and granular in texture, and is mainly composed of plagioclase, orthoclase, microcline and green hornblende. No mineralization has been found in this.

4-5 Periphery of Santa Lucia de Pichigua Town

A large intrusive mass is exposed as an inlier in the Tertiary rocks along Rio Aprimac and its branches in the vicinity of Santa Lucia de Pichigua. The exposure is 1 to 3 km wide by more than 12 km long, and extends in the NNW-SSE direction. This may continue to the granodiorite of the Coporaque district.

This has a dioritic to granodioritic composition, similar to those of Tintaya and Velille batholiths, but definitely differs from them in petrographic texture. It appears to be plutonic or sub-plutonic at its southern portion, but at the north it becomes distinctly porphyritic, suggesting its shallow intrusion.

The relation between both plutonic and hypabyssal facies is mostly transitional at the south portion, but at the north it seems that the plutonic facies is either intruded or captured in the mode of a batholith by the hypabyssal one.

The rock type of the south is mostly quartz diorite and granodiorite, varying in texture from medium-grained, hypidiomorphic and granular facies to fine-grained and a little porphyritic one. Granodiorite mainly consists of plagioclase, quartz,

K-feldspar, green hornblende and brown biotite with minor amount of clinopyroxene and cummingtonite. A granodiorite sample, taken at Puente Santo Domingo, has shown an K-Ar age of 86 m. y.

At the central portion, its composition is mostly dioritic to quartz dioritic, but its petrographic texture is remarkably heterogeneous, changing its facies from equigranular diorite to diorite porphyrite. Very locally, the differentiation ranging from diorite to monzonite is also present. Diorite is mainly composed of plagioclase, clinopyroxene, green hornblende and brown biotite, accompanied with minor K-feldspar, cummingtonite and quartz. The constituent minerals of diorite porphyrite appear essentially to be same as those of diorite, but cummingtonite and quartz are uncommon in porphyrite. Monzonite mainly contains K-feldspar, plagioclase, hornblende and biotite. A diorite sample, collected at 3.5 km west of Santa Lucia de Pichigua, has been dated as 74 m. y. in the K-Ar age. At the northern portion, it is mostly composed of diorite porphyrite and granodiorite, partially including plutonic facies such as diorite, granodiorite and monzonite.

This mass produces local dissemination zones of pyrite, and masses of magnetite and hematite which are presumably orthomagmatic in its central and northern portions. These iron mineralizations are accompanied with weak but fairly pervasive copper mineralization, and alterations such as tourmalinization, silicification and argillization.

Incidentally, saline sodium-carbonate springs are gushing out from the intrusives at several points along the riverside of Rio Aprimac near the village of Saltapata, but their genesis has not been studied.

4-6 Upper Stream of Rio Paycchuma

A batholithic intrusive mass of granite porphyry is present at the northeastern corner of Yauri Quadrangle. This mass extends to the adjacent Sicuani and Ayaviri Quadrangles. According to Audebaud and Pecho (1970), its hypabyssal nature changes into plutonic one (granite/granodiorite) in the Sicuani Quadrangle.

In the present district, the mass is mostly composed of pinky granite porphyry, characteristically containing abundant large phenocrysts of K-feldspar, plagioclase and a little quartz, nearly 1 cm to 2 cm in size, but very locally plutonic facies is observed near the top of Cerro Carayani.

As for the mineralization associated with this, only pyrite disseminations in the fractured zones and a narrow vein or lens of barite are observable near the Hda. Soclla Grande. Tourmalinization often occurs at the east side of Cerro Labandera.

A hot spring (probably carbonate) is gushing near the Exsalcacion in the northern fringe of the intrusive mass.

CHAPTER 5 GEOLOGICAL STRUCTURE

Interpretation of the geological structures in the first-phase survey is considered to have been fundamentally precise, although some corrections, of course, has been required in details.

Structures marked in the respective rock units have been outlined in Chapters 3 and 4, and therefore the areal structure will be comprehensively described here-under.

According to Bellido (1969), the geostructural trend in the Peruvian Andes generally shows a NW-SE direction, but in the areas such as Andahuaylas, Abancay and the northern part of Cuzco, the geological structure is chiefly controlled by an E-W trend, and he named this local bend of the Andean structure the "Cuzco-Abancay inflexion".

The present area is adjacent to the south or southeast of the Cuzco-Abancay structural province, and hence the areal geostructure is controlled by a major trend of NW-SE to NNW-SSE, and minor trends of NE-SW and E-W.

5-1 Folding

The Puno rocks and older sediments are strongly controlled by foldings which have the NW-SE to NNW-SSE axes, while they are suffered from local controls by the E-W and NE-SW trending folds as well.

In the Laramani Massif, the Mesozoic formations and Puno group are largely controlled by sub-regional and repeating synclines and anticlines which have NW-SE trending axes, generally striking parallel to this fold system. But from the center to the northern parts of the region, local fold systems roughly

having the NW-SW and E-W trending axes are superposed on the main fold system, becoming responsible for the local formation of small dome and basin structures.

The Mesozoic and Coporaque formations in and around the Western Yauri Basin show mostly the NNW-SSE orientation only. The Mesozoic sediments exposed in the northwestern part of the Velille Quadrangle are, however, controlled by a composite fold system consisting of a large NNW-SSE trending fold and small folds of the E-W bearing.

Whereas, in the Lower Tacaza formation, the main trend mentioned above is scarcely observed; and the formation predominantly shows the NE-SW trend in the north Yauri Quadrangle, and also the E-W bearing structure in the northwestern part of Velille Quadrangle.

Structures of the Middle Tacaza formation, which are mainly marked by "flow structure" of the lavas and generally much less intensive than that of the Lower Tacaza, shows predominantly the E-W trend rather.

The upper Tacaza formation and subsequent volcanics are generally sub-horizontal except near "vents".

The Lower Descanso formation, the oldest lake sediments of Yauri Basin, forms gentle synclinal and anticlinal structures having axes of the NNW-SSE bearing. The Upper Descanso and Yauri formations distribute sub-horizontally, and neither their strikes nor dips show any definite trend.

Such modes of folds as mentioned above may suggest a possibly that the E-W tectonic trend represented by the "Cuzco-Abancay inflection" was formed by a temporary and rather short tectogenesis which occurred later than the main tectonic movement, probably from the close of Lower Tacaza time to the Middle Tacaza.

5-2 Faulting

Faults are particularly well developed from the Laramani Massif to the Yauri Basin, mainly displacing the Mesozoic formations and Puno group.

In the Laramani Massif, three large normal faults are present. They strike NW-SE to NNW-SSE and lower the west side of the faulted blocks. Especially, the westernmost one makes the boundary between the two tectonic units, the Laramani Massif and the Yauri Basin, evidently being very important tectonic line in the area. These faults are cut and displaced by the subsequent faults striking E-W and NW-SE.

In the eastern part of Yauri Basin, the Lower Descanso clastics, definitely showing the NNW-SSE trend, are thickly accumulated, and moreover the east and west sides of this zone differ from each other in types or lithofacies of pre-Lower Descanso rocks. These facts suggest a possibility that the zone makes a graben structure depressed by the faulting of the NNW-SSE trend.

No clear faults are observed along the western border of the Yauri Basin. But the distribution of lake sediments and the topography too, are strongly controlled by both the NW-SE and NE-SW trends, hence the western margin of the Basin is also presumed to be demarcated by "hidden" faults. The presence of the said fault systems has been confirmed in the Tintaya region of the southwestern Yauri Basin.

In the western Cordillera, only two faults have been confirmed; one passes through close-west of the Velille town in the N-S direction, dislocating the Mesozoics, intrusives, and Lower Tacaza rocks, the other cuts the Middle and Upper Tacaza formations in the northeastern part of the Velille Quadrangle.

Tintaya batholith definitely shows the NNW-SSE to NW-SE trend, and the

Pichigua intrusives has probably the trend of NE-SW. The Coporaque intrusives are located at the apparent intersection of west extensions of Tintaya and Pichigua intrusives. This pattern of intrusives appears to suggest that the tectonic control by the above two trends was already present at the time of intrusion. However, the most active age of these tectonic lines is presumed to be post-Puno to pre-Middle Tacaza.

The fault system of E-W bearing is evidently younger than those of NW-SE and NE-SW, and seems to have been formed in relation to the movement of the "Cuzco-Abancay inflection".

CHAPTER 6 GEOLOGIC HISTORY

There is little way of studying the Palaeozoic history in the present area due to the lack of exposed rocks in which Palaeozoic episodes are clearly recorded. However, in the Sicuani Quadrangle adjacent to the north of the Yauri, Audebaud and Pecho (1970) have confirmed a Palaeozoic sequence consisting of Pre-Devonian, marine Devonian, terrestrial Lower Carboniferous, marine Upper Carboniferous to Lower Permian, and terrestrial Upper Permian. The present area too, therefore, must have experienced such Palaeozoic sedimentations as aforesaid, though their records are concealed deep under the ground. The Coporaque red terrestrial formation has been tentatively considered as the Upper Permian, in the present survey. But only the evidence for this correlation is its considerable similarity to the Upper Permian continental sediments in lithofacies and it, of course, has to be confirmed by some chronologic evidences.

No record of sedimentation and igneous activity during Triassic and Early Jurassic ages has been found in the high Andes of Southern Peru. Although many geologic incidents might have taken place in this period, there is nothing to tell them except an assumption that the area may have been a land undergoing erosion in the Early Jurassic. In the Later Jurassic, a marine transgression was possibly started from the west of the area towards the east; and netric (?) Yura clastics in the west, and littoral or terrestrial Huancané red sediments in the east were deposited respectively. Subsequently, a slight, temporary and possibly westward regression took place, causing interruption of the sedimentation in the east. In the west, the littoral or terrestrial Murco clastic formation was deposited, but its thickness too,

rapidly decreases eastwards. Without long interval, marine conditions again prevailed, and both Ferrobamba and Ayabacas limestones were deposited. The Ayabacas in the east is of a littoral or coral origin, whereas the Ferrobamba in the west shows deeper facies. These characteristics of sedimentations well suggest a geosyncline dipping westward.

Following the above geosynclinal sedimentation, an orogeny occurred and accompanied the intrusion of batholiths. The batholithic intrusive activity was restricted within the "western Region" and distinctly controlled by both NW-SE and NE-SW trends, there by suggesting that some tectonic movements preceded or accompanied the emplacement of batholiths. Further, during this period of intrusive activity, considerable uplift and superficial erosion must have taken place, judging from the hypabyssal nature of the youngest Pichigua batholith.

The geologic age from the Yura sidimentation to the batholithic intrusion is considered as the late Mesozoic. But no definite dates of each of those events can be settled because of discrepancies between their ages previously accepted and those estimated from the dating results as repeated in preceding pages of this report.

Anyway, with the above intrusive activity as a momentum, the west and east sides of the Yauri Basin become defined as independent structural units respectively. According to Bellido's (1969) structural division of Peru, the western unit may possibly correspond to the "Western Cordillera" and the eastern is considered to belong to the "Interandes Valleys".

Thence, the area as a whole was uplifted and greatly eroded, but a large interior basin was formed in the "Interandes Valleys" and the Puno red clastics were thickly deposited in the basin.

This formation of the interior basin is considered as a definite announcement of the birth of the "Interandes Valleys" between both Eastern and Western Cordilleras. The basin widely extended from the vicinity of Cuzco through the Bolivian Corocoro Basin far to the northeastern Argentina. The present area lies along the northeastern edge of the basin, and the deposition of Puno group here seems to have taken place during the period from Late Cretaceous(?) to Early Tertiary. The Puno group of the area is divided to the Lower and Upper formations by a clear unconformity. The Lower formation consists of ill-sorted and cobble to coarse pebble conglomerates, suggesting to be piedmont deposits poured into the basin. Whereas the Upper formation is essentially composed of an alternation of well-stratified sandstones and fine pebble conglomerates intercalating thin shales in its upper section, indicating lake sediments under some comparatively stable environment.

In contrast, sediments correlated to the Lower Puno formation are absent in the Western Region (the Western Cordillera). In stead, erosion and hypabyssal intrusive activity possibly took place at that time, and the igneous activity brought about very important copper mineralization in this Region. At the correlative age of the Upper Puno sedimentation, first volcanism occurred in the Western Region, and pyroclastics of fairly acidic nature (Lower Tacaza volcanics) were accumulated. This volcanism was possibly responsible for the predominance of acidic volcanic materials in the Upper Puno formation.

Prominent tectonic movements followed the deposition of the Upper Puno formation (or the Lower Tacaza volcanics). This tectogenesis produced the main structures of the area, trending NW-SE to NNW-SSE, and the subordinate structures of NE-SW and E-W trends at the closing stage.

The NNW-SSE bearing block faulting caused an important depression along the boundary-zone between the West and East Regions, resulting in the establishment of the present three geomorph-structural units; the Laramani Massif, the Yauri Basin, and the Western Cordillera. There is a possibility that the depression of the Yauri Basin, or the uplifting of the Laramani Massif, may have taken place little by little since the closing stages of the Puno sedimentation, because the Puno Group appears to decrease gradually its dips from the eastern slope of the Laramani Massif towards the Yauri Basin. Namely, A sedimentary environment of taphrogeosyncline* type may have already been budding out at that age.

*One of epeirogenic basins formed in the orthogeosyncline, by the classification of M. Kay (1951). The name of "Taphrogeosyncline" was given to the basin demarcated by the high-angle faults and filled with thick sediments (sedimentary basin consisting of trench and graben). Sedimentation generally occurs at same stages of the fault movement, but sediments occasionally covers the faults ("Geological Dictionary" HEIBONSHA PRESS).

The above tectogenesis accompanied, or was followed by, the widespread erosion (Stage I of Puna erosion).

Thence, in the Western Cordillera volcanic eruptions repeated, and in the Yauri Basin lake sediments were accumulated. In the Laramani Massif, however, erosion possibly continued except for the inappreciable eruption of the Eocene Middle Tacaza volcanics.

The volcanic activity in the Western Cordillera involved the following events; basaltic lava flows in Early Eocene time (Middle Tacaza); lavas and pyroclastics, intermediate to acidic in composition, from the Middle Eocene to the beginning of

the Miocene (Upper Tacaza); acidic pyroclastics in the Pliocene (Sencca); and basaltic to andesitic volcanics (Barroso). During the intervals of the volcanic eruptions, erosions occurred. The foundation of the present topography of the Western Cordillera was possibly formed by the post-Tacaza erosion (stage 2 of Puna erosion) and the deposition of Sencca volcanics.

In the Yauri Basin, the Lower Descanso formation consisting of an alternation of sandstones and conglomerates was accumulated at the earlier stage. This clastic formation has cross-beddings and ripple marks, suggesting that its deposition took place in the shallow and running waters. At medial stage, the Upper Descanso formation was deposited. This formation is composed of tuffs and the texture, though stratified partly near the base, is mostly massive. These tuffs appear to have been deposited during a fairly short period chiefly in an ashore-like environment. Finally, the Yauri formation, consisting of an alternation of tuffs, tuffaceous and calcareous siltstones, was deposited. These sediments is considered to have been accumulated in some shallow and stagnant waters judging from the results of its pollen analysis and its well-sorted and stratified nature. The deposition of these lake sediments seem to have intermittently continued since the formation of the first graben (Late paleocene age?) until as young as the Pliocene.

The epeirogenic upheaval possibly continued since the Early Tertiary, but in the Medial Pliocene the area was still temperate. In the "Lake Yauri", Osteichyess was sailing about, and plants belonging to Rasaceae, Compositae and Gramineae were growing along the shore. In the Pleistocene, however, the area was uplifted and glaciers were formed at various places of the high land.

In the Recent, the Río Aprímac and its branches reached into the area from the "Interandes Valleys", dissecting actively the surface until now.

CHAPTER 7 ECONOMIC GEOLOGY

7-1 General Remarks (PL. I-5-1 and I-5-2)

The geochemical reconnaissance for stream sediments has disclosed a dominant and large anomalous zone in the Tintaya region. This attractive anomalous zone is not limited to the known mineralized zones such as Tintaya Mine and Quechua property, but is stretched widely to the east. Copper anomalies have been also detected in other districts consisting of the intrusives and the older volcanics (Lower and Middle Tacaza), but they generally lie sporadically and do not make "anomalous zones". Those scattered anomalies appear to have been derived from isolated and small sources of mineralizations.

Metalliferous mineralizations, as suggested by the above geochemical reconnaissance, occur in the intrusives, intruded Mesozoic sediments and older extrusives up to the Middle Tacaza, and so far 36 mineral indications have been confirmed in the area as listed in Table I-2.

The metallic elements are mostly copper and iron, but a few of silver-lead-zinc type as well are present. Mineral showings in the batholiths and volcanics seem too small in size or too low in ore content for resources. Whereas, mineralizations which accompany the younger intrusives (monzonitic porphyries) are considerably strong, and often make excellent copper deposits or attractive showings such as Tintaya, Ataraya and Quechua, etc. Two attractive showings of porphyry copper type which have the close spatial and genetic relationships of high possibility with porphyritic monzonite, have been discovered at Corrocohuayco and Huacollo in the eastern part of the Tintaya region.

The Tintaya region is an important cupriferous area consisting possibly of

three main zones of mineralization; western Ataraya, central Quechua-Tintaya, and eastern Coroccohuayco-Huaccollo zones. Further investigations, therefore, will be required not only for the Coroccohuayco-Huaccollo zone but also for other interesting zones.

As described in Chapter 4, the Pichigua batholith, contrary to other batholiths, is of a shallow-intrusion type, and often bears dissemination zones of pyrite, and magnetite masses. Copper anomaly of the geochemical reconnaissance here is not so excellent, but the above iron mineralizations are accompanied with weak but pervasive copper mineralization. Some brief investigation may be necessary to check on the copper content.

As for the non-metallic resources, the Islalcocha oil seepage, which has been confirmed near the boundary between the Yauri Basin and Laramani Massif, is noteworthy. Whether this showing indicates the latency of economical oil deposit can not be judged at present stage. Somewhat complicated geostructure of the area seems very unfavourable for the formation of large oil field. However, if there is any deposit of economic value, it even small in scale, would greatly contribute to the social development of the Yauri Area and the vicinity. Hence, the survey on oil resources too, is no less important than those of metallic resources.

7-2 Geochemical Reconnaissance for Stream Sediments

7-2-1 Treatment of Samples

The sampling method and the reason for the selection of Cu and Mo as the pathfinders have been explained in Chapter 1.

1) Analytical Method

The chemical analysis was entrusted to Maria Lau, a skilled geochemical analyst

In Peru, and the representative results of Maria Lau's analysis were further checked up by the Central Research Laboratory of Mitsui Mining and Smelting Co. , Tokyo. Analytical techniques adopted by Maria Lau are the 2, 2'-biquinoline method for the copper determination and the thiocyanate method for the determination of molybdenum as shown in the attached Tables I-3 and I-4.

The Central Research Laboratory of Mitsui adopted the atomic absorption spectrography method for the determination of copper, and the thiocyanate method for the analysis of molybdenum.

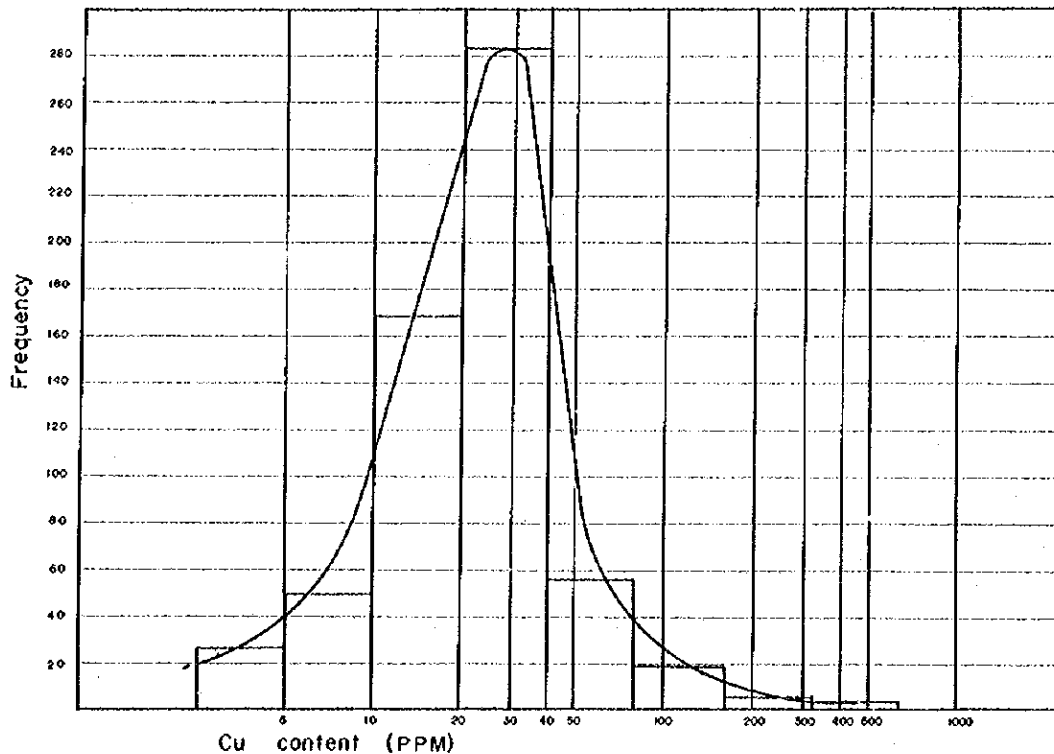
In comparison of the both analytical results, the molybdenum contents after Maria Lau showed a tendency to be a little lower than those after Mitsui, and as for analytical values of copper, both Mitsui and Maria Lau were nearly agreed with each other. Therefore, the results of Maria Lau were judged available. The Maria Lau's results are shown in the attached Table I-15.

2) Interpretation Procedure of Analytical Results

Rocks usually contain minor amounts of copper and molybdenum independently of any mineralization, and their contents generally differ according to rock types. Some rocks of special types occasionally contain them so high as to mask the anomalies originated from mineralization. However, original contents of copper and molybdenum in each of rock types do not differ so much in this area. Hence, the above problem was taken to be negligible and was disregarded. The frequency curve of copper contents shown in Fig. 4 indicates semilogarithmically a smooth curve of normal distribution, serving an excellent evidence of this judgement. There are various methods to interpret analytical results and to extract "geochemical anomalies", and some suitable method would be adopted according to the areal conditions of geology, climate and

topography, etc.

Fig. 4. Histogram and Frequency Curve of Cu (Stream Sediment)



In the present area, rivers become torrents and wash away fine sands in the rainy season, whereas in the dry season, most of them, except larger ones, are dried up. Thus, it generally seems impossible to expect a long-term accumulation of metallic components in the stream sediments except special heavy metal as gold. Molybdenum was hardly detected in the stream sediments. This appears because molybdenum content is absolutely little and also molybdenum minerals are liable to take easily washable forms as seen in flaky one of molybdenite.

The geochemical anomalies of the present area, therefore, were picked out through the investigation of copper contents in the stream sediments, considering the areal characteristics as mentioned above. The following two threshold values were adopted here in order to select "anomalous zones":

Threshold value of strong anomaly : Average value + standard deviation =
 $29 + 62 = 91 \approx 90 \text{ ppm Cu}$

Threshold value of weak anomaly: The 10% - value from the highest = 50 ppm Cu

7-2-2 Geological Interpretation on Anomalies

Geochemical anomalies so picked out are shown in the attached plans PL. I-5-1 and PL. I-5-2. These anomalies are geologically interpreted as follows:

1) Anomalous Zone in the Tintaya Region

This region makes the largest and most excellent anomalous zone within the surveyed area. Anomalies here have been detected along a considerable number of rivers and ravines in the region. Especially, intensive anomalies have been found at the three districts; the northeastern, the southwestern and the eastern parts of the region.

The anomaly of northeastern district is observed at the upper reaches of Rios Tintaya and Ccamac Mayo, and is considered to have originated from the Tintaya ore deposits.

The anomaly of southwestern district corresponds to the Quechua mineralized zone.

Small and weak anomalies are present between Tintaya and Quechua (upper stream of Q. Huaccetiana), and to the west of Tintaya (uppermost of Rio Huinimayo). They appear to have been derived from the nearby magnetite skarns.

The anomaly of eastern district is found along the streams of Q. Huaccollo, Q. Ccaccamayo and its branches, and Q. Surahualco. In this anomalous zone, mineralizations of the porphyry copper type have been discovered at the middle reaches of Q. Huaccollo, and at Q. Coroccohuayco (a tributary of Q. Ccaccamayo). However, this zone so widely spreads that its expansion can not be explained without presuming some

other sources of anomaly besides the above mineralizations, thereby suggesting some mineralizations in addition to the confirmed ones.

2) Anomalies in the Pichigua Region

Three weak anomalies have been detected from Rios Aprimac and Collpamayo near the town of Santa Lucia de Pichigua in the eastern Yauri Quadrangle. All these anomalies are found near the dissemination zone or veins of pyrite in the Pichigua intrusives. Being accompanied by pyritization, weak copper mineralization fairly pervades, which is most likely responsible for the anomalies.

3) Anomalies in the Southern Velille Quadrangle

Sporadic and small anomalies have been detected in the Middle Tacaza volcanics and Coporaque formation. Close to most of these anomalies, mineral showings are found, suggesting their direct relationship with the mineralization. However, anomalies are always isolated each other and never form intensive anomalous zones. This possibly suggests that the mineralizations discovered by the geological survey are so small and weak that no anomalies corresponding them have been detected by the geochemical reconnaissance.

4) Anomalies of the Northwestern Velille Quadrangle

Six small anomalies have been detected in the batholith, Mesozoic formations, and Lower and Middle Tacaza volcanics in the vicinity of Velille town.

These anomalies too, show the distributing pattern similar to that of the southern Velille Quadrangle, and are considered as being originated from isolated and small mineralizations.

7-3 Metallic Resources

36 mineral showings conformed are listed in Table I-2, and their localities are

marked on PL. I-5-1 and PL. I-5-2.

Generally speaking, all these showings are located in the regions where geo-chemical anomalies have been detected.

7-3-1 Tintaya Region in the Southwestern Yauri Quadrangle

This is a very important cupriferous region, and includes all of the known deposits or large mineralized zones such as Tintaya, Atraraya and Quechua, etc.

Tintaya Mine is a well known copper deposit of large scale skarn type as outlined in the last report, but recently an attractive mineralization of porphyry copper has been discovered in the stock of quartz monzonite porphyry, being prospected by drilling now.

Ataraya Mine is increasing its production from 300 tons of ore daily to the aimed rate of 500 tons. This deposit as well is of a skarn copper type, but local disseminations of copper ores are found in the stock of quartz monzonite.

Quechua mineralized zone is of a porphyry copper type. It consists of a large hydrothermal alteration zone with pervasive dissemination of pyrite. Mineralizations of copper and molybdenum, too, appear fairly common, but no details of their contents are obtained as the prospecting has been just begun.

Aside from the said known mineralization, two noteworthy showings of porphyry copper type have been discovered at Coroccohuayco and Huaccollo valleys.

1) Coroccohuayco Showing (cf. PL. I-4 and I-5, Photo. 8 and 9)

The rocks of Coroccohuayco district are mainly composed of batholithic diorite, stock-like porphyritic monzonite and dykes of quartz monzonite porphyry. Several small bodies of copper-bearing magnetite skarn are formed by the replacement of limestone roof pendants.

Batholithic diorite extends to the NNW-SSE direction, and porphyritic monzonite penetrates it in sub-parallel as a stock of 200 to 800 m wide and more than 2.5 km long. Quartz monzonite porphyry cuts them in the form of NW-SE bearing thin dykes in the southern part.

Hydrothermal alteration spreads in the porphyritic monzonite and surrounding diorite, but its type and intensity vary from place to place. The southern part of monzonite stock is intensely silicified by numerous networks of quartz, whereas its central part is suffered from moderate silicification and strong argillization. Its northern part is affected by moderate or weak argillization. Although the alteration of diorite is generally weak, silicification fairly pervades in its southern part, and skarnization is locally observed. Hybrid rocks are locally formed by reaction between diorite and limestone. Dykes of quartz monzonite porphyry themselves are scarcely altered, but rocks intruded by them are suffered from very intense silicification, suggesting that the porphyry intruded after or final stage of the alteration.

Geochemical survey has detected excellent anomalies of copper over the altered zone (PL. I-6). The copper contents of geochemical samples has shown such a histogram as Fig. 5, being 263 ppm Cu in average (\bar{X}) and 445 ppm Cu in standard deviation (σ). Although the copper contents of the back ground have not been strictly defined as most of samples were taken from the "altered zone", the following classification has been adopted in the present detection of anomalous zones:

Threshold value of "transitional zone":

$$X = 263 \text{ ppm Cu} \quad \hat{=} \quad \underline{\underline{300 \text{ ppm Cu}}}$$

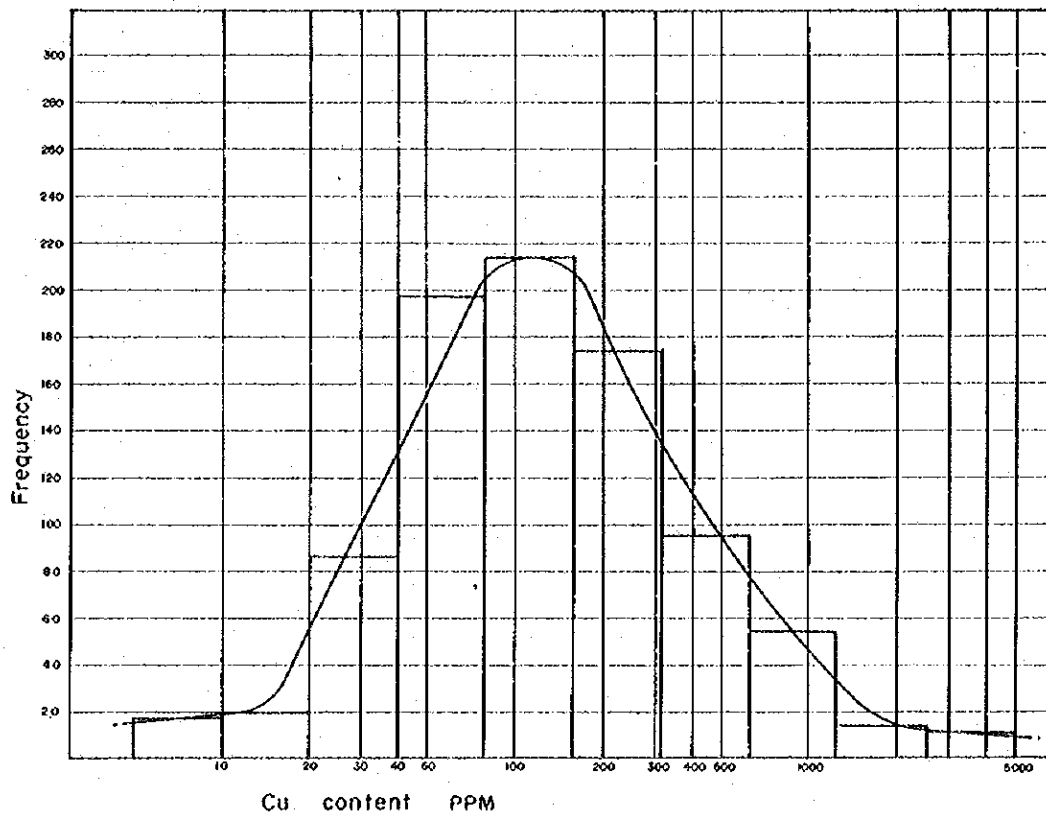
Threshold value of weak anomaly:

$$X + \sigma = 708 \text{ ppm Cu} \quad \hat{=} \quad \underline{\underline{700 \text{ ppm Cu}}}$$

Threshold value of strong anomaly:

$$X + 2\sigma = 1153 \text{ ppm Cu} \approx 1100 \text{ ppm Cu}$$

Fig. 5. Histogram and Frequency Curve of Cu at Coroccohuayco



9% of samples have shown copper contents of more than 700 ppm, and high contents of more than 3,000 ppm Cu have been detected from a little over 1% of all.

Strong anomalies of 100 to 200 m in diameter are formed in many places of the altered zone. They tend to concentrate at and near the copper-bearing magnetite skarns of the north, and around the strongly silicified zone in the central and southern parts.

Oxide ores of copper have been found from most of geochemical anomalies, and some parts have been proven to carry fairly high contents of copper by assay (PL. I-4).

A particularly attractive showing of mineralization occurs near the central part of altered monzonite stock, where an old working exists. In the southeastern part of altered zone, diorite is distinctly skarnized and mineralized by copper oxides. Molybdenum, though minor in amount, is generally accompanied by the copper mineralization.

2) Huaccollo Showing

This is located 2.5 km north-northwest of the Corocochuayco, in the Huaccollo valley. Mineralization here occurs in the porphyritic monzonite and "penetrated" diorite, and is mostly composed of primary sulphides.

Pervasive dissemination of pyrite, chalcopyrite and minor amounts of molybdenite occur in monzonite, and the samples taken from its exposure, about 350m wide, by the channel method have shown an average grade of 0.55% Cu. (see PL. I-4).

Diorite bears veins or veinlet swarms of pyrite abundantly, and some veins have shown fairly high copper contents including an assay result of 5.18 % Cu for 1.2 m wide.

Mineralized zone here crops out only along the valley stream, being overlain by the roof pendant of Mesozoic quartzite to the north, and by the alluvium to the south. The monzonite and diorite, the host rocks of mineralization, however, intrude in the definite direction of NNW-SSE, and probably connect with those of Cococochuayco. This suggests a possibility of the latence of a large mineralized zone including the two showings.

3) Other Mineral Showings

There are a considerable number of bodies of magnetite skarn in this region, but they are generally small in size and very poor in copper content.

An weak dissemination of pyrite and chalcopyrite has been found in an altered

intrusive, possibly a narrow dyke, at Co. Ccatunchoro to the west of Tintaya Mine.

As mentioned hitherto, the important copper mineralization zones in the region are formed in accompaniment with the intrusive activities of porphyritic monzonite stocks, and an interesting feature of their arrangement is that they appear to have intruded along the following three tectonic lines which run in parallel in the NNW-SSE direction:

Eastern Coroccohuayco-Huaccollo Line

Central Quechua-Tintaya Line

Western Ataraya-"West of Ccatunchoro?" Line

Such hypothetical arrangement of the stocks may have very important significance for future exploration.

7-3-3 Pichigua Region of Eastern Yauri Quadrangle

The Pichigua intrusive rocks were formed by earlier intrusive activity as mentioned previously, but they are of the shallow-intrusion type, different from other batholithes, and their mineralization is pretty conspicuous.

Mineralization in Pichigua region mainly consists of pyrite and magnetite, often accompanied with a minor amount of chalcopyrite. Up to the present, no mineralized zone having an economical significance has been found in this region, but magnetite ore bodies and the dissemination zone of pyrite have large dimensions, and leave a room for future exploration.

1) Río Pichigua Mineralized Zone (PL. I-5-2.)

This mineralized zone is exposed along the Río Pichigua 3 km west of the town of Santa Lucía de Pichigua, and consists of a dissemination zone of about 100 m in width which has been formed in diorite porphyrite. The dissemination of pyrite is pretty

conspicuous, and analysis of a sample has shown a grade of 3.09% S. No copper ore was found in this mineralized zone, but its extension has not yet been thoroughly explored.

2) Rio Collpamayo Mineralized Zone

This mineralized zone is located in the Rio Collpamayo 1 km north of the Quicsane village, and consists of diorite porphyrite which bears an ore mass of magnetite likely to be of the orthomagmatic type and a dissemination zone of pyrite.

The magnetite ore body is about 70 m wide and extends itself in the NW-SE direction, but the limit of its extension is unknown. This ore body consists of magnetite and minor hematite which is unaccompanied with skarn minerals, and is traversed by a bunch of veinlets of pyrite and chalcopyrite (partially altered to covellite) of the later stage. The assay result of a representative sample has shown the grades of 0.11% Cu, tr. Pb, tr. Zn, 4.40% S and 57.4% Fe.

The pyrite dissemination zone occurs in a zone of porphyrite breccia, which is accompanied with chalcopyrite. The zone is more than 50 m in width, but its details are still unknown owing to incomplete exploration.

3) Other Indications of Mineralization

This intrusive mass contains thin and scattered veins of pyrite.

Near the village of Salinpata at the upper reaches of Rio Aprimac, thin veins consisting of pyrite, arsenopyrite, tourmaline and quartz are observed. The tourmaline is sometimes found also as an accessory mineral of the intrusives.

In this region are found the mineralization of magnetite formed by magnetic differentiation and the mineralization of pyrite formed in the xenothermal environment. At Rio Collpamayo, both the mineralizations are presumed to have overlapped each

may not be expected.

(4) Indication near Checcane Village

In the andesite dyke intruding the Coporaque formation, a small lenticular ore body (0.5 m x 6 m x 15 m) lies, which consists of pyrite, chalcopyrite, hematite and chlorite. In the sandstone near the dyke, another small lenticular ore body (0.3 m x 2 m x 2 m) containing green copper ores, native copper and chalcopyrite occurs along the fault.

7-3-4 North Western Part of Velille Quadrangle

Mineralizations are observed at the Mesozoic formations, intrusive rocks and the Lower and Middle Tacaza Volcanics, but all of these mineralizations are too small to have any economic values.

The representative mineral indications in this region are as follows:

1) Mina Titiminas

This mineral indication is a quartz-calcite vein formed in limestone in the NW-SE direction, locally accompanied with galena and green copper ores. There is a adit of 5 m in length along the vein.

2) Huachana Indication

There is a narrow shear zone of about 1 m in width, trending E-W along the boundary between the Lower and Middle formations of the Tacaza group, and several calcite veinlets of 1 cm to 1.5 cm wide accompanied with chalcopyrite, native copper and green copper ores occur in this zone.

Although the shear zone is also disseminated by a minor amount of copper ores, its copper content is estimated at less than 1% Cu. A small adit exists.

3) Chullo Indication

This mineral indication is a 10-cm-wide quartz vein of fissure-filling type in granodiorite, accompanied with galena, sphalerite, and hematite. There is an adit of 20 m long following the vein.

4) Condrococha Indication

This indication consists of magnetic skarns, five ore bodies in all, which have been formed on granodiorite and at the boundary between the granodiorite and limestone. No copper mineralization is observed in any of the five.

7-3-5 Northeastern Part of Yauri Quadrangle

A batholith of granite porphyry intrudes the Ayabacas limestone, and along their south contact are found local and weak pyrite dissemination, fine-veinlets of gypsum and pyrite, and a small vein of barite, all of which have no values as mineral resources.

7-4 Petroleum Resources

An oil seepage is at Hda. Islaicocha in the eastern part of the Yauri Quadrangle. This seepage seems to have been known for some time, and the oil seeping out little by little has been collected in several shallow pits and used as lamp-oil (Photo. 11).

The economic value of this oil seepage is difficult to evaluate at the present stage. In fact, none of the mechanisms and conditions of growth and accumulation of oil in the surveyed area has been definitely clarified, although a certain degree of assumption may be allowed.

According to the general criteria of the current petroleum geology, it may be very difficult to expect for the occurrence of large oil field in the area. Because the geological structure of the area is too complicated to allow the expectation of a

other. Copper mineralization is presumed to have accompanied by the later pyrite mineralization.

7-3-4 Southern Part of the Vellille Quadrangle (PL. I-5-1.)

The Mineralization of this region occurs mainly in the Middle Tacaza formation, and some are in the Coporaque formation and intrusives.

Mineral indications are many in number, but they are all of a small scale and have no economic values.

The representative mineral indications of the region are as follows:

(1) Co. Quinsachata Indication

In the alkali basalt flow of the Middle Tacaza formation, quartz-epidote veins of the fissure-filling type are found, partially accompanied with copper oxide ore. Three old pits are present, but their mineralization is poorly recognized.

(2) Mina Dulzura

This indication is about 3 km south of Coporaque and consists of copper-lead-zinc quartz veins associated with an andesite dyke which have intruded the granodiorite. The main vein, striking NNW-SSE, is about 40 cm wide (max. 1 m) and 15 m long, and its estimated ore grade is 1.5% Cu and 2% Pb + Zn. This has been almost mined out by means of a short inclined-shaft. There are several thin veinlets striking NW-SE.

(3) Mina Mamanhuaeta

The Middle Tacaza volcanics here are intruded by a rhyolite dyke, in which irregular lenses or reticulated veins of quartz occur, containing small amount of galena, sphalerite and pyrite. The silver content is estimated at some 320 gr/t (10 oz/t) at the high-grade portion, but the ore body is too small and its expansion

gentle and large anticlinal structure which constitutes an important prerequisite for the trap of large oil field.

However, some possibilities of economical oil deposits, too, still remain in this area, and therefore fundamental investigation on this problem should be pushed forward.

7-4-1 Geology of Islaicocha District

The seepage is immediately east of the NNW-SSE-beating fault which makes a boundary between the Yauri Basin and the Laramani Massif.

The rocks here consist of the Ayabacas limestone, the Puno red clastics, the Middle Tacaza volcanics and the Quarternary.

The Puno red rocks are most widely distributed, controlled by synclinal and anticlinal structures having the NNW-SSE trending axes and gently undulating with dips of 10° or less.

The Ayabacas limestone is exposed as a small inlier along the crest of a small anticline in the Puno group.

The oil is seeping out from the alluvium (pampa sediments) which covers the west limb of the Ayabacas limestone.

Consequently, geological situation of the seepage is east side of the large fault, and at the west limb of the Ayabacas limestone which forms a gentle anticlinal structure.

7-4-2 Properties of Oil Samples

The results of the property test of the crude oil and "mixed" water sampled from the seepage are summarized in Tables I-5 and I-6 respectively.

1) Discussion on Crude Oil

(1) The sampled oil is of a paraffin-base as indicated by the UOP coefficient,

pour point, wax content, aniline point and cetane index shown in Table 1-5, but its pour point is very high. This abnormally high pour point may be attributable to the fact that at the time of the seeping-out of the crude oil, its gasoline content has been already scattered and lost.

2) The oil color, the quantity of residual carbon, and the results of the ingredient analysis indicate that the crude oil is poor in asphaltic matter and has an especially low sulphur content. In the periphery of the oil seepage, however, gushing-out of H_2S -rich gas is observed. Hence, there is a possibility of sulphur being separated from the crude oil before the latter seeps out.

3) Light oil and kerosene obtained by the distillation test have the properties of excellent fuel oil.

4) Lubricating oil separated from the crude oil also has an excellent viscosity index as far as performance is concerned. But since such lubricating oil has a high pour point, it is necessary to de-wax the lubricating oil.

5) Crude oil having an UPO coefficient of more than 12 is comparatively few, but the Minas crude oil of Brazil, which is famous for its high wax content, has an UPO coefficient of 12.5, and the crude oil imported from Peru to Japan shows an UPO coefficient of 12.0 being similar to that of Islaicocha oil.

2) Discussion on Water Sample

(1) Quality of Water Sample

As shown in Table 1-6, this water has much lower soluble salts concentration than ordinary water of oil or gas-field, whereas contains abnormally high quantities of sulphuric radical and iron.

Connate waters accompanying the oil or gas fields are usually of a salt

water containing large amounts of salts mainly consisting of Na^+ and Cl^- . When considered from the viewpoint of the composition, such water contains large quantities of inorganic ingredients as I^- , Br^- , HCO_3^- and NH_4^- which constitute sources of organic radicals, and of hydrocarbons as CH_4 , C_2H_6 , and C_3H_8 . On the other hand, it contains no ingredient such as sulphuric radical due to reduction.

The sampled water belongs to the $\text{SO}_4^{2-} - \text{Na}^+$ type according to the classification by Sulin, and is considered to be of a non-reduction environment, or of an open system according to the terminology of water chemistry.

It is concluded, therefore, that the water in question is not the so-called "connate water", but is ordinary ground water.

(2) Composition of Soluble Gases

Most of soluble gases in the water sampled may have been scattered and lost, as a pretty long time has elapsed during the period from sampling to analysing. The result of analysis obtained, therefore, may not indicate true values at the time of sampling.

However, various residual gases of hydrocarbon, although they are of minute quantities, have been detected from the water, suggesting the following characteristics of "the oil field gas".

The analytical result of hydrocarbon gases indicates a clear tendency that the more number of carbons the gas consists of (i.e. heavier gas), the rapider its content decrease as shown in Table I-6. Generally speaking, such an oil-field gas is often found in the oil deposits which have been intensively infiltrated by ground water, or in those being transported from afar by diffusion and permeation.

The soluble gases of this mixed water are considered as the latter type, and heavier ingredients of the oil-field gas must have been removed during a far-away transportation.

(3) Summary

The Islalcocha crude oil is of a low-sulphur and paraffin-base, and its properties are comparatively similar to those of other Peruvian crude oils. It is, however, distinctly different from other Peruvian oils in its poor contents of the lightest gasoline as well as the heaviest asphalt, and in its high pour point.

The "mixed" water is intrinsically different from the usual connate waters of oil fields, being suggestive of a ground water. Hydrocarbon gases solved in the mixed water strongly suggest that this crude oil has come from a considerably far-away place. For exploration of oil resources, therefore, the regional survey is required in addition to the examination of the Islalcocha district.

7-4-3 Areal Environment on Petroleum Resources

1) Requirement for Formation of Oil Deposit

Four geologic factors required for the occurrence of oil field, although well-known facts, are briefly reviewed hereunder owing to discuss the areal environment and potentiality of oil resources.

(1) Existence of Source Rock of Petroleum

Marine or sub-marine sediments containing a great deal of extractable organic matters are indispensable as the source rock of petroleum.

(2) Existence of Highly Permeable Formation

Permeable strata are necessary through which oil can migrate easily enough to accumulate. Generally speaking, porous clastic rocks and chemically

soluble limestone or dolomite are considered to be suitable reservoir rocks.

(3) Existence of Impermeable Rocks Overlying Oil-bearing Bed

In order to prevent oil from freely flowing and being lost, some impermeable strata overlying the oil reservoir is necessary. Generally, shale or clay is suitable for this purpose.

(4) Existence of Oil Trap

Some geological structure known as "trap" is required which can control the migration of oil and cause the oil to be stored. The anticlinal trap is common, and all the large oil fields originate from this type of trap, but the fault trap too, is not so rare.

2) Stratigraphical Conditions for Oil Occurrence of the Area

In the surveyed area, neither source nor reservoir rocks of petroleum have been definitely confirmed. However, the paper by Newell (1949) regarding Pirin oil field in the Titicaca area gives a very useful suggestion to this problem.

He says: "Oil produced as well as important oil seepage in the Pirin region are all restricted to the Ayabacas limestone and thin beds of sandstone right on it, being sealed by highly impervious shales and clayey breccias of the upper beds of Moho formation and basal beds of the Puno group."

The Isclalcocha oil seepage occurs adjoining the west side of a small inlier of the Ayabacas limestone in the Puno group and has a similar oil-bearing condition to that of the Pirin oil field. Therefore, it may safely be said that the Ayabacas limestone constitutes at least an important reservoir rock in the area.

According to Newell, the Ayabacas limestone in the Pirin region is only about 30 m thick. On the other hand, its thickness is estimated to reach more than 500 m in the...

surveyed area. Therefore, as far as the reservoir rock is concerned, the surveyed area is considered to be in more favorable condition than the Pirin.

Regarding the source rock of petroleum, Newell says as follows:

"In Titicaca area, fossiliferous marine sediments were deposited in the Devonian, Permian, Jurassic and Cretaceous ages respectively, all of which might have contributed to the formation of petroleum, but the Devonian rocks, however, were considerably altered by metamorphism and organic material originally contained in the rocks has probably been destroyed. The Permian and Jurassic rocks, being highly fossiliferous, might be a source for petroleum. All direct indications of petroleum in the region, however, are limited to the Middle Cretaceous rocks (Ayabacas limestone and associated beds). The most likely source of the petroleum found at Pirin, is the Middle Cretaceous rocks in which it is found."

It may be difficult for us to justify the views of Newell, but his views may serve as a guide for our exploration.

The area of occurrence of petroleum resources, therefore, is presumed to be the area of distribution of the Ayabacas limestone. This limestone is presumed to be distributed over the area ranging from the Laramani Massif to the Yauri Basin, but is already exposed in the northern part of the mountainous area.

3) Structural Conditions for Oil Occurrence of the Area

As the folding of the Ayabacas limestone in the surveyed area generally is small in dimension, it is difficult to expect a large-scale anticlinal trap. However, the fact that local but gentle anticlines are formed in the area is sufficient for enabling us to expect such traps although they may be of a small-scale. Especially, the Yauri Basin

appears noteworthy in this respect since the structure becomes comparatively gentle.

In this area, normal faults of the NNW-SSE direction develop. In general, it is said that normal faults is more favorable to trap oil than reverse or thrust faults. Thus fault traps too, can be expected in this area.

For instance, it may be possible that the trap of the Islalcocha oil seepage is formed as a combination trap of an anticlinal structure and a fault structure, judging from the structural environment as mentioned previously.

References

- Audebaud, E. E. & Pecho, V. G. (1970)
Mapa Geologico del Cuadrangulo de Sicuanl Departamento Cuzco,
Servicio de Geologia y Minería , Peru (in Spanish)
- Bellido, E. B. y Simons, F. S. (1957)
Memoria Explicativa del Mapa Geologico del Peru
Boletin de 11, Sociedad Geologica del Peru Tomo 31
- Bellido, E. B. (1969)
Sinopsis de la Geologia del Peru
Servicio de Geologia y Minería Boletin No. 22 (in Spanish)
- Bellido, E. B. others (1972)
Aspectos Generales de la Metalogenia del Peru
Servicio de Geologia y Minería , Peru
- Cenozoic Reserch Group of Yamagata (1970)
The Field Survey of Green Tuff (in Japanese)
Cenozoic Reserch Group of Yamagata
- Giletti, B. J. & Day, H. W. (1968)
Potassium-Argon Ages of Igneous Intrusive Rocks in Peru
Nature Vol. 220 November 9
- Harrison, J. V. (1940)
Nota preliminar sobre la geologia de los Andes central del Peru
Soc. Geolog. del Peru Bol. 10 (in Spanish)
- Jenks, W. F. (1948)
Geology of the Arequipa Quadrangle
Instituto Geologico del Peru Boletin 9 (In Spanish & in English)
- Jenks, W. F. (1956)
Handbook of South America Geology
Geological Society of America Memoir 65
- Jenks, W. F. & Goldish, S. S. (1956)
Rhyolitic Tuff Flows in Southorn Peru
Geological Society of America Bulletin vol. 64
- Kuno, H. (1963)
Volcano and Volcanic Rocks (in Japanese)
Iwanami Shoten, Japan

- Martines, M. & Huerta, T. (1965)
Informe Geologico de la Zona CMTE Espinal, Cuzco, Puno
- Mendivil, S. (1965)
Geologia de los Cuadrangulos de Maure y Antajave
Servicio de Geologia y Minería, Peru
- Metallic Minerals Exploration Agency of Japan (1971)
Combined Airborne Geological and Photogeological Survey
The Cuzco--Apurimac Area South Peru
- Metallic Minerals Exploration Agency of Japan (1971)
Report on Geotectonic Survey of the Southern Peru, 1970 (in Japanese)
- Metallic Minerals Exploration Agency of Japan (1972)
Report on Geotectonic Survey of the Southern Peru, 1971 (in Japanese)
- Newell, N. D. (1949)
Geology of the Lake Titicaca Region, Peru and Bolivia
Geological Society of America Memoir 36
- Overseas Technical Cooperation Agency
Metallic Minerals Exploration Agency
Government of Japan (1972)
Report on Geological Survey of The Yauri Area, Southern Peru
(in Japanese & in English)
- Peacock, M. A. (1931)
Classification of Igneous Series
Journal of Geology vol. 39
- Perales, F. (1970)
Tabla de Correlacion de las Unidades Estratigraficas del Peru
- Peterson, G. (1949)
Condiciones Geograficas y Geologicas de la Cuencas del Rio Zarumilla
Soc. Geol. del Peru Vol. Jubilar Parte II (in Spanish)
- Peterson, G. (1954)
Informe Preliminar Sobre la Geologica de la Faja Costamera del
Departamento de Ica
Emp. Pet. Fiscal Bol. Tec. No. 7 (in Spanish)
- Takeda, H. (1972)
Geology and Ore Deposits of the Andes Region, South America
Geological News (Chishitsu News), No. 217 (in Japanese)

Takeda, H. (1973)

Geology and Ore Deposits of the Andes Region, South America
Geological News (Chishitsu News), No. 224 (In Japanese)

Terrones, A. J. (1958)

Structure Control of Contact Metasomatic Deposits in the Peruvian Cordillera
Mining Engineering, March

Vargas, L. V. (1970)

Geologia del Cuadrangulo de Arequipa
Servicio de Geologia y Minería Boletín No. 24 (In Spanish)

PARTICULARS

PART II. GEOPHYSICAL SURVEY

CONTENTS

PART II GEOPHYSICAL SURVEY

1. Introduction	II - 1
1-1 Object	II - 1
1-2 Outline of operations	II - 1
1-2-1 Gravity survey	II - 1
1-2-2 Electrical survey	II - 2
2. Gravity survey	II - 3
2-1 Gravity meter	II - 5
2-2 Gravity stations	II - 6
2-3 Reference of observed gravity values	II - 7
2-4 Leveling	II - 9
2-4-1 Leveling by means of automatic level	II - 9
2-4-2 Leveling by means of precision barometric altimeter	II - 10
2-5 Correction of gravity values	II - 10
2-5-1 Drift correction	II - 10
2-5-2 Earth tide correction	II - 11
2-5-3 Terrain correction	II - 11
2-5-4 Elevation correction	II - 13
2-5-5 Latitude correction	II - 14
2-6 Assumption of density	II - 15
2-7 Map of Bouguer anomaly	II - 15
2-8 Maps after various filtering	II - 20

2-8-1	Regional trend map	II - 20
2-8-2	Residual gravity map	II - 20
2-8-3	Residual filtered gravity map	II - 21
2-9	Profiles of underground structure	II - 22
2-9-1	Method of calculation and initial density model	II - 22
2-9-2	Contour map of underground magnetic structure	II - 23
2-9-3	Construction of density model	II - 23
2-9-4	Assumption of calculation	II - 24
2-10	Underground structure map	II - 24
2-11	Two-layer structure contour map	II - 25
2-12	Results of calculations	II - 26
2-12-1	Table of gravity calculation I	II - 26
2-12-2	Table of gravity calculation II	II - 27
2-12-3	Table of gravity calculation III	II - 28
2-12-4	Table of gravity calculation IV	II - 29
2-12-5	Table of gravity calculation V	II - 30
3	Electrical survey by Schlumberger's method	II - 31
3-1	Method	II - 31
3-2	System	II - 33
3-3	Traverse lines and stations	II - 34
3-4	Laboratory measurement of resistivity	II - 35
3-5	Analysis	II - 37
4	Results	II - 41
4-1	Map of Bouguer anomaly	II - 41

4-1-1	General trend	II - 41
4-1-2	Local character	II - 50
4-2	Map of filtered gravity	II - 51
4-2-1	Map of noise structure	II - 52
4-2-2	Map of normal structure	II - 53
4-2-3	Map of local structure	II - 54
4-3	Map of regional gravity trend	II - 55
4-3-1	Map of regional gravity trend expressed by the polynomial of first order	II - 55
4-3-2	Map of regional gravity trend expressed by the polynomial of second order	II - 55
4-3-3	Map of regional gravity trend expressed by the polynomial of third order	II - 58
4-4	Map of residual gravity	II - 58
4-4-1	Residual map of third order	II - 60
4-5	Profile	II - 60
4-5-1	G-G' section	II - 61
4-5-2	F-F' section	II - 61
4-5-3	A-A' section	II - 62
4-5-4	B-B' section	II - 63
4-5-5	C-C' section	II - 63
4-5-6	D-D' section	II - 64
4-5-7	E-E' section	II - 64
4-6	Resistivity profile	II - 65
4-6-1	Traverse line I	II - 67
4-6-2	Traverse line II	II - 69

4-6-3	Traverse line III	II - 69
4-7	Contour map of underground structure by two-layer model	II - 70
4-8	Map of underground structure	II - 72
4-9	Comparison between airborne magnetic survey and gravity survey	II - 73
4-9-1	Contour map of underground magnetic structure	II - 74
4-9-2	Comparison between the contour map of underground magnetic structure and the map of Bouguer anomaly	II - 75
5	Underground structure estimated from geophysical survey	II - 77
5-1	Outline	II - 77
5-2	Underground structure along profile lines	II - 78
5-2-1	Underground structure estimated from electric survey	II - 78
5-2-2	Gravity survey G-G' section	II - 78
5-2-3	Gravity survey F-F' section	II - 79
5-2-4	Gravity survey A-A' section	II - 80
5-2-5	Gravity survey B-B' section	II - 81
5-2-6	Gravity survey C-C' section	II - 81
5-2-7	Gravity survey D-D' section	II - 82
5-2-8	Gravity survey E-E' section	II - 82
5-3	Distribution of intrusiver rocks	II - 83
5-4	Distribution of sedimentary rocks	II - 85

LIST OF ILLUSTRATIONS

Fig.	1-1.	Gravimetric Value-Elevation Curve	II - 16
Fig.	1-2.	Gravimetric Value-Elevation Curve	II - 16
Fig.	1-3.	Gravimetric Value-Elevation Curve	II - 17
Fig.	1-4.	Gravimetric Value-Elevation Curve	II - 17
Fig.	2-1.	Regional Gravity Trend Calculated by Polynomial of First Order	II - 56
Fig.	2-2.	Regional Gravity Trend Calculated by Polynomial of Second Order	II - 57
Fig.	2-3.	Regional Gravity Trend Calculated by Polynomial of Third Order	II - 59

LIST OF TABLES

Table	1.	Flow Chart of Geophysical Survey in Yauri Area	II - 3
Table	2.	Scale Constant Expressed Milligal for La Coste & Romberg ..	II - 6
Table	3.	Calculation of Gravity Standard Value	II - 8
Table	4.	Densities of Rock Samples	II - 18
Table	5.	Comparison of Resistivity	II - 66

LIST OF PLATES

Plate II-1-1.	Map of Geophysical Survey Area and Locality of Rock Samples	(1:100,000 - 1:200,000)
II-2-1.	Map of Bouguer Anomaly (Density; $\rho - 2.67$)	(1:100,000 - 1:200,000)
II-2-1-1.	Map of Bouguer Anomaly (Density; $\rho - 2.67$)	(4 Sheets) 1: 50,000
II-2-2.	Map of Bouguer Anomaly (Density; $\rho - 2.00$)	(1:100,000 - 1:200,000)
II-2-3.	Map of Short Wave-Length Bouguer Anomaly (Map of Noise Structure)	(1:100,000 - 1:200,000)
II-2-4.	Map of Intermediate Wave-Length Bouguer Anomaly (Map of Normal Structure)	(1:100,000 - 1:200,000)
II-2-5.	Map of Long Wave-Length Bouguer Anomaly (Map of Local Structure)	(1:100,000 - 1:200,000)
II-2-6.	Map of Residual Gravity (Polynomial of Third Order)	(1:100,000 - 1:200,000)
II-2-7.	Profile of Underground Structure (A-A' and B-B')	(1:100,000 - 1:200,000)
II-2-8.	Profile of Underground Structure (C-C' and D-D')	(1:100,000 - 1:200,000)
II-2-9.	Profile of Underground Structure (E-E', F-F' and G-G')	(1:100,000 - 1:200,000)
II-2-10.	Map of Underground Structure	(1:100,000 - 1:200,000)
II-2-11.	Contour Map of Underground Structure by Two-Layer Model (Difference Density of 0.5 g/cm^3 , Nodal Plane 500 m)	(1:100,000 - 1:200,000)
II-3-1.	Analysis of VES Curve at Stations B, C, D and E on Line I	
II-3-2.	Analysis of VES Curve at Stations F, G, H and I on Line I	
II-3-3.	Analysis of VES Curve at Stations B, C, D and E on Line II	
II-3-4.	Analysis of VES Curve at Stations F, G, H and I on Line II	
II-3-5.	Analysis of VES Curve at Stations B, C, D and E on Line III	
II-3-6.	Analysis of VES Curve at Stations F, G, H and I on Line III	
II-3-7.	Profile of Resistivity	(1:10,000)
II-3-8.	Interpretation of Electrical Basement	(1:20,000)
II-4-1.	Contour Map of Underground Magnetic Structure	(1:100,000 - 1:200,000)

CHAPTER 1 INTRODUCTION

1-1 Object

The gravity survey was carried out in the area shown in the Plate II-1-1 (map of Yauri). This area extends over 2500 km². The aims of this survey were to estimate the structure of subterranean base and the distribution of intrusives in the survey area whose surface is mostly covered by alluvium, and to obtain the necessary data to determine the sites of structural boring following and determine the operation area for IP survey (Induced Polanization method, abbreviated to IP hereafter), and for EM survey (Electro Magnetic method, abbreviated to EM hereafter) which area effective for direct survey with the data obtained by other surveys together.

Taking the tendency is gravity survey into consideration that the depth to the basement is highly dependent on a assumption of the density of underground rock, the vertical electrical soundings as a support of gravity survey were carried out also by Schlumberger's method in a part of the area and the estimations of the depth to the basement were made by the analysis of the variation of resistivity for the purpose of an improvement of an accuracy of subterranean strucure obtained from gravity survey.

1-2 An outline of operations

1-2-1 Gravity survey

Gravity measurements were made at 1312 stations. This group of gravity stations consists of 154 stations along main roads, 886 stations in the detailed survey area, and 272 stations along the roads in surrounding area, These are

by solid lines and chain lines, hatching and chain lines respectively in Plate II-1-1.

Leveling was carried out as follows. Bench mark Q-237, which was established by the government of Peru near the fork to Yauri on the road from El Descanso to Hector Tejada, was taken as a base station. Bench marks were set along the main roads by means of the automatic level (B-2). The elevations of the gravity stations outside main roads were obtained by barometric height measurements. Two Paulin precision surveying altimeters were used for this survey, one was set at the base station and the other was carried to each station. Earth tide correction, drift correction, elevation correction, latitude correction and terrain correction, latitude correction and terrain correction were applied to measured gravity data.

1-2-2 Electric survey

Three measuring lines with a length of 8.5 km each were established as shown in Plate II-1-1. These lines were each composed of eight stations and 25.5 km in length and had 24 stations in total.

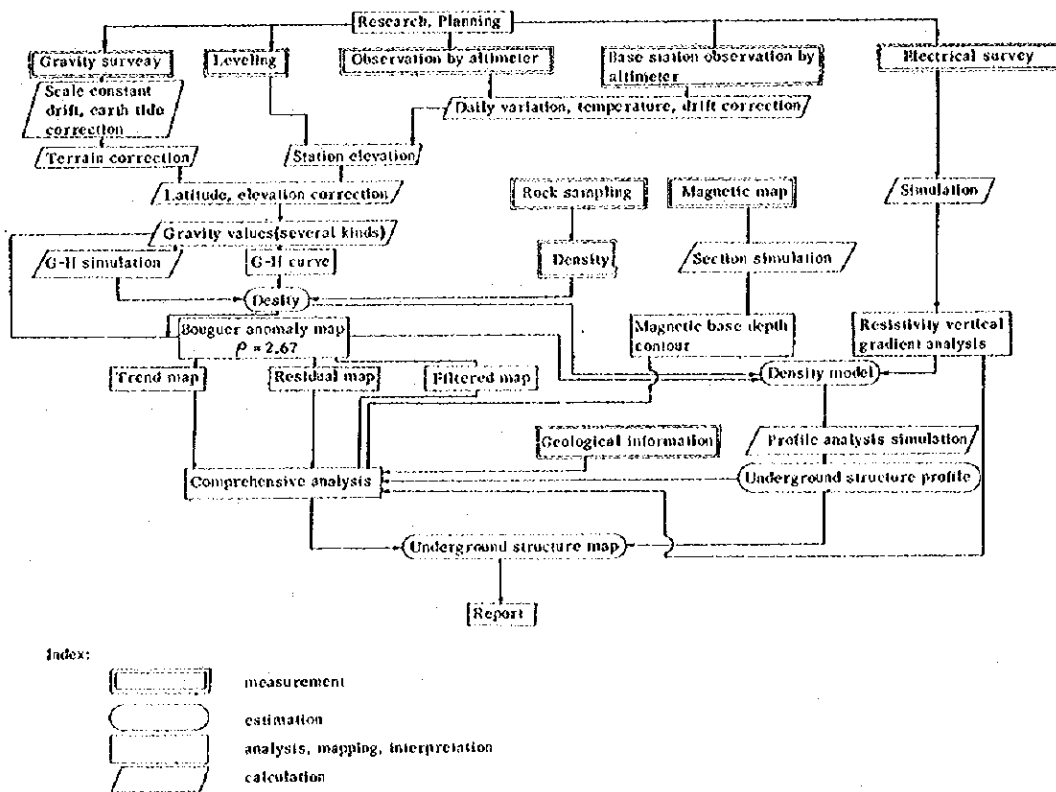
Vertical gradients of resistivity were measured by Schlumberger system. Separation of current electrodes was extended to 750 m.

CHAPTER 2 GRAVITY SURVEY

This chapter contains explanation on methods of measurement, data processing and analysis on gravity survey.

The process of the research from gravity survey to make this report is shown in the following flow chart.

Table - 1 Flow chart of geophysical survey in Yauri area



Following terms and symbols on gravity survey, which are widely used, are used in this report.

No. Station number

Vr Observed value (Reading of the gravity meter)

hi (m) Instrument height (height of the gravity meter from the

bench mark or ground level)

V_{rk} (mgal) Observed value $\times K$ (the number obtained from observed value by multiplying the scale constant of the gravity meter.
($V_{rk} = V_r \times \text{scale const.}$)

V_{et} (mgal) Earth-tide correction

V_{hi} (mgal) Instrument height correction ($V_{hi} = 0.3086 \times h_i$)

V_e (mgal) Corrected value ($V_e = V_{rk} + V_{et} + V_{hi}$)

V_d (mgal) Drift correction

V_g (mgal) Gravity value of the base station

D_g (mgal) Difference in gravity between the observed station and the base station

B_g (mgal) Gravity value of the reference station

g (mgal) Gravity value

δg_o (mgal) Free-air correction

g_o (mgal) Gravity value applied free-air correction

$$(g_o = g + \delta g_o)$$

$\delta g'_o$ (mgal) Terrain correction

g_o' (mgal) Gravity value applied free-air and terrain corrections

$$(g_o' = g + \delta g_o + \delta g'_o)$$

$\delta g_o''$ (mgal) Bouguer correction

g_o'' (mgal) Gravity value applied free-air, terrain and Bouguer

corrections ($g_o'' = g + \delta g_o + \delta g'_o + \delta g_o''$)

γ_o (gal) Normal gravity

g_{φ} (mgal)	Gravity value applied latitude correction ($g_{\varphi} = g - r_0$)
Δg_0 (mgal)	Bouguer anomaly ($\Delta g_0 = g_0 - r_0$)
φ (deg)	Latitude of the station
λ (deg)	Longitude of the station
ρ	Density
$\Delta \rho$	Density difference
H	High gravity anomaly (Gravity anomaly high)
L	Low gravity anomaly (Gravity anomaly low)
Hm	Magnetic anomaly high
Lm	Magnetic anomaly low

2-1 Gravity meter

Three La Coste and Romberg gravity meters, G-204, G-206 and G-283 were used for this research. These gravity meters have reading range of 7,000, and cover gravity range of about 7,300 mgal. The reading accuracy of these gravity meters is about 0.01 mgal. One of the excellent characters of the La Coste-Romberg gravity meter is that it has very small drifting rate, and it is usually less than 0.5 mgal/day.

Table 2 shows parts of scale constants of each gravity meter.

Table 2. Scale Constant Expressed Milligal for La Coste & Romberg

Modal of Gravity Meter Reading	Value in Milligal			Factor for Interval		
	G-204	G-206	G-283	G-204	G-206	G-283
400	413.73	418.88	421.70	1,034.44	1,047.13	1,054.14
500	517.17	523.59	527.12	1,034.49	1,047.11	1,054.11
600	620.62	628.30	632.53	1,034.58	1,047.10	1,054.10
700	724.08	733.01	737.94	1,034.70	1,047.10	1,054.10
800	827.55	837.72	843.35	1,034.85	1,047.10	1,054.12
900	931.03	942.43	948.76	1,035.00	1,047.12	1,054.17
1,000	1,034.53	1,047.15	1,054.18	1,035.12	1,047.15	1,054.23
1,100	1,138.04	1,151.86	1,159.60	1,035.24	1,047.12	1,054.29

2-2 Gravity station

Total number of stations is 1,312 and this is classified as follows.

along main roads (elevation measured by the automatic level,

station interval 1 km) 154 stations

detailed survey area (elevation measured by the altimeter,

density 1 station/km²) 886 stations

surrounding area (elevation measured by the altimeter,

station interval 2 km) 272 stations

Total number of station 1,312 stations

The locations of stations were determined on the topographic maps by judging from surrounding geographical features such as roads, rivers, mountains and build structures.

When prominent features could not be found, the locations were determined by traverse starting from pre-determined station using clinometers, range finders and tapes. The locations of stations and their distribution are shown in each map of anomalies, Plate II-2-1 ~ Plate II-2-6.

2-3 Reference of observed gravity values

Observed gravity values were connected to the results of gravity survey of El Servicio de Geofisico, Republic of Peru. The gravity value of Bench mark Q-237, $g = 979196.605$ mgal was adopted as the reference value. Bench mark Q-237 is near the fork to Yauri on the road linking Hector Tejada with El Descanso.

Bench mark No. 603 was established at Yauri town and used as the gravity base station. The gravity value of this base station was determined by the reoccupation measurement from Bench mark Q-237. The result of this measurement are listed in Table 3.

Table 3. Calculation of Gravity Standard Value

G	No. of Station	Time	Reading Value (Vr)	$\Delta V_r \times K$	$V_r K$ ($V_r' + \Delta V_r \times K$)	Correction of Tidal Gravity (Vet)	Height of Gravitometer (hi)	Vhi $\times 0.3086$	Corrected Value ($V_r K + V_{et} + V_{hi}$)	Correction of Diurnal Drift (Vd)	$V_r K + V_{et} + V_{hi} + V_d$	Dg	g
204	BM Q 237	9 : 58	801,019	1,055	828,605	0.145	0.268	-0.083	828,667	0.000	828,667		977,196.605
	603	10 : 45	844,991	46,559	874,109	0.122	0.275	-0.085	874,146	-0.010	874,136	45,469	977,242.074
	BM Q 237	11 : 41	801,104	1,142	828,692	0.081	0.270	-0.084	828,689	-0.022	828,667		977,196.605
283	BM Q 237	9 : 58	799,492	104,275	842,815	0.145	0.19	-0.059	842,901	0.000	842,901		977,196.605
	603	10 : 48	842,685	44,995	888,345	0.120	0.27	-0.084	888,381	0.003	888,384	45,483	977,242.088
	BM Q 237	11 : 42	799,546	104,931	842,871	0.080	0.18	-0.56	842,895	0.006	842,901		977,196.605

This table shows that the difference between the results of two gravity meters (G-204 and G-283) is only 0.014 mgal. Consequently the mean value of two results, 977,242.081 mgal, was adopted as the gravity value of the base station.

2-4 Leveling

Six automatic levels and six precision altimeters were used for leveling. Field notes, calculation tables and tables of results were appended.

2-4-1 Leveling by means of automatic levels

Automatic levels model B-2 made by Sokkisha were used. The elevation of above mentioned Bench mark Q-237, 3, 983. 193m, was adopted as the reference value. Sub Bench marks Nos. 100, 200, 300, 400 and 603 were established on the roads to Santa Lucia, to Yauri and Hector Tejada. These bench marks and roads concerned are shown in Plate II-1-1. Elevations of respective bench marks were determined by going and returning observation along the road shown by solid lines in Plate II-1-1.

Levelings were also carried out along the roads shown in the same plate by chain lines from El Descanso to Hacienda Desvio, from Hector Tejada to El Santoario, from Hector Tejada to Ocoruro and from Yauri to Ataraya by means of automatic levels. These leveling routes were connected to above mentioned sub bench marks. (Refer to Plate II-1-1, map of geophysical survey area and locality of rock samples.)

Closing errors of leveling are within the limit of $e \leq 30\sqrt{D}$ (mm)

(D : length of route in km)

Total length of leveling routes reached to 221 km.

2-4-2 Leveling by means of precision barometric altimeter

Elevations of other stations whose elevations were not measured by automatic levels were obtained by precision barometric altimeter and connected to above mentioned subbench marks. The instruments used were American Paulin System Model MM-1, whose range is 0m to 5000m and reading accuracy is 1 m.

In making barometric leveling, one barometric altimeter was kept at the base station and the observation of daily variations of atmospheric pressure and air temperature there were made. In reducing the reading value of altimeter into elevation, temperature correction, correction to daily variation of atmospheric pressure and drift correction were applied in order to increase the accuracy of elevation value of each station.

2-5 Correction of gravity value

Many kinds of corrections are necessary for the reduction of observed data in gravity survey. These corrections were carried out by means of a electronic computer.

2-5-1 Drift correction

The drift is an inevitable character of a gravity meter and must be eliminated from observed values. Though it varies in proportion to time usually, its variation rate is not always constant. The correction of drift must be applied to every closing loop separately.

Station No.603 was used as a gravimetric base station and the observation was closed by reoccupying base station every day.

Correction was applied under such an assumption that the drift is proportional to time. Drift rates are listed in gravity calculation tables.

2-5-2 Earth tide correction

Earth tide correction is applied for the purpose of eliminating the effects of the moon and the sun to the observed values. The earth-tide effect depends on the positions of the moon and the sun, and it varies with time (year, month, day, hour, minute) and the position of observing station (latitude, longitude).

By applying this correction, an accuracy of observation can be improved because the drift of an instrument after the earth-tide correction becomes detectable by a simple closing observation.

2-5-3 Terrain correction

This is a correction to eliminate the influence of the attraction of the surrounding topography to the gravity meter. Terrain correction is obtained by following method. The topography map concerned is divided into grids of equal size squares. Mean elevation is estimated for each square prism and difference in elevations between respective squares and the observing station are taken. Each square prism is approximated in shape to such as cone, cylinder and pyramid according to its conditions. Attractions of these prisms are calculated and summed up to the terrain correction. Because the attraction becomes greater as the distance between the gravity station and concerned prism is smaller and vice versa, terrain corrections for nearer blocks were calculated in high precision and precision of calculation was lowered with distance.

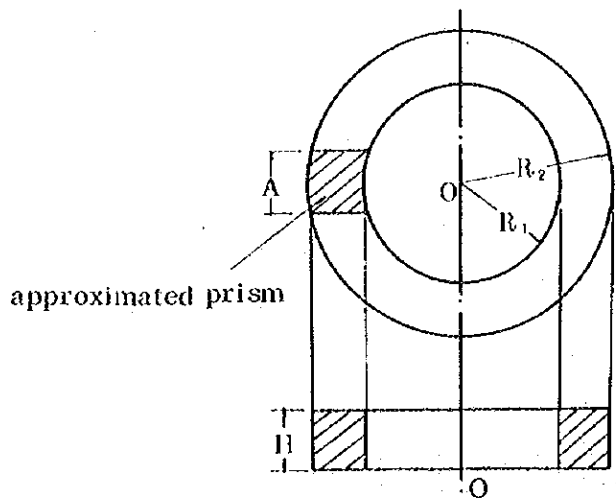
Scales of topographic maps, ranges of correction area, grid distances,

numbers of points where the topographic elevation were read and latitude and longitude of initial point are as follows.

	distant area	mediate distant area	vicinity	adjacent area
Scale of map	1/200,000	1/100,000	1/25,000	sketch map
Correction range	-70°27'~-72°03', -13°57'~-15°33'	-70°51'~-71°39', -14°21'~-15°09'	-70°58'~-71°32'15", -14°27'45"~-15°02'20"	circle of 20 m radius
Grid distance	3' x 3'	45" x 45"	15" x 15"	
Number of read point	1,024	4,096	18,769	
Latitude of initial point	-13°57'	-14°21'	-14°27'45"	
Longitude of initial point	-72°08'	-71°39'	-71°32'15"	

Each calculation of correction was carried out by an electronic computer. Following Kane's formula³⁾ was used for actual calculation in which a prism is approximated to an appropriate segment of an annular circle ring.

$$g = 2\gamma\rho\Delta^2 \left(R_2 - R_1 + \sqrt{R_1^2 + H^2} - \sqrt{R_2^2 + H^2} \right) / (R_2^2 - R_1^2)$$



- g : terrain correction
- γ : gravitational constant
- ρ : density
- R_1 : distance from the station to inside of terrain correction
- R_2 : distance from the station to outside of terrain correction
- H : height of terrain correction
- O : gravity station

The double slope cone approximation method which is reported by Momose and others⁴⁾ was employed, after drawing sketch maps of the area whose distance is within 20 m from the observing station.

The correction area contains Lake Langui Layo. Because the depth of this lake is unknown, the water level of the lake was assumed to be ground level considering this assumption does not change correction too much.

In the calculation of terrain correction the elevations of observing stations were taken from topographic maps.

2-5-4 Elevation correction

The elevation correction is applied for the purpose of eliminating the different effects of elevations among the stations. The observed values are reduced to that of geoid (mean sea level). This correction divided into two parts. One is the free air correction which correct the effect of differences of elevation only, the other is the Bouguer correction which eliminates the different effects of the attraction of a slabs between geoid and observing stations. The Bouguer correction is affected by the background density of the survey area. The free air correction δg_0 is represented as follows using the mean vertical gradient of the earth's gravitation field.

$$\delta g_0 = 0.3086 \cdot H \text{ mgal (H : elevation in m)}$$

The Bouguer correction $\delta g''_0$ is represented as follows under such an assumption that an infinite slab having a thickness H and a density ρ exists between geoid and an observing station.

$$\delta g_0'' = - 2 \pi G \rho H = - 0.0419 \rho H \text{ mgal}$$

G : Gravitational constant

ρ : density (gr/cm³)

H : elevation of station (m)

The free air correction and the Bouguer correction are both a function of elevation H and can be put together into a form of

$$\delta g_0 + \delta g_0'' = (0.3086 - 0.0419 \rho) H \text{ mgal}$$

and called the elevation correction.

Elevations of each station obtained by leveling by means of automatic levels and precision barometric altimeters were used for this correction.

2-5-5 Latitude correction

The shape of the earth is not a complete sphere but an oblate spheroid of revolution whose axis is coincide with the axis of rotation.

The gravity along the surface of the earth varies with latitude because of the centrifugal force of rotation and of the shape of the earth. It has the minimum value at the equator and the maximum at the poles. Consequently the latitude correction has to be applied to observed gravity values.

The international gravity formula (1930) was used for the calculation of normal gravity.

This is

$$\gamma_0 = 978.0490 (1 + 0.0052884 \sin^2 \varphi - 0.0000059 \sin^2 2\varphi) \text{ gal}$$

φ : latitude

Bouguer anomaly $\Delta g_0''$ is obtained by

$$\Delta g_0'' = g_0'' - \gamma_0$$

where g_0'' is an gravity value after Bouguer correction and γ_0 , is normal gravity.

2-6 Assumption of density

The assumption of subsurface rock density in survey area is an important problem in gravity survey. This assumption affects not only elevation correction and terrain correction but also to the result of analysis of underground structure using the Bouguer anomaly.

This section treats the assumption for corrections. The assumption of density for analysis is appeared in the section 2-9-3.

The rock density in this survey was determined in consideration of the following investigations.

- 1) The drawings of five kinds of Bouguer maps under the conditions that the density is 2.00, 2.30, 2.40, 2.60 and 2.67.
- 2) The comparison between the topographic profiles and that of Bouguer anomalies ($\rho = 2.00, 2.30, 2.40, 2.60, 2.67$ and 2.80).
- 3) On the gradient of G - H curve (refer to Fig. 1-1 ~ Fig. 1-4)
- 4) G - H simulation

The density of the survey area was determined to be $\rho = 2.67$ after the above investigations and the discussion to the official supervisor.

2-7 Maps of Bouguer anomaly

According to appendix 1 the gravity calculation tables I, II, III, two kinds of Bouguer anomaly maps were drawn for density assumptions of $\rho = 2.67$ and $\rho = 2.00$. These maps are shown in Plate II-2-1 and II-2-2 respectively. The contour interval is 1.0 mgal for both maps. The outlines and analyses of these maps are treated in the section 4-1.

Fig. 1-1. Gravimetric Value-Elevation Curve

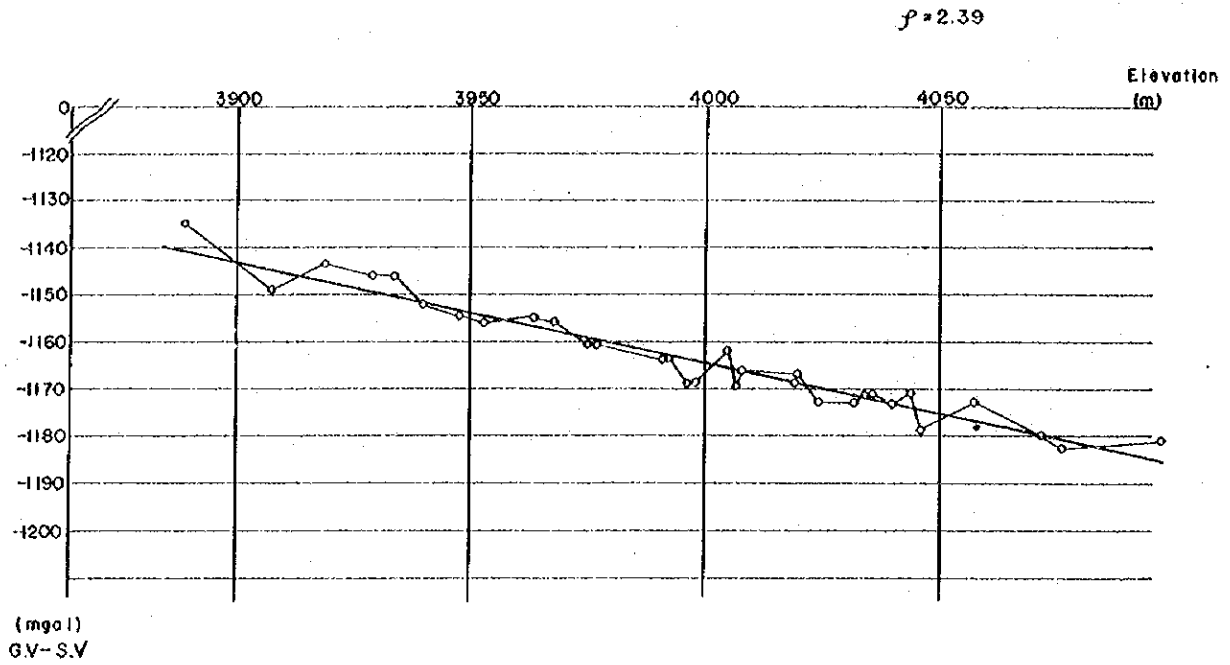


Fig. 1-2. Gravimetric Value-Elevation Curve

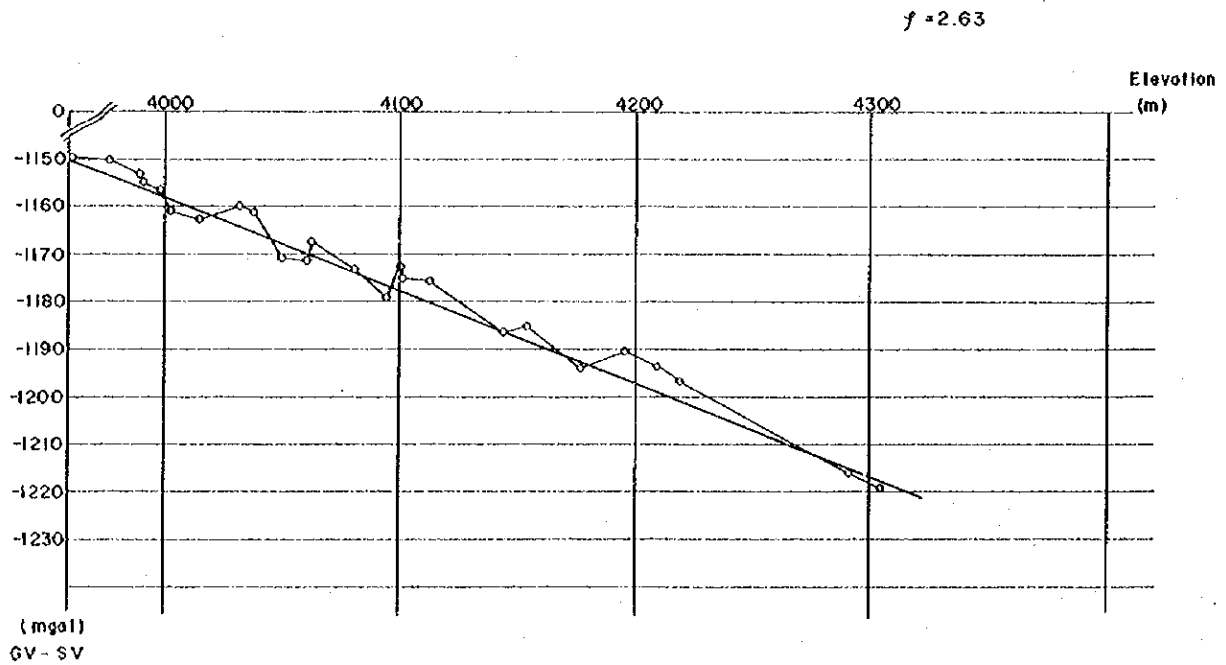


Fig. 1-3. Gravimetric Value-Elevation Curve

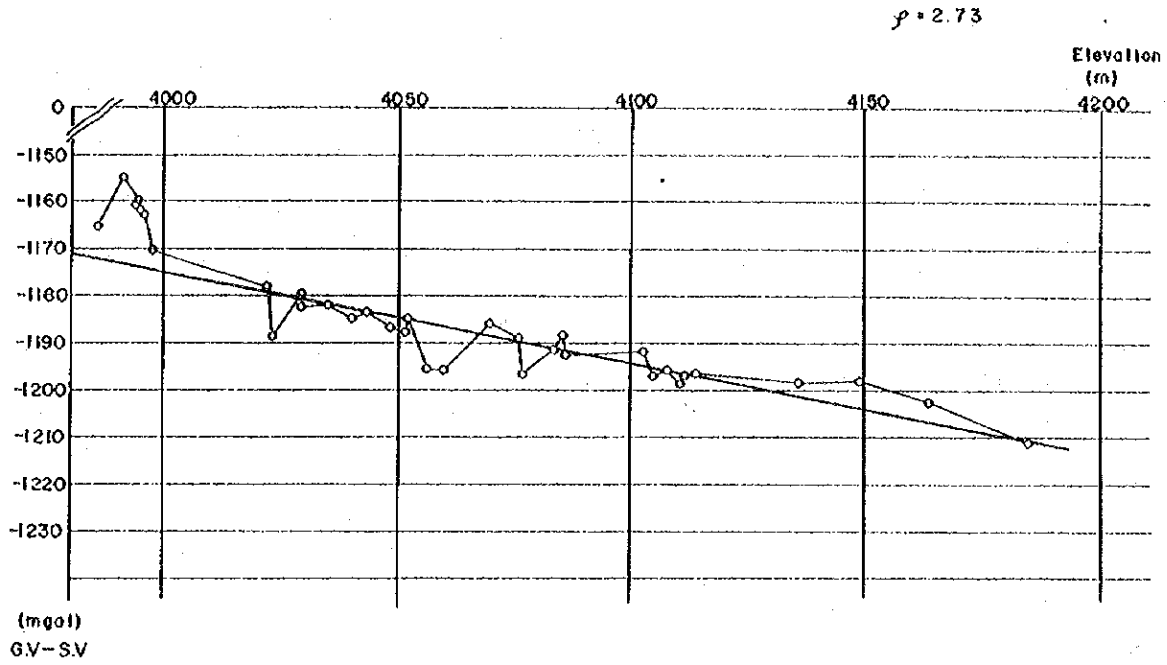


Fig. 1-4. Gravimetric Value-Elevation Curve

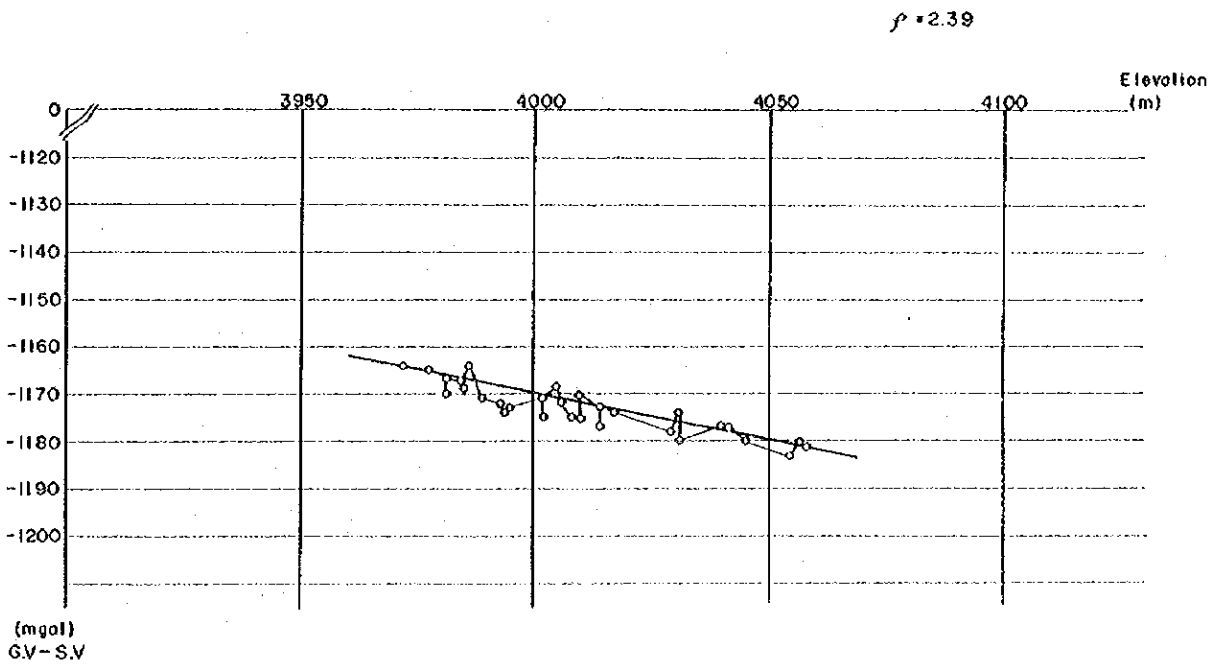


Table 4. Densities of Rock Samples

ERA	PERIOD	GEOLOGICAL UNIT		ROCK	ABBRE- VIATION	NO.	SAMPLE NO.	A	B	C	
CENOZOIC	QUATER- NARY	Barroso V.		andesite	and	1	10.	2.39	2.39	2.39	
	TERTIARY	Yauri f.		sandstone	ss	1	28.	2.51	2.24	2.24	
				tuff	tuff	1	64.	1.97			
		Descanso f.		sandstone	ss	1	78.	2.27	1.91	1.74	
				tuff	tuff	3	94, 95, 98	1.56			
		Sencca f.		dacite	da	4	9, 79, 93, 104.	2.24	2.24	2.24	
		Tacaza g.		middle	tuff	tuff	4	26, 30, 84, 92.	2.13	2.44	2.49
					trackyte	tryt	1	83.	2.49		
					anadesite	and	4	31, 33, 76, 91.	2.42		
					basalt	bas	7	6, 7, 11, 25, 35, 56, 70.	2.73		
					tuff	tuff	3	80, 82, 89	2.06		
		Puno g.		upper	sandstone	ss	7	34, 52, 62, 85, 99, 100, 101.	2.16	2.13	2.11
	tuff				tuff	3	4, 5, 51.	1.80			
	conglomerate				cong	1	55.	2.34			
	rhyolite				rhy	2	61, 63.	2.32			
	obsidian				obs	1	86.	2.03			
	lower			sandstone	ss	5	32, 40, 57, 72, 39.	2.56	2.58	2.58	
conglomerate				cong	3	50, 59, 74	2.60				

ERA	PERIOD	GEOLOGICAL UNIT	ROCK	ABBRE- VIATION	NO.	SAMPLE NO.	A	B	C
MESOZOIC	CRETACEOUS	Munani ~ Catacucho f.	sandstone	ss	1	47.	2.41	2.54	2.54
			shale	sh	1	48.	2.66		
		Moho Ayabacas f.	sandstone	ss	1	46.	2.12	2.35	2.50
			limestone	ls	5	41. 44. 60. 75. 77.	2.58		
	Ferrobamba f.	limestone	ls	7	3.23.24.27. 65.73.105.	2.68	2.68	2.68	
	JURASSIC	Yura f.	quartzite	qte	5	1. 2. 17. 19. 66.	2.53	2.67	2.58
			shale	sh	1	15.	2.80		
Intrusive rocks			granite	gr	7	14. 29. 38. 49. 54. 58. 81.	2.58	2.67	2.62
			monzonite	monz	10	8.18.22.36. 37. 43. 69. 87.88.106.	2.56		
			porphyrite	pot	3	53.90.103.	2.58		
			diorite	di	9	12. 20. 42. 67. 68. 71. 96.97.102.	2.68		
			gabbro	gb	1	13.	2.94		
Others			garnet	gar	1	16.	3.46	3.97	3.97
			magnetite	mg	1	21.	4.18		
			barite	ba	1	45.	4.27		

A = average

B = equal average

C = weighed average

2-8 Maps after various filtering

Some kinds of filtered maps were made from the Bouguer anomaly map ($\rho = 2.67$) through several kinds of filters. These filtered maps are shown in Plate II-2-3 ~ Plate II-2-6 and Fig. 2-1 ~ Fig. 2-3. The methods of filtering and their characteristics are as follows.

2-8-1 Regional trend map (first order, second order and third order)

Fig. 2-1 ~ Fig. 2-3 represent the regional tendencies of gravity anomalies of the survey area by fitting a plane (first order) and curved surfaces (second order and third order) by the methods of least square.

The following approximation formulas were obtained after the calculation with the electronic computer.

first order :

$$Z_1(X, Y) = - 372.781 - 1.251 X + 0.468 Y \text{ mgal}$$

second order :

$$Z_2(X, Y) = - 363.384 - 2.638 X + 0.214 Y + 0.060 X^2 - 0.012 XY + 0.010 Y^2 \text{ mgal}$$

third order

$$Z_3(X, Y) = - 317.608 - 8.733 X - 4.963 Y + 0.199 X^2 + 0.363 XY + 0.259 Y^2 + 0.008 X^3 - 0.025 X^2Y + 0.007 XY^2 - 0.006 Y^3 \text{ mgal}$$

The unit of parameters X, Y is minutes of arc and their origin is latitude $14^{\circ} 30'S$, longitude $71^{\circ} 31'W$, and X axis and Y axis are extended toward the east and the south respectively.

2-8-2 Residual gravity map

The distribution of third order residual is shown in Plate II-2-6. This

Is obtained by subtracting the third order trend from the Bouguer anomalies at every station.

Third order residual $\Delta g(X, Y) = \Delta g_0'' - Z_3(X, Y)$. As this third order residual map does not contain the regional trend of the third order, it cannot be used for the analysis of the large scale structure. But the local anomaly which does not always appear in the Bouguer anomaly map can be evident rather clearly in this kind of residual map.

2-8-3 Filtered gravity maps (noise, normal and local structures (bi-structures))

The map of short, intermediate and long wave-length Bouguer anomaly were produced by Seya's method⁶⁾. *

The grid points of 1 km interval were marked on the Bouguer anomaly map and the values of Bouguer anomaly at each grid point were read on the map. $\Delta f(X, Y)$ at a grid point (X, Y) were calculated according to the following formulas.

$$\text{noise: } \Delta f_1(X, Y) = \Delta g(X, Y) - \frac{1}{6} \left\{ \sum_{i=-1}^1 \Delta g(X_i, Y) + \sum_{i=-1}^1 \Delta g(X, Y_i) \right\}$$

$$\text{normal: } \Delta f_2(X, Y) = \frac{1}{6} \left\{ \sum_{i=-1}^1 \Delta g(X_i, Y) + \sum_{i=-1}^1 \Delta g(X, Y_i) \right\} - \frac{1}{14} \left\{ \sum_{i=-3}^3 \Delta g(X_i, Y) + \sum_{i=-3}^3 \Delta g(X, Y_i) \right\}$$

$$\text{local: } \Delta f_3(X, Y) = \frac{1}{14} \left\{ \sum_{i=-3}^3 \Delta g(X_i, Y) + \sum_{i=-3}^3 \Delta g(X, Y_i) \right\} - \frac{1}{30} \left\{ \sum_{i=-7}^7 \Delta g(X_i, Y) + \sum_{i=-7}^7 \Delta g(X, Y_i) \right\}$$

These three groups of anomaly, noise, normal and local structure are separated selectively from the original Bouguer anomaly map according to the respective wave lengths by the above formulas and represent the short, inter-

* See reference

mediate and long wavelength anomalies. These groups of anomalies have such characters as follows in relation to the underground structure.

Noise structure is effective to detect shallow rocks which have different densities from neighbouring and are separated from the basement, to detect the density contrast accompanying with the fault and to determine the boundary of a rock of larger scale. But the attention must be paid to the fact that the noise structure emphasizes small apparent anomalies which originate from errors.

Normal structure is considered to represent normal structures after taking out small and large scaled structures from the original structure. In the area where the basement is rather shallow, the undulation of the basement or small sized intrusive rocks can be represented. In the area where the basement is deep, normal structure represents the larger structure of the basement and the distribution of intrusive rocks rather well.

Local structure represents the deepest structure, or the largest scaled structure and it shows rough tendency of the undulation and density of the basement.

2-9 Profile of underground structure

Profiles of the underground structure were also made by the simulation method of two dimensional profile analysis. These profiles are shown in Plate II-2-7 ~ Plate II-2-9.

2-9-1 Method of calculation and initial density model

The correspondence between the gravity distribution and an underground structure is not unique. The result of simulation calculation depends on the

initial conditions and on the boundary conditions. The initial density model was estimated referring the above mentioned filtered map and the results of the airborne magnetic survey, the electrical survey, the laboratory measurement of the densities of rock samples and the geological survey.

The calculation was carried out in such a way that the initial densities and their coordinates as parameters were changed within a range of boundary conditions to increase the fitness of the model to the observed Bouguer anomaly in the sense of the least square.

2-9-2 Contour map of underground magnetic structure

When the calculation is carried out to construct the gravimetric basement according to the method mentioned above, the regional trend of the survey area has to be taken into consideration. Generally speaking, it is expected that the magnetic mineral rich rocks have higher densities and that the distributions of high density rocks in the gravimetric basement usually coincide with that of high magnetic materials. Taking these tendencies into consideration, the contour map of underground magnetic structure was drawn. In making this map the magnetic anomaly map obtained from the airborne magnetic survey carried out in 1972 was used and the simulation of two dimensional analysis was employed. The result was mapped and is shown in Plate II-4-1.

2-9-3 Construction of density model

Although the Tacaza formation is contained in table 4, this formation appears only at the edge of survey area. If this formation is omitted out of consideration, the mean density of the lake deposits and the upper Puno

formation is about 2.00 and the Puno lower formation and the Mesozoic sediments have densities of 2.50 ~ 2.60. This latter layer clearly forms the gravimetric basement. The intrusive rocks have also the densities of 2.50 ~ 2.70. Considering these facts, the following initial density model was adopted. The density of the first layer (upper) is 2.00 and the density of the second layer (lower) is 2.60 or 2.70. The density 2.70 corresponds to the magnetic basements mentioned in 2-9-2.

2-9-4 Assumption of calculation

The density model was considered to the depth to 4,000 m. The value of the Bouguer anomaly -366 mgal of the point in the south of Yauri where the mesozoic group outcrops, was assumed to correspond to the gravitation of the basement.

The calculation of simulation concerned only to the deviation from -366 mgal and this is equivalent to the assumption that the effect of the basement below 4,000 m reaches to the survey area uniformly.

The depths of the boundary layers obtained at the points B to I along the line II of the electrical survey, which coincide with the gravity profile G-G' were adopted as the initial values of calculation. These initial values were extended to the depth of the sequential gravity profiles successively.

2-10 Underground structure map

This map shows the depth contours of the boundary layer between the first layer of which density is 2.00 and the second layer of which density is 2.60 or 2.70. The boundaries of the densities 2.60 and 2.70 ~ 2.82 which rise near to the ground surface are represented as the position of the intrusives.

The basin structures and the fault-like structure which were recognized by the profile analysis are included in the map. The distribution of magnetic rocks are also indicated in the same map which were determined by the airborne magnetic survey and the analysis of gravimetric analysis.

2-11 Two-layer structure contour map

The two-layer structure analysis is one of the method to estimate the underground structure from gravity distribution. The $\sin x/x$ method⁸⁾ was used in this analysis.

This method is independent of the filtering analysis and the profile analysis described in 2-8 and 2-9. It calculates the depth undulations between two layers from the gravity distributions directly. This method determines the undulation of the upper boundary of the second layer under the given conditions on the density contrast between upper and lower layers and the mean depth of the boundary (nodal plane). This method has high confidence to detect the structures which have sufficiently longer wave lengths than the sampling interval of Bouguer anomaly. (It was the same interval when map was made as described in the section 2-8-3.) It should be noticed that this method is used to detect the positions of the change in structure effectively and their depths cannot be determined absolutely. It shows high accuracy when the actual depth of the boundary of two layers is coincide with the depth of the assumed underground basement.

The calculations were carried out under the assumptions that the density contrast is 0.5 g/cm^3 and the depth of the underground basement is 500 m and 1,000 m. As the result is 0.5 g/cm^3 and the depth of the underground basement is 500 m and

1,000 m. As the result under the assumption of the 1,000 m depth showed the exaggeration of small scale structures and the poor consistency to the result of the profile analysis, the result of analysis under the assumption that the density contrast is 0.5 g/cm^3 and that the depth of the underground basement is 500 m is offered in Plate II-2-11.

2-12 Result of calculations

The results of each calculation are listed in the table of results of calculations of gravity survey appended to this report.

This table is separated into five parts from I to V. All the calculations were made by the computer IBM-370. The table is outputs of the computer. The contents of the table are as follows.

2-12-1 Table of gravity calculation I

This table shows the processes and the results of the calculation from the observed values to gravity values. The earth tide corrections, the drift corrections, the instrument height corrections and the normalization of the observed values at each station to the gravity value at the base were carried out in this table.

The contents of the table are as follows.

The order of the description in the following list corresponds with the order from left to right in the table.

YMD	date of observation (year, month and day)
NO	station number
TIME	observation time (hour and minute)
READING (V_r)	reading value

INST. H (h_i)	Instrument height (m)
x FACT (V_{rk})	observed value x K (mgal)
ECTOR (V_{et})	earth-tide correction (mgal)
INST. COR (V_{hi})	Instrument height correction (mgal)
+ COR (V_c)	corrected value (mgal)
DRIFTCOR (V_d)	drift correction (mgal)
GRVTY DIF (D_g)	difference in gravity between the observed station and the base station (mgal)
GRVTY VAL (g)	gravity value (mgal)

The process of calculation of these data is as follows.

V_{rk} is obtained by multiplying the scale constant K to the reading value V_r . The instrument height correction V_{hi} and the earth-tide correction V_{et} are applied to V_{rk} and it becomes V_c . The drift correction V_d is determined from the time distribution of V_c and then it is added to V_c . The gravity difference D_g is obtained by taking the difference between the two values at the observed station and the base station which are derived from the above mentioned procedure. The gravity value at the observing station is determined by adding this difference D_g to the gravity value at the base station V_g which fixed on the basis of the gravity value of the reference station B_g .

2-12-2 Table gravity calculation II

This table contains the terrain corrections of the far area, the middle distance area, the near area and the close area.

The calculations were carried out for every station independently and the electronic computer was used for these calculation.

The order of the description in the following list corresponds with the order from left to right in the table.

STATION-NO	station number
LATITUDE (φ)	latitude of the station (degree and minute of arc)
LONGITUDE (λ)	longitude of the station (degree and minute of arc)
FAR	terrain correction due to the far area (mgal)
MIDDLE	terrain correction due to the middle distance area (mgal)
NEAR	terrain correction due to the near area (mgal)
CLOSE	terrain correction due to the close area (mgal)
SEA	terrain correction due to the ocean (mgal)
LAKE	terrain correction due to the lake (mgal)
TOTAL	total of respective terrain correction (mgal)

The value 2.67 as rock density was used for the calculation of these corrections.

2-12-3 Table of gravity calculation III

In this table the Bouguer anomalies are calculated from the gravity values at each station by applying the elevation, terrain and latitude corrections. The gravity values corrected only for latitude effect are also listed in the same table which are necessary to draw the G-H relation chart.

The order of the description in the following list corresponds with

the order from left to right in the table.

STATION-NO	station number
LATITUDE (φ)	latitude of the station (degree, minute and second of arc)
LONGITUDE (λ)	longitude of the station (degree, minute and second of arc)
ALTITUDE	station altitude (m)
G. V. - S. V. (g, φ)	gravity value applied latitude correction (mgal)
2.00	} ($\Delta g_0''$) Bouguer anomaly calculated for respective density assumptions
2.20	
2.40	
2.60	
2.80	
2.67	

2-12-4 Table of gravity calculation IV

This table shows the results of the calculations of the regional trends and the residuals of gravity. These calculations were carried out by fitting of the plane, the surface of second order and that of third order to the distribution of gravity. The results are represented for every observation station and the coefficients of respecting surface are also shown in the table.

The order of the description in the following list corresponds with the order from left to right in the table.

STATION-NO	station number
LATITUDE (φ)	latitude of the station (degree, minute and second of arc)
LONGITUDE (λ)	longitude of the station (degree, minute and second of arc)

G. V. - S. V. (g, φ)	gravity value applied latitude correction (mgal)
2.67 ($\Delta g_0''$)	Bouguer anomaly (mgal)
RESIDUAL	residual gravity (mgal)
TREND	smoothed gravity (mgal)

The residual gravity map and the regional trend gravity map were made according to the values of RESIDUAL and TREND respectively.

2-12-5 Table of gravity calculation V

Three kinds of filtered gravity are listed in this table. These gravity values represent the noise, normal and local structures respectively. These calculations were carried out at the grid point in survey area, consequently the results of calculation are also tabulated by the same arrangement.

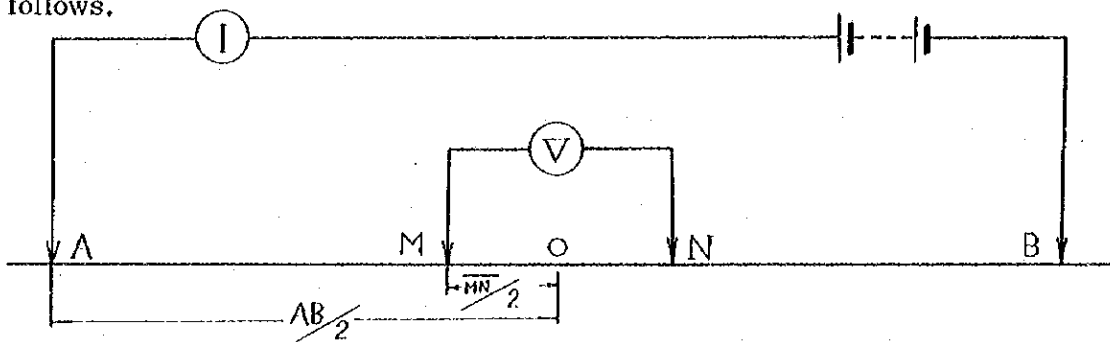
The origin of the grid was located at the point, latitude $14^{\circ}13'S$ longitude $71^{\circ}30' W$, and the X axis and Y axis were extended toward the east and the south respectively. The grid points were distributed by the 1 km interval in this coordinated area.

CHAPTER 3 ELECTRICAL SURVEY BY SCHLUMBERGER METHOD

3-1 Method

This survey was the vertical electrical sounding by Schlumberger's system of electrodes. In Schlumberger electrodes system the positions of potential electrodes M, N are fixed and the measurement is made by changing the distance between current electrodes A, B in principle.

The actual spacings of electrodes in the present prospecting were as follows.



$\overline{AB}/2$ (m)	$\overline{MN}/2$ (m)	$\overline{AB}/2$ (m)	$\overline{MN}/2$ (m)
750	50	100	10
500	50	65	10
325	50	65	5
225	50	40	10
225	10	40	5
150	50	25	5
150	10	15	5

Ten kinds of the separation of current electrodes $\overline{AB}/2$ were employed, the maximum of which was 750 m. The separation of potential electrodes $\overline{MN}/2$ was changed within the range $\overline{MN}/2 \leq \overline{AB}/2$ ($1/3 \sim 1/5$), because a potential difference between fixed electrodes decreases with the increase of a separation of current electrodes. These procedures were carried according to the specifications.

In the cases when $\overline{AB}/2$ was 225 m, 150 m, 65 m and 40 m where $\overline{MN}/2$ was changed, the measurement repeated in different $\overline{MN}/2$. Consequently the total number of measurements at one observation site was 14, 4 of which repeated observations. As the survey area belongs to the dry pampas and has high grounding resistance, the site of every current electrode was arranged to dig a square scoope of 50 cm x 50 cm and to spread salt and water there for the purpose of lowering the grounding resistance. A cupper plate of 50 cm x 50 cm was used for a current electrode. Under such a preperation the current reached to the minimum 0.4 A and the maximum 1.5 A in spite of the dry area. Non-polarizing electrode by supersatulated solution of copper sulphate was used for potential electrode.

The observation condition was excellent owing to no artificial noise. Although the rectangular wave of frequency 0.3 Hz was used for feeding current because the used apparatus in this survey was for the induced polarization method, the result is almost equivalent to that of direct current because of its low frequency.

3-2 System

The apparatus for IP method Model 2004 made by McPHAR Geophysics Limited (Toronto, Canada) was used for this survey.

The specifications of this system are as follows.

a)	high power transmitter	Model 2004
	input capacity	2.5 kw
	output voltage	0 ~ 850 V
	output current	0 ~ 5 A
	transmitting frequency	D. C. , 0.05, 0.1, 0.31, 1.25, 2.5, 5.0, 10.0 Hz
		current stability is kept within the range of 10% of fluctuation of input voltage.
	environmental temperature	- 20 °C ~ 60°C
		for 2.5 KW input
	weight	approx. 24 kg
b)	receiver	Model 29 D
	input impedance	1.9 MΩ
	sensibility	Max. 50 μV full scale
		500 μV ~ 5 mV, 1 mV ~ 10 mV, 10 mV ~ 100 mV, 100 mV ~ 1V, 1V ~ 10V, 10V ~ 100V
	receiving frequency	D.C., 0.3, 1.25, 2.5, 5.0 Hz

filter	filters for D. C. and frequency of commercial line, filters of 12 dB down for the third higher harmonics outside D. C. and of 12 dB down for 0.12 Hz frequency for earth current.
enviromental temperature	- 15°C ~ 50°C for 0.5 dB change of amplification in 75% of its capacity.

c) engine and generator

engine	JLO, L 125, 3,000 R. P. M.
generator	400 Hz, 115, 2.5 KW

Although this measuring system is originally designed for the use of the induced polarization method, it could be used with enough capability for the present survey because its transmitter has a current stabilization circuit of high quality and the receiver has high measuring accuracy.

3-3 Traverse lines and stations

The location of the traverse lines are shown in Plate II-1-1, and details of lines are as follows.

total length of traverse lines	25.5 km
length of one traverse line	8.5 km
number of traverse lines	3
separation of traverse lines	4.0 km
number of middle points	24 (8 per line)
distance of middle points	1.0 km (in the line)

orientation of traverse line

N 75°E

The traverse lines and stations were established by simple transits and tapes. As the positions of middle points are important in vertical electrical sounding, eight middle points were set with 1.0 km separations, moreover the auxiliary points were located with 100 m interval among them. The auxiliary points were also put at the extended position 750 m from the end of the line which correspond the maximum $\overline{AB}/2$. In the measurement the electrode sites were located by taping between the auxiliary points. The traverse lines were numbered as I, II and III from the north toward the south. The middle points were named from No. 8 to No. 1 from the west toward the east for each traverse line.

3-4 Laboratory measurement of resistivity

The measurements of resistivity of the rock samples which were collected in and around the survey area as a aid of the analysis of survey were carried out. Four-electrode method was employed for the measurement. The result is as follows.

Sample No.	Resistivity Ω -m	Rocks	Period Formation
1	1.8×10^2	Medium sandstone	Tertiary upper Puno
2	2.2×10^2	Coarse arkosic sandstone	Tertiary upper Puno
3	2.7×10^2	Coarse arkosic sandstone	Tertiary upper Puno
4	1.3×10^3	Sandstone	Tertiary lower puno
5	1.8×10^3	Sandstone	Tertiary
6	3.8×10^3	Shale	Tertiary
7	4.3×10^4	Limestone	Cretaceous Ferrobamba
8	3.2×10^4	Gabbroic diorite	Cretaceous Intrusive
9	1.2×10^4	Black shale	Jurassic Yura
10	1.4×10^4	Quartzite	Jurassic Yura

According to this result, the rocks of Tertiary the lower Puno formation and that of the Mesozoic group such as the Cretaceous and Jurassic have higher resistivity than that of Tertiary the upper Puno formation without exception and the differences in resistivity are clear and reach almost $10 \sim 10^2 \Omega$ -m. Consequently the boundary between the upper Puno formation and the lower Puno formation or the Mesozoic group forms the resistivity discontinuity surface and this surface can be detected by the electrical survey.

Attention should be paid to the following that the results on the rock samples in the laboratory measurement should be used for mutual com-

parison and cannot be compared directly with the result of field survey.

The difference in resistivity is highly dependent on the conditions on such as circumstances, volume and measurements and the equalizations of these conditions are difficult in the present state of arts.

3-5 Analysis

The result of the vertical electrical sounding is represented by the potential difference V between potential electrodes M, N and the current I fed to the ground through current electrodes A, B .

The apparent resistivity of the ground corresponding the respective current electrodes spacing $AB/2$ is obtained from the measuring results by using the following relation.

$$\rho_a = \frac{\pi}{4} \cdot \frac{\overline{AB}^2 - \overline{MN}^2}{\overline{MN}} \cdot \frac{V}{I}$$

$$\rho_a : \Omega - m$$

$$\overline{AB}, \overline{MN} : m$$

$$V : mV$$

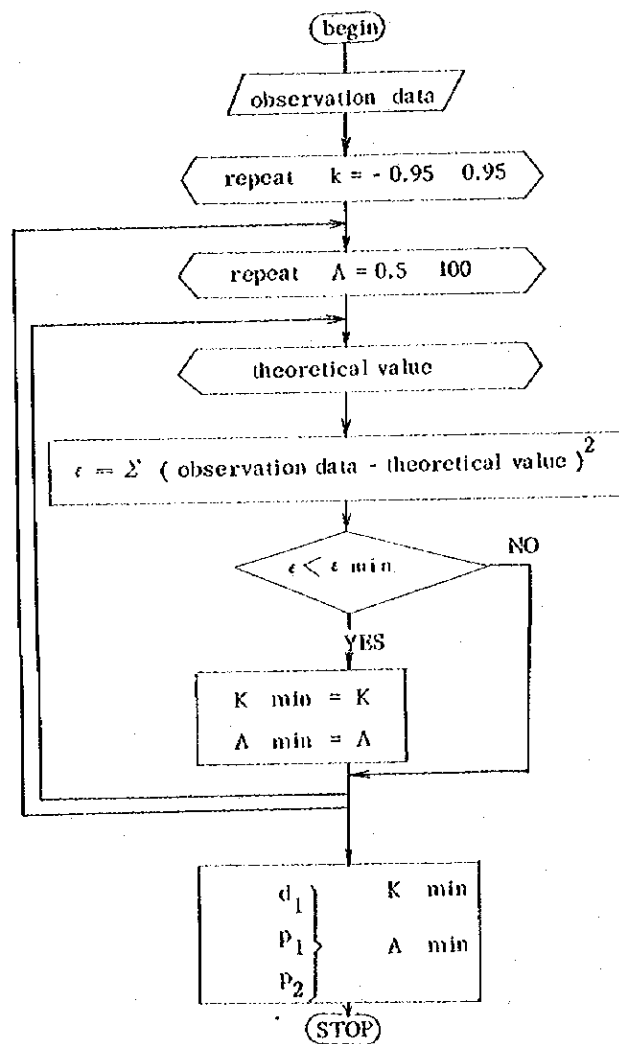
$$I : mA$$

Plates numbered from II-3-1 to II-3-6 show VES curves. These curves were drawn by taking ρ_a as ordinate and $\overline{AB}/2$ as abscissa on logarithmic charts. The vertical distribution of resistivity at middle point and the depth of resistivity discontinuity surface can be determined by analysing the VES curve.

The analysis of the VES curve is made by the matching of the obtained VES curve with the standard curve. Schlumberger's two-layer standard curve for two-layer structure and Ono's auxiliary curve⁵⁾ for three-layer structure were adopted as standard curves.

The initial analysis was carried out by the electronic computer and its output was compared with the obtained VES curve. For the part where the matching is poor, the analysis was repeated.

The flow chart of the computer analysis is illustrated as follows.



The input data was divided into several groups and the calculation was repeated to determine the depth and the resistivity of respective multi-layer models.

The theoretical apparent resistivity of two-layer structure in Schlumberger's system is given by the following equation.

$$\rho_a = \rho_1 \left[1 + 2 \sum_{n=1}^{\infty} \frac{Kn}{\left\{ 1 + 4n^2 \left(\frac{2d}{AB} \right)^2 \right\}^{\frac{3}{2}}} \right]$$

$$K = \frac{\rho_2 - \rho_1}{\rho_2 + \rho_1},$$

- AB : separation of current electrodes
- ρ_1 : resistivity of the first layer
- ρ_2 : resistivity of the second layer
- d : depth of the first layer

Values of ρ_a/ρ_1 are calculated by an electronic computer in the range of $K = -0.95 \sim 0.95$ and $AB/2d = 0.5 \sim 100$. The part which makes the square sum of the deviation from the observational value minimum is adopted and then ρ_1, ρ_2 and d are determined. This procedure is the same for three-layer structure. ρ_c and d_e are determined and ρ_3 and d_2 are obtained from these results.

The calculation was carried out by the large electronic computer CDC-6, 600 and it became possible to process a great number of data in

a short time reasonably. As compared with the computer aided analysis, the conventional method using the standard and auxiliary curves has such disadvantages that the treaties are complicated and the result is liable to be too subjective. But it cannot be disregarded that the latter disadvantage becomes a merit from another point of view because it means the possibility of human judgement of an analyser to the fitting of the curves.

It should be mentioned that the result of the computer analysis is subject to be too erroneous in the case that the resultant VES curve has some local errors. Consequently the final result was obtained from the computer analysis by applying partially the conventional curve fitting method.

The results of analysis are shown by the resistivity columnar section under the respective VES curves in the Plate from II-3-1 to II-3-6, in which the values of resistivity and the positions of the boundaries corresponding to the difference in the resistivities of the strata were described.

CHAPTER 4 RESULTS

The result of gravity survey is represented by the map of Bouguer anomaly. Various maps of filtered data, two dimensional profile charts and maps of underground structures were further made in the present survey. The result of electrical survey is represented by the profiles of resistivity which is made from the analysis of obtained VES curves. The structure of the resistivity basement is further expressed by the estimated profile of the electrical basement for the electrical survey area.

4-1 Map of Bouguer anomaly

Plate II-2-1 and II-2-2 are the maps of Bouguer anomaly, the correction density of which is $\rho = 2.67$ and 2.00 respectively. The adopted correction density is $\rho = 2.67$ in this survey as explained in the section 2-6. Assumption of density and the investigation is made mainly for Plate II-2-1.

4-1-1 General trend

The distribution of gravity in the map of Bouguer anomaly is rather complicated and a number of plate show diverse anomalies. The Bouguer anomalies (for $\rho = 2.67$) distribute in the range between about -400 mgal and -355 mgal. Considering the extent of the survey area the general trend of gravity is not so steep.

The gravity distribution of this area generally has remarkably strong negative Bouguer anomaly and such a negative anomaly is considered to be caused by the effect of isostasy. As for the isostatic negative Bouguer anomaly, the profile across the North American Continent has the character ⁷⁾ in which

the Bouguer anomaly shows positive correction with the depth of Mohorovičić discontinuity and negative correlation with topography. The negative Bouguer anomalies in the range of - 100 mgal. and - 200 mgal are observed at the highlands of Nevada, Utah and Colorado in North America. According to the gravity survey in Utah state the negative Bouguer anomaly of - 193 mgal was observed and the depth of Mohorovičić discontinuity is estimated to be 47.7 km at this point.

According to the report of the gravity observation from the Atlantic coast to the Pacific coast across the South America continent along the route in 32°S zone, the strong negative Bouguer anomaly of about - 300 mgal (for $\rho = 2.67$) was observed at the highlands of about 4,000 m elevation in the Andes near the border between Chile and Argentine, to the contrary the Bouguer anomaly in the plain of elevation 100 m ~ 200 m in Argentine and Uruguay is nearly zero. The two dimensional model calculation also estimates the depths of Mohorovičić discontinuity at 59 ~ 75 km for the highlands and at 31 ~ 33 km for the plains. It is clearly recognized that the profile of Bouguer anomaly has a positive correlation with the depth of Mohorovičić discontinuity and a negative correlation with the topography in South America like North America. Although such an example is not known in Perú, the estimation that the depth of Mohorovičić discontinuity is 64.9 km or 51.7 km at the Andes plateau of Perú suggests that the strong negative Bouguer anomaly of the survey area derives from the deep Mohorovičić discontinuity. The estimation of the depth of Mohorovičić discontinuity in the results of the present survey is about 50 ~ 55 km as

shown in notes 1) ~ 4). This estimation coincides with the depth mentioned above.

As shown in note 5), the fact that the free air anomaly of the survey area distributes in the range about from + 50 mgal to + 150 mgal expresses clearly the isostatic tendency of the coexistence of the positive free air anomaly and the negative Bouguer anomaly. According to note 1) the free air anomaly is almost 0 in the area where the wave-length of topography is long and the isostasy is well established. Such an area does not exist in the present survey, and the positive free air anomaly in this area corresponds to the deviation from the isostasy as shown in notes 2) and 4).

The gravity distribution in this area has the trend of the orientation of NNW-SSE and such a tendency is clearly recognized in the distribution of the Bouguer anomaly and the general orientation of the anomaly contours.

The Bouguer anomaly is low in the central area and high in the north-east and south-west areas. The increasing trend from north-east toward south-west overlaps this pattern. This trend of the gravity distribution and Bouguer anomaly is clearly expressed in the regional trend maps. Especially the figure 2-1 in which the regional gravity trend is approximated by the surface of the first order, shows this regional tendency by the gravity contours which run along N 20° W line and the interval of which is 0.8 mgal/km.

The largest gravity anomaly in the survey area is the anomaly low L1 situated in the central area and governs the regional trend of this area of the NNW-SSE direction with the lowest anomaly L2 next to L1 which lies in the south-east part of the area. The anomaly low L1 is definitely expressed

by closing contours and has the scale of 34 km major axis and of about 15 km minor axis according to the contour of -390 mgal ($\rho = 2.67$). This anomaly L1 has the minimum Bouguer anomaly in the area at its center. The anomaly L2 is estimated to have the same scale as L1 and the closing pattern. The -390 mgal contour shows the minor axis of the order of about 12 km on L2. But the entire picture is not known because of the boundary of the survey area.

The anomaly low L6 is pointed out as another large anomaly which is recognized in the west area and shows the trend of west to south-west. The detail of this anomaly is not clear because it situates at the west end of the survey area. But it should be pointed out that the protrusion of anomaly low L1 combines L1 with L6 and forms the low anomaly zone of NE-SW trend reaching about 20 km length. This protrusion of NE-SW trend accompanying L1 is clearly expressed in the Bouguer anomaly map Plate II-2-2 ($\rho = 2.00$). As another low anomaly zone, the continuation is recognized which begins at L1 of the central area runs through L5, L9 and reach L10 of the southern area. The extension of this belt exceeds the length of 50 km. It shows the approximate orientation of NNW-SSE to N-S trend with meandering.

As for the anomaly high, the anomaly group which develops with H3 as its center at the south-west area is remarkable and shows a big scale and concentration. H3 has many local high anomalies around it and it clearly forms the isolated high anomaly region as shown by the closing contour of -370 mgal ($\rho = 2.67$).

The anomaly high group in the north-west with H1 and H2 as its center is a little smaller than H3 group. It has the trend of NE-SW and the maximum

value of the Bouguer anomaly at H2. The previously mentioned low anomaly zone of NE-SW trend reaching L6 from L1 separates the high anomaly of H3 system from that of H1 and H2 system.

The big scale anomaly high expressed by H10 and H11 is observed at the north-east part of the area. Though the detail of this anomaly high is not clear because it situates at the end of the survey area, this high anomaly overlaps the topography of the mount Laramani which extends to NNE - SSE direction and is estimated to continue to the anomaly high H12 which is reorganized in the south-east area and to form the big high anomaly zone.

The gradient of Bouguer anomaly is highest at the east part of anomaly high H1 in the north-west area, but it is no more than 8 mgal/km ($\rho = 2.67$).

In the regions between the anomaly low L1 and the anomaly high H3 and of the east part along L1 and L2 and of the west part of L2, the systematic contour lines running in N - S direction are observed. The length of these lines exceed 10 km. The local gradients of anomaly are shown more clearly in Plate II-2-2 ($\rho = 2.00$) than in Plate II-2-1 ($\rho = 2.67$) of the Bouguer anomaly maps.

Many of such large scale anomalies correlate to the topography, the anomalies low L1 and L2 are in the plain and the anomalies high H3, H10 and H11 are in the mountain area. But the plains do not always correspond to anomaly low, nor the mountain always correspond to anomaly high.

Note 1) the case when isostasy effects.

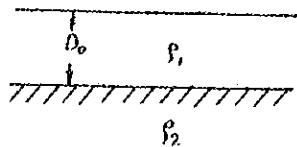


Fig 1

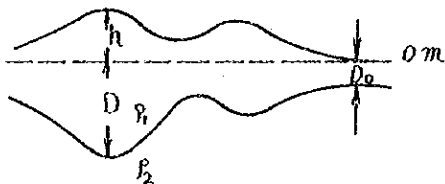


Fig 2

Figure 1 shows a standard model of underground structure at the plain. It is supposed that the elevation of ground surface of the plain is 0 m, the density to the depth D_0 is ρ_1 and the density under the depth D_0 is ρ_2 . It is said that the isostasy is attained for the topography the wave length of which is longer than 140 km. The depth of the underground structure is supposed to be D corresponding to the elevation of the mountain h in the mountain area,

If the isostasy is attained for this case,

$$(h + D - D_0) \rho_1 = (D - D_0) \rho_2$$

from the Archimedes' principle

$$D = D_0 + \frac{\rho_1}{\rho_2 - \rho_1} h \quad \dots\dots\dots (1)$$

Free air anomaly of this station Δg_0 , when the free air anomaly of the plain on Figure 1 is taken zero,

$$\begin{aligned} \Delta g_0 &= 2\pi G \rho_1 (h + D - D_0) - 2\pi G \rho_2 (D - D_0) \\ &= 2\pi G \{ \rho_1 (h + D - D_0) - \rho_2 (D - D_0) \} \dots\dots\dots (2) \end{aligned}$$

then from (1)

$$\Delta g_0 = 0$$

the Bouguer anomaly $\Delta g_0''$ is

$$\Delta g_0'' = \Delta g_0 - 2\pi G \rho_1 h \dots\dots\dots (3)$$

when the isostasy attains

$$\Delta g_0'' = -2\pi G \rho_1 h \dots\dots\dots (4)$$

Note 2) deviation from the isostasy.

The deviation from isostasy is supposed to be δ , that is $D \rightarrow D + \delta$ in

$$\text{equation (2)} \quad \Delta g_0 = -2\pi G \delta (\rho_2 - \rho_1) \dots\dots\dots (5)$$

$$\Delta g_0'' = -2\pi G \{ \rho_1 h + \delta (\rho_2 - \rho_1) \} \dots\dots\dots (6)$$

the change in the Bouguer anomaly equals to

$$-2\pi G \delta (\rho_2 - \rho_1) \dots\dots\dots (7)$$

Note 3) effect of the superficial layer

It is supposed that the thickness and the density of the superficial layer are ϵ and ρ_0 respectively as is shown in Figure 3.

Then the equation (1) becomes

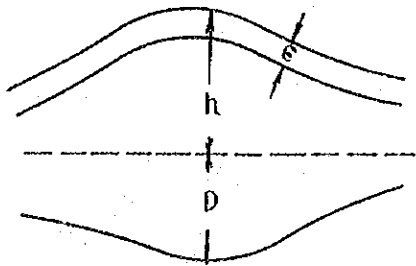


Fig 3

$$D = D_0 + \frac{1}{\rho_1 + \rho_2} \{ \epsilon \rho_0 + (h - \epsilon) \rho_1 \} \dots\dots (8)$$

and if $\Delta g_o = 0$

$$\Delta g_o'' = - 2 \pi G \{ \epsilon \rho_o + \rho_1 (h - \epsilon) \} \dots\dots\dots (9)$$

Note 4) application to the result of the present survey,

$$\rho_o = 2.00, \quad \rho_1 = 2.67, \quad \rho_2 = 3.12, \quad h = 4,000 \text{ m}, \quad \epsilon = 1,000 \text{ m}$$
$$\Delta g_o'' = - 375 \text{ mgal} \quad (\rho = 2.67)$$

- a) ρ_o is an estimation from the laboratory measurement of the rock samples.
- b) ρ_1 is the mean density of the crust
 ρ_2 is the mean density of the mantle by the literature.
- c) h is an approximate mean elevation of the survey area.
- d) ϵ is an estimated depth of ρ_o .
- e) $\Delta g_o''$ is an approximate mean value of the observed Bouguer anomaly of the survey area.

from the equation (4) the isostatic Bouguer anomaly of this area is calculated

$$\Delta g_o'' i \approx - 449 \text{ mgal}$$

and from the equation (1),

$$D \approx D_o + 24 \text{ km}$$

as $D_o > 0$, then $D > 24 \text{ km}$.

Taking the deviation of the observed Bouguer anomaly $\Delta g_o''$ from the isostatic Bouguer anomaly into consideration,

from the equation (7),

$$\delta \approx -4 \text{ km}$$

then $D + \delta > 24 \text{ km} - 4 \text{ km}$

$$D + \delta \approx D_0 + 20 \text{ km} \quad \dots\dots\dots (10)$$

on the other hand, if the effect of the superficial layer is considered, from the equations (8) and (9),

$$\Delta g_0'' \approx -420 \text{ mgal}$$

$$D \approx D_0 + 22 \text{ km}$$

and from the equation (7),

$$\delta \approx -2 \text{ km}$$

then $D + \delta > 22 \text{ km} - 2 \text{ km}$

$$D + \delta \approx D_0 + 20 \text{ km} \quad \dots\dots\dots (11)$$

The coincidence between the equations (10) and (11) indicates the negligible effect of the superficial layer.

It is said that D_0 is usually 30 - 35 km, consequently the depth of the Mohorovičić discontinuity of this area $D + \delta$ is estimated to be 50 - 55 km.

Note 5) Free-air anomaly of representative stations

No.	hm	Δg_0	$\Delta g_0''$	Area	Remarks
3402	4050.90	49.81	-402.95	central	minimum g
3029	4112.60	59.26	-400.37	south-east	minimum g next to 3402
5020	3868.00	77.98	-353.48	west	maximum g
2220	4015.40	88.07	-358.90	south-west	maximum g next to 5020
4549	4686.20	143.96	-397.92	north-east	highest elevation
4512	3844.80	55.41	-373.35	north-west	lowest elevation

- (1) No. station number
- (2) hm elevation of the station (m)
- (3) Δg_0 free-air anomaly (mgal)
 $\Delta g_0 = g + \delta g_0 - \gamma_0$ positive for all the stations
in the survey area
- (4) $\Delta g_0''$ Bouguer anomaly (mgal) $\rho=2.67$
 $\Delta g_0'' = g + \delta g_0 + \delta g_0' + \delta g_0'' - \gamma_0$ negative for all the
stations in the survey area
- (5) area location of the station
- (6) remarks characteristic feature of the station

4-1-2 Local trend

There are many local anomalies in the survey area. The noticeable anomalies are described below.

- (1) A number of anomalies is around the anomaly high H3 in the south-west area, and forms the anomaly aggregating area as a whole. The anomalies high such as H4, H5, H6, H7, H8 and H13 are dominant and only L4 and L9 and others of anomalies low are recognized in this area. Though these local anomalies surround H3, each has a tendency of isolating others and has no other systematic tendency. The complicated pattern is a distinctive feature of this area. The anomalies high H4, H7 and H8 are expressed with steep gradients in Plate II-2-2 ($\rho = 2.00$).
- (2) A pair of anomalies, high H9 and low L3 are recognized between H3 and L2. The trend of these anomalies is both N-S direction. These anomalies are particularly remarkable in Plate II-2-2 ($\rho = 2.00$).

- (3) The contour lines are generally systematic around the central anomaly low L1. The local disturbances are only shown by the protrusion at the east end and by the small anomaly low in the north-west part. The south-east low L2 has little local anomaly.
- (4) The anomaly low L5 in the central area has the high anomaly protrusion in its east side and forms an anomaly pair.
- (5) The anomalies low L1 and L2 have low anomaly protrusions toward south and north which show the continuity of both anomalies. The middle area between L1 and L2 presents both the graben pattern and the low gradient.
- (6) The anomalies high H1 and H2 in the north-west area have little local anomaly. But the boundary of these anomalies shows the steep gravity gradient.
- (7) The anomaly high H14 is observed to the south-east of H2 and the contour lines of the steep anomaly gradient run between them.
- (8) The whole patterns of L7 in the north-east area, L8 in the north-west and L10 in the south are not known because they all locate at the edge of the survey area. But L7 and L8 correspond to the large scale high anomaly of H10 and H1 and the estimation can be made that these anomalies extend outside the area.

4-2 Map of filtered gravity

Maps of filtered gravity express the results of the running average method, they correspond to the gravity map after the passing through band pass filters. Plate II-2-3 is the maps of noise structure. Plate II-2-4 is that of normal structure and Plate II-2-5 is that of local structure (bi-structure).

4-2-1 Map of noise structure

There are eight negative anomalies and twelve positive anomalies over ± 1.0 mgal and the remarkable anomalies exceeding ± 1.5 mgal are distinguished only one place for negative zone and two for positive zone in the map.

(1) All the anomalies are irregular and local and most of them are distributed in the west and south-west area. It should be noted that no negative anomaly exists corresponding to the anomaly low L1 and L2. This means the large size of L1 and L2.

(2) The most remarkable positive anomalies are that correspond to anomaly high H5 and H7. The negative anomalies are recognized in the north part of the area between H5 and L5. The positive anomalies that reach 1 mgal and also corresponding to H1, H8, H9 and H13 are also recognized in the map. These anomalies extracted in the map of noise structure are the expression of the local anomalies contained in the Bouguer anomaly.

(3) Most of other anomalies are caused by the protrusions of H and L expressed by the windings of the contour lines, and they have no systematic tendencies.

(4) The fact that the negative anomalies accompanying L3, L4, L5, L6, L7, L8, L9 and L10 and the positive anomalies accompanying H2, H3, H4, H6, H10, H11, H12 and H14 all do not exceed 0.5 mgal and are in small scales indicates that the size of the local anomaly is not big.

(5) The map of noise structure has no oriented disposition of gravity anomalies but it shows that the positive anomalies prevails over the negative anomalies.

4-2-2 Map of normal structure

There are a number of anomalies over ± 1.0 mgal, and if an anomaly over ± 1.5 mgal is taken as remarkable one, nine negative and thirteen positive anomalies are pointed out.

(1) The most remarkable anomalies are distributed in the north-west to south-west areas like the pattern extracted in the map of noise structure. The east and south-east areas do not have such an anomaly. This means the scales of the anomalies in the areas. The evidences that the negative anomalies corresponding to the Bouguer anomalies are small in size and lie scattered suggest the bigger scales of the negative anomalies L1 and L2, then appearing in the normal structure map.

(2) The anomalies high H1 and H2 also form remarkable positive anomalies in the normal structure map. As for H4, H5, H6 and H8 around H3, each forms an independent positive anomaly. These separate positive anomalies in the normal structure indicates that the high anomaly in the area around H3 contains the smaller scale anomaly components.

(3) H4, H9, H13 and the high protrusion of anomaly high between L5 and H5 are expressed by anomalies high, and L3, L4, L5, L8, L9 and the protrusion of L10 form negative anomalies.

The negative anomalies are seen at the south and north sides of H14.

(4) The positive anomalies are generally dominant a little in the map of normal structure. The remarkably oriented anomaly zone and a line of anomalies are not distinguished.

4-2-3 Map of local structure

If an anomaly over ± 1.5 mgal are picked up as remarkable one, there are four negative anomalies and three positive anomalies in the area.

- (1) The negative anomaly corresponding to the anomaly low L1 has the biggest scale and the one corresponding to L2 succeeds it in scale. These negative anomalies express the big scale of L1 and L2.
- (2) The negative anomalies corresponding to L4 and L5 occupy larger areas than those appearing in the Bouguer anomaly map. This suggests that L4 and L5 have bigger scales than being estimated in the Bouguer anomaly map.
- (3) The larger positive anomaly corresponding to the anomaly high H1 expresses the big scale of H1 distinctly.
- (4) The positive anomaly corresponding to H3 has also a large scale. As mentioned before, the many complex local anomalies exist around H3. This anomaly group is expressed as a large single positive anomaly in the local structure map. This means that the area around H3 forms a large anomaly zone.
- (5) The positive anomaly corresponding to H9 occupies larger area than that appearing in the Bouguer anomaly map. This suggests that H9 has bigger scale than being estimated in the Bouguer anomaly map.
- (6) Bouguer anomalies other than described here are all small and are not detected in the local structure map. The negative anomalies prevail in the local structure map.
- (7) The negative anomaly zones extending from L1 to L2 along the direction NNW-SSE and extending from L1 toward SW direction are clearly distinguished.

On the other hand, the negative line extending from L1 to L10 through L5 and L9 is rather indistinct though it is considered to belong to N-S system.

4-3 Map of regional gravity trend

A map of regional gravity trend expressed the general trend of Bouguer anomaly in the area. The map of the regional gravity trend expressed by first, second and third order polynomials were made in this survey.

4-3-1 Map of regional gravity trend expressed by the polynomial of first order

Fig 2-1 is the map of regional gravity trend expressed by the polynomial of first order. The contour lines running in N20°W direction with the gradient about 0.8 mgal/km are shown in the figure. The Bouguer anomaly increases toward south-west part of the area. This contour lines correspond to the most fundamental trend of gravity distribution and express the largest scale component of distribution.

4-3-2 Map of regional gravity trend expressed by the polynomial of second order

Fig. 2-2 is the map of regional gravity trend expressed by the polynomial of second order. It shows the large low anomaly in the north-east area and the value of Bouguer anomaly and its gradient increases toward south-west part of the area. These features express that the gravity anomaly low prevails in this area. The gravity contours running in the direction of NNW-SSE express well the regional trend of the gravity distribution in the area.

Fig. 2-1. Regional Gravity Trend Calculated by Polynomial of First Order

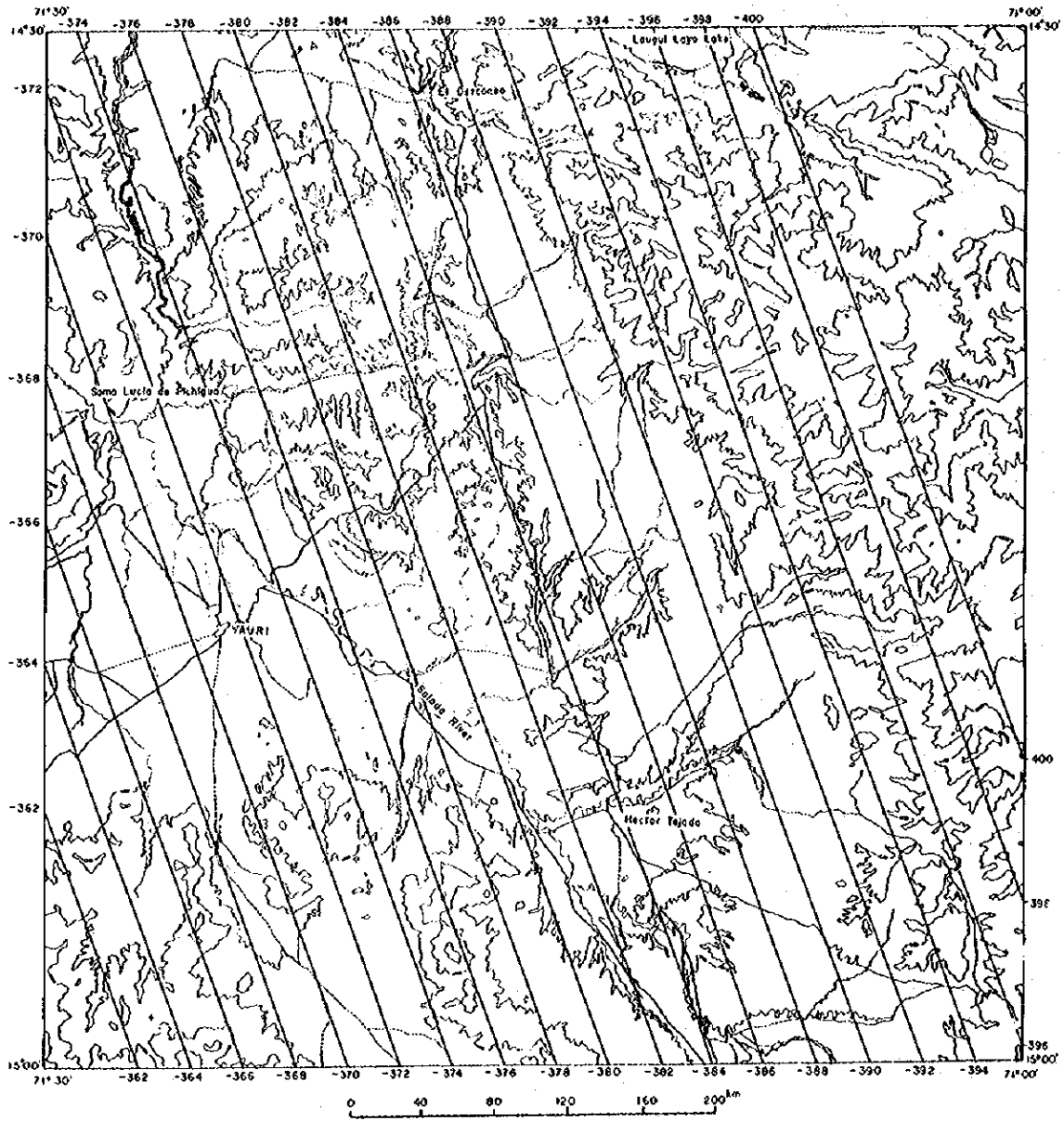
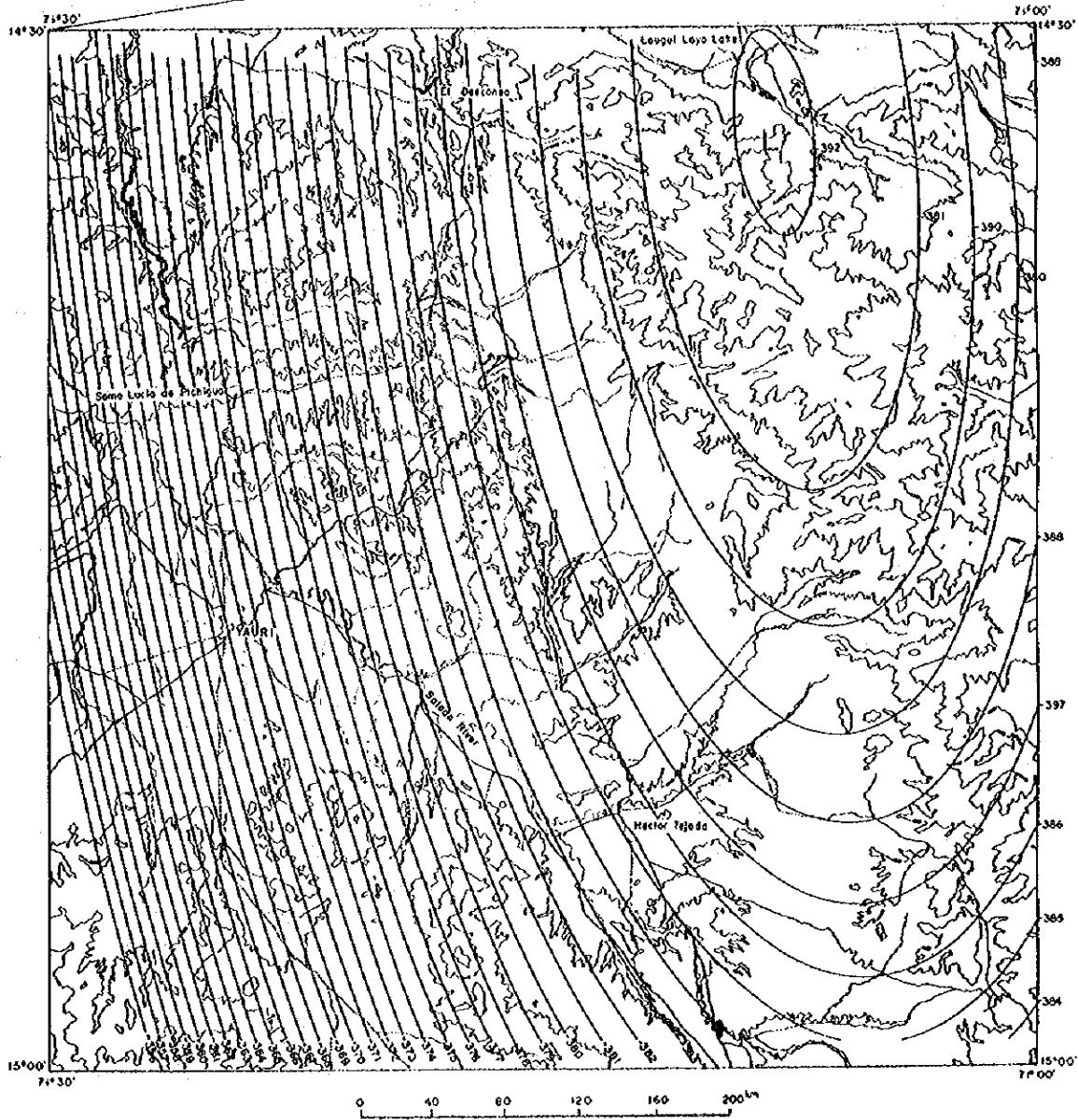


Fig. 2-2. Regional Gravity Trend Calculated by Polynomial of Second Order



4-3-3 Map of regional gravity trend expressed by the polynomial of third order

Fig. 2-3 is the map of regional gravity trend expressed by the polynomial of third order. The gravity anomaly low in the northern part of central area and the anomaly high in the south-west area are shown. Both anomalies have trends of NNW-SSE direction. This map resembles to that of Bouguer anomaly. The anomaly low is dominant, the Bouguer anomaly increases toward south-west direction and the contour lines show the trend of NNW-SSE. These characters are expressions of the general features of the area.

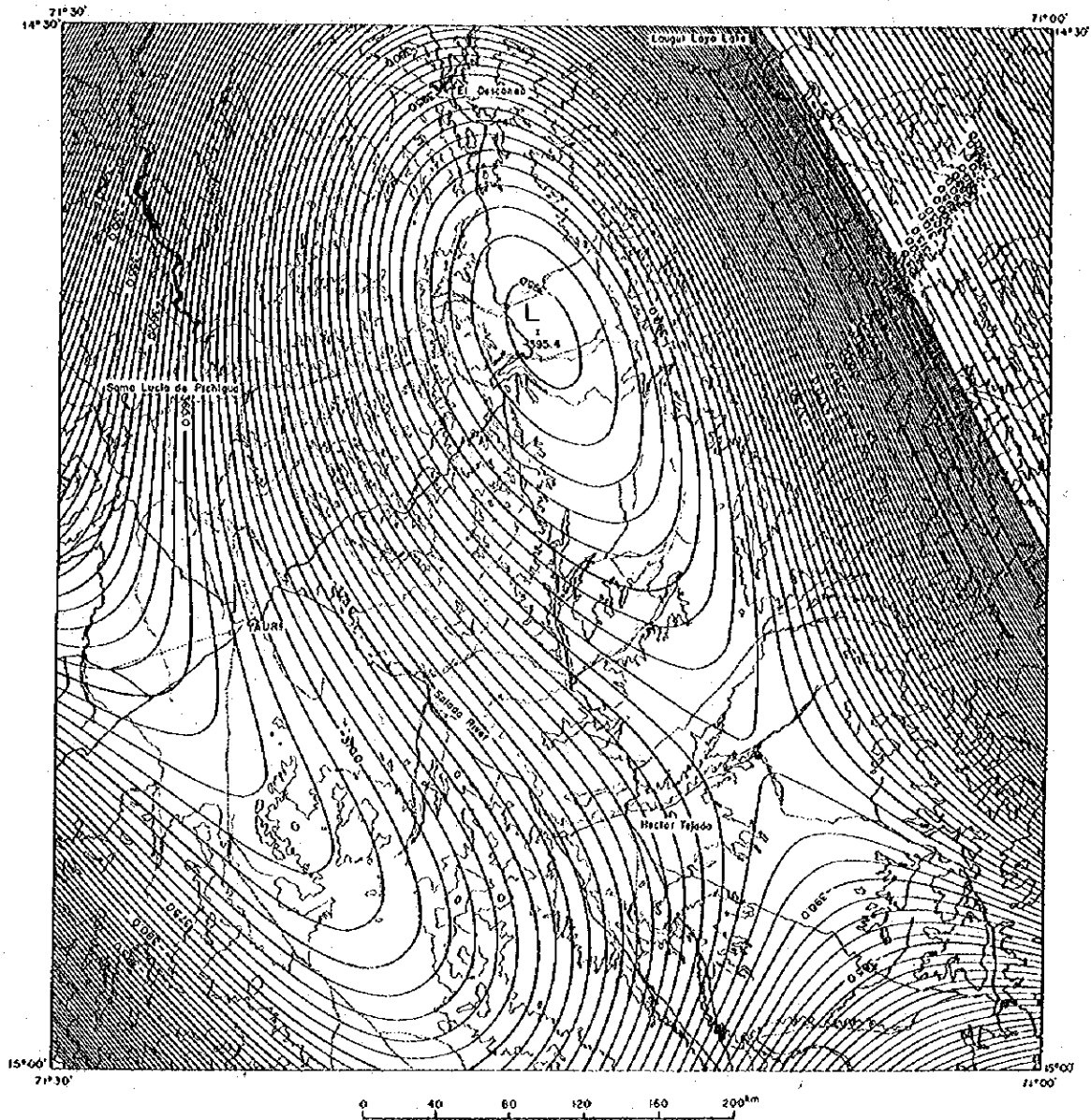
4-4 Map of residual gravity

This map is made by subtracting the regional gravity trend from the Bouguer anomaly and shows the residual gravity after removing the regional anomaly. This map has the tendency of emphasizing local gravity anomalies. The smaller anomaly or noise structure becomes conspicuous with advancing the order of the map.

The first, second and third order residual maps were made and analyzed. The most anomalies in the Bouguer anomaly map form corresponding positive or negative anomalies in the residual maps.

Among these anomalies, positive anomalies corresponding to H3, H4, H7, H8 and H9 and negative anomalies to L2, L5 and L6 can be pointed out as prominent anomaly in the residual map of higher order. Consequently, when these anomalies are analyzed as local anomalies the second or third order residual map is suitable because it expresses these anomalies accurately. On the other hand, the positive anomalies corresponding to anomalies high H1,

Fig. 2-3. Regional Gravity Trend Calculated by Polynomial of Third Order



H2, H5 and H14 and the negative anomalies corresponding to L1 and L5 are expressed as rather small anomalies in the residual map of higher order. This means that these anomalies contains the regional trend of gravity and the care must be paid when estimating the scales of each anomaly in the residual map.

The residual map of third order only is attached to this report.

4-4-1 The residual map of third order

Plate II-2-6 is the residual map of third order. It has poor resemblance to the Bouguer anomaly map and emphasizes the characteristic local anomalies.

(1) The remarkable anomalies corresponding to H1, H3, H4, H5, H7, H9, L1, L2, L5, L6, L7 and L8 are recognized. But their distribution is generally irregular and complex.

(2) The distinct anomaly corresponding to H1 is rather irregular, H2 does not form an isolated anomaly and an anomaly corresponding to H14 disappears.

(3) The anomalies corresponding to H3, H4 and H9 are shown with emphasizing their each original anomaly. These anomalies are expressed in isolated forms. The anomaly corresponding to H9 has the largest scale.

(4) The anomalies corresponding to L1 and L2 are of the same scale. The anomalies corresponding to L5 and L6 are recognized distinctly.

4-5 Profile

The locations of the lines of cross section are indicated by the seven lines marked by A - A' to G - G' in the Bouguer anomaly map and other maps. Each profile chart contains the cross sections of the observed Bouguer anomaly, calculated Bouguer anomaly from the density model, the density model of

underground structure, magnetic total intensity and the filtered Bouguer anomalies such as local, normal, noise structure. An estimated geological underground structure obtained from such profiles is also added.

Although the calculation depth of structure was taken until 4,000 m in the analysis, the profile represents the structure above 2,000 m depth because of the accuracy of analysis of deeper structure and the convenience of mapping.

4-5-1 G - G' profile

This line of section included the traverse line II of the electrical survey. The gravimetric basement was estimated on the electrical basement. Plate II-2-9 shows this section. The marked points from B to I at the central part of the profile correspond to the middle points in Schlumberger method. The depth of the first layer ($\rho = 2.00$) around this area was estimated to be 300 m ~ 350 m which was obtained by the electrical survey.

According to the result of analysis, the first layer whose density is 2.00 has nearly flat structure from the central area to the east. The minimum thickness is about 400 m. It decreases in thickness toward the west and vanishes at the west end of the line. The high density layer whose density is 2.70 from the central area to the west and 2.60 to the east lies below the first layer. This high density layer of $\rho = 2.60$ outcrops at the west end where the first layer is missing.

4-5-2 F - F' profile

This section was analyzed on the basis of the structure of the G - G' profile which intersects F - F' section at its center. According to the analysis the first layer of $\rho = 2.00$ has the maximum thickness at the intersecting point

with B - B' section and decreases its thickness toward the south and north sides and the high density layer of $\rho = 2.60$ lies below it.

High density layer of $\rho = 2.70$ with the layer of $\rho = 2.82$ at its center grows at the north of the line, it inclines gently toward both the south and the north sides. This layer of $\rho = 2.82$ and 2.70 partially outcrops. The layer of $\rho = 2.60$ is recognized at the north end of line.

The high density layer of $\rho = 2.70$ extends over wide area near the intersecting point to C - C' section and the density layer of $\rho = 2.60$ is partially recognized. The most part of layer outcrops because of the lack of the first layer of $\rho = 2.00$. But the coincidence between the calculated Bouguer anomaly and the observed anomaly is rather poor in this area, judging from the observed Bouguer anomaly, it might be necessary to set the low density layer at places of the model. The high density layer of $\rho = 2.60$ outcrops at the southern part of the area and the south end of the line has the first layer of $\rho = 2.00$.

The analysis on the sections A - A', B - B', C - C' and D - D' were carried out on the basis of the structure at the intersecting points of F - F' section to corresponding lines.

4-5-3 A - A' profile

The first layer of $\rho = 2.00$ is distributed at the central part taking the intersecting point with E - E' as its center. The thickness of this layer is estimated to be about 800 m at its maximum and decreases toward both east and west sides. The high density layer of $\rho = 2.60$ grows below it. The high density layer of $\rho = 2.70$ with the higher density layer of $\rho = 2.82$ at its center grows near the intersecting point to F - F' section at the south-west area.

Both high density layers outcrop there. The west side of the layer has a gentle inclination and the dip of the east side is steep.

The high density layer of $\rho = 2.60$ which contains the surface layer of $\rho = 2.20$ in places outcrops at the south-west end and the high density layer of $\rho = 2.65$ and the low density layer of $\rho = 2.00$ are distributed locally.

4-5-4 B - B' profile

The first layer of $\rho = 2.00$ is distributed in almost whole section with gentle undulations. Its thickness has the maximum value of about 1,140 m at most at the south-west of the intersecting point with E - E' section and a tendency to decrease toward both east and west sides.

The lower structure is constructed with the high density layers of $\rho = 2.60 \sim 2.70$. The layer of $\rho = 2.60$ outcrops a little at the north-east end and it contains the layer of $\rho = 2.54$ locally. On the other hand the high density layer of $\rho = 2.70$ is distributed in the south-west area and the boundary between these two layer dips toward the north-east.

Although a small fault-like structure is shown at the central part, the coincidence between the calculated and the observed Bouguer anomaly is not so good. The map of the underground structure should be drawn after retouching the profile.

4-5-5 C - C' profile

The first layer of $\rho = 2.00$ which is distributed along the line from the central to the north-east area is flat and its maximum thickness is only about 300 m. The very thin first layer is distributed in the south-west area. The high density layer of $\rho = 2.60$ grows along the whole section and the high density

layer of $\rho = 2.70$ is detected at three localities. The middle part of which outcrops locally and it contacts to the layer of $\rho = 2.60$ on both sides with gentle slopes. The south-west layer of $\rho = 2.70$ has similar structure but the slope is steeper a little and its outcrop extends over a wide range. The north-east layer of $\rho = 2.70$ does not outcrop and has steep slopes on both sides. The high density area of $\rho = 2.60$ is exposed at the center and the north-east end of the area and the south-west end of the area has an outcrop of the high density layer of $\rho = 2.50$.

4-5-6 D - D' profile

The first layer of $\rho = 2.00$ is distributed along the line from the center to the north-east area and it appears at the south-west end in a small scale. The thickness of the first layer was calculated to be about 770 m at most in the central part. It decreases toward both sides from the intersecting point with E - E' section. The lower layer is constructed by the high density layer of $\rho = 2.60$ and this layer outcrops at the place where the first layer is missing.

The high density layer of $\rho = 2.70$ grows in the layer of $\rho = 2.60$ in contact with the bottom of the first layer at the place where the first layer is very thin, the peculiar structure is shown in this area. Because there is a place where the coincidence is poor between the calculated and the observed Bouguer anomaly in the south-west area of the section, it is necessary to put some local low density layer in the area.

4-5-7 E - E' profile

This section is represented by two layer structure of the first layer of $\rho = 2.00$ and the high density layer of $\rho = 2.60$ and the high density layer is

completely covered by the first layer.

The thickness of the first layer is thinnest at the places near the C - C' and G - G' sections and increases at the south and the north area. But its general undulations are gentle. The thickness of the layer was calculated to be about 860 m at the north area at most and 900 m at the south. It has local upheaval structure at the intersecting point with B - B' section and the middle part of the intersecting points with C - C' and G - G' sections.

4-6 Resistivity profile

Table - 5 was drawn up on the basis of the resistivity columnar sections obtained from the analyses of the VES curves for each middle point. It shows the resistivity of each layer, the depth of the boundary and the correlation of layers along the traverse line. Plate II-3-7 is the resistivity profile along the traverse line showing these results. It represents the result of the electrical survey. The definite boundary is expressed by solid line and the estimated boundary is expressed by dashed line in the Plate.

The vertical dashed line expresses the very clear discontinuity and does not mean the underground structure. The topography of the ground surface is almost flat and can be expressed as horizontal with in an accuracy of mapping. The resistivity layers are classified as the first, second and the third layer and the resistivities of respective layers are named ρ_1 , ρ_2 and ρ_3 in order from the surface to the basement.

The distribution of the resistivity in the profile is rather clear generally and forms three-layer structure as a whole. The resistivity of the lowest layer is the highest, the first layer corresponding to the surface layer succeeds

Table 5 Correspondence of resistivity layer along traverse line

clear continuity
 vague continuity
 discontinuity

	B	C	D	E	F	G	H	I	
I	the first layer	89 165	181 (6) 78 (103)	25	13	28 (12) 12 (88)	17 (15)	21 (30) 189 (83)	
	the second layer	19 (249)	35 (452)	47 (?)	20 (270)	50 (256)	58 (?)	35 (473) 64 (9)	18 (330)
	the third layer	741	140	144	180	144	702		
II	the first layer	56 (86)	40 (30)	28 (30)	26 (21)	17 (19) 96 (26)	90 (12)	91 (15)	338 (4)
	the second layer	16 (260)	13 (343)	7 (171)	11 (241)	14 (328)	13 (309)	13 (296)	18 (203)
	the third layer	113	524	273	429	285	499	505	84
III	the first layer	37 (30)	43 (30)	6 (11)	48 (30)	50 (13)	29 (30)	3 (24)	35 (30)
	the second layer	62 (497)	32 (306)	35 (194) 65 (7)	23 (424)	19 (72) 5 (160)	6 (200)	6 (225)	12 (302)
	the third layer	765	224	218	909	241	112	451	

Unit: Ω -m () represents the depth beneath ground surface

It and the second layer, the middle layer, has the minimum resistivity. The followings are the characteristics features of this area. The second layer forms a stable low resistivity layer. The boundary between the second and the third layer is clear, though there are some exceptions. The third layer forms a stable high resistivity layer. On the other hand the first layer usually has higher resistivity than the second layer and its thickness is very varied. It is obscure at some places.

As for the comparison between traverse lines, the resistivity of the line II has the highest continuity and stability among them and the north line I succeeds it but the south line III is full of variety in resistivity. The third layer has a tendency to increase its depth from the line III to the line I that is from the south to the north. Each line is described below.

4-6-1 Traverse line I

This line has a typical three-layer structure at the westernmost middle point B and the easternmost middle point I, and the third layer is expressed as a distinct high resistivity layer. Although the surface layer at the middle point I is separated into the 21 Ω -m layer and the 189 Ω -m layer, it is considered that both layers compose the first layer and the relation of $\rho_2 < \rho_1 < \rho_3$ is clear. It is quite same for the point B. Although the third layer does not forms a distinct high resistivity layer at C, E and F, the well-defined rises up of the VES curve which mean the existence of a high resistivity layer are observed at the right end of the curve corresponding a deeper layer for respecting points. But the separation of electrodes was too small comparing with the depth of the third layer, the absolute value of the resistivity of the third

layer is not known. Consequently the absolute values of resistivity at these points have low accuracies, but the depth of the third layer corresponding to the boundary between the second and the third layer is definite. The relation of $\rho_2 < \rho_1 < \rho_3$ is obvious at point C. ρ_1 and ρ_2 are approximately equivalent and the relation $\rho_2 < \rho_1 < \rho_3$ are observed at point E. ρ_1 is minimum at station F and this station has the relation of $\rho_1 < \rho_2 < \rho_3$.

The third layer is not detected at other middle points D, G and H at all because of the short separation of electrodes comparing with the depth of the third layer. Although the surface layer at point D is separated into 181 Ω -m and 78 Ω -m and that of point G into 28 Ω -m and 12 Ω -m, it should be considered that both layers compose the first layer altogether. The relations $\rho_1 > \rho_2$ at point D and $\rho_1 < \rho_2$ at G are observed. The second layer at point H is separated into 35 Ω -m and 64 Ω -m and has a slightly obscure relations to neighbouring point G and I.

The first layer shows the relation of $\rho_1 > \rho_2$ at B, C and D, and it has a discontinuity between D and E, and it shows the approximate relation of $\rho_1 < \rho_2$ at E, F, G and H. On the other hand the second layer shows the continuous low resistivity over the entire length with exceptions of a little vague continuation on both sides of H especially toward G.

As for the third layer, though its depth was not detected at D, G and H, it is expressed as a high resistivity layer with the relation of $\rho_2 < \rho_3$ at other points. The third layer has its maximum depth of 452 m below the ground surface at point C and the minimum of 249 m at B and mean depth of 300 m ~ 350 m.

4-6-2 Traverse line II

This line has a typical third-layer structure with a distinct relation of $\rho_2 < \rho_1 < \rho_3$ at all points. The third layer at from C to H other than the westernmost B and the easternmost I is expressed as a distinct high resistivity layer. Although the third layer does not form a distinct high resistivity layer at points B and I, it was due to the short separation of electrodes comparing with the depth of the third layer judging from the clear rise up at the right end of VES curve corresponding to a deeper layer. Consequently the absolute value of resistivity of the third layer at these points has a low accuracy but its depth is clearly detected.

The first layer is separated into two parts of 17 Ω -m layer and 96 Ω -m layer at point F. The low resistivity is to the west of this boundary and the high resistivity is to the east of the boundary. The resistivity of the first layer is remarkably high at point I. The first layer forms a distinct higher resistivity layer with contrast to the second layer and it has good continuity. The second layer has better continuity and its resistivity is distributed in the range between 7 Ω -m and 18 Ω -m and forms a stable distinct low resistivity layer. The third layer also forms a continuous distinct high resistivity layer and it was detected in its depth at all the middle points. This layer shows its maximum depth of 343 m below ground surface at point C and the shallowest depth of 171 m at point D and the mean depth is about 300 m.

4-6-3 Traverse line III

The clear three-layer structure was detected at points B, C, E, G, H and I, and the third layer is expressed as a high resistivity layer at these points.

On the other hand, though point D has three-layer structure, the third layer which would show high resistivity was not detected and though the third layer with high resistivity was detected at point F, it has fourlayer structure.

The third layer forms a distinct high resistivity layer at B, E and I, but it does not show high resistivity at points C, F, G and H. It was due to the short separation of electrodes comparing with the depth of the third layer and the well defined rise up which means the existence of a high resistivity layer is shown at the right end of the VES curve at each point. Consequently the depth of the third layer was clearly detected, but the accuracy of the absolute value of the resistivity is rather low.

The second layer is separated into two parts of $35\Omega\text{-m}$ and $65\Omega\text{-m}$ at point D and of $19\Omega\text{-m}$ and $5\Omega\text{-m}$ at point F. The west part of point F has higher resistivity and the east part of point F has lower resistivity, but generally it forms a stable low resistivity layer. The amplitude of variation of resistivity in the first layer is rather large, in comparison with the second layer, it has a relation of $\rho_1 > \rho_2$ at points E, F, G and I, and $\rho_1 < \rho_2$ at points B, D and H and $\rho_1 > \rho_2$ at point C. The depth of the third layer was not detected at point D, but the third layer has the relation of $\rho_2 < \rho_3$ at the other stations. The maximum depth of the third layer is 497 m below the ground surface at point B and the minimum depth is 160 m at point F. The mean depth is about 300 m. The third layer has large undulations.

4-7 Contour map of underground structure by two-layer model

Plate II-2-11 shows the two-layer structure. Contours express positive or negative undulations from the standard depth of nodal plane of 500 m below the ground surface. That is, the value which is obtained by subtracting 500 m

from a numeral on the contour should be the depth of upper surface of the second layer below the ground surface. But the numeral of the contour is so taken here as to be obtained the depth of the second layer by subtracting 250 m taking the result of electrical survey into consideration. The pattern of depth contours on the map has remarkable resemblances to the results of electrical survey and profile analysis in the west and the south-west area.

The upheaval structures corresponding to the anomalies high H1 and H3 were calculated to have elevations of about + 250 m to + 500 m. This means that the high density layer almost outcrops taking the topography into consideration.

The upheaval structures corresponding to the anomalies high around H3 and H9 are clearly recognized. On the other hand the coincidence to the anomaly map is not so good in the east and north-east area, though the structures corresponding to the anomalies low L1 and L2 are easily recognized, the maximum depths of L1 and L2 were calculated to be about -1,700 m and -1,600 m respectively. These results are deeper a little than that of the profile analysis. This discrepancy is due to the inadequate assumptions on the depth of the nodal plane and the density contrast. It might be necessary to divide the area into several sections and the different assumptions would be necessary to each section to obtain better result. But there are local subsidences in the circumference of L1 and the central part of L2 shows a flat structure. These features are considered to express the underground structure roughly. The flatness of the result along the traverse line of electrical survey matches well to that of electrical survey.

4-8 Map of underground structure

Plate II-2-10 is the map of underground structure drawn collectively according to the above results of research.

Gravity anomaly low of L1 and L2 represent a large basin structure and its depth is calculated to be about 1,140 m at the center of L1 and 900 m at the center of L2. There is a large fault-like structure running in the direction of NNW - SSE along the east side of the basin structure. This forms the NNW - SSE system tectonic line together with the syncline structure along the axis of the basin structure. Gravity anomaly low L5 also shows the local semi basin structure which opens toward the north. Large fault-like structure also exists along the west side of basin structures. Along the west side of L1 are the N - S and NE-SW system fault-like structures and along the west side of L2 is the N - S system fault-like structure. There are the E - W and NW - SE system basin structures on the south side of the L5. These basin structure as a whole are distributed in the direction of NNW - SSE and form the circumference of the basin structure.

High density intrusive rocks are distributed at shallow depth in wide area in the west of the fault-like structure along the west side of L1. These intrusive bodies corresponds well with clear gravity anomalies high. Some of these bodies also correspond to the high magnetic intrusive rocks estimated from airborne magnetic survey consequently the correspondences between high density bodies and high magnetic bodies are very clear.

High density intrusive rocks are also distributed in wide area in the south-west area of the boundary of the fault-like structures as a boundary

which grow along the west side of L2 and the south side of L5. This body is divided into five parts and each body shows good coincidence with high magnetic intrusive rock partly or perfectly and also with gravity anomaly high. Fault-like structures grow around these intrusives and some of them contact with intrusive bodies. Local syncline structure of NNW - SSE system are recognized near the boundary of the intrusive bodies.

To sum up, the sharp contrast of the structure is conspicuous on both sides of the fault-like structure which composes the west side of L1 and L2 and the south side of L5 and it is estimated that the large basin structure is the north-east side of the fault-like structure and the distribution of the high density intrusive bodies is predominant.

4-9 Comparison between airborne magnetic survey and gravity survey

A comparison between the analysis of the airborne magnetic survey carried out in 1972 and the result of this gravity survey is mentioned in this section with newly obtained geological information.

A correction is necessary on the result of the airborne magnetic survey. The result of quantitative analysis on deep magnetic rocks in the Interpretation Map of Deep Magnetic Component which is contained in the volume III of the report of the airborne magnetic survey in 1971 on this area shows one of the several solutions. Such a result is subject to change with adding a new information. The detection of the boundary of the magnetic body running in the east-west direction is very difficult especially in low latitude zone, and special attention should be paid to the analysis of its orientation. Under such a circumstance the contour map of underground magnetic structure was drawn again with

adding fault-like structures. This map is attached as Plate II-4-1. An explanation on the map is made and then its relation to the result of gravity survey and the geology of the area is mentioned.

4-9-1 Contour map of underground magnetic structure

In Plate II-4-1, high magnetic anomalies Hm-1, Hm-2 and low magnetic anomaly Lm-2 are estimated to compose the same body, and the apparent deep situation of Lm-2 is considered to be due to a intrusive rocks of weak magnetization.

The local high magnetic parts in the large intrusive body which is formed by the high magnetic rocks, Hm-3, Hm-4 and Hm-6 may be estimated to be due to magnetic mineral rich bodies. An intrusive rock in the north of Hm-6 has low magnetization. Quartzite is distributed in the south of Hm-6, this body outcrops on the ground surface and it is estimated that an intrusive rock lies below this body and it extends to reach Quechua.

High magnetic bodies Hm-5, Hm-8 and Hm-15 are estimated to be derived from large intrusives around Tintaya and these bodies form a part of the Yauri basin structure.

High magnetic anomalies Hm-9, Hm-13 indicating the existence of high magnetic rocks lie over the fault-like structure to the east of the basin structure indicated by L1 and L2. It is considered that these magnetic rocks outcrop or lie in the shallow depth and their thickness are thin, these anomalies are estimated to express no magnetic basement but effusive rocks in the Tacaza group.

Consequently it is estimated that the magnetic basement lies deep in this area and the low anomaly Lm-5 corresponds to the basement, and it is not in accord with the lower Puno formation and the Mesozoic group which were taken to be gravity basement. That is the magnetic basement and that of gravity are different from each other.

4-9-2 Comparison between the contour map of underground magnetic structure and the map of Bouguer anomaly

The features in the contour map of underground magnetic structure are classified as follows. The shallow high magnetic body group laying in the north of Pichigua, the high magnetic body group extending to the NW - SE direction with Tintaya as center, the high magnetic body group distributed in the NNW - SSE direction and low magnetic anomaly body* in the deeper layer.

Taking a wide view of the anomaly, the shallow high magnetic bodies correspond well to gravity anomalies high, and deep low magnetic anomaly bodies to gravity anomalies low.

If a comparison between the result of magnetic analysis and that of gravity survey after classifying the area by the boundary of anomalies high and low and by the fault-like structure detected by gravity survey, the following characteristics are listed.

*As the indication of deeper part in the contour map of underground magnetic structure means the existence of low magnetic body comparing with surrounding rocks and it gives no information on its actual depth, this deep magnetic basement is called low magnetic anomaly body.

- (1) The shallow high magnetic body and gravity anomaly high have comparatively good correspondence, but some of them do not correspond well especially the correspondence varies in each gravity high anomaly.
- (2) The intrusives of high magnetic bodies are detected near the boundary of fault-like structure estimated by gravity survey (Hm-5, 8, 10, 11, 13, 15).
- (3) No igneous activities are detected in the basin structure in the central survey area, but the undulations of the basement are known by the Bouguer anomaly map.
- (4) Several magnetic anomalies are detected near Pichigua. These anomalies are estimated from gravity survey to derive from an identical large body.
- (5) The existing mines all situate along the circumferences of shallow high magnetic bodies and the gravity anomalies high.

According to the geological map there are large distributions of intrusives near Pichigua, around Tintaya and in the east of Quechua. Each intrusive corresponds to the gravity anomaly high in the Bouguer anomaly map, but some of them do not have corresponding shallow high magnetic rocks in the contour map of underground magnetic structure. It is estimated that these absences of shallow magnetic bodies are due to the variations of deep high magnetic rocks to shallow low magnetic rocks with approach to the ground surface or due to demagnetization by intrusion of comparatively low magnetic monzonite.

CHAPTER 5 UNDERGROUND STRUCTURE ESTIMATED FROM GEOPHYSICAL SURVEY

5-1 Outline

The main structure of the survey area has NNW-SSE trend. There is an arrangement of large basin structures to the direction of NNW-SSE. It governs the general structure of the area. Although the gravity anomalies low L1 and L2 in the anomaly map show independent basin structures, they are considered to have continuity with each other. The axis of both basin structure are of NNW-SSE direction. It is also estimated that these anomalies form a large graben structure of NNW-SSE trend as a whole which becomes shallower to the north of Hector Tejada. These basin structure is surrounded by fault-like structures in the east and west sides. The east side is adjacent to upheaval of the lower Puno formation or the Mesozoic group which is lying in Laramani mountains. The west side is adjacent to the north-west intrusives near Pichigua and the south-west intrusives at Tintaya, Ataraya, Quechua and Coroccohuayco.

Special feature of the fault-like structures adjoining the basin structure is that the east side has low gravity gradient and the west side has high gravity gradient. These results suggest that the lower Puno formation of the Mesozoic group which outcrop in Laramani mountains increase their depths gently toward the west and that these sediments group is contacted by intrusive rocks with intrusion or fault relations in the east side.

The intrusives group in the north-west area near Pichigua and that in the south-west area around Tintaya, Ataraya, Quechua and Coroccohuayco

have no relations and are isolated with each other taking Yauri area as a boundary.

5-2 Underground structure along profile lines

5-2-1 Underground structure estimated from electrical survey

The electrical basement shown in Plate II-3-8, the interpretation of electrical basement, is composed of the Mesozoic sediments or the rocks of Tertiary lower Puno formation with intrusives. As the difference between these two formations in resistivity is not large, the separation of the formations is impracticable. Consequently through the depth of the basement where the lower Puno formation might be missing represents that of the Mesozoic group, the necessary data was not available to determine which is the case. The depth of the basement estimated from the electrical survey is distributed in the range of 300 m ~ 350 m below the ground surface and does not have rugged undulations, but it is estimated that the electrical basement has the tendency to increase its depth gently from the traverse line III to the line I, that is from the south to the north.

5-2-2 Gravity survey G-G' section

The depths of the electrical basement along the traverse line which is included in the G-G' section were obtained at from point B to point I. With comparing these results with that of the gravity survey, they show good coincidence except point D. Consequently the first layer of $\rho = 2.00$ is considered to be formed with the Quaternary sediments, the Tertiary lake deposits and the upper Puno formation which are detected on the ground surface. But the thickness of respective layers can not be known because of their low density contrast.

The second layer of $\rho = 2,60$ which lies to the east of the central area is considered to be composed of the lower Puno formation and the Mesozoic sediments, but it is not possible to determine their thickness because of their small differences in physical properties such as density and resistivity as is the same to the first layer. The formation to the west of the central area of $\rho = 2,70$ is considered to be mainly composed of the intrusives such as diorite and granite. According to the result of airborne magnetic survey the head of this body is high magnetic comparing with surrounding rocks. The origin of this ferromagnetism is estimated to be magnetite formed at the contact place of lower part of the Mesozoic limestone by the intrusion of above mentioned rocks or to be due to the local ferromagnetism of the intrusives themselves. The formation at the west end of the area of $\rho = 2,60$ is considered to be the Mesozoic sediments without the lower Puno formation judging from the geological features, and it is also possible to consider the existence of acidic intrusives, such as granite or monzonite, according to the density and magnetic differences.

5-2-3 Gravity survey F-F' section

The stratum of $\rho = 2,00$ with the depth of about 320 m at the intersecting point to B-B' section is identical to the first layer in the G-G' section, but the existence of the upper Puno formation is unknown. The layer of $\rho = 2,60$ below it is considered to be the Mesozoic sediments. The layer of $\rho = 2,60$ below it is considered to be the Mesozoic sediments. The body of $\rho = 2,70$ in the north area is composed of intrusives and the high density body of $\rho = 2,82$ in the body of $\rho = 2,70$ is particularly considered to be of mafic mineral rich rock

such as gabbro or hornblende diorite. The body of $\rho = 2.60$ at the north end ground surface corresponds to the outcropping effusive rocks in the Tacaza group which is recognized on the ground surface.

The bodies of $\rho = 2.70$ and 2.60 near the intersecting point to C-C' section correspond to the outcropping intrusives and the Mesozoic sediments, as for the body situated to a little in southern area, the composition is estimated to be a lighter intrusives such as granite or monzonite. The body of $\rho = 2.60$ in further southern area is estimated to have a structure that the outcropping Mesozoic sediments continue to the deeper layer. It is covered by the surface layer of $\rho = 2.00$ at the south end of the area.

5-2-4 Gravity survey A-A' section

The layer of $\rho = 2.00$ distributing around the intersecting point to E-E' section is identical to the first layer of G-G' section. The upper Puno formation in the layer outcrops in the north-east area and shows the boundary to the lake deposits. It has gentle inclination but the estimation of the depth of its extension is difficult. (This situation is same for the B-B' and D-D' sections.)

The second layer of $\rho = 2.60$ detected in further north-east area has the lower Puno formation until to the end of the section, this was confirmed by geological survey, and limestone outcrops at the far east end of the section. Geophysical detection of the boundary between the lower Puno formation and the limestone is difficult because of the same reason mentioned before.

The bodies of $\rho = 2.70 \sim 2.80$ in the south-west area are estimated to be intrusives, and the body of $\rho = 2.82$ centering the intersecting point to F-F' section is particularly considered to be of mafic mineral rich rock

such as gabbro or hornblende diorite as mentioned in the section of F-F' section. There are considered to be respectively outcropping the Tacaza group and the Mesozoic sediments below it.

5-2-5 Gravity survey B-B' section

The first layer of $\rho = 2.00$ is identical to that of G-G' section. The fact that the upper Puno formation in the first layer outcrops and has a gentle inclination is recognized like the case of A-A' section. The maximum depth of the first layer is estimated to be about 1,140 m and it corresponds to the depth of the boundary between the upper Puno formation and the second layer of $\rho = 2.60$. The second layer of $\rho = 2.60$ is considered to be the lower Puno formation and the Mesozoic sediments. The concealed body of $\rho = 2.70$ in the south-west area is estimated to be intrusives corresponding to the gravity anomaly high H14 in Plate II-2-1, the map of Bouguer anomaly.

5-2-6 Gravity survey C-C' section

The first layer of $\rho = 2.00$ is identical to that of G-G' section. The second layer of $\rho = 2.60$ extending from the central to the north-east area is considered to be the lower Puno formation and the Mesozoic sediments. The body of $\rho = 2.70$ in the second layer is the high magnetic rock with the structures of continuing from the deeper to shallow place and it suggests the existence of intrusives. An alternation of strata of intrusives and limestones is detected on the ground surface near the intersecting point to F-F' section. These intrusives are estimated to have comparatively low density according to the result of gravity survey and a number of granites or monzonites is considered to be the composition of the intrusives.

Intrusive rocks are not detected on the ground surface in the area from Atalaya mine to the south-west. But the existence of the high magnetic rocks with high density of $\rho = 2.70$ suggests concealed intrusives. On the other hand the stratum of $\rho = 2.50$ in the south-west end of the area corresponds to outcropping the Tacaza group.

5-2-7 Gravity survey D-D' section

The first layer of $\rho = 2.00$ is identical to that of G-G' section. The stratum of $\rho = 2.60$ extending from the central to the north-east area is considered to be the lower Puno formation and the Mesozoic sediments. As intrusive rocks outcrop near Coroccohuayco, the lower density intrusives such as granite or monzonite are considered to be distributed around the area. The high density layer of $\rho = 2.70$ exists in the layer of $\rho = 2.60$ contacting with the first layer at its bottom in the central area. As this pattern is the same structure in G-G' section, the existence of intrusive rocks are estimated.

The intersecting point to F-F' section is near Quechua and the intrusions of monzonite have been detected there. The geophysical separation of these intrusives from the Mesozoic sediments is difficult and the layer of $\rho = 2.60$ represents both bodies collectively.

5-2-8 Gravity survey E-E' section

The first layer of $\rho = 2.00$ is identical to that of G-G' section. The upper Puno formation outcrops in the northern area of the intersecting point to G-G' section. The southern area is covered by the Tertiary lake deposits and the Quaternary sediments. The second layer of $\rho = 2.60$ is estimated to be

composed of the lower Puno formation and the Mesozoic sedimentary rocks.

5-3 Distribution of Intrusives

The north-east part of the survey area has few local gravity anomalies high, and these anomalies are considered not to represent intrusives according to the comparison with the result of airborne magnetic survey.

On the other hand local gravity anomalies high and many magnetic anomalies have been detected in the west part of the central basin structure and this area is considered to have a distribution of a number of intrusives. The distribution of granite near Pichigua and Tintaya, Ataraya, Quechua and Coroccohuayco was confirmed by means of geological survey.

These intrusives distributed in the west part of the basin structure are classified into two groups, one is the intrusives near Pichigua in the north-west part of the other is those near Tintaya, Quechua, Ataraya and Coroccohuayco in the south-west part of the area. The intrusives in the north-west area are one big body in macroscopic view and the intrusives in the south-west area compose an aggregation of intrusives protruding from a bigger body.

It is considered that the separation of the gravity anomalies H1 and H2 corresponding to outcropping intrusives in the north-west is due to the change in physical properties in the same rock body and that the gravity anomaly high H14 to the south-east of H2 is concealed intrusive rock protruded from above mentioned body. The gravity anomaly high H3 in the north-west of Tintaya is the most remarkable among the gravity anomalies high in the south-west area and it clearly forms a local gravity anomaly

high in the south-west area and it clearly forms a local high gravity anomaly zone and corresponds to the outcropping intrusives. On the other hand the gravity anomalies high H4, H5, H6, H7, H8, H9, surrounding H3 have no corresponding intrusive rocks except H4. After filtering process of the gravity data, it has been detected that these anomalies form a high gravity anomaly zone on the whole but at the same time many of them are extracted as isolated anomalies. These feature characterize the gravity anomalies high of the area.

In contrast with the high gravity gradient corresponding to the fault-like structure adjoining the gravity anomalies high in the north-west area, the low gravity gradient and disordering of contour lines in the south-west area suggest the existence of isolated intrusive rocks in the area. The local gravity anomalies low lying scattered among these local anomalies suggest existence of sedimentary rocks or low density intrusives.

The high density rock adjoining to the east of the gravity anomaly high H5 in the west part of G-G' profile and that adjoining to the north-east of the gravity anomaly low L9 in the south-west part of C-C' profile, though these high density bodies are not expressed in the map of Bouguer anomaly, were detected by filtering process and profile analysis. These bodies also overlap the high magnetic rocks detected by airborne magnetic survey. This result is noticeable as a remarkable example of increasing an accuracy of result by using different kinds of methods of geophysical survey with different characters.

5-4 Distribution of sediments

The outcropping sediments in Laramani mountains in the north-east part of survey area is estimated to subside toward the south-west of Yauri basin in the central part of the area with gentle inclination from the result of density measurement mentioned in the section 2-6 and the map of underground basement structure.

The sediments which is estimated to be the gravimetric basement is considered to be the lower Puno formation or the Mesozoic group. Intrusive rock is estimated to be almost nonexistent in the east of the fault-like structure in the west part of the survey area.

It is also estimated that these sinking sediments from the north-east toward the south-west contact unconformably with intrusive rocks near the fault-like structure in the west part of survey area, and the Mesozoic sediments are prevailing among the sediments in the west area.

Reference

- 1) Danbara T. and Tomoda Y.: (1969), Geodesy, Geophysics, Lecture on Earth Science, Vol. 5, Kyoritsu shuppan (Japanese).
- 2) Introcaso A. and Huerta E.: (1972), Perfil Gravimetrico Transcontinental Sudamericano Paralelo 32° S-, Universidad Nacional de Rosario, Argentina.
- 3) Kane M. F.: (1962), Terrain Corrections Using an Electronic Digital Computer, Geophysics, Vol 27, No. 4, p. 455.
- 4) Momose H., Hagiwara Y. and Wani K.: (1961), On Gravity Prospecting in Metallic Ore Deposit Area, Geophysical Prospecting, Vol. 14, No.2 (Japanese).
- 5) Ono Y.: (1959), An Improvement of Method of Analysis of Vertical Electrical Sounding, Monthly Report of Geological Survey of Japan, Vol. 10, No. 8,
- 6) Seya K.: (1963), On the New Method of Analysis in Gravity Prospecting, Geological Survey of Japan, Report No. 201.
- 7) Shimazu Y.: (1971), Physics of the Earth, Shoka-bo. (Japanese)
- 8) Tomoda H. and Aki, K. : (1955), Use of the Function $\sin x/x$ in Gravity Problems Proc. Japan Acad. , 31, 443.

APPENDICES
(GEOLOGY)

LIST OF APPENDICES (GEOLOGY)

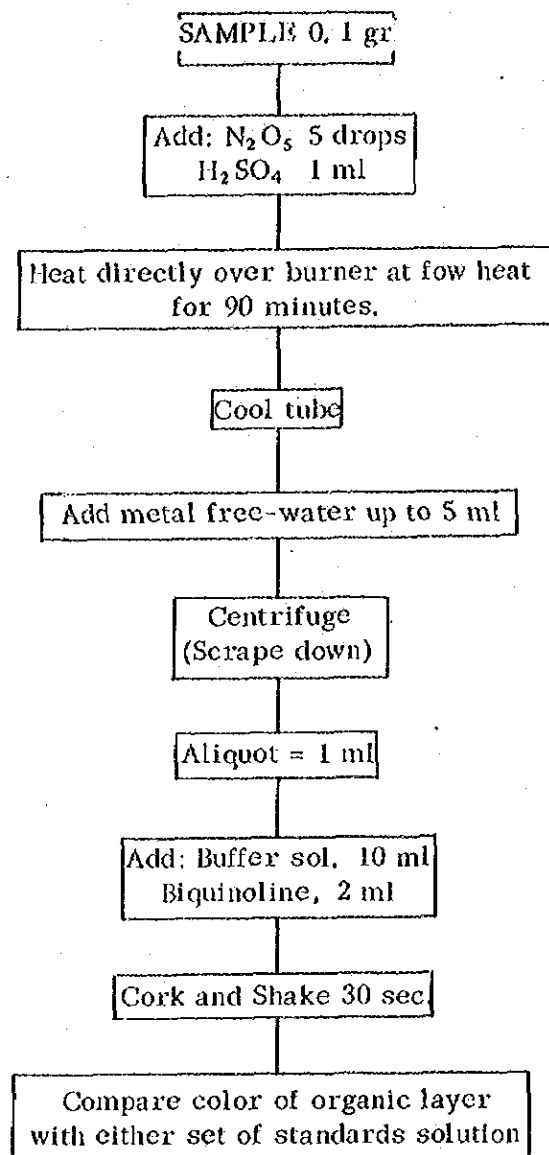
Table I-2	MINERAL SHOWINGS OF THE YAURI AREA
Table I-3	FLOW SHEET OF GEOCHEMICAL ANALYSIS ON COPPER
Table I-4	FLOW SHEET OF GEOCHEMICAL ANALYSIS ON MOLYBDENUM
Table I-5	PROPERTY TEST OF CRUDE OIL FROM ISLAICOCHA
Table I-6	QUALITATIVE ANALYSIS OF THE "MIXED" WATER FROM ISLAICOCHA OIL SERPAGE
Table I-7	LIST OF ROCK SAMPLES
Table I-8	MICROSCOPIC OBSERVATIONS
Table I-9	MICROPHOTOGRAPHS
Table I-10	CHEMICAL ANALYSIS OF ROCKS
Table I-11	ALKALI-LIME INDEX OF VOLCANIC ROCKS FROM THE YAURI AREA
Table I-12	TRIANGULAR DIAGRAM SHOWING THE RATIO NORMATIVE ORTHOCLASE (Or), ALBITE (Ab) AND ANORTHITE (An) OF VOLCANIC ROCKS FROM THE YAURI AREA
Table I-13	<u>AFM</u> DIAGRAM OF VOLCANIC ROCKS FROM THE YAURI AREA
Table I-14	CLASSIFICATION OF INTRUSIVE ROCKS BY NORMATIVE QUARTZ AND FELDSPARS
Table I-15	GEOCHEMICAL ANALYSIS OF STREAM SEDIMENTS
Table I-16	CHEMICAL ANALYSIS OF ORES
Table I-17	CHART OF X-RAY DIFFRACTIVE ANALYSIS
Table I-18	K-Ar AGES OF IGNEOUS ROCKS FROM THE YAURI AREA
Table I-19	FOSSILS
Table I-20	POLLEN ANALYSIS
Table I-21	PHOTOGRAPHS

Table I-2 Mineral Showings of the Yauri Area

NO.	Location	Block	Mineralization	Host rock
1	Condorcocha	Velille I	Fe (contact)	granodiorite, limestone
2	Co. Antrecoña	"	Pb, Zn (vein)	granodiorite
3	Mina Titiminas	"	Pb vein	limestone
4	Rio Chillorolla	"	pyritization	sandstone
5	Huacaña	"	Cu (vein)	andesite
6	Q. Cunduruma	"	Pb (vein)	sandstone, limestone
7	Q. Huaracco	Velille III	hematitization	rhyolite
8	Pampa Callancapampa	"	Fe	tuff
9	Q. Quesillo	Velille IV	Cu stain	andesite
10	Mina Dulzura	"	Cu, Pb, Zn (vein)	andesite
11	Co. Sanacchua	"	Cu stain	andesite
12	Q. Chilasayhua	"	Cu stain	sandstone
13	Q. Cconumayo	"	Cu (vein)	andesite
14	Rio Sanu	"	Cu (vein)	andesite
15	Q. Otoro	"	Cu (vein)	andesite
16	Q. Chapi Chapi	"	Cu stain	andesite
17	Q. Challos	"	Cu stain	andesite
18	Q. Pacamapa	"	Cu stain	andesite
19	Mina Mamanihueta	"	Ag (vein)	rhyolite
20	Q. Marmontoni	"	Cu stain	andesite
21	Co. Pucara	"	Cu stain	andesite
22	Rio Apurimac	Yauri V	Fe	andesite
23	Saltapata	"	pyrite (vein)	andesite
24	Rio Apurimac	"	pyrite (dissem.)	granodiorite
25	Rio Pichigua	"	Cu stain	granodiorite
26	Rio Ccamac Mayo	Yauri VII	Fe (contact)	granodiorite, limestone
27	Co. Ccachatirr	"	Fe (contact)	granodiorite, limestone
28	Minas Tintaya	"	Cu, Fe (contact)	monzonite, limestone
29	Minas Tintaya	"	Cu (contact)	monzonite, limestone
30	Loma Micayo	"	Fe (contact)	granodiorite, limestone
31	Q. Huacchetta	"	Fe (contact)	granodiorite, limestone
32	Q. Huacollo	"	Cu (dissem.)	granodiorite,
33	Q. Quechuaccoto	"	Cu stain	alluvial deposits
34	Q. Coroccohuayco	"	Fe, Cu (contact)	granodiorite, limestone
			Cu (vein)	monzonite, quartzite
			Cu (dissem.)	monzonite
35	Quechua	"	Cu (dissem.)	monzonite, quartzite
36	Co. Yoraccasa	Yauri VIII	Fe (contact)	granodiorite, limestone

Table I-3 Flow Sheet of Geochemical Analysis on Copper

by Maria Lau

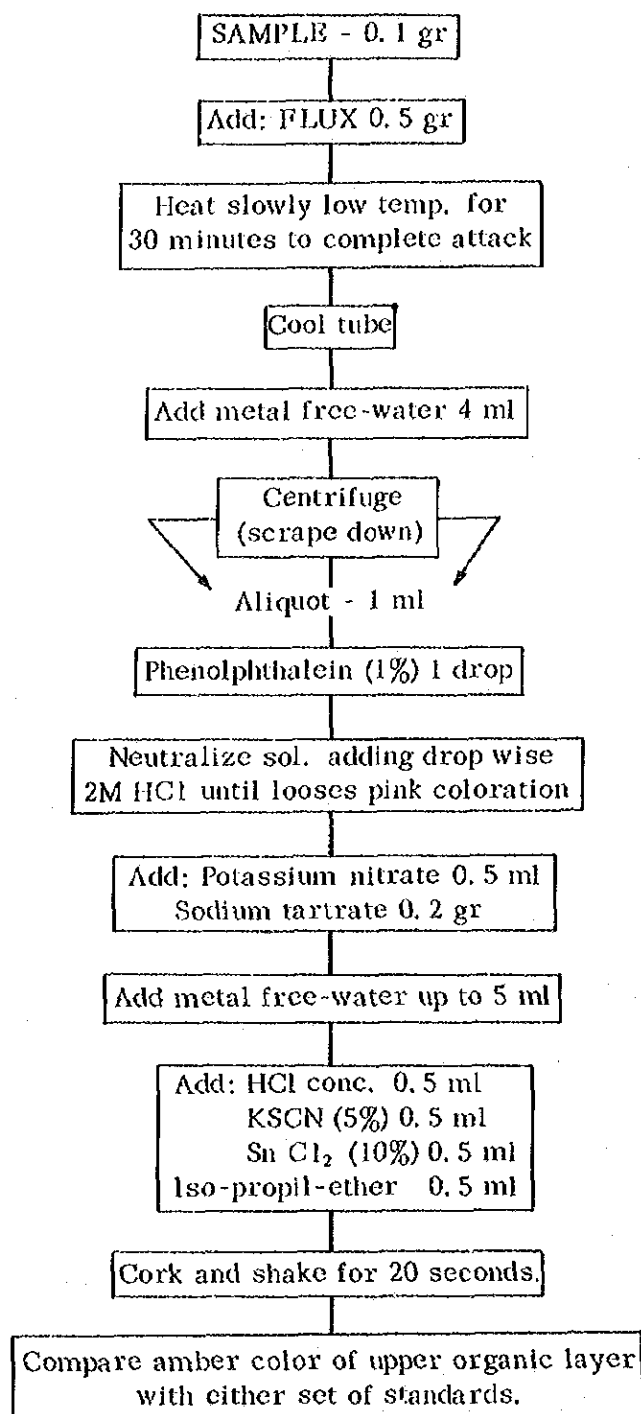


REAGENTS FOR Cu

- Nitric acid, $N_2 O_5$
- Sulphuric acid, $H_2 SO_4$
- Buffer solution: Dissolve
 - 400 gr sodium acetate ($Na C_2 H_3 O_2 \cdot 3H_2 O$)
 - 100 gr sodium tartrate ($Na_2 C_4 H_4 O_6 \cdot 2H_2 O$)
 - 20 gr hydroxylamine hydrochloride ($N H_2 OH \cdot HCl$)in 1 liter of metal free-water, adjust the pH to 6
- Biquinoline solution:
 - Add 0.2 gr 2, 2'-biquinoline to about 900 ml iso-amyl alcohol in a beaker. Warm on a steam bath in a well-ventilated area away from open flame until the biquinoline is dissolved. Allow solution to cool and dilute to 1 liter with iso-amyl alcohol.
 - The solution should be colorless if it is yellow the reagent is impure and should not be used.
- Standard copper solution 100 $\mu g/ml$
 - Dissolve 0.2 gr copper sulphate, $Cu SO_4 \cdot 5H_2 O$; in 500 ml 0.1M HCl.
- Standard copper solution 10 $\mu g/ml$
 - Can be prepared by dilution of appropriate aliquots of standard copper solution 100 $\mu g/ml$ with 0.1M HCl.

Table I-4 Flow Sheet of Geochemical Analysis on Molybdenum

by Maria Lau



REAGENTS FOR Mo

- Sodium tartrate, $\text{Na}_2 \text{C}_4 \text{H}_4 \text{O}_6 \cdot 2 \text{H}_2\text{O}$
- Hydrochloric acid
- Potassium thiocyanate, K S C N
- Stannous chloride, Sn Cl_2
- Iso-propyl-ether
- Flux : Sodium carbonate, $\text{Na}_2 \text{CO}_3$ - 50%
Potassium nitrate, KNO_3 - 50%
- Phenolphthalein 1%, - dissolve 1 gr. in 100 ml water
- Standard molybdenum solution : 100 $\mu\text{g}/\text{ml}$
Dissolve 0.075 gr pure molybdic acid anhydride in 1M NaOH,
dilute with water, add 1M HCl until solution is just acid, then
dilute to 500 ml with water.

$$\text{ppm} = \frac{\text{vol. of sample solution (ml)}}{\text{weight of sample (gr.)}} \times \frac{\mu\text{g of matching standard}}{\text{aliquot (ml)}}$$

Table I-5 Property Test of Crude Oil from Islalcocha

Examined property	Result																											
Density	0.8500 (D15/4°C)																											
Viscosity	11.70 cst (15°C) 9.09 cst (37.8°C)																											
Coefficient of UOP	12.2																											
Pour point	12.5°C																											
Sulphur content	0.14%																											
Wax content	4.75%																											
Residual carbon	0.30%																											
Distillation	<table border="0"> <tr> <td>first distillate</td> <td>200°C</td> <td></td> </tr> <tr> <td>1.5%</td> <td>250°C</td> <td></td> </tr> <tr> <td>16%</td> <td>275°C</td> <td></td> </tr> <tr> <td>35%</td> <td>300°C</td> <td></td> </tr> <tr> <td colspan="3">(as a result of distillation)</td> </tr> <tr> <td>gasoline</td> <td>(-200°C)</td> <td>0%</td> </tr> <tr> <td>kerosene</td> <td>(200-275°C)</td> <td>16%</td> </tr> <tr> <td>light oil</td> <td>(275-300°C)</td> <td>19%</td> </tr> <tr> <td>heavy oil</td> <td>(300°C-)</td> <td>65%</td> </tr> </table>	first distillate	200°C		1.5%	250°C		16%	275°C		35%	300°C		(as a result of distillation)			gasoline	(-200°C)	0%	kerosene	(200-275°C)	16%	light oil	(275-300°C)	19%	heavy oil	(300°C-)	65%
first distillate	200°C																											
1.5%	250°C																											
16%	275°C																											
35%	300°C																											
(as a result of distillation)																												
gasoline	(-200°C)	0%																										
kerosene	(200-275°C)	16%																										
light oil	(275-300°C)	19%																										
heavy oil	(300°C-)	65%																										
Aniline point of light oil	82°C																											
Cetane index of light oil	62.3																											
Chemical composition of heavy oil	<table border="0"> <tr> <td>P - N</td> <td>83.1%</td> </tr> <tr> <td>Ar</td> <td>7.8%</td> </tr> <tr> <td>As</td> <td>1.3%</td> </tr> <tr> <td>Re</td> <td>7.8%</td> </tr> </table>	P - N	83.1%	Ar	7.8%	As	1.3%	Re	7.8%																			
P - N	83.1%																											
Ar	7.8%																											
As	1.3%																											
Re	7.8%																											

Table I-6 Qualitative analysis of the water around the Islaicocha oil seepage

Analysis	Result
pH	2.6 (15°C)
Cl ⁻	16 mg/l
Consumption of alkali	5 moq/l (pH 5.0) 7 moq/l (pH 8.1)
I ⁻	0.2 mg/l
Br ⁻	2.0 mg/l
SO ₄ ²⁻	415 mg/l
Na ⁺	38 mg/l
K ⁺	22 mg/l
NH ₄ ⁺	34 mg/l
Ca ⁺⁺	55.3 mg/l
Mg ⁺⁺	15.9 mg/l
Fe	28.8 mg/l
Mn	0.75 mg/l
Ni	0.05 mg/l
Consumption of KMnO ₄	68 mg/l
Total solid	1,005 mg/l

Composition of gas resolved in water

O ₂	19.86%	N ₂	79.95%
CH ₄	0.18%	C ₂ H ₆	0.01%
C ₃ H ₈	0.00 ₂₂ %	i-C ₄ H ₁₀	0.00 ₀₆ %
n-C ₄ H ₁₀	0.00 ₁₃ %	i-C ₅ H ₁₂	0.00 ₀₀ %
n-C ₅ H ₁₂	0.00 ₀₀ %		

Table I-7 List of Rock Samples

Sample No.	Location	Formation	Rock	Thin section	Polished section	Chemical analysis		X-ray analysis	Dating	Fossil	Pollen	Remarks
						Rock	Ore					
1	1-a	Intrusives	Granodiorite	○								
2	"	Tacaza	Rhyodacitic tuff									
3	1-b	Intrusives	Granodiorite	○								
4	"	"	"	○		○						
5	"	"	Altered granite	○								
6	"	Sencca	Welded tuff breccia	○								
7	"	Intrusives	Granodiorite			○		○				
8	"	"	"									
9	"	"	Quartz diorite	○		○			○			
10	"	"	"									
11	"	Ferrobamba	Magnetite skarn			○						
12	1-c	Murco	Slaty shale	○								
13	"	"	Sandstone									
14	"	Intrusives	Granodiorite	○								
15	"	Murco	Shale	○								
16	"	"	Tuffaceous shale									
17	"	Tacaza	Tuff breccia									
18	"	Intrusives	Granodiorite									
19	1-d	"	Quartz diorite	○								
20	"	Murco	Sandstone	○								
21	"	Tacaza	Trachyte									
22	"	"	"	○								
23	"	"	Rhyolitic tuff breccia	○								
24	"	"	Trachyte	○								

Sample No.	Location	Formation	Rock	Thin section	Polished section	Chemical analysis		X-ray analysis	Dating	Fossil	Pollen	Remarks
						Rock	Ore					
25	1-d	Tacaza	Trachyte	○		○						
26	"	"	Tuff breccia	○								
27	"	"	Trachyte	○								
28	"	"	"	○								
29	"	"	"	○								
30	1-e	"	Trachy andesite	○								
31	1-f	"	Trachyte	○								
32	1-g	"	Altered basalt	○								
33	"	"	"									
34	"	"	Trachyte									
35	"	"	"	○								
36	"	"	Trachybasalt									
37	"	"	"									
38	"	"	Basalt									
39	"	"	Trachybasalt									
40	"	"	Trachyte	○		○			○			
41	2-a	"	Tuff breccia	○								
42	"	"	"	○								
43	"	"	Dacite	○								
44	"	"	Sandstone									
45	"	"	Volcanic breccia									
46	"	"	Tuff breccia									
47	"	"	Volcanic breccia									
48	"	"	Tuff breccia									

Sample No.	Location	Formation	Rock	Thin section	Polished section	Chemical analysis		X-ray analysis	Dating	Fossil	Pollen	Remarks
						Rock	Ore					
49	2-b	Ferrobamba	Limestone	○								
50	"	Tacaza	Tuff breccia									
51	"	"	Porphyritic trachy andesite	○		○						
52	"	"	Sandstone									
53	"	"	"	○								
54	"	Ferrobamba	Veinlets of galena		○							
55	2-c	Intrusives	Quartz diorite	○								
56	"	"	Granodiorite	○								
57	"	Tacaza	Lapilli tuff	○								
58	2-d	"	Basalt	○		○		○				
59	"	"	Trachyandesite	○								
60	"	"	Basalt	○								
61	"	"	Porphyritic trachyte	○		○		○				
62	"	"	Trachy andesite	○		○		○				
63	"	"	Trachybasalt	○								
64	"	"	"	○								
65	"	"	Altered andesitic rock	○								
66	"	"	Trachy andesite	○		○		○				
67	"	"	"	○								
68	"	"	"	○								
69	"	"	Trachyte	○		○						
70	"	"	"	○								
71	"	"	Trachy andesite	○								
72	"	"	"	○		○						

Sample No.	Location	Formation	Rock	Thin section	Polished section	Chemical analysis		X-ray analysis	Dating	Fossil	Pollen	Remarks
						Rock	Ore					
73	2-d	Tacaza	Trachyte	○								
74	"	"	Trachybasalt	○		○		○				
75	"	"	"	○		○						
76	"	"	Olivine basalt	○								
77	"	"	Basalt									
78	"	"	Trachybasalt									
79	2-e	"	Trachyte	○		○			○			
80	"	"	"									
81	"	"	Trachyte									
82	"	"	Trachyandesite									
83	"	"	Trachyte	○		○						
84	2-f	"	Basalt									
85	"	"	Tuff breccia									
86	2-g	Sencca	Lapilli tuff									
87	"	Tacaza	Porphyritic trachyte	○		○			○			
88	"	Sencca	Trachyte (tuff breccia)									
89	"	"	Trachytic tuff breccia									
90	"	Tacaza	Porphyritic trachyte	○								
91	"	"	"									
92	"	"	"									
93	"	"	Basalt									
94	"	"	Trachytic tuff breccia									
95	"	"	Andesite									
96	"	Descanso	Rhyolitic pumice-tuff	○								

Sample No.	Location	Formation	Rock	Thin section	Polished section	Chemical analysis		X-ray analysis	Dating	Fossil	Pollen	Remarks
						Rock	Ore					
97	3-a	Intrusives	Altered microgranite	○								
98	"	Tacaza	Altered dacite									
99	3-b	Sencca	Dacitic tuff breccia									
100	"	Barroso	Basaltic andesite									
101	3-c	Tacaza	Trachyandesite	○								○
102	"	Sencca	Rhyolitic pitchstone	○								
103	"	"	Dacitic lapilli tuff									
104	"	Barroso	Andesite	○								
105	3-d	"	Basaltic andesite									
106	3-e	Tacaza	Andesite									
107	"	"	Basalt	○								
108	"	"	Trachybasalt									
109	"	"	Porphyritic trachyte									
110	"	"	Trachybasalt									
111	3-f	"	Porphyritic trachyte									
112	4-a	Sencca	Tuff breccia									
113	"	Tacaza	Altered basalt	○								
114	4-b	Sencca	Rhyolitic tuff	○								
115	"	"	"	○								
116	"	Tacaza	Altered basalt									
117	4-c	Ferrobamba	Recrystallized limestone									
118	"	"	Sandstone									
119	"	Tacaza	Trachybasalt	○								
120	"	Sencca ?	Trachyte	○								

Sample No.	Location	Formation	Rock	Thin section	Polished section	Chemical analysis		X-ray analysis	Dating	Fossil	Pollen	Remarks
						Rock	Ore					
121	4-c	Tacaza	Basaltic andesite									
122	"	Barroso	"									
123	"	Tacaza	Trachybasalt									
124	4-d	"	Pumice-tuff									
125	"	"	Trachy andesite	○			○					
126	"	Tacaza ?	Rhyolite (welded tuff ?)	○								
127	"	Tacaza	Porphyritic basalt	○								
128	"	"	Altered olivine basalt									
129	"	"	Porphyritic basalt									
130	4-e	Descanso	Tuff breccia									
131	"	Tacaza	Basaltic andesite									
132	"	Descanso	Pumice-tuff									
133	"	"	"									
134	4-f	Tacaza	Basaltic andesite									
135	"	"	Basalt									
136	"	Coporaque	Sandstone									
137	4-g	Sencca	Rhyolite (tuff ?)	○								
138	5-a	Barroso	Basaltic andesite									
139	"	Sencca	Porphyritic trachyte									
140	"	"	Dacite									
141	"	"	Andesitic tuff breccia									
142	"	"	Rhyolite	○			○					
143	5-b	"	Tuff									
144	"	"	"									

Sample No.	Location	Formation	Rock	Thin section	Polished section	Chemical analysis		X-ray analysis	Dating	Fossil	Pollen	Remarks
						Rock	Ore					
145	S-b	Sencca	Welded tuff									
146	"	"	Porphyritic trachyte									
147	"	"	"									
148	"	"	Trachyandesite									
149	"	Barroso	Basaltic andesite									
150	S-c	Sencca	Porphyritic trachyte									
151	"	"	Trachyandesite									
152	"	"	"									
153	"	"	Lapilli tuff									
154	"	Tacaza	Andesitic tuff breccia									
155	"	Barroso	Basalt									
156	"	Sencca	Porphyritic trachyte									
157	S-d	Tacaza	Agglomerate									
158	"	Barroso ?	Tuff breccia									
159	"	Barroso	Andesite									
160	"	Sencca	Altered trachyandesite									
161	"	Tacaza	Porphyritic andesite									
162	"	Sencca	Altered olivine basalt									
163	S-c	Tacaza	Altered basalt									
164	"	Sencca	Rhyolitic tuff									
165	"	"	Olivine basalt									
166	"	"	Liparite									

Sample No.	Location	Formation	Rock	Thin section	Polished section	Chemical analysis		X-ray analysis	Dating	Fossil	Pollen	Remarks
						Rock	Ore					
167	S-e	Tacaza	Trachybasalt									
168	"	Sencca	Rhyolitic tuff	○								
169	S-f	Tacaza	Altered andesite									
170	"	Sencca	Dacitic tuff breccia	○								
171	"	Intrusives	Granite									
172	"	"	Granodiorite	○								
173	"	Coporaque	Sandstone									
174	"	"	"	○								
175	"	"	"									
176	"	"	Mineralized sandstone									
177	S-g	Descanso	Volcanic ash									
178	"	"	Sandy tuff									
179	"	Tacaza	Prophyritized volcanics									
180	"	"	Trachybasalt									
181	"	"	Propyritized volcanics									
182	"	Intrusives	Granodiorite	○								
183	"	"	Calcite-quartz vein in granodiorite									
184	"	Descanso	Dacitic tuff									
185	6-a	Barroso	Basaltic andesite									
186	"	Sencca	Tuff									
187	"	Tacaza	Tuff breccia									
188	"	Sencca	Lapilli tuff									
189	"	"	Porphyritic trachyte									
190	"	"	"									

Sample No.	Location	Formation	Rock	Thin section	Polished section	Chemical analysis		X-ray analysis	Dating	Fossil	Pollen	Remarks
						Rock	Ore					
191	6-a	Barroso	Andesite									
192	6-b	Tacaza	"									
193	"	Barroso	Basaltic andesite									
194	"	Tacaza	Andesite agglomerate									
195	"	"	Trachyandesite									
196	"	"	"									
197	"	"	Basaltic andesite									
198	"	"	"									
199	"	Barroso	"									
200	"	"	Andesite	○								
201	"	Sencca	Basaltic andesite									
202	"	Tacaza	Porphyritic andesite									
203	"	"	Trachy andesite	○								
204	"	Sencca	Tuff breccia									
205	"	"	Tuff									
206	6-c	"	Dacite									
207	"	Tacaza	Trachybasalt									
208	"	"	Andesite									
209	"	"	Basaltic tuff									
210	"	"	Tuffaceous siltstone									
211	"	Sencca	Rhyolite									
212	"	Tacaza	Andesite									
213	"	"	"									
214	6-d	Sencca	Trachyandesite									

Sample No.	Location	Formation	Rock	Thin section	Polished section	Chemical analysis		X-ray analysis	Dating	Fossil	Pollen	Remarks
						Rock	Ore					
215	6-d	Barroso	Andesite	○								
216	"	"	"									
217	"	Tacaza	Altered andesite	○								
218	"	Seneca	Altered rhyolite	○								
219	"	Tacaza	Porphyritic basalt									
220	"	"	Trachybasalt									
221	"	"	Tuff breccia	○								
222	"	Seneca	Rhyolitic welded tuff	○								
223	6-e	Tacaza	Trachybasalt									
224	"	Seneca	Porphyritic liparite									
225	"	"	Jasper vein in propyritized volcanics									
226	"	"	Basalt dyke									
227	"	"	Rhyolite (welded tuff ?)									
228	6-f	Tacaza	Altered basalt									
229	"	Seneca	Lapilli tuff									
230	"	Tacaza	Porphyritic basalt									
231	"	"	Altered basalt									
232	7-a	Barroso	Basaltic andesite									
233	"	Tacaza	Basalt									
234	"	Barroso	"									
235	"	"	"									
236	"	Tacaza	Trachyandesite									
237	"	"	Liparite dyke									
238	"	Barroso	Basaltic andesite									

Sample No.	Location	Formation	Rock	Thin section	Polished section	Chemical analysis		X-ray analysis	Dating Fossil	Pollen	Remarks
						Rock	Ore				
239	7-b	Sencca	Trachyandesite	○							
240	"	"	Dacite	○							
241	7-b	Tacaza	Basalt								
242	"	"	"								
243	"	"	Trachyandesite	○							
244	"	Sencca	Porphyritic trachyte								
245	"	Tacaza	Basalt								
246	"	Sencca	Porphyritic trachyte	○				○			
247	"	"	Dacitic tuff								
248	"	"	"	○							
249	"	"	Tuff	○							
250	7-c	Tacaza	Andesitic tuff								
251	"	"	Tuffaceous sandstone								
252	"	"	Siltstone								
253	"	Sencca	Dacite						○		
254	"	"	Fumice-tuff	○							
255	"	"	Andesite ?								
256	"	"	Dacitic tuff								
257	"	"	Dacite								
258	"	Barroso	Andesite	○							
259	"	"	Altered andesite								
260	"	Sencca	Porphyritic trachyte								
261	"	Tacaza	White tuff								
262	7-d	"	Lapilli tuff								

Sample No.	Location	Formation	Rock	Thin section	Polished section	Chemical analysis		X-ray analysis	Dating	Fossil	Pollen	Remarks
						Rock	Ore					
263	7-d	Tacaza	Basalt									
264	"	Sencca	Pumice-tuff									
265	"	"	Trachyandesite									
266	"	Tacaza	Basalt									
267	"	"	Altered basalt									
268	"	Sencca	Tuff breccia	○								
269	"	Tacaza	Trachybasalt									
270	"	"	"									
271	"	"	Trachyandesite									
272	7-e	Barroso	Olivine basalt	○								
273	"	"	Olivine basalt	○								
274	"	"	Pumice-tuff	○								
275	"	"	Andesite	○								
276	7-f	Tacaza	Basalt	○								
277	7-g	Sencca ?	Rhyolite with Ag-quartz vein									
278	"	Sencca	Tuff	○				○				
279	"	"	Rhyolitic tuff									
280	"	Descanso	Massive tuff	○					○			
281	"	Tacaza	Basalt	○								
282	"	"	"									
283	"	"	Scoriatic basalt	○								
284	"	"	Olivine basalt	○								
285	"	"	Altered basalt	○								
286	"	Barroso	Andesite	○								

Sample No.	Location	Formation	Rock	Thin section	Polished section	Chemical analysis		X-ray analysis	Dating	Fossil	Pollen	Remarks
						Rock	Ore					
287	1-g	Tacaza	Trachy andesite	○		○		○				
288	1-h	"	Altered scoria									
289	"	"	Trachyte			○						
290	"	"	Lapilli tuff									
291	"	"	Trachyte									
292	"	"	Lapilli tuff									
293	"	"	Trachy andesite			○						
294	"	"	Porphyritic trachyte									
295	"	"	"									
296	"	"	Altered basalt	○		○						
297	"	"	Andesitic tuff									
298	"	"	Trachyte									
299	"	"	Porphyritic trachyte									
300	"	"	Andesite									
301	"	"	Porphyritic trachyte									
302	"	"	"	○		○						
303	1-1	Yauri	Lignite									
304	"	"	Calcarene									
305	"	Puno	Calcareous sandstone									
306	"	Descanso	Calcarene			○						
307	"	Puno	Shale									
308	"	"	Obsidian									
309	1-j	"	Sandstone									
310	"	"	Lapilli tuff									

Sample No.	Location	Formation	Rock	Thin section	Polished section	Chemical analysis		X-ray analysis	Dating	Fossil	Pollen	Remarks
						Rock	Ore					
311	1-j	Puno	Sandstone									
312	"	"	Tuffaceous sandstone									
313	"	"	Conglomerate					○				
314	"	"	Sandstone									
315	"	"	"									
316	1-k	"	Sandstone	○								
317	"	"	Tuffaceous sandstone	○								
318	1-m	Ayabacas	Limestone							○		
319	"	"	"							○		
320	"	"	"							○		
321	"	"	"							○		
322	"	"	"							○		
323	"	Intrusives	Granite									
324	"	"	Granite porphyry									
325	1-n	Munani ?	Hornfels									
326	"	Intrusives	Granite porphyry									
327	"	"	"									
328	2-h	Tacaza	Trachy andesite	○								
329	"	"	Scoria									
330	"	"	Altered basalt									
331	"	Sencca	Dacite									
332	"	"	Tuff breccia	○								
333	"	Descanso	Tuffaceous sandstone									
334	"	"	Lapilli tuff									

Sample No.	Location	Formation	Rock	Thin section	Polished section	Chemical analysis		X-ray analysis	Dating	Fossil	Pollen	Remarks
						Rock	Ore					
335	2-i	Tacaza	Sandstone									
336	"	"	Basalt									
337	"	Descanso	Sandy tuff									
338	"	Puno	Sandstone	○								
339	"	Descanso	"							○		
340	2-k	Puno	Conglomerate									
341	2-l	Tacaza	Olivine basalt	○				○				
342	"	"	Trachy andesite	○								
343	2-m	Puno	Conglomerate									
344	3-h	Tacaza	Basalt	○								
345	"	Sencca	Tuff									
346	"	Tacaza	Lapilli tuff									
347	"	"	Trachyte									
348	"	Intrusives	Monzonite									
349	"	"	Diorite	○					○			Pyritization
350	"	"	Granodiorite	○								
351	"	"	Microdiorite		○							
352	"	"	Porphyrite									Pyritization
353	"	"	Microdiorite									Pyritization
354	"	"	Diorite porphyrite	○								
355	"	"	Granodiorite	○								Pyritization
356	"	"	Diorite									
357	"	"	Meta-diorite porphyrite									
358	"	"	"	○								Pyrite vein

Sample No.	Location	Formation	Rock	Thin section	Polished section	Chemical analysis		X-ray analysis	Dating	Fossil	Pollen	Remarks
						Rock	Ore					
359	3-h	Intrusives	Meta porphyrite									
360	"	"	Porphyrite with evaporite									
361	"	"	Diorite with magnetite		○							
362	"	"	Meta diorite porphyrite									
363	3-1	"	Biotite monzonite	○								
364	"	Descanso	Pumice-tuff	○								
365	"	"	Andesitic tuff									
366	"	"	Lapilli tuff									
367	"	"	Sandstone									
368	"	"	Tuff									
369	"	"	White tuff									
370	3-j	"	Sandstone									
371	"	Puno	Tuffaceous and silty sandstone									
372	"	Yauri	Tuff									
373	3-m	Tacaza	Basalt									
374	"	Puno	Tuffaceous sandstone	○								
375	"	Tacaza	Volcanic breccia	○								
376	4-h	Intrusives	Granodiorite	○								
377	"	Sencca	Dacite	○					○			
378	"	Tacaza	Olivine basalt									
379	"	Tacaza ?	Dacitic lapilli tuff									
380	"	Descanso	White tuff									
381	"	"	Conglomerale									
382	4-i	Yauri	Lapilli tuff									

Sample No.	Location	Formation	Rock	Thin section	Polished section	Chemical analysis		X-ray analysis	Dating	Fossil	Pollen	Remarks
						Rock	Ore					
383	4-i	Descanso	Lapilli tuff									
384	"	Yauri	Calcarenite									
385	"	Descanso	Tuffaceous sandstone									
386	4-j	Yauri	Calcarenite							○		
387	"	"	"									
388	"	"	Pumice-tuff									
389	4-k	Descanso	Dactylic tuff	○								
390	4-l	Ayabacas	Limestone	○								
391	"	Tacaza	Andesitic tuff breccia									
392	"	"	Lapilli tuff									
393	4-m	"	Porphyritic andesite									
394	"	"	Trachy andesite	○								
395	5-i	Descanso	Sandy tuff	○							○	
396	5-m	Puno	Liparite									
397	"	Ayabacas	Limestone							○		
398	"	"	"							○		
399	"	"	"							○		
400	"	Tacaza	Andesite	○								
401	"	Puno	Conglomerate	○								
402	"	Ayabacas	Dolomitic limestone	○								
403	"	Puno	Sandstone									
404	5-n	Tacaza	Altered andesite									
405	"	"	Andesite breccia									
406	"	Ayabacas	Dolomitic limestone	○								

Sample No.	Location	Formation	Rock	Thin section	Polished section	Chemical analysis		X-ray analysis	Dating	Fossil	Polled	Remarks
						Rock	Ore					
407	6-h	Ferrobamba	Limestone									
408	"	Tacaza	Tuff breccia									
409	"	"	Pumice tuff									
410	"	"	Olivine basalt									
411	"	Yura	Quartzite									
412	"	"	"									
413	"	Ferrobamba	Altered limestone									
414	6-i	"	Limestone				○					
415	"	"	"				○					
416	"	Intrusives	Granodiorite	○								
417	"	"	Gabbroic diorite									
418	"	"	Quartz monzonite porphyry	○								
419	"	"	Granodiorite									
420	"	"	"	○								
421	6-j	Ferrobamba	Magnetite skarn									
422	"	Intrusives	Quartz monzonite porphyry	○								
423	"	"	Monzonite porphyry	○								
424	"	"	Quartz monzonite									
425	"	Ferrobamba	Garnet skarn	○								
426	"	Intrusives	Granodiorite	○								
427	"	Yura	Quartzite									
428	"	"	Black shall									
429	"	Intrusives	Porphyritic diorite									
430	"	"	Monzonite porphyry	○								

Sample No.	Location	Formation	Rock	Thin section	Polished section	Chemical analysis		X-ray analysis	Dating	Fossil	Pollen	Remarks
						Rock	Ore					
431	6-j	Intrusives	Granodiorite	○				○				
432	6-k	Yauri	Lapilli tuff									
433	"	"	Siltstone							○	○	
434	"	Ferrobamba	Limestone									
435	"	Yauri	Sandstone							○		
436	6-m	Tacaza	Lapilli tuff	○								
437	"	Puno	Liparite	○								
438	7-h	Tacaza	Dacite	○								
439	"	"	Tuff braccia									
440	"	"	Basalt									
441	"	"	Olivine basalt	○								
442	"	"	Basalt	○				○				
443	"	Seneca	Dacite	○								
444	"	Barroso	Altered andesite									
445	7-i	Intrusives	Porphyry									
446	"	Tacaza	Basalt	○								
447	"	"	Olivine basalt									
448	"	"	Basalt	○								
449	"	Yauri	Calcarene									
450	"	Ferrobamba	Limestone									
451	7-j	Intrusives	Quartz monzonite porphyry	○								
452	"	"	Granite porphyry									
453	"	"	Quartz monzonite porphyry with ore									
"	"	"	Monzonite with copper ore									Drill hole of Quechua No. 1-hole 73.00 m No. 2-hole 76.25 m

Sample No.	Location	Formation	Rock	Thin section	Polished section	Chemical analysis		X-ray analysis	Dating	Fossil	Pollen	Remarks
						Rock	Ore					
453	7-j	Intrusives	Quartz monzonite porphyry with ore		○							No. 3-hole 37.80 m
"	"	"	Copper ore		○							No. 5-hole 74.00 m
" 1	"	"	Quartz monzonite porphyry	○								No. 3-hole 138.80 m
" 2	"	"	Porphyritic monzonite	○								No. 1-hole 251.58 m
" 3	"	"	Quartz monzonite porphyry	○								No. 1-hole 56.62 m
" 4	"	"	Monzonite porphyry	○								No. 2-hole 78.55 m
" 5	"	"	Quartz monzonite porphyry	○								No. 2-hole 78.55 m
" 6	"	"	Monzonite	○				○				No. 1-hole 10m-30m
" 7	"	"	Porphyritic monzonite	○				○				No. 1-hole 161m-176m
454	"	"	Monzonite ? with copper ore									
455	7-k	"	Gabbro	○								
456	"	Yauri	Rhyolitic tuff									
457	"	Ferrobamba	Limestone									
458	"	Intrusives	Gabbroic diorite									
459	"	"	Monzonite porphyry	○								
460	"	"	Diorite									
461	"	"	Granodiorite	○								
462	"	Ferrobamba	Limestone									
463	7-l	Yura	Quartzite									
464	7-n	Puno	Rhyolite	○								
465	"	"	Sandstone									
466	"	"	Tuffaceous sandstone	○								
467	"	Tacaza	Volcanic breccia									
468	7-k	Intrusives	Porphyritic monzonite	○								

Sample No.	Location	Formation	Rock	Thin section	Polished section	Chemical analysis		X-ray analysis	Dating	Fossil	Pollen	Remarks
						Rock	Ore					
469	7-1	Intrusives	Monzonite porphyry	○								
"	"	"	Quartz monzonite porphyry	○								
"	"	Ferrobamba	Copper ore in limestone	○	○							

Table I-8 Microscopic Observations

Sample No.	Location	Formation	Rock	Microscopic observations	Remarks
1	1-a	Intrusives	Hornblende-biotite granodiorite	The rock is hypidiomorphic and composed of plagioclase, quartz, potash feldspar, biotite and hornblende (partly altered to chlorite) with accessory iron ore, apatite and sphene.	
4	1-b	Intrusives	Granodiorite	The rock is hypidiomorphic and composed mainly of plagioclase, potash feldspar, quartz and hornblende with accessory iron ore and apatite. Feldspars are partly altered to sericite, carbonates and chlorite. Veinlets of carbonates filling the fine cracks are observed.	See Table I-10
5	1-b	Intrusives	Altered hornblende granite	The rock is hypidiomorphic and mainly composed of plagioclase, potash feldspar, quartz and hornblende with accessory iron ore, apatite and sphene. Plagioclase and potash feldspar are partly altered to sericite and/or carbonates. Some crystals of plagioclase are replaced by epidote.	
6	1-b	Sandstone	Dacitic and welded tuff breccia	Crystal fragments (up to 3mm in size) of biotite and plagioclase and lithic fragments (up to 5mm) of basalt are in a argillaceous and partly spherulitic matrix. Crystal fragments are corroded.	
9	1-b	Intrusives	Hornblende-biotite quartz diorite	The rock shows a medium-grained and hypidiomorphic texture. The main constituent minerals are plagioclase (subhedral, up to 3mm, zoned, mainly andesite but having the core of labradorite or bytownite in the comparatively large crystals), quartz (anhedral, up to 2mm, often showing the wavy extinction), hornblende (sub-hedral columnar, up to 2mm, with a pleochroism of Z=yellowish brown, Y=yellowish green, X=pale brownish green) and biotite (sub-hedral to anhedral, up to 1.5mm, with a pleochroism of Z and Y=dark brown, X=brown to pale brown). The minor or accessory minerals are potash feldspar (anhedral, occurring as the interstices), clinopyroxene (observed in the core of hornblende crystals without exception), apatite, iron ore (magnetite and hematite), sphene, chlorite, epidote and sericite.	See Table I-10
12	1-c	Murco	Slaty shale	The rock shows the phyllitic texture and is composed of sericite, quartz, plagioclase (albite to oligoclase), potash feldspar, altered augite (relicts) and opaque minerals. The grain size is less than 0.2mm in diameter. The rock is considered to be affected by some weak metamorphism.	

Sample No.	Location	Formation	Rock	Microscopic observations	Remarks
14	1-c	Intrusives	Augite-hornblende granodiorite	The rock is equigranular and composed of plagioclase (andesine), poezah feldspar, green hornblende and augite with accessory epidote, sphene and apatite. Feldspars are partly altered to sericite-laceous matters. The rock is well sorted.	
15	1-c	Murco	Shale	Angular to subangular crystal grains (up to 0.2mm in size) of quartz, feldspar, sericite and iron ore are cemented by argillaceous matters. The rock is well sorted.	
22	1-d	Tacaza	Biotite-hornblende trachyte	Phenocrysts of biotite, hornblende (both are replaced by opaque minerals), plagioclase (andesine, up to 2mm) and sanidine are in a fine-grained and interstitial groundmass of plagioclase (andesine, lath-shaped), anorthoclase, augite, iron ore, apatite and glass. The groundmass shows the flow structure. Plagioclase laths are thinly mantled by anorthoclase. Cristobalite is formed in the drusy cavities.	See Table I-10
23	1-d	Tacaza	Rhyolitic tuff breccia	Corroded crystals of biotite, quartz and plagioclase are in a spherulitic and argillized matrix.	
24	1-d	Tacaza	Biotite trachyte	Phenocrysts of biotite (euhedral prismatic, up to 0.5mm, with a pleochroism of pale greenish brown to dark brown), plagioclase (euhedral columnar, up to 3mm long, distinctly zoned, twinned after albite and Carlsbad law) and sanidine (up to 5mm long) are in a fine-grained, argillaceous and partly spherulitic groundmass.	
25	1-d	Tacaza	Biotite trachyte	Phenocrysts of brown biotite (corroded, up to 3mm, including apatite and magnetite), plagioclase (up to 4mm, andesine, zoned, twinned after albite and Carlsbad law, mantled by anorthoclase) and sanidine are in a medium-grained and trachytic groundmass of plagioclase laths (oligoclase), anorthoclase, K-rich plagioclase and iron ore with subordinate augite, apatite and brown glass. Phenocrystic crystals of opaque minerals and apatite are present.	See Table I-10
26	1-d	Tacaza	Tuff breccia	Corroded crystals of quartz and plagioclase are in a fine grained and altered matrix of albitized plagioclase, quartz, iron ore and clay minerals.	

Sample No.	Location	Formation	Rock	Microscopic observations	Remarks
27	1-d	Tacaza	Biotite trachyte	Phenocrysts of biotite (prismatic, up to 1 mm, with a pleochroism of pale brown to reddish brown, corroded and replaced by opaque minerals), plagioclase (prismatic, up to 2mm, andesine zoned, twinned after albite and Carlsbad law) and sanidine are in a fine-grained and almost holocrystalline groundmass of plagioclase (oligoclase to albite), anorthoclase, iron ore and mafic microclites with subordinate apatite and rare brown glass.	
28	1-d	Tacaza	Biotite trachyte (or alkalic dacite)	Phenocrysts of brown biotite (columnar to short prismatic, up to 1 mm, rimmed by opaque minerals and also including opaque minerals and apatite) and plagioclase (prismatic, up to 3mm, andesine, corroded, twinned after albite and Carlsbad law) are in a fine-grained and almost holocrystalline groundmass of plagioclase (oligoclase to andesine), iron ore, subordinate mafic microclite and augite.	
29	1-d	Tacaza	Biotite trachyte	Phenocrysts of brown biotite (subhedral ragged, up to 1 mm, replaced by opaque minerals) and plagioclase (prismatic, up to 3mm, andesine but changed marginally to albite due to the zoning, twinned after albite and Carlsbad law) are in a fine grained and almost holocrystalline groundmass of plagioclase (andesine to oligoclase), iron ore, mafic microclites, apatite and glass. Glass is altered to chlorite.	
30	1-d	Tacaza	Augite-biotite-hornblende trachy andesite	Phenocrysts of augite (subhedral prismatic, corroded, zoned up to 1 mm), biotite (subhedral columnar, up to 1 mm, marginally opacitized, with a pleochroism of pale yellowish brown to brown) hornblende (acicular to prismatic, up to 1 mm, mostly replaced by opaque minerals and/or sericite, with a pleochroism of pale brown to greenish brown), plagioclase (columnar, up to 2mm, corroded, zoned, twinned after albite and Carlsbad law) and sanidine (columnar, up to 3mm) are in a fine-grained and intergranular groundmass of plagioclase lath, hypersthene, augite, iron ore and anorthoclase mesocrysts with subordinate apatite (microphenocrystic) and brown glass. Xenocrysts of plagioclase showing honeycomb texture, up to 3 mm long, are present. The rock shows distinct flow structure.	

Sample No.	Location	Formation	Rock	Microscopic observations	Remarks
31	1-f	Tacaza	Biotite trachyte	Phenocrysts of biotite (columnar, up to 3mm, corroded and thinly mantled by opacite, with a pleochroism of pale greenish brown to dark brown), plagioclase (subhedral columnar, up to 5mm, corroded, weakly zoned, twinned after albite and Carlsbad law), and sanidine (subhedral columnar, up to 5mm) are in a fine-grained and intersertal groundmass of plagioclase, potash feldspar, pyroxene, iron ore, apatite (microphenocrystic) and glass. Tridymite and cristobalite are formed in drusy cavities.	
35	1-g	Tacaza	Biotite-pyroxene-hornblende (alkalic) andesite	Phenocrysts of hornblende (prismatic to acicular, up to 5mm, fairly opacitized, with a pleochroism of pale yellowish green to greenish brown), biotite (columnar or prismatic, up to 1 mm, marginally opacitized, with a pleochroism of brown to dark brown), augite (prismatic to short prismatic, up to 0.5mm, zoned), hypersthene (prismatic, up to 0.5mm, with a pleochroism of pale green to pale brown), sanidine (columnar, up to 2mm) and plagioclase (columnar, up to 2mm, marginally embayed by opacite, with distinct polysynthetic twinning) are in a medium-grained and intersertal groundmass of plagioclase, potash feldspar, augite, hypersthene, iron ore, apatite and brown glass. Flow structure is distinct. A euhedral microphenocryst of sphene is present.	
40	1-g	Tacaza	Biotite trachyte (or alkalic dacite)	Phenocrysts of sanidine (subhedral, up to 3mm), plagioclase (andesine to oligoclase, subhedral, up to 3mm, zoned), quartz (anhedral, up to 1 mm) and brown biotite (subhedral, up to 2 mm) are in a percrystalline and intersertal groundmass of plagioclase, iron ore (magnetite and hematite), silica minerals and brown glass.	See Table I-10
41	2-a	Tacaza	Tuff breccia	Fragments of andesite and crystal fragments of plagioclase, augite, hornblende, biotite, quartz, apatite, opaque minerals and carbonates are in a fine grained and andesitic ash.	
42	2-a	Tacaza	Tuff breccia	Fragments of plagioclase, hypersthene, biotite, apatite, carbonates after pyroxene, epidote after plagioclase and opaque minerals, and lithic fragments of andesite are in a fine grained matrix of andesitic ash.	
43	2-a	Tacaza	Alkalic dacite	Phenocrysts of plagioclase, biotite, hornblende and potash feldspar are in a holocrystalline and intergranular groundmass of potash feldspar, plagioclase, quartz, iron ore and apatite. Apatite and iron ore occur as the microphenocrysts	

Sample No.	Location	Formation	Rock	Microscopic observations	Remarks
49	2-b	Ferrobamba	Limestone	The rock is mainly composed of equigranular and euhedral to sub-hedral calcite with a little opaque minerals and quartz.	
51	2-b	Tacaza	Altered olivine bearing trachy andesite	The rock may be thermally metamorphosed and originally presumed to be andesite. It is divided into two parts from the different facies; one is fine-grained and the other is coarse-grained. The fine-grained part shows flow texture and is composed of lath-shaped plagioclase, potash feldspar, iron ore and apatite with pseudomorphitic phenocrysts after olivine and plagioclase. It has prismatic biotite and cristobalite in the drusy cavities. The coarse-grained part is composed of columnar plagioclase (probably recrystallized), potash feldspar, iron ore and apatite with pseudomorphitic phenocrysts after plagioclase and olivine.	See Table I-10
53	2-b	Tacaza	Sandstone	The rock is mainly composed of crystal grains of quartz and altered feldspar, and fragments of volcanics, up to 1 mm in size. The grains of quartz and feldspar are rounded and irregularly cracked.	
56	2-c	Intrusives	Hornblende-biotite granodiorite	The rock is equigranular and composed mainly of plagioclase (oligoclase), potash feldspar, quartz, biotite and hornblende with accessory iron ore, sphene and apatite. Quartz and potash feldspar show the graphic texture.	
58	2-d	Tacaza	Olivine (alkali) basalt	Phenocrysts of olivine (euhedral tabular, up to 1 mm, altered wholly to iddingsite, occasionally embayed by magmatic corrosion, commonly including octahedral magnetite), titanite (euhedral prismatic but rarely rounded, up to 1 mm, distinctly zoned and occasionally showing the hour-glass structure, with a distinct pleochroism of colourless to very pale brown, commonly including magnetite) and zeolites (euhedral to subhedral columnar, occurring as the aggregates of crystals filling the drusy cavities) are in a coarse grained, almost holocrystalline and subophitic to intergranular groundmass of plagioclase laths (sytomite to labradorite, mantled by anorthoclase), olivine (altered wholly to iddingsite), titanite and iron ore with subordinate anorthoclase, zeolites (occurring as the interstices), K-rich plagioclase and brown glass.	See Table I-10

Sample No.	Location	Formation	Rock	Microscopic observations	Remarks
60	2-d	Tacaza	Aphiric basalt	The rock is aphiric and rare phenocrysts of augite (euhedral to subhedral, up to 0.5mm, showing parallel intergrowth with hypersthene) are in a medium grained and intergranular groundmass with distinct flow structure composed of plagioclase laths (labradorite to bytownite), augite, anorthoclase interstices and iron ore with subordinate olivine (altered to iddingsite, with the reaction rim of augite), apatite, biotite, cristobalite (rare, occurring as the mesostasis) and brown glass.	
61	2-d	Tacaza	Oxyhornblende-biotite trachyte (or alkalic andesite)	Phenocrysts of oxyhornblende (euhedral, prismatic, up to 1 mm, with a pleochroism of pale green to reddish brown), biotite (euhedral, up to 2mm, with the similar pleochroism as oxyhornblende), sanidine and plagioclase (prismatic, up to 5mm, oligoclase, twinned after albite and Carlsbad law) are in a fine grained and intersertal groundmass of plagioclase laths, potash feldspar, iron ore, apatite and chloritized glass. Plagioclase of the groundmass is also oligoclase.	See Table I-10
62	2-d	Tacaza	Hypersthene bearing augite-biotite trachy andesite	Phenocrysts of brown biotite (prismatic to short prismatic, up to 1 mm, replaced largely by opaque minerals), augite (prismatic to granular, up to 1 mm, distinctly zoned), hypersthene (less abundant than augite, prismatic, up to 0.5mm) and pseudomorph after hornblende (aggregates of opaque minerals and augite) are in a medium grained and intersertal groundmass of plagioclase laths (andesine), augite, hypersthene, iron ore with subordinate apatite and brown glass. Zeolites and cristobalite are formed in the crusty cavities.	See Table I-10
63	2-d	Tacaza	Aegirine-augite-olivine trachybasalt	Phenocrysts of olivine (subhedral tabular, up to 0.5mm, altered to iddingsite and rimmed by opacite), augite (subhedral prismatic to granular, up to 0.5mm, distinctly zoned) and aegirine (euhedral prismatic to bladed, up to 0.5mm, with a pleochroism of brown to greenish colour) are in a coarse grained, almost holocrystalline and intergranular groundmass of lath-shaped plagioclase (labradorite to andesine), anorthoclase interstices, olivine, augite, aegirine and iron ore with subordinate apatite, K-rich plagioclase and a little brown glass. Phenocrystic aggregates of magnetite and augite are probably pseudomorph after phenocrysts of augite.	

Sample No.	Location	Formation	Rock	Microscopic observations	Remarks
64	2-d	Tacaza	Aegirine bearing augite-olivine trachybasalt	Phenocrysts of augite (subhedral, up to 0.5mm, including magnetite, distinctly zoned) and olivine (euhedral tabular to subhedral, up to 0.5mm, altered wholly to iddingsite) are in a coarse grained, porphyrocrystalline and intergranular groundmass of lath-shaped plagioclase (labradorite), olivine, augite, anorthoclase, iron ore, aegirine, biotite and a little brown glass. Olivine and aegirine are altered to iddingsite. Analcite is formed in the drusy cavities. Phenocrystic aggregates of magnetite and augite are present. Flow structure is distinctly marked.	
65	2-d	Tacaza	Altered olivine bearing andesitic rock	The rock is wholly altered but phenocrysts of mafic minerals such as olivine, hornblende and biotite (now perfectly replaced by opaque minerals) and plagioclase (altered to clay minerals and adularia) are estimated from their pseudomorphic crystal forms. The groundmass is also entirely altered to clay minerals.	
66	2-d	Tacaza	Olivine-augite trachy andesite	Phenocrysts of augite (subhedral, up to 0.5mm, distinctly zoned) and olivine (euhedral to subhedral tabular, up to 0.5mm, wholly altered to iddingsite) are in a coarse to medium grained, almost holocrystalline and intergranular to intersertal groundmass of plagioclase (labradorite to andesine), olivine, augite, aegirine, iron ore and anorthoclase with subordinate K-rich plagioclase, apatite, analcite mesostasis and brown glass. Analcite is also formed in the drusy cavities.	See Table I-10
67	2-d	Tacaza	Olivine-titanaugite trachy andesite	Phenocrysts of olivine (euhedral tabular, up to 3mm, altered to iddingsite) and titanite (subhedral prismatic, up to 1 mm, including magnetite and apatite, commonly twinned) are in a medium grained and intergranular to intersertal groundmass of plagioclase laths (andesine), olivine, augite, iron ore, anorthoclase interstices, apatite, analcite and a little brown glass. Apatite occurs occasionally as a phenocryst. Olivine of the groundmass is also altered to iddingsite. The flow structure is marked.	

Sample No.	Location	Formation	Rock	Microscopic observations	Remarks
68	2-d	Tacaza	Biotite-olivine bearing hypersthene-augite trachyte andesite	Phenocrysts of augite (euhedral prismatic to subhedral granular, up to 0.5mm), olivine (subhedral tabular, up to 1 mm), slightly altered to iddingsite, surrounded by minute grains of augite, biotite and plagioclase), hypersthene (euhedral prismatic, up to 1 mm), plagioclase (euhedral columnar, up to 2mm, zoned from Ab ₅₀ An ₅₀ to Ab ₆₅ An ₃₅ , twinned after albite and Carlsbad law. Including brown glass) and biotite (columnar, up to 0.5mm, with a pleochroism of pale brown to dark reddish brown, commonly rimmed by opacite) are in a medium grained and intersertal groundmass of plagioclase laths (andesine), hypersthene, augite and iron ore with subordinate apatite and brown glass. Xenocrysts of plagioclase (rounded due to the corrosion, up to 2mm) are present.	
69	2-d	Tacaza	Hypersthene-augite-biotite trachyte	Phenocrysts of augite (subhedral, up to 1.5mm but commonly finer than 0.5mm, zoned, marginally chloritized), hypersthene (subhedral, up to 0.5mm, marginally chloritized), biotite (subhedral, up to 0.5mm, corroded and marginally opacitized) and plagioclase (columnar, up to 3mm, from Ab ₄₀ An ₆₀ to Ab ₇₀ An ₃₀ , twinned after albite and Carlsbad law) are in a fine to medium grained and intersertal groundmass of plagioclase (andesine to oligoclase), iron ore, hypersthene and augite with subordinate apatite (often microphenocrystic) and brown glass. Tridymite and/or cristobalite are formed in the drusy cavities.	See Table I-10
70	2-d	Tacaza	Hornblende-hypersthene-augite bearing biotite trachyte	Phenocrysts of biotite (subhedral rounded to columnar, up to 2mm, thinly mantled by opacite), hornblende (subhedral acicular, up to 0.5mm, thinly rimmed by opacite), augite (subhedral prismatic, up to 2mm, including magnetite and apatite), hypersthene (subhedral columnar to prismatic, up to 2mm) and plagioclase (columnar to prismatic, up to 2mm, about Ab ₅₀ An ₅₀ , twinned after albite and Carlsbad law) are in a medium grained and intersertal groundmass of plagioclase (andesine), hypersthene, augite and iron ore with subordinate anorthoclase interstices, apatite (microphenocrystic) and brown glass. Cristobalite occurs in the drusy cavities. Xenocrysts of plagioclase (corroded, up to 3mm, with many dusty dark inclusions) are present.	

Sample No.	Location	Formation	Rock	Microscopic observations	Remarks
71	2-d	Tacaza	Hyperssthene-augite trachy andesite	Phenocrysts of augite (subhedral, up to 2mm, zoned and corroded), hyperssthene (subhedral, up to 1 mm) and pseudomorphic augite (aggregates of magnetite and augite) are in a medium grained and intergranular groundmass of plagioclase (Ab ₅₀ An ₅₀ to Ab ₇₀ An ₃₀), augite, olivine, anorthoclase and iron ore with subordinate apatite, analcite mesostasis and a little brown glass. Xenocrysts of plagioclase (corroded and with many inclusions) are present. The groundmass shows the distinct flow structure.	
72	2-d	Tacaza	Hyperssthene bearing augite trachy andesite	Phenocrysts of augite (subhedral, up to 0.5mm, distinctly zoned and showing hour-glass structure in some crystals) and aggregates of augite and magnetite after augite phenocrysts are in a medium-grained and intersertal groundmass of plagioclase, augite, hyperssthene, anorthoclase, iron ore, apatite and a little brown glass.	See Table I-10
73	2-d	Tacaza	Hyperssthene-augite-biotite trachy andesite	Phenocrysts of augite (subhedral, corroded, up to 1 mm, zoned), biotite (subhedral, up to 1 mm, with a pleochroism of pale yellowish brown to dark brown, surrounded by hyperssthene, plagioclase and magnetite), hyperssthene (subhedral, up to 1 mm, with a pleochroism of pale green to pale brown, slightly altered to sericite), plagioclase (columnar, up to 2mm, twinned after albite and Carlsbad law) and potash feldspar (subhedral columnar, up to 2 mm) are in a medium-grained and intersertal groundmass of plagioclase, potash feldspar, augite, hyperssthene, iron ore, apatite and glass.	
74	2-d	Tacaza	Olivine trachybasalt	Phenocrysts of olivine (subhedral tabular, elongated parallel to c-crystallographic axis, up to 1 mm long, partly altered to iddingsite, occasionally embayed by magmatic corrosion) are in a coarse-grained and intergranular groundmass of lath-shaped plagioclase, olivine, augite, anorthoclase interstitials, iron ore with subordinate K-rich plagioclase, biotite, apatite and brown glass. Olivine and augite of the groundmass are fairly altered to iddingsite. Biotite may be titanbiotite. Flow structure is distinctly marked.	See Table I-10
75	2-d	Tacaza	Olivine trachybasalt	Phenocrysts of olivine (euhedral tabular, up to 1 mm, almost wholly replaced by opaque minerals) are in a medium-grained and intergranular groundmass of plagioclase, anorthoclase, olivine, augite, iron ore with subordinate zeolites and brown glass. Zeolites are secondary products and also occur in drusy cavities.	See Table I-10

Sample No.	Location	Formation	Rock	Microscopic observations	Remarks
76	2-d	Tacaza	Olivine (alkali) basalt	Phenocrysts of olivine (subhedral tabular, elongated parallel to c-crystallographic axis, somewhat corroded, fairly altered to iddingsite) and plagioclase (euhedral prismatic, up to 0.5mm, zoned, twinned after albite and Carlsbad law) are in a coarse-grained and intergranular groundmass of plagioclase laths, anorthoclase, olivine, augite, iron ore, apatite and brown glass. Plagioclase laths are thinly mantled by anorthoclase and their compositions are estimated as $Ab_{40}An_{60}$ to $Ab_{30}An_{70}$.	
79	2-e	Tacaza	Hypersthene bearing augite-biotite trachyte	Phenocrysts of plagioclase (andesine, subhedral to euhedral, up to 4mm, zoned), augite (subhedral to euhedral, up to 4 mm) and biotite (subhedral to anhedral, up to 2mm, opacitized and replaced by iron ore) are in a intersertal groundmass of plagioclase, augite, hypersthene, iron ore (magnetite and hematite), brown glass, apatite and silica minerals including quartz.	See Table I-10 and I-18
88	2-e	Tacaza	Olivine-biotite bearing hypersthene-augite trachyte	Phenocrysts of olivine (euhedral, up to 1 mm, entirely altered to iddingsite and chlorite, surrounded by anorthoclase), augite (subhedral, up to 1.5 mm, partly chloritized), hypersthene (subhedral, up to 1.5mm, with a pleochroism of pale green to pale brown, partly chloritized) plagioclase (columnar, up to 2mm, distinctly zoned from andesite to albite, twinned after albite and Carlsbad law), sanidine (columnar, up to 2 mm) and acicular biotite are in a medium-grained and intersertal groundmass of plagioclase, potash feldspar, augite, hypersthene, iron ore, apatite and brown glass. Plagioclase of the groundmass is $Ab_{60}An_{40}$ or more acidic. Brown glass is commonly altered to chlorite. Xenocrysts of plagioclase (rounded by corrosion and showing honeycomb texture) are present.	See Table I-10
91	2-g	Tacaza	Augite bearing hornblende-biotite trachyte	Phenocrysts of augite (subhedral, up to 2mm, distinctly zoned), hornblende (acicular to short prismatic, up to 0.5mm, marginally opacitized, with a pleochroism of pale yellowish green to brownish green), biotite (columnar, up to 2mm, marginally opacitized, with a pleochroism of yellowish brown to reddish brown), plagioclase (columnar but slightly rounded, up to 2mm, distinctly zoned, twinned after albite and Carlsbad law) and sanidine (subhedral columnar, up to 2 mm) are in a fine-grained and intersertal groundmass of plagioclase, potash feldspar, augite, biotite, iron ore, apatite and brown glass. A rounded xenolith, about 5mm in diameter, is contained. The xenolith is a coarse-grained and equigranular rock showing recrystallized texture by thermal effect and is composed of plagioclase, augite, biotite, iron ore and apatite. The original rock may be basic tuff. Further, the compositions of plagioclase are andesine to labradorite in the phenocrysts and andesine in the groundmass.	

Sample No.	Location	Formation	Rock	Microscopic observations	Remarks
95	2-g	Tacaza	Bronzite-augite andesite	Phenocrysts of augite (subhedral prismatic, up to 0.5 mm, distinctly zoned) and bronzite (subhedral prismatic, up to 0.5 mm, with a pleochroism of colourless to pale brown, having the dispersion of $\gamma > \alpha$, often surrounded by augite) are in a medium-grained and intersertal groundmass of plagioclase lath, cristobalite? mesostasis, anorthoclase interstices, augite, bronzite, iron ore with subordinate apatite and brown glass. The rock is fairly aphyric and similar to Sanulcite. The flow structure is distinct.	
97	3-a	Intrusive	Altered microgranite	Phenocrysts of plagioclase, potash feldspar and pseudomorphitic hornblende (altered to the aggregates of iron ore and carbonates) are in a holocrystalline and microgranular groundmass of plagioclase, quartz and iron ore. Some microphenocrysts of apatite are present. Plagioclase are partly replaced by carbonates and epidote.	
101	3-c	Tacaza	Olivine bearing hornblende-biotite trachy andesite	Phenocrysts of biotite (euhedral, up to 1 mm, intensely opacitized), hornblende (euhedral, up to 1 mm, marginally opacitized and also wholly replaced by opaque minerals), olivine (entirely altered to iddingsite) and plagioclase (less abundant than the former three minerals, anhedral, twinned after albite and Carlsbad law, andesine) are in a medium grained and intersertal groundmass of plagioclase laths (andesine), olivine, pyroxene and iron ore with subordinate brown glass.	See Table I-10
102	3-c	Sencca	Biotite-hornblende rhyolitic pitchstone	Phenocrysts of biotite (euhedral prismatic, up to 1 mm), hornblende (euhedral prismatic, up to 1 mm) and plagioclase (oligoclase, euhedral columnar, up to 2 mm, partly corroded and containing brown glass) are in a vitric groundmass composed mainly of brown glass with subordinate hornblende needles, plagioclase microclites, iron ore and apatite. The groundmass shows the flow structure and also the perlitic texture.	
104	3-c	Barroso	Augite bearing hornblende andesite	Phenocrysts of hornblende (euhedral acicular to prismatic, up to 1 mm, wholly replaced by opaque minerals and augite) and augite (subhedral prismatic, up to 0.3 mm) are in a medium grained and perocrystalline groundmass of plagioclase, hypersthene, augite, cristobalite mesostasis and iron ore with subordinate apatite and brown glass. Trichymite is formed in the drusy cavities.	

Sample No.	Location	Formation	Rock	Microscopic observations	Remarks
107	3-c	Tacaza	Olivine (alkali) basalt	Phenocrysts of olivine (euhedral to subhedral tabular, up to 0.5 mm, marginally and along fine fractures of crystals altered to iddingsite, often deeply embayed by magmatic corrosion), augite (less abundant than olivine, subhedral, up to 1 mm, distinctly zoned) and plagioclase (columnar, up to 1 mm, twinned after albite and Carlsbad law but rare polysynthetic twin, zoned from Ab ₃₀ An ₇₀ to Ab ₄₀ An ₆₀) are in a coarse-grained and intergranular groundmass of plagioclase (Ab ₃₀ An ₇₀ to Ab ₅₀ An ₅₀), olivine, augite, iron ore, anorthoclase, K-rich plagioclase, analcite, apatite and brown glass. Analcite also occurs in fine amygdaloidal cavities.	
113	4-a	Tacaza	Altered olivine (alkali) basalt	Phenocrysts of olivine-pseudomorph (euhedral, up to 1 mm, entirely altered to iddingsite and carbonates) are in a coarse-grained, almost holocrystalline and intergranular groundmass of lath-shaped plagioclase, olivine, augite and iron ore with subordinate apatite, anorthoclase and a little brown glass. The alteration in the groundmass is also very advanced. Olivine and augite are altered to iddingsite and chlorite. Plagioclase and anorthoclase are albitized and sericitized.	
114	4-b	Seneca	Rhyolitic tuff	Fragments of quartz and altered plagioclase (up to 0.5 mm in size) and altered lithic fragments are in a very fine grained and partly spherulitic groundmass of volcanic ash.	
115	4-b	Seneca	Rhyolitic tuff	Fragments of quartz, plagioclase and biotite and lithic fragments of dacite are in a fine-grained and vitric groundmass with altered plagioclase, quartz, iron ore and apatite. Biotite and plagioclase are partly replaced by carbonates.	
119	4-c	Tacaza	Olivine-augite trachy basalt	Phenocrysts of olivine (euhedral tabular, up to 1 mm, altered wholly to iddingsite), titanite (euhedral prismatic to short prismatic, distinctly zoned, including magnetite and occasionally olivine, up to 2 mm in size) and plagioclase (labradorite to bytownite, euhedral, up to 2 mm, twinned after albite and Carlsbad law, thinly mantled by anorthoclase) are in a coarse-grained, almost holocrystalline and intergranular groundmass of lath-shaped plagioclase (labradorite), olivine, titanite and iron ore with subordinate anorthoclase, apatite and brown glass. Analcite occurs in the amygdaloidal cavities.	

Sample No.	Location	Formation	Rock	Microscopic observations	Remarks
120	4-c	Seneca	Hornblende-augite trachyte (or alkalic dacite)	Phenocrysts of augite (corroded, including magnetite, showing slightly purplish tint, distinctly zoned), plagioclase (subhedral columnar, up to 3mm, andesine in composition, zoned) and pseudo-morphic hornblende (elongated aggregates of augite and magnetite, up to 1.5mm) are in a medium-grained and almost holocrystalline groundmass of plagioclase laths, augite, cristobalite mesostasis, iron ore with subordinate anorthoclase, apatite and brown glass. Cristobalite also occurs in the drusy cavities.	
125	4-d	Tacaza	Augite-olivine trachy andesite	Phenocrysts of olivine (ragged in shape, up to 1 mm, altered entirely to iddingsite) and augite (subhedral, up to 0.5mm, partly altered) are in a medium-grained, holocrystalline and intergranular groundmass with distinct flow structure which is composed of plagioclase laths (labradorite to andesine), anorthoclase interstices, olivine, augite and iron ore with subordinate analcite and rare brown glass. Olivine of the groundmass is also altered to iddingsite or replaced by magnetite. Analcite and other zeolites occur in the drusy cavities.	See Table I-10
126	4-d	Tacaza	Rhyolite	Phenocrysts (up to 3mm in size) of corroded quartz, plagioclase and sanidine are in a very fine-grained and spherulitic groundmass. Cristobalite and tridymite are formed in the drusy cavities.	
128	4-d	Tacaza	Altered olivine basalt	Phenocrysts of olivine (subhedral, wholly altered to iddingsite) and augite (subhedral, up to 1 mm, zoned) are in a coarse-grained and hyalophitic groundmass of plagioclase lath, augite, iron ore anorthoclase and a little glass. Zeolites occur in drusy cavities. Secondary cristobalite is formed in the groundmass.	
136	4-f	Coporaque	Sandstone	Crystal grains of plagioclase, potash feldspar, quartz and iron ore, and fragments of volcanic rocks are in a fine-grained matrix of quartz, plagioclase, chlorite, sericite and clay minerals.	
142	5-a	Seneca	Biotite rhyolite	Phenocrysts of brown biotite (subhedral columnar, up to 1 mm, marginally opacitized), quartz (angular, corroded, up to 2mm) and plagioclase (andesine to albite, corroded, always mantled by albite) are in a fine-grained groundmass of abundant spherules and feldspars altered wholly to albite and clay minerals.	See Table I-10

Sample No.	Location	Formation	Rock	Microscopic observations	Remarks
155	5-c	Barroso	Augite-olivine basalt	The rock is aphyric. A little phenocrysts of olivine (surrounded by reaction rim of hypersthene, altered wholly to iddingsite) and augite (short prismatic, up to 0.3mm, generally embayed by magmatic corrosion) are in a medium grained and intergranular groundmass of lath-shaped plagioclase (about Ab ₄₀ An ₆₀ , thinly mantled by anorthoclase), augite, hypersthene, iron ore, anorthoclase, apatite and brown glass. The granular hypersthene of the groundmass occasionally contains minute olivine (altered to iddingsite).	
160	5-d	Seneca (Tacaza?)	Altered olivine-pyroxene trachy andesite	Phenocrysts of mafic minerals are wholly altered to sericite and chlorite but are estimated to be olivine and pyroxene from their pseudomorphic crystal forms. Plagioclase phenocrysts are euhedral prismatic in shape, up to 2mm in size, twinned after albite and Carlsbad law, zoned and labradorite in composition. The groundmass is medium-grained and intersertal, and consists of plagioclase laths (andesine), iron ore, chloritized pyroxene, apatite and chloritized glass.	
163	5-e	Tacaza	Olivine (alkali) basalt	Phenocrysts of olivine (euhedral tabular, up to 1 mm, wholly altered to iddingsite) are in a coarse-grained, almost holocrystalline and intergranular groundmass of plagioclase (lath-shaped, labradorite), olivine, titanite, iron ore, analcite and little brown glass. Analcite and other zeolites are formed in drusy cavities.	
165	5-e	Tacaza	Olivine (alkali) basalt	Phenocrysts of olivine (euhedral tabular, up to 0.5mm, marginally chloritized), plagioclase (labradorite, up to 0.5mm, zoned and twinned after albite and Carlsbad law) are in a coarse-grained, almost holocrystalline and intergranular groundmass of plagioclase laths (labradorite, mantled by anorthoclase), olivine, augite, iron ore, anorthoclase, apatite, biotite (titanbiotite?) and chloritized glass.	
168	5-e	Seneca	Rhyolitic tuff	Crystals of quartz and plagioclase, aggregates of opaque minerals and chlorite after mafic minerals and lentic fragments of volcanics (up to 1.5mm in size) are in a fine-grained and albitized groundmass. The groundmass partly shows spherulitic texture.	
170	5-f	Seneca	Dacitic tuff breccia	Crystal fragments (up to 3mm in size) of plagioclase (andesine to oligoclase) and sanidine and lentic fragments of altered volcanic rocks are in a fine-grained matrix of dusts and spherules.	

Sample No.	Location	Formation	Rock	Microscopic observations	Remarks
172	5-f	Intrusive	Granodiorite		The rock is hypidiomorphic and the main constituent minerals are plagioclase (oligoclase to acidic andesine), potash feldspar, microcline and hornblende. Accessory minerals are apatite, sphene and iron ore. Hornblende is ragged in shape and includes magnetite and apatite. Plagioclase is partly replaced by sericite or epidote and hornblende is altered to chlorite.
174	5-f	Copraque	Sandstone		Subangular to rounded crystals (up to 2mm in size) of quartz, potash feldspar and plagioclase, and lithic fragments are in a fine grained and carbonatized matrix. The coating is bad.
182	5-g	Intrusives	Granodiorite		The rock shows hypidiomorphic texture and is composed of subhedral and green hornblende, brown biotite, euhedral to subhedral plagioclase (andesine to oligoclase), subhedral microcline, orthoclase and quartz with accessory iron ore and apatite. Orthoclase is slightly altered to kaolinite.
200	6-b	Barroso	Hypersthene-augite-olivine andesite		Phenocrysts of olivine (euhedral tabular, up to 1 mm, partly altered to iddingsite, occasionally embayed by magmatic corrosion and surrounded by reaction rim of hypersthene), augite (subhedral prismatic, up to 1 mm, zoned and twinned) and hypersthene (prismatic, up to 0.5mm), and xenocrysts of plagioclase (anhedral, up to 2mm, containing arranged dusty inclusions along the crystal margin, about $Ab_{70}An_{30}$) are in a medium-grained and intergranular groundmass with flow structure, which is composed of lath-shaped plagioclase (about $Ab_{50}An_{50}$), hypersthene, olivine, anorthoclase interstices, iron ore, apatite, biotite and a little brown glass.
203	6-b	Tacaza	Olivine-augite trachy andesite		Phenocrysts of olivine (euhedral tabular, up to 0.5mm, wholly replaced by iddingsite and/or magnetite), augite (euhedral prismatic, up to 1 mm, slightly chloritized) and plagioclase (euhedral prismatic, up to 2mm, twinned after albite and Carlsbad law, zoned from labradorite to andesine) are in a medium-grained and interstitial groundmass of plagioclase (lath-shaped, andesine), olivine, augite and iron ore with subordinate anorthoclase, apatite, analcite and brown glass. Olivine and augite in the groundmass are almost altered to chlorite. Plagioclase laths are thinly mantled by anorthoclase.

See Table I-10

Sample No.	Location	Formation	Rock	Microscopic observations	Remarks
215	6-d	Barroso	Hornblende-hypersthene-augite andesite	Phenocrysts of augite (euhedral prismatic, up to 0.5 mm, twinned and zoned), hypersthene (prismatic, up to 0.5 mm, with a pleochroism of colourless to pale brown) and altered hornblende (wholly replaced by opaque minerals) are in a fine-grained and intersertal groundmass with flow structure, which is composed of plagioclase laths (andesine), cristobalite mesostasis, hypersthene, iron ore, apatite, and brown glass. Phenocrysts of plagioclase are absent.	
217	6-d	Tacaza	Altered andesitic rock	Phenocrysts are wholly altered to carbonates, but the original minerals are considered to be olivine, pyroxene and plagioclase from their pseudomorphic crystal forms. The groundmass shows a medium-grained and intersertal texture, and is composed of plagioclase laths (albitized), augite (altered to iddingsite and/or carbonates), iron ore, anorthoclase, apatite and glass. Cristobalite occurs in drusy cavities.	
218	6-d	Sencca	Altered rhyolite	Phenocrysts (up to 3mm in size) of subhedral quartz and plagioclase (oligoclase) are in a fine grained and altered groundmass of quartz, albitized plagioclase, potash feldspar altered intensively to clay minerals, apatite, iron ore and altered glass.	
221	6-d	Tacaza	Tuff breccia	Crystals of quartz, albitized plagioclase, altered mafic minerals and opaque minerals, and lithic fragments of volcanics are in a vitric matrix.	
222	6-d	Sencca	Rhyolitic welded tuff	Crystals of angular and corroded quartz, Na-rich plagioclase and sanidine (up to 2mm in size) are in a vitric matrix partly showing spherulitic texture.	
240	7-b	Sencca	Hypersthene-augite bearing biotite dacite	Phenocrysts of biotite (prismatic but marginally opacitized and ragged, up to 1 mm, with a pleochroism of colourless to brown), augite (subhedral, up to 1.2mm, distinctly zoned), hypersthene (subhedral, up to 0.5mm, with a pleochroism of colourless to pale brown), plagioclase (euhedral prismatic to short prismatic, up to 2mm, twinned after albite and Carlsbad law, distinctly zoned, corroded in large ones) and quartz (anhedral rounded and cracked, up to 2mm) are in a fine grained and hyalopilitic groundmass with flow structure, which is composed of plagioclase laths, cristobalite mesostasis, iron ore, apatite, microclites and brown glass.	

Sample No	Location	Formation	Rock	Microscopic observations	Remarks
243	7-b	Tacaza	Pyroxene bearing hyalopilitic trachy andesite	Plagioclase (euhedral prismatic, up to 2mm, twinned after albite and Carlsbad law, distinctly zoned from Ab ₆₀ An ₄₀ to Ab ₇₅ An ₂₅) are in a fine-grained and hyalopilitic groundmass with flow structure which is composed of plagioclase laths, anorthoclase, iron ore, apatite, pyroxene and chloritized glass.	See Table I-10
246	7-b	Sencca	Pyroxene bearing hornblende trachyte	Phenocrysts of plagioclase (euhedral prismatic, up to 3mm, twinned after albite and Carlsbad law, distinctly zoned from Ab ₄₀ An ₆₀ to Ab ₇₀ An ₃₀), hypersthene (subhedral rounded, up to 0.3mm, with pleochroism of colourless to pale brown), augite (subhedral rounded, up to 0.3mm, less abundant than hypersthene) and hornblende (anhedral ragged, up to 1 mm, with pleochroism of pale yellowish green to brownish green, marginally opacitized) are in a fine grained and hyalopilitic groundmass of plagioclase laths, anorthoclase, iron ore, apatite and brown glass. Cristobalite occurs in drusy cavities.	See Table I-10
248	7-b	Sencca	Augite-biotite bearing dacite	The rock is aphyric. A little phenocrysts of plagioclase, augite and biotite are in a medium grained and almost holocrystalline groundmass with flow structure, which is composed of plagioclase laths, cristobalite interstices, iron ore, biotite, apatite and a little brown glass. Cristobalite and apatite are occasionally phenocrysts. Plagioclase laths are about Ab ₆₅ An ₃₅ in the composition.	
249	7-b	Sencca	Dacite	Plagioclase (albitized and recrystallized) is in a argillaceous and partly spherulitic matrix of albitized plagioclase, silica minerals, clay minerals and iron ore.	
257	7-c	Sencca	Augite bearing biotite dacite	Phenocrysts of brown biotite (up to 1 mm, replaced by opaque minerals and other alteration products), plagioclase (prismatic, up to 4mm, twinned after albite and Carlsbad law, zoned from Ab ₆₀ An ₄₀ to Ab ₇₀ An ₃₀) and augite (euhedral prismatic, up to 0.5mm, less abundant than biotite and plagioclase) are in a fine-grained and intersertal groundmass of plagioclase, cristobalite-tridymite, augite, iron ore, apatite and brown glass. Large xenocrysts of plagioclase (2mm in size, corroded, with many inclusions of dark dusts) are present. Apatite and cristobalite occur as micropteno-crysts.	
268	7-d	Sencca	Tuff breccia	Litic fragments of volcanic rocks (up to 5mm in size, andesite and a little basalt) and crystal fragments of altered plagioclase and mafic minerals are in a fine-grained and strongly chloritized matrix.	

Sample No.	Location	Formation	Rock	Micro-copic observations	Remarks
272	7-e	Barroso	Olivine (alkali) basalt	Phenocrysts of olivine (euhedral tabular, up to 1 mm, elongated parallel to c-crystallographic axis, occasionally embayed by magmatic corrosion) are in a coarse-grained, almost holocrystalline and intergranular groundmass of plagioclase laths (basic labradorite), olivine, augite, anorthoclase interstices, analcite mesostasis and a little brown glass. Plagioclase laths are mantled by anorthoclase. Analcite occurs in drusy cavities.	
273	7-e	Barroso	Olivine basalt	Phenocrysts of olivine (tabular or granular, up to 3mm, marginally altered to iddingsite, occasionally embayed by magmatic corrosion, commonly including magnetite) and plagioclase (prismatic, up to 0.5mm, distinctly zoned) are in a coarse-grained and intergranular to intersertal groundmass of plagioclase, olivine, augite, iron ore, anorthoclase, apatite, analcite and brown glass.	
274	7-e	Barroso	Pumice-tuff	Crystals of quartz, biotite, opaque minerals and plagioclase, and lithic fragments of andesite (up to 3mm in size) are in a vitric welded and partly porous matrix.	
275	7-e	Barroso	Biotite-hornblende andesite	Phenocrysts of biotite (long prismatic to prismatic, up to 2mm, thinly rimmed by opacite), hornblende (long prismatic, up to 6mm, commonly containing apatite, biotite and magnetite, thinly mantled by opacite) and plagioclase (prismatic to columnar, up to 3mm, oligoclase in composition, zoned and twinned after albite and Carlsbad law) are in a medium-grained and intersertal groundmass of plagioclase laths, iron ore, wholly opacitized hornblende needles, cristobalite mesostasis, hypersthene, apatite and brown glass.	
276	7-f	Tacaça	Hypersthene-augite-olivine basalt	Phenocrysts of olivine (granular, up to 0.5mm, rimmed by augite, altered to iddingsite), augite (euhedral prismatic, up to 0.7mm, distinctly zoned and occasionally showing hour-glass structure), hypersthene (up to 1 mm, deeply embayed by magmatic corrosion, zoned) and plagioclase (less abundant than other phenocrysts, distinctly zoned) are in a coarse-grained, perocrystalline and intergranular to intersertal groundmass of plagioclase laths (labradorite), olivine, augite, iron ore, apatite and brown glass. Zeolites are formed in drusy cavities.	
278	7-g	Seneca	Tuff	The rock is composed of very fine volcanic ash including powdery feldspar.	

Sample No.	Location	Formation	Rock	Microscopic observations	Remarks
281	7-g	Tacaza	Olivine (alkali) basalt	Phenocrysts of augite (granular or ragged by magmatic corrosion, up to 2mm but generally less than 1 mm, partly altered to carbonate, distinctly zoned) are in a coarse grained and intergranular groundmass of plagioclase laths (labradorite to basic andesine), olivine (pseudomorph), augite, anorthoclase interstices, iron ore, apatite (microphenocrystic), biotite and brown glass. Xenocrysts of granular quartz (up to 3mm) are surrounded by augite and secondary carbonates.	
283	7-g	Tacaza	Olivine basalt	The rock shows the vitrophyric texture, and euhedral crystals (up to 2mm in size) of olivine, augite, plagioclase and iron ore are scattered in the brown glass. Olivine is slightly altered to iddingsite.	
284	7-g	Tacaza	Olivine bearing bronzite-augite andesite	Phenocrysts of olivine (euhedral tabular, altered to iddingsite, bronzite (euhedral prismatic, with pleochroism of colourless to pale green, with dispersion of $\gamma > \beta$) and augite (euhedral, often rimmed by hypersthene) are in a medium-grained, intergranular and perocrystalline groundmass with distinct flow structure, composed of lath-shaped plagioclase ($Ab_{40}An_{60}$ to $Ab_{30}An_{70}$), augite, hypersthene and iron ore with subordinate anorthoclase, K-rich plagioclase and a little brown glass.	
285	7-g	Tacaza	Olivine bearing basalt	Phenocrysts of olivine (deeply embayed by magmatic corrosion and reacting with augite) and plagioclase (euhedral, up to 1 cm, including olivine, magnetite and dusty substance, distinctly zoned and commonly twinned after albite and Carlsbad law) are in a coarse grained and holocrystalline groundmass of plagioclase, olivine, augite and iron ore with subordinate hypersthene, apatite and a little cristobalite. Augite is formed by the reaction of olivine and liquid, and hypersthene occurs as the intergrowth to augite. The compositions of plagioclase are about $Ab_{25}An_{75}$ in the phenocrysts and $Ab_{15}An_{85}$ in the groundmass.	

Sample No.	Location	Formation	Rock	Microscopic observations	Remarks
286	7-g	Barroso	Olivine bearing augite-hypersthene andesite	Phenocrysts of olivine (euhedral, up to 0.5mm, occasionally embayed by magmatic corrosion, intensely altered to iddingsite), augite (euhedral prismatic, up to 1 mm), hypersthene (euhedral prismatic, up to 1 mm, with pleochroism of colourless to pale green) and plagioclase (euhedral, up to 2mm, distinctly zoned, about Ab ₃₀ An ₇₀ in crystal core, twinned after albite and Carlsbad law) are in a fine grained and intersertal groundmass of lath-shaped plagioclase, augite, hypersthene and iron ore with subordinate cristobalite, apatite and brown glass. Cristobalite and mica are also formed in drusy cavities. The composition of plagioclase in the groundmass is estimated at about Ab ₅₀ An ₅₀ .	
287	1-g	Tacaza	Olivine bearing biotite trachy andesite	Phenocrysts of biotite (euhedral, up to 1 mm, with pleochroism of pale brown to brown, marginally opacitized), plagioclase (euhedral but slightly rounded, up to 5mm, twinned after albite and Carlsbad law, distinctly zoned from Ab ₆₀ An ₄₀ to more acidic) and olivine (microphenocrystic, euhedral, perfectly altered to opaque minerals and/or adularia) are in a intersertal groundmass of plagioclase, analcite, iron ore and apatite with a little augite and pseudomorph olivine. The composition of plagioclase in the groundmass is about Ab ₇₅ An ₂₅ .	See Table I-10
296	1-h	Tacaza	Altered olivine basalt	Phenocrysts of pseudomorph olivine (altered to carbonates and/or magnetite) and carbonatized plagioclase are in a intersertal groundmass of carbonates after mafic minerals, plagioclase (rimmed by anorthoclase, albitized), anorthoclase and microphenocrystic apatite.	See Table I-10
302	1-h	Tacaza	Olivine bearing biotite trachyte	Phenocrysts of altered olivine, biotite (euhedral, up to 1 mm, with pleochroism of pale green to reddish brown, marginally opacitized) and plagioclase (euhedral, up to 1 cm, twinned after albite and Carlsbad law, distinctly zoned from Ab ₆₀ An ₄₀ to Ab ₈₀ An ₂₀ , generally but weakly replaced by analcite) are in a fine grained and intersertal groundmass of plagioclase (about Ab ₈₀ An ₂₀), pyroxene, iron ore, analcite, microphenocrystic apatite and brown glass. Cristobalite, tridymite and zeolites are formed in drusy cavities.	

Sample No.	Location	Formation	Rock	Microscopic observations	Remarks
316	1-k	Puno	Sandstone	Fine fragments (up to 0.5mm in size) of augite, hornblende, plagioclase, quartz, iron ore, apatite and crushed pumice are in a fine grained and argillaceous matrix composed mainly of minute powders of same substances as above-mentioned fragments.	
317	1-k	Puno	Tuffaceous sandstone	Crystal fragments (up to 0.5mm in size) of biotite, hornblende, augite, plagioclase, hypersthene, iron ore and apatite, fragments of glass, pumice and lithic fragments of andesite are in a fine grained and essential matrix. Recrystallized cristobalite occurs in the matrix.	
328	2-h	Tacaza	Olivine-augite-hypersthene trachy andesite	Phenocrysts of olivine (euhedral, rimmed by vermicular magnetite and hypersthene, partly opacitized), augite (euhedral prismatic, up to 1 mm, distinctly zoned and occasionally showing hour glass structure), hypersthene (euhedral prismatic, up to 1 mm, with pleochroism of pale green to pale brown) and plagioclase (Ab30An70 or more basic, euhedral columnar, twinned after albite and Carlsbad law) are in a medium-grained and intersertal groundmass showing distinct flow structure and composed of lath-shaped plagioclase, augite, hypersthene and iron ore with subordinate anorthoclase, biotite and apatite.	See Table I-10
332	2-h	Sencca	Tuff breccia	Crystal fragments of quartz (rounded and corroded, up to 2mm) and a little plagioclase (entirely altered to clay minerals) are in a fine grained and argillaceous groundmass of minute silica minerals, clay minerals and dusty substances. Flow structure is marked.	
338	2-j	Puno	Sandstone	Fine fragments (under 0.5mm in size) of quartz, augite, hypersthene, hornblende, apatite and iron ore are in a argillaceous matrix which is sericitized and/or carbonatized.	
341	2-l	Tacaza	Altered olivine basalt	Phenocrysts of olivine (euhedral, up to 1 mm, entirely altered to chlorite and adularia, marginally replaced by magnetite) and plagioclase (euhedral, up to 1.5mm, twinned after albite and Carlsbad law, including minute olivine and/or magnetite, slightly altered to kaolinite) are in a medium grained, intersertal to intergranular and devitrified groundmass of lath-shaped plagioclase, pseudomorph olivine, zoned augite and apatite with subordinate anorthoclase and brown glass.	

Sample No.	Location	Formation	Rock	Microscopic observations	Remarks
342	2-1	Tacaza	Olivine-augite trachyandesite	Phenocrysts of olivine (altered to iddingsite), plagioclase (altered to chlorite or epidote) and partly chloritized augite are in a intersertal to intergranular groundmass of lath-shaped plagioclase, augite, olivine and iron ore with anorthoclase, apatite and weakly chloritized brown glass.	
344	3-h	Tacaza	Augite-olivine trachybasalt	Phenocrysts of augite (subhedral, up to 0.5mm, less abundant than olivine) olivine (subhedral tabular, up to 0.5mm, wholly altered to iddingsite) and plagioclase (subhedral, up to 0.5mm, distinctly zoned, a little in amount) are in a coarse grained, intergranular and per-crystalline groundmass of lath-shaped plagioclase (about Ab ₄₀ An ₆₀), olivine, augite and iron ore with subordinate anorthoclase, K-rich plagioclase, apatite and a little brown glass. Plagioclase laths are always mantled by thin film of anorthoclase.	See Table I-10
349	3-h	Intrusives	Cummingronite bearing biotite-hornblende-clinopyroxene diorite	The rock shows a medium-grained and hypidiomorphic texture. The main constituent minerals are plagioclase (subhedral, up to 4mm, occasionally showing weak zoning), clinopyroxene (subhedral, up to 5mm, with exsoluton lamellae, occasionally forming symplektite with iron ore), hornblende (isolated and anhedral crystals up to 0.8mm and columnar crystals with clinopyroxene core up to 2mm, with a pleochroism of Z=green, Y=yellowish green, X=pale green) and biotite (anhedral, with a pleochroism of Z=γ=reddish brown, X=pale brown). The minor constituent minerals are potash feldspar interstite, cummingronite, quartz, iron ore (magnetite and hematite), apatite and sphene. Cummingronite is anhedral and often occurs at the junction of clinopyroxene and hornblende. Subhedral crystals of apatite are remarkable.	See Table I-10 and I-18
350	3-h	Intrusives	Granodiorite	The rock shows a coarse-grained and hypidiomorphic texture, and consists of hornblende (subhedral to subhedral, commonly including minute magnetite and apatite, with a pleochroism of brownish green to dark green), plagioclase (subhedral to subhedral, distinctly zoned and about Ab ₅₀ An ₅₀ in crystal core, twinned after albite and Carlsbad law), potash feldspar (anhedral) and perthite (anhedral) with accessory iron ore and apatite.	

Sample No.	Location	Formation	Rock	Microscopic observations	Remarks
354	3-h	Intrusives	Biotite-hornblende porphyrite	The rock shows a porphyritic texture. The main constituent minerals are plagioclase (phenocrystic, about Ab ₅₀ An ₅₀ to Ab ₇₀ An ₃₀ , twinned after albite and Carlsbad law), potash feldspar (less abundant than plagioclase), hornblende and biotite. A little relics of augite are present. By the breakdown of hornblende, biotite is formed. Apatite and iron ore present as the accessory minerals.	See Table I-10
355	3-h	Intrusives	Hornblende-biotite granodiorite	Hornblende, biotite, potash feldspar, plagioclase and quartz are the main constituent minerals, and apatite and iron ore occur as the accessory minerals. The texture is hypidiomorphic but crystals of plagioclase are somewhat larger than those of other minerals. Plagioclase is marginally zoned and changes its composition from Ab ₆₀ An ₄₀ to Al ₉₀ An ₁₀ .	
358	3-h	Intrusives	Biotite bearing augite-hornblende diorite porphyrite	The rock shows a porphyritic texture. The main constituent minerals are plagioclase, augite, hornblende and biotite, and apatite and iron ore are present as the accessory minerals. Plagioclase is phenocrystic and distinctly zoned from andesite to oligoclase. Sericitization is fairly advanced and augite remains only as relict. Some of plagioclase are entirely replaced by epidote.	
363	3-i	Intrusives	Biotite monzonite	The rock shows hypidiomorphic texture and is mainly made up of biotite (euhedral but ragged by opacitization, with pleochroism of yellowish brown to brown), plagioclase (twinned after albite and Carlsbad law, distinctly zoned from Ab ₄₅ An ₅₅ to Ab ₈₀ An ₂₀) and potash feldspar with accessory apatite, sphene and iron ore.	
364	3-i	Descanso	Pumice-tuff	Fine fragments (up to 1 mm in size) of biotite, plagioclase, iron ore, apatite and altered minerals are in a argillaceous matrix.	
374	3-m	Pumo	Tuffaceous sandstone	Fragments (up to 1.5mm in size) of plagioclase, hornblende, biotite, iron ore, sphene and augite are in a fine-grained matrix composed of albitized plagioclase, dark dusty substances and crushed pumice.	

Sample No.	Location	Formation	Rock	Microscopic observations	Remarks
376	4-h	Intrusives	Clinopyroxene-cummingtonite bearing biotite-hornblende granodiorite	The rock shows a medium-grained and hypidiomorphic texture. The main constituent minerals are plagioclase (subhedral, up to 4mm, weakly zoned but rarely having the core of calcic plagioclase), quartz (anhedral, up to 2mm, with wavy extinction), potash feldspar (anhedral, up to 2mm, occurring as interstices), hornblende (subhedral, up to 2mm, including poikilocratically crynopyroxene and cummingtonite, with a pleochroism of green to pale greenish yellow) and biotite (anhedral to subhedral, with a pleochroism of dark brown to yellowish brown). The minor constituent minerals are cummingtonite, clinopyroxene, iron ore (magnetite and hematite), apatite, sphene, tourmaline, chlorite, epidote and zircon. Cummingtonite occurs at the junction of hornblende and clinopyroxene in hornblende crystals, and also is occasionally formed as sole inclusions without clinopyroxene.	See Table I-10
377	4-h	Seneca	Dacite	Phenocrysts of quartz (anhedral rounded, up to 5mm, including dark dusty substances and rarely muscovite) and albite (less abundant than quartz) are in a hyalopilitic groundmass with subordinate plagioclase, cristobalite and iron ore.	
389	4-x	Descanso	Dacitic tuff	Crystal fragments (up to 0.5mm in size) of quartz, sericitized biotite, plagioclase, apatite, hornblende and iron ore are in a argillaceous matrix partly showing perlitic texture.	
390	4-1	Ayahacas	Schistosed limestone	The rock is composed of calcite. Crystals of calcite are elongated and arranged with orientation. The rock seems to be affected by dynamical stress.	
394	4-m	Tacaza	Hypersthene bearing olivine-augite trachy andesite	Phenocrysts of olivine (euhedral, up to 0.5mm, entirely altered to chlorite), augite (euhedral, up to 1 mm, including magnetite, distinctly zoned), hypersthene (less abundant than augite, with pleochroism of colourless to pale green), hornblende (euhedral, up to 2mm, with pleochroism of pale greenish brown to greenish brown, zoned, thickly mantled by opacite), plagioclase (Al ₂₀ An ₇₀ to Ab ₄₀ An ₆₀ , euhedral, up to 1.5mm, twinned after albite and Carlsbad law, distinctly zoned) are in a intergranular to interseral groundmass of lath-shaped plagioclase (about Ab ₆₀ An ₄₀), augite and iron ore with subordinate anorthoclase, apatite and a little brown glass.	

Sample No.	Location	Formation	Rock	Microscopic observations	Remarks
400	5-m	Tacaza	Altered hypersthene-augite andesitic rock	Phenocrysts of augite (euhedral, up to 1 mm, including magnetite), hypersthene (euhedral to subhedral, up to 1 mm, with pleochroism of colourless to pale brown), plagioclase (about Ab70An30, subhedral, up to 1.5mm, intensely sericitized and/or albitized) and phenocrystic grains of magnetite (up to 2mm) are in a fine-grained and intersertal groundmass of lath-shaped plagioclase, pyroxene (wholly altered to sericite and carbonates), iron ore and microclites.	
406	5-m	Ayabaca	Dolomitic limestone	The rock is mainly composed of fine-grained and irregularly shaped dolomite and calcite.	
416	6-i	Intrusives	Hornblende granodiorite	The texture is hypidiomorphic and hornblende (with pale yellowish green to green, including magnetite, apatite and rare plagioclase), potash feldspar (orthoclase, partly sericitized), plagioclase (albite to acidic oligoclase, distinctly twinned after albite and Carlsbad law, partly sericitized) and microcline are the main constituent minerals. Iron ore, apatite and sphene are observed as the accessory minerals.	
418	6-i	Intrusives	Quartz monzonite porphyry	The texture is porphyritic. Phenocrysts of hornblende (euhedral, up to 2mm, with pleochroism of pale green to green, rimmed by colourless amphibole), plagioclase (generally euhedral, up to 5mm, twinned after albite and Carlsbad law, slightly altered to sericite or epidote), and potash feldspar (subhedral, up to 5mm, partly sericitized) are in a microgranitic groundmass of quartz, potash feldspar and plagioclase with accessory apatite and iron ore.	
420	6-i	Intrusives	Augite-hornblende granodiorite	The texture is hypidiomorphic and it is mainly composed of augite, green hornblende fairly sericitized, plagioclase (sericitized, oligoclase to andesine) and potash feldspar. Apatite and sphene occur as accessory minerals.	
422	6-j	Intrusives	Quartz monzonite porphyry	The rock is porphyritic and phenocrysts of pseudomorphic hornblende (entirely altered to chlorite and/or sericite), potash feldspar (euhedral to subhedral, up to 5mm, partly sericitized), plagioclase (euhedral, up to 5mm, albite to acidic oligoclase, partly sericitized) and quartz (anhedral rounded, up to 1 mm) are in a microgranitic groundmass of quartz, potash feldspar and plagioclase with accessory opaque minerals and apatite. Quartz veinlets fill the cracks.	

Sample No.	Location	Formation	Rock	Microscopic observations	Remarks
423	6-j	Intrusives	Monzonite porphyry	The rock shows a porphyritic texture. Phenocrysts of green hornblende (forming secondary biotite), potash feldspar (euhedral, up to 3mm), plagioclase (much less than orthoclase, euhedral up to 3mm) and a little quartz (anhedral, up to 2mm) are in a microgranitic groundmass of quartz, potash feldspar, plagioclase and iron ore with accessory apatite and sphene. Apatite and sphene are generally euhedral and occasionally occur as the microphenocryst. Quartz veinlets fill the fine cracks of the rock. Feldspars are slightly sericitized.	
425	6-j	Ferrobomba	Garnet skarn	The major constituent mineral is granular garnet and a little actinolitic green-hornblende, sericitic and opaque minerals are accompanied with garnet.	
430	6-j	Intrusives	Biotite monzonite porphyry	The rock shows porphyritic texture. Phenocrysts of biotite (euhedral, with pleochroism of pale yellowish brown to dark brown, partly opacitized and/or chloritized), potash feldspar and plagioclase (less abundant than potash feldspar, albite and a little oligoclase) are in a microgranitic groundmass of quartz, potash feldspar and plagioclase with subordinate and microphenocrystic apatite. Feldspars are affected by albitization. Pyrite and chalcopyrite are disseminated.	
431	6-j	Intrusives	Biotite-hornblende granodiorite	The texture is hypidiomorphic. It consists of hornblende (rather ragged, forming secondary biotite due to break down, with pleochroism of pale green to green), biotite (with pleochroism of greenish brown to dark brown), potash feldspar and plagioclase (zoned and albitized, acidic oligoclase to albite) with accessory apatite, sphene and iron ore.	
436	6-m	Tacaza	Lapilli tuff	Crystal fragments (up to 0.5mm) of quartz, plagioclase, opaque minerals and mafic minerals (almost altered to chlorite and/or sericitic) and lithic fragments (up to 3mm, andesite and rhyolite) are cemented by argillaceous matrix.	

Sample No.	Location	Formation	Rock	Microscopic observations	Remarks
438	7-h	Tacaza	Olivine bearing biotite dacite	Phenocrysts of biotite (euhedral columnar, up to 1.5mm, thickly surrounded by opacite), plagioclase (euhedral columnar, up to 3mm, distinctly zoned, twinned after albite and Carlsbad law) and a little olivine (subhedral, up to 0.3mm, rimmed by opacite) are in a fine-grained and intersertal groundmass of lath-shaped and albitized plagioclase, cristobalite, microcline, iron ore and brown glass. Phenocrysts of plagioclase have many inclusions such as apatite and dark drusy substances. Clay minerals and adularia are often formed in drusy cavities. The alteration is advanced.	
441	7-h	Tacaza	Olivine trachybasalt	Phenocrysts of olivine (euhedral tabular or elongated parallel to c-crystallographic axis, up to 4mm, often ragged by magmatic corrosion and commonly including octahedral magnetite) are in a medium-grained, intergranular and percrystalline groundmass of lath-shaped plagioclase, olivine, augite, hypersthene and iron ore with subordinate anorthoclase and apatite. Large xenocryst of plagioclase (up to 4mm in size), surrounded by minute grains of augite, is recognized. The rock may be mugearite. The composition of plagioclase of the groundmass is about Ab ₆₀ An ₄₀ .	
442	7-h	Tacaza	Olivine trachybasalt	Phenocrysts of olivine (euhedral, up to 1 mm, almost wholly altered to iddingsite) are in a coarse-grained and intergranular groundmass of lath-shaped plagioclase (about Ab ₄₀ An ₆₀), olivine (almost altered to iddingsite), augite and anorthoclase with subordinate iron ore, apatite and little brown glass. The reaction between olivine and augite is not recognized. Adularia is formed in the drusy cavities.	See Table I-10
443	7-h	Sencca	Biotite dacite	Phenocrysts of biotite (euhedral prismatic, up to 1 mm, with pleocrism of pale brown to dark brown) and plagioclase (euhedral, up to 0.7mm, Ab ₅₅ An ₄₅ to Ab ₆₅ An ₃₅) are in a fine-grained and hyaloplitic groundmass of plagioclase (about Ab ₇₀ An ₃₀), brown glass, cristobalite, iron ore and microcline. Cristobalite also occur in drusy cavities.	

Sample No.	Location	Formation	Rock	Microscopic observations	Remarks
446	7-i	Tacaza	Olivine-augite (alkali) basalt	Phenocrysts of olivine (euhedral tabular or elongated parallel to c-crystallographic axis, up to 4mm, slightly altered to chlorite), augite (euhedral prismatic, up to 0.7mm, distinctly zoned and occasionally showing hour-glass structure) and plagioclase (not abundant, euhedral, zoned, twinned after albite and Carlsbad law) are in a medium-grained, intergranular and holocrystalline groundmass of lath-shaped plagioclase (Ab ₄₀ An ₆₀), augite, olivine and iron ore with subordinate anorthoclase. K-rich plagioclase, apatite and biotite.	See Table I-10
448	7-i	Tacaza	Olivine-analcite (alkali) basalt	Phenocrysts of pseudomorphic olivine (entirely altered to carbonates and opacite but remaining euhedral crystal form), plagioclase (euhedral, up to 6mm, about Ab ₄₀ An ₆₀) and granular analcite are in a almost holocrystalline and intergranular groundmass of lath-shaped plagioclase (about Ab ₆₀ An ₄₀), carbonates after olivine, intensely carbonatized augite and iron ore with subordinate anorthoclase, K-rich plagioclase and brown glass. Analcite and other zeolites occur in drusy cavities.	
452	7-j	Intrusives	Granite porphyry	The rock shows porphyritic texture, and phenocrysts of potash feldspar (euhedral, up to 2mm, sericitized), plagioclase (euhedral, up to 2mm, sericitized) are in a microgranitic matrix composed of potash feldspar, (altered to clay minerals), quartz, plagioclase (albitized and also altered to clay minerals) and iron ore. Apatite and iron ore occur as accessory minerals of phenocrysts. Mafic minerals are not recognized in the observed section.	
453-(1)	7-j	Intrusives	Quartz monzonite porphyry	Abundant phenocrysts of potash feldspar and a little phenocrysts of plagioclase and quartz are in a microgranitic groundmass of potash feldspar, plagioclase, quartz and iron ore with accessory apatite and sphene. Phenocrysts of feldspar are euhedral columnar and up to 3mm in size, and are altered partly to sericite and/or carbonates. Phenocrysts of quartz are generally rounded.	
453-(2)	7-j	Intrusives	Porphyritic monzonite	The rock shows a porphyritic texture. Phenocrysts of potash feldspar (columnar, up to 5mm), plagioclase (columnar, up to 5mm, distinctly zoned, twinned albite and Carlsbad law characterized especially by polysynthetic twinning) and biotite (subbedal columnar, up to 0.5mm) are in a fine-grained and microgranitic groundmass of plagioclase, iron ore and apatite.	

Sample No.	Location	Formation	Rock	Microscopic observations	Remarks
453-(3)	7-j	Intrusives	Quartz monzonite porphyry	The rock shows a porphyritic texture. Phenocrysts of biotite (columnar to prismatic, up to 0.5mm), potash feldspar (euhedral columnar, up to 2mm), plagioclase (subhedral, up to 2mm, distinctly zoned) and anhedral quartz are in a microgranitic groundmass of potash feldspar, quartz, plagioclase and opaque minerals with accessory apatite. Feldspar are intensively altered to sericite and/or carbonates, and the groundmass also slightly carbonatized.	
453-(4)	7-j	Intrusives	Monzonite porphyry	Phenocrystic crystals of potash feldspar and a little plagioclase are in a microgranular groundmass of potash feldspar, quartz, plagioclase and opaque minerals with accessory sphene and apatite. The alteration is rather advanced; feldspars are sericitized and/or carbonatized, and secondary carbonates fill the cracks.	
453-(5)	7-j	Intrusives	Quartz monzonite porphyry	The rock shows a porphyritic texture. Phenocrysts of potash feldspar, plagioclase (much less than potash feldspar) and a little quartz are in a microgranitic groundmass of potash feldspar, quartz, plagioclase and opaque minerals with accessory apatite. Feldspars are strongly altered to sericite and/or carbonates. Opaque minerals are often present as the phenocrysts.	
453-(6)	7-j	Intrusives	Altered porphyritic monzonite	Phenocrysts of feldspars (wholly altered to sericite and carbonates) hornblende (with opacite margin, perfectly altered to sericite and carbonates) and biotite (perfectly altered to sericite and opacite) are in a microgranitic and altered groundmass.	See Table I-10 and I-18
453-(7)	7-j	Intrusives	Porphyritic monzonite	Phenocrysts of potash feldspar (weakly altered to carbonate), plagioclase (rarely altered to carbonate), biotite (fairly altered to chlorite) and hornblende (perfectly altered to carbonate and marginally opacitized) are in a microgranitic groundmass of plagioclase, potash feldspar, quartz and opaque minerals.	See Table I-10 and I-18
455	7-k	Intrusives	Biotite-olivine-cummingtonite bearing hornblende gabbro	The rock shows a medium-grained, and hypidiomorphic texture. The main constituent minerals are plagioclase (subhedral, up to 3mm but usually 1.5 mm, zoned especially in the comparatively large crystals), hornblende (subhedral columnar, poikilitically including fine crystals of olivine, clinopyroxene and cummingtonite, with a pleochroism of Z=brown, Y=yellowish brown, X=pale brown) and clinopyroxene (anhedral, always occurring as an inclusion of hornblende). The minor or accessory minerals are cummingtonite, olivine, biotite, sphene, apatite, iron ore (magnetite and hematite) and chlorite.	See Table I-10 and I-18

Sample No.	Location	Formation	Rock	Microscopic observations	Remarks
459	7-k	Intrusives	Hornblende-biotite monzonite porphyry	The rock is somewhat porphyritic. Phenocrysts of potash feldspar (euhedral, up to 4mm), plagioclase (less abundant than potash feldspar, euhedral, up to 4mm), brown biotite (columnar, up to 1 mm.) and green hornblende (subhedral ragged, up to 1 mm) are in a micro-granitic groundmass of quartz, potash feldspar, plagioclase and iron ore with accessory apatite and sphene.	
461	7-k	Intrusives	Biotite granodiorite	The rock is composed of plagioclase (basic oligoclase), potash feldspar, interstitial quartz, biotite and a little hornblende with accessory apatite and opaque minerals.	
464	7-n	Puro	Rhyolite	Phenocrysts are quartz and plagioclase. Groundmass is composed of feldspar spherulites.	
466	7-n	Puro	Tuffaceous sandstone	The rock is made up of crystal fragments (up to 0.3 mm in size) of quartz, biotite, carbonate, sericite, chlorite, hornblende and opaque minerals. Hornblende and some of feldspar show euhedral crystal form but the others are rounded.	
468	7-k	Intrusives	Biotite-hornblende porphyritic monzonite	The rock shows a porphyritic texture. Phenocrysts of green hornblende (subhedral prismatic, up to 3mm, including magnetite), potash feldspar (euhedral columnar, up to 3mm), plagioclase (oligoclase, euhedral columnar, up to 3mm) and quartz (a little in amount, anhedral, 1 mm) are in a microgranitic groundmass of quartz, potash feldspar, plagioclase, biotite (formed due to the breakdown of hornblende) and opaque minerals with accessory apatite and sphene. Some crystals of apatite and sphene are microphenocrystic.	
469-(1)	7-i	Intrusives	Biotite-hornblende monzonite porphyry	The texture is porphyritic. Phenocrysts of potash feldspar, plagioclase, biotite and hornblende are in a microgranitic groundmass of quartz, plagioclase and potash feldspar with accessory apatite and opaque minerals. Plagioclase and hornblende are fairly altered to sericite and/or epidote. A little secondary biotite are formed due to the breakdown of hornblende.	
469-(2)	7-i	Intrusives	Hornblende-biotite quartz monzonite porphyry	The texture is porphyritic. Phenocrysts of potash feldspar, green hornblende, green biotite, plagioclase and quartz are in a micro-granitic groundmass composed mainly of plagioclase, potash feldspar and quartz. Feldspars are rather strongly altered to sericite and/or epidote, and mafic minerals are also altered to chlorite and epidote. Microphenocrystic opaque minerals and apatite are present.	

Table I-9 Microphotographs

Thin section

	Sample No.	Rock name	Location
(1)	1	Granodiorite	1-a
(2)	9	Quartz diorite	1-b
(3)	27	Trachyte	1-d
(4)	40	Dacite	1-g
(5)	43	Dacite	2-a
(6)	49	Limestone	2-b
(7)	58	Basalt	2-d
(8)	79	Trachyte	2-e
(9)	142	Rhyolite	5-a
(10)	275	Andesite	7-e
(11)	280	Massive tuff	7-g
(12)	316	Sandstone	1-k
(13)	349	Granodiorite	3-h
(14)	350	Monzonite	3-h
(15)	376	Granodiorite	4-h
(16)	394	Andesite	4-m
(17)	430	Granite porphyry	6-j
(18)	442	Basalt	7-h
(19)	453	Monzonite	7-j
(20)	455	Gabbro	7-k

Polished section

(21)	20	Sandstone	1-d
(22)	361	Magnetite ore	3-h
(23)	361	Magnetite ore	3-h
(24)	430	Granite porphyry	6-j
(25)	453	Monzonite	7-j
(26)	469	Garnet skarn	7-i

(1)



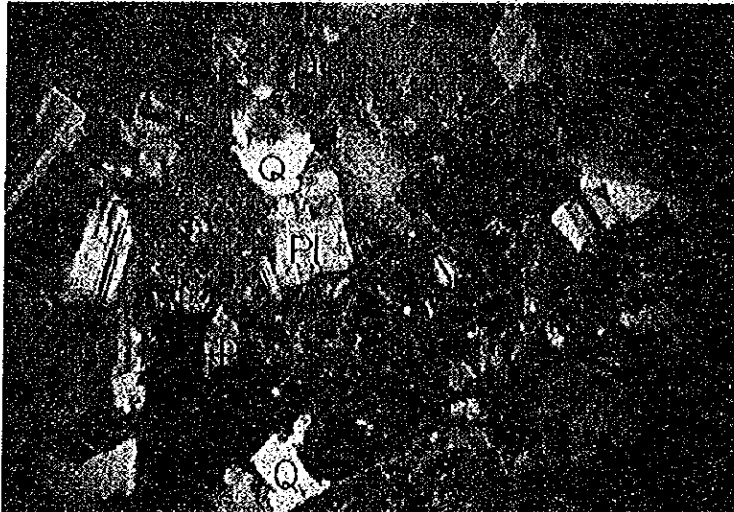
Sample No. 1.
Granodiorite
Location 1-a

Pl : plagioclase
Bi : biotite
Q : quartz

Scale 0 0.5 mm

Crossed nicols

(2)



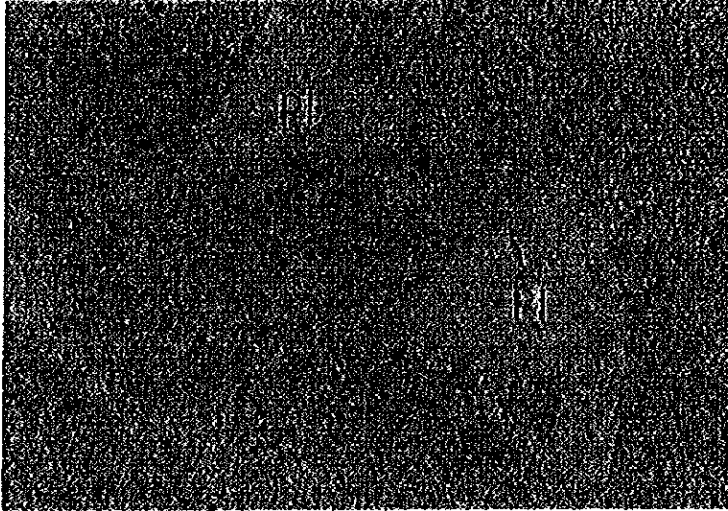
Sample No. 9.
Quartz diorite
Location 1-b

Hb : hornblende
Bi : biotite
Ep : epidote
Pl : plagioclase
Q : quartz

Scale 0 1 mm

Crossed nicols

(3)



Sample No. 27.

Trachyte

Location 1-d

Pl : plagioclase

Scale 0 0.5 mm

Open nicol

(4)



Sample No. 40.

Dacite

Location 1-g

Pl : plagioclase

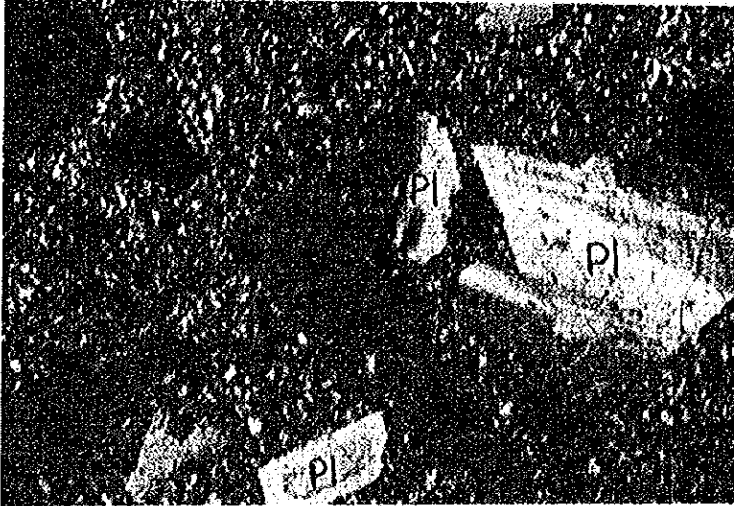
Bi : biotite

Mt : magnetite

Scale 0 1 mm

Crossed nicols

(5)




Sample No. 43.

Dacite

Location 2-a

Pl : plagioclase

Bi : biotite

Scale 0  0.5 mm

Crossed nicols

(6)



Sample No. 49.

Limestone

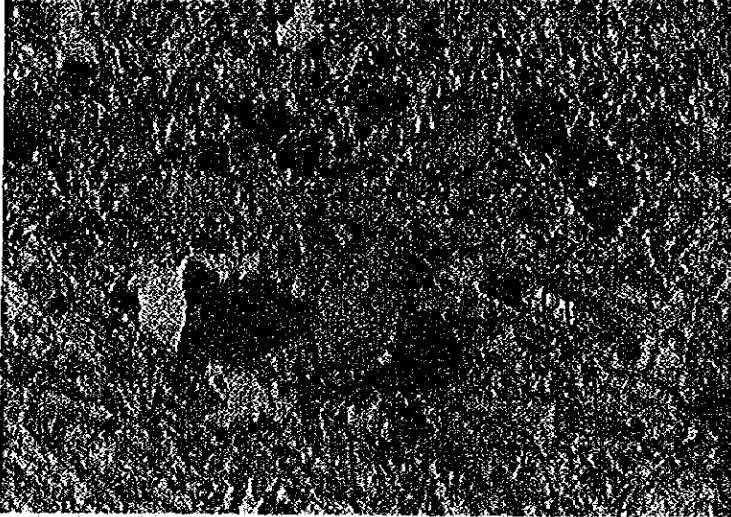
Location 2-b

Ca : calcite

Scale 0  0.5 mm

Crossed nicols

(7)



Sample No. 58.

Basalt

Location 2-d

Ol : olivine

Cp : clinopyroxene

Pl : plagioclase

Scale 0 0.5 mm

Open nicol

(8)



Sample No. 79.

Trachyte

Location 2-e

Cp : clinopyroxene

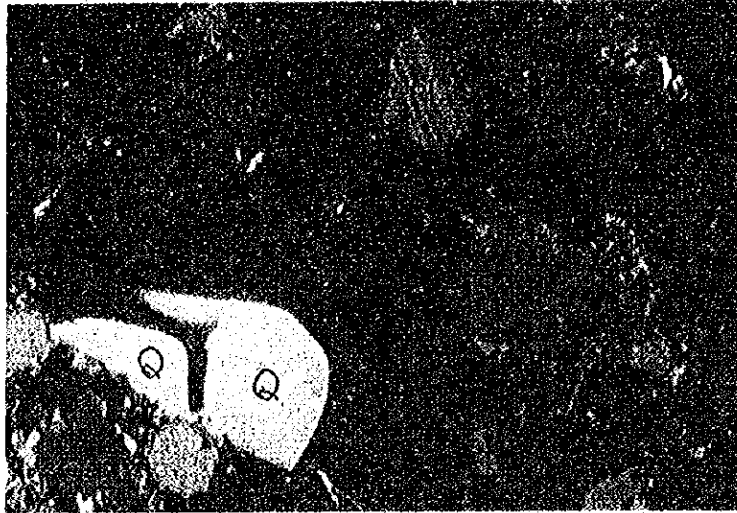
Bi : biotite

Pl : plagioclase

Scale 0 1 mm

Crossed nicols

(9)



Sample No. 142.
Rhyolite
Location 5-a

Bi : biotite
Pl : plagioclase
Q : quartz

Scale 0 _____ 0.5 mm

Crossed nicols

(10)



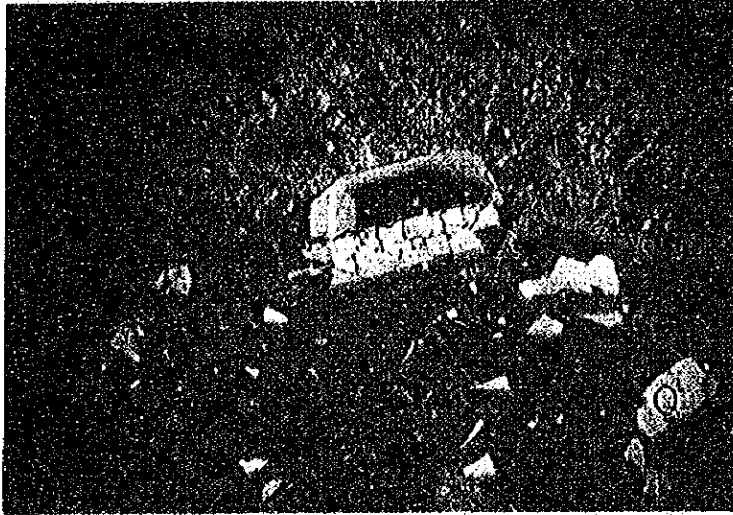
Sample No. 275.
Andesite
Location 7-a

Hb : hornblende
Pl : plagioclase

Scale 0 _____ 0.5 mm

Crossed nicols

(11)



Sample No. 280.

Massive tuff

Location 7-g

Pl : plagioclase

Bi : biotite

Q : quartz

Scale 0 1 mm

Crossed nicols

(12)



Sample No. 316.

Sandstone

Location 1-k

Pl : plagioclase

Bi : biotite

Q : quartz

Scale 0 0.5 mm

Crossed nicols

(13)



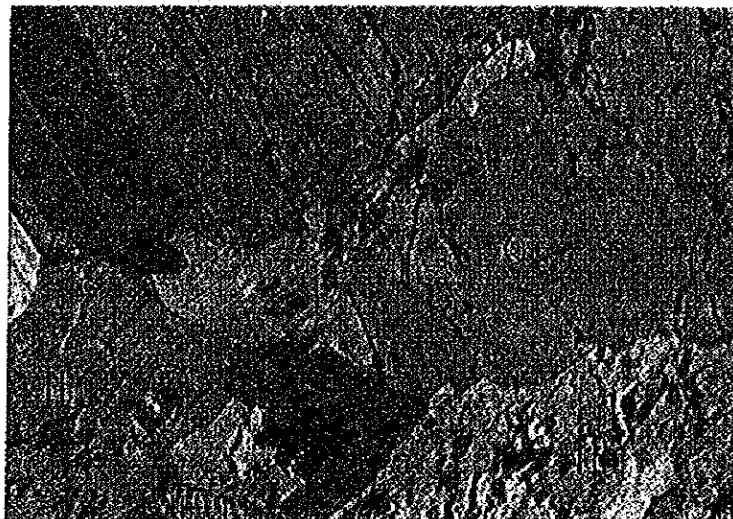
Sample No. 349.
Granodiorite
Location 3-h

Cp : clinopyroxene
Hb : hornblende
Bi : biotite
Pl : plagioclase
Q : quartz
Mt : magnetite

Scale 0 1 mm

Crossed nicols

(14)



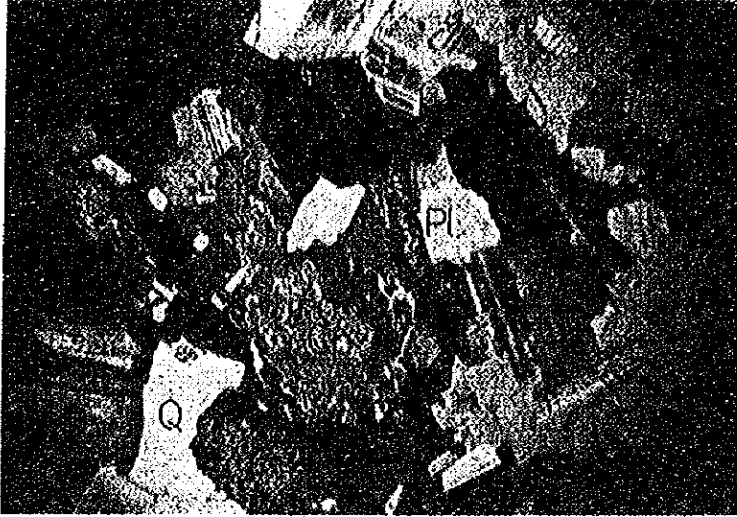
Sample No. 350.
Monzonite
Location 3-h

Hb : hornblende
Pl : plagioclase
Q : quartz

Scale 0 0.5 mm

Crossed nicols

(15)



Sample No. 376.

Granodiorite

Location 4-h

Hb : hornblende
Cp : clinopyroxene
Ct : cummingtonite
Bi : biotite
Pl : plagioclase
Q : quartz

Scale 0 1 mm

Crossed nicols

(16)



Sample No. 394.

Andesite

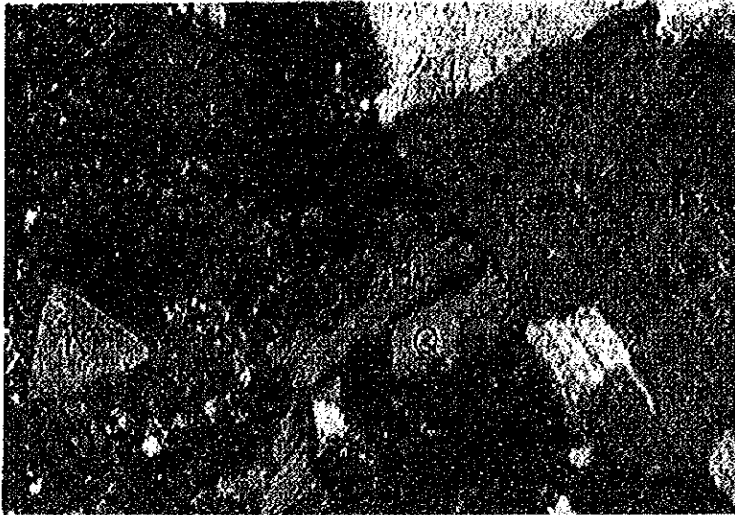
Location 4-m

Hb : hornblende
Pl : plagioclase

Scale 0 0.5 mm

Crossed nicols

(17)



Sample No. 430.
Granite porphyry
Location 6-j

K : K-feldspar
Bi : biotite
Q : quartz

Scale 0 _____ 0.5 mm

Crossed nicols

(18)



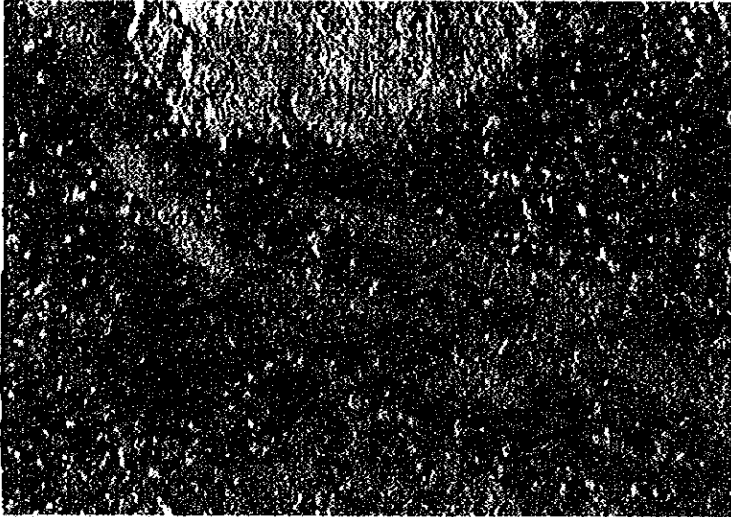
Sample No. 442.
Basalt
Location 7-h

Z : zeolite
Ol : olivine
Pl : plagioclase

Scale 0 _____ 0.5 mm

Crossed nicols

(19)



Sample No. 453.

Monzonite

Location 7-j

Wm : white mica

Pl : plagioclase

Ca : calcite

Scale 0 0.5 mm

Crossed nicols

(20)



Sample No. 455.

Gabbro

Location 7-k

Hb : hornblende

Cp : clinopyroxene

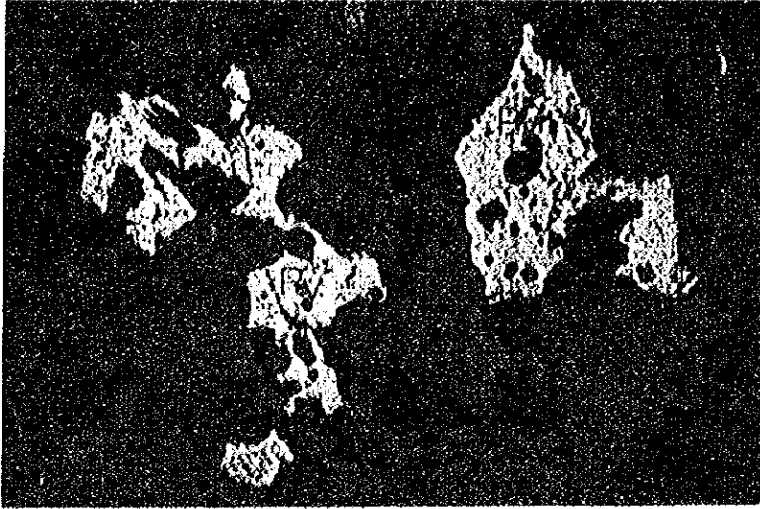
Ct : cummingtonite

Pl : plagioclase

Scale 0 1 mm

Crossed nicols

(21)



Sample No. : 20.

Disseminated pyrite
Country rock : Sandstone
Location : 1-d

Py : pyrite

Scale 0 0.5 mm

Open nicol

(22)



Sample No. : 361.

Pyrite chalcopyrite
bearing magnetite ore
Location : 3-h

Cop : chalcopyrite

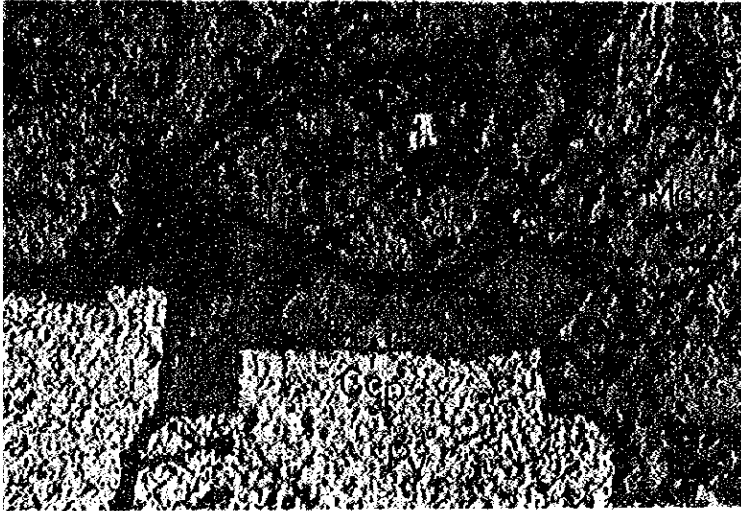
Py : pyrite

Mg : magnetite

Scale 0 0.5 mm

Open nicol

23)



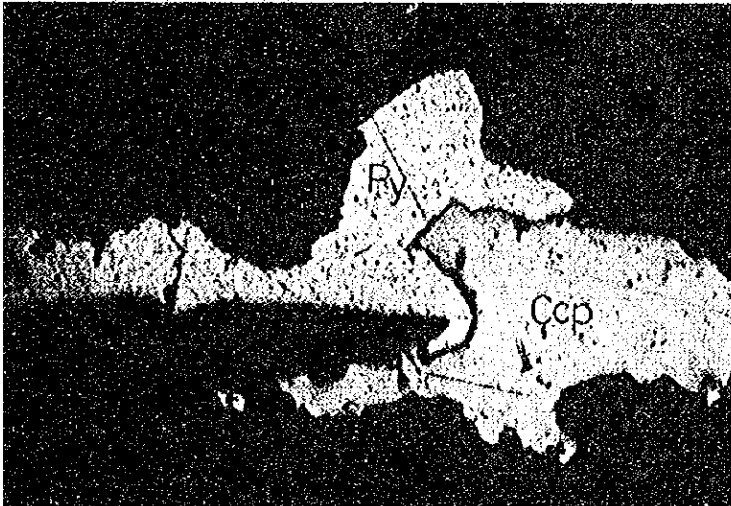
Sample No. : 361.
Pyrite chalcopyrite
bearing magnetite ore
Location : 3-h

Py : pyrite
Ccp : chalcopyrite
Cov : covellite
Mg : magnetite

Scale 0 0.2 mm

Open nicol

24)



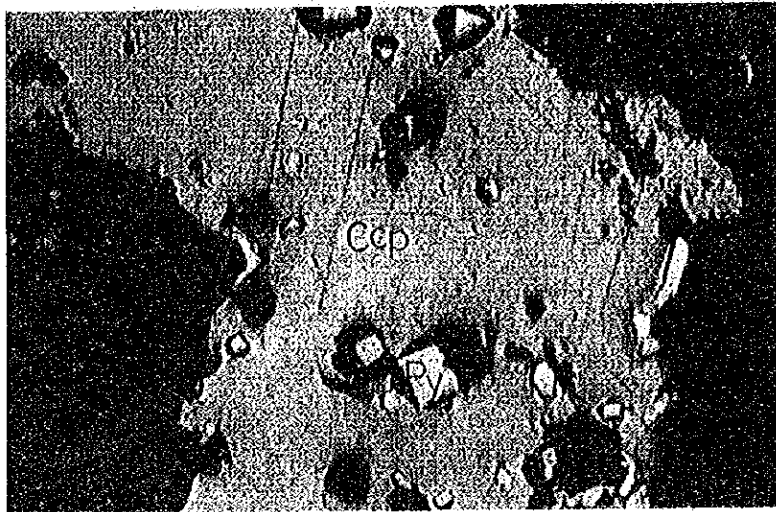
Sample No. : 430.
Disseminated pyrite and
chalcopyrite
Country rock : Granite
porphyry
Location : 6-j

Py : pyrite
Ccp : chalcopyrite

Scale 0 0.5 mm

Open nicol

(25)



Sample No. : 453.

Disseminated copper ore

Country rock : Monzonite

Location : 7-j

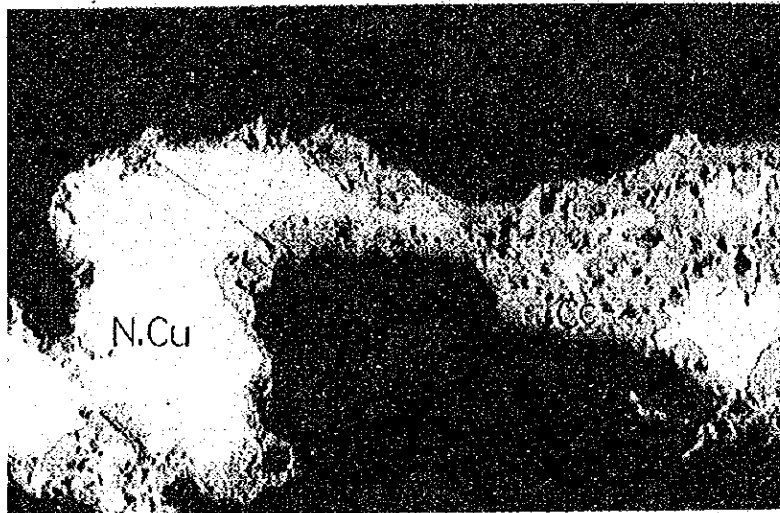
Ccp : chalcopyrite

Py : pyrite

Scale 0 0.2 mm

Open nicol

(26)



Sample No. : 469.

Secondary enrichment ore

Country rock : Garnet skarn

Location : 7-i

N.Cu : Native copper

Cc : chalcocite

Scale 0 0.2 mm

Open nicol

Table I-10 Chemical Analysis of Rocks

No.	142	280	21	453-(7)	246	40	25
Rock Name	Rhyolite	Massive tuff	Trachyte	Porphyritic monzonite	Porphyritic trachyte	Trachyte	Trachyte
Locality	5-a	7-g	1-d	7-j	7-b	1-g	1-d
SiO ₂	78.06	68.96	67.02	65.12	64.90	64.81	64.74
TiO ₂	0.21	0.40	0.64	0.17	0.72	0.88	0.73
Al ₂ O ₃	12.49	16.02	16.76	18.16	16.82	16.36	16.24
Fe ₂ O ₃	0.77	2.01	2.59	0.43	3.10	2.17	2.91
FeO	0.09	0.25	0.37	0.77	0.49	0.65	0.43
MnO	0.06	0.07	0.03	0.04	0.04	0.02	0.06
MgO	0.08	0.40	0.36	0.36	0.40	0.72	0.82
CaO	0.18	2.01	1.16	2.56	2.90	2.06	2.04
Na ₂ O	3.03	4.12	5.84	5.82	4.38	3.49	5.62
K ₂ O	3.79	4.84	4.62	2.83	3.83	4.20	4.24
P ₂ O ₅	0.01	0.08	0.07	2.16	0.27	0.29	0.19
H ₂ O (+)	0.92	0.97	0.54	1.03	1.78	3.19	0.89
H ₂ O (-)	0.41	0.08	0.50	0.22	0.53	0.74	0.39
Total	100.10	100.21	100.50	99.67	100.16	99.58	99.30
MgO	1.0	3.5	2.7	3.5	3.4	6.5	6.0
FeO	10.2	18.0	20.0	11.4	27.6	23.6	22.2
(Na,K) ₂ O	88.8	78.5	77.3	85.1	69.0	69.9	71.8
Q	45.60	22.32	12.66	14.58	18.66	23.88	11.16
C	3.16	0.82	0.31	1.43	0.92	3.16	
or	22.24	28.36	27.24	16.68	22.80	25.02	25.02
ab	25.68	34.58	49.26	49.27	37.20	29.34	47.68
an	0.56	8.90	5.00	11.12	12.23	7.78	6.39
fc							
ne							
Sal. total	(97.24)	(94.98)	(94.47)	(93.08)	(91.81)	(89.18)	(90.25)
ac							
wo							
en	0.20	1.00	0.90	0.90	1.00	1.80	0.93
fs				0.92			2.10
fo							
fa							
mt				0.70			
hm	0.80	2.08	2.56		3.04	2.24	2.88
il	0.30	0.61	0.76	0.30	1.22	1.37	1.06
ap		0.34		0.67	0.67	0.67	0.34
tl	0.20	0.20	0.59		0.20	0.39	0.39
Fem. total	(1.50)	(4.23)	(4.81)	(3.49)	(6.13)	(6.47)	(7.70)
Or	45.9	39.5	33.4	21.6	31.6	40.3	31.6
Ab	53.0	48.1	60.5	63.9	51.5	47.2	60.3
An	1.1	12.4	6.1	14.5	16.9	12.5	8.1
D. I.	93.52	85.26	89.16	80.53	78.66	78.24	83.86

No.	302	453-(6)	101	62	69	395	289
Rock Name	Porphyritic	Monzonite	Trachy-	Trachy-	Trachyte	Sandy tuff	Trachyte
Locality	1-h	7-j	3-c	2-d	2-d	5-1	1-h
SiO ₂	63.82	62.23	62.16	62.14	61.91	61.81	61.74
TiO ₂	0.96	0.56	1.24	0.79	0.97	0.17	1.01
Al ₂ O ₃	14.96	17.72	15.64	16.68	15.55	14.84	16.76
Fe ₂ O ₃	5.56	0.98	6.06	3.90	4.64	1.31	3.76
FeO	0.16	0.85	0.22	0.67	0.56	0.10	0.26
MnO	0.03	0.08	0.03	0.04	0.05	0.04	0.03
MgO	1.00	0.49	0.30	2.15	1.87	0.21	0.38
CaO	2.49	2.71	3.10	3.57	4.58	0.90	4.04
Na ₂ O	3.78	2.94	5.16	5.61	5.58	3.28	5.71
K ₂ O	3.89	5.38	3.27	3.30	3.42	6.15	3.96
P ₂ O ₅	0.20	3.79	0.09	0.13	0.18	0.01	0.10
H ₂ O (+)	1.90	1.74	1.19	0.92	0.80	3.26	0.98
H ₂ O (-)	0.55	0.13	0.77	0.68	0.06	8.05	0.51
Total	99.30	99.60	99.23	100.58	100.17	100.13	99.24
MgO	7.2	4.7	2.1	14.1	12.0	1.9	2.8
FeO	37.3	16.4	39.4	27.4	30.4	11.7	26.6
(Na,K) ₂ O	55.5	78.9	58.5	58.5	57.6	86.4	70.6
Q	21.30	18.66	13.98	7.92	7.44	17.10	6.96
C	1.43	2.55				1.12	
or	22.80	31.69	19.46	19.46	20.02	36.14	23.35
ab	31.96	24.63	43.49	47.16	47.16	27.77	48.21
an	8.62	12.51	9.73	10.84	7.23	4.45	8.34
lc							
ne							
Sal. total	(86.11)	(90.04)	(86.66)	(85.38)	(81.85)	(86.58)	(86.86)
ac			0.46	2.55	5.80		3.48
wo			0.80	5.40	4.70	0.50	1.00
en	2.50	1.20					
fs							
fo							
fa							
mt		1.32					
hm	5.60		6.08	3.84	4.64	1.28	3.84
il	0.30	1.06	0.46	1.52	1.37	0.30	0.61
ap	0.34	0.34	0.34	0.34	0.34	0.34	0.34
tl	1.96		2.55		0.59		1.76
Rem. total	(10.70)	(3.92)	(10.69)	(13.65)	(17.44)	(2.08)	(11.03)
Or	36.0	46.0	26.8	25.1	26.9	52.9	29.2
Ab	50.4	35.8	59.8	60.9	63.4	40.6	60.3
An	13.6	18.2	13.4	14.0	9.7	6.5	10.5
D. I.	76.06	74.98	76.93	74.54	74.62	81.01	78.52

No. Rock Name Locality	125 Trachy andesite 4-d	61 Porphyritic trachyte 2-d	83 Trachyte 2-e	79 Trachyte 2-e	148 Trachy andesite 5-b	7 Granodiorite 1-b	243 Trachy andesite 7-b
SiO ₂	61.28	61.17	61.03	60.97	60.78	60.76	60.34
TiO ₂	1.15	1.22	1.18	1.04	1.13	1.11	0.77
Al ₂ O ₃	14.53	14.93	16.07	16.42	15.50	14.50	17.93
Fe ₂ O ₃	7.87	5.62	5.11	2.84	5.95	2.32	6.07
FeO	0.25	0.46	1.03	2.05	0.57	2.56	0.05
MnO	0.08	0.06	0.06	0.10	0.08	0.07	0.65
MgO	0.75	2.13	1.52	2.61	1.63	1.43	0.49
CaO	5.38	2.95	3.74	4.13	4.57	7.84	4.20
Na ₂ O	4.20	4.05	4.63	4.18	4.76	5.01	4.67
K ₂ O	2.19	3.05	3.44	4.36	2.92	3.22	3.03
P ₂ O ₅	0.55	0.08	0.44	0.35	0.19	0.54	0.20
H ₂ O (+)	1.01	2.89	1.26	0.79	1.17	0.72	1.48
H ₂ O (-)	0.33	0.52	0.32	0.42	0.19	0.36	0.30
Total	99.57	99.13	99.83	100.26	99.44	100.44	100.18
MgO	5.2	14.5	10.0	16.6	10.7	10.0	3.6
FeO	50.7	37.4	37.0	29.2	38.9	32.5	40.2
(Na,K) ₂ O	44.1	48.1	53.0	54.2	50.4	57.5	56.2
Q	19.32	17.58	12.24	9.48	12.06	7.50	12.66
C		0.71					
or	12.79	17.79	20.57	25.58	17.24	18.90	17.79
ab	35.63	34.06	39.30	35.11	40.35	42.44	39.30
an	14.18	11.68	12.79	13.34	12.23	7.51	19.18
lc							
ne							
Sal. total	(81.92)	(81.82)	(84.90)	(83.51)	(81.88)	(76.35)	(88.93)
ac							
wo	2.55		1.28	2.24	3.48	11.60	0.35
en	1.90	5.30	3.80	6.50	4.10	3.60	1.20
fs						1.06	
fo							
fa							
mt				3.71		3.48	
hm	7.84	5.60	5.12	0.32	5.92		6.08
il	0.61	1.06	2.28	1.98	1.37	2.13	1.52
ap	1.34	0.34	1.01	0.67	0.34	1.34	0.34
ti	1.96	1.57			0.98		
Fem. total	(16.20)	(13.87)	(13.49)	(15.42)	(16.19)	(23.21)	(9.49)
Or	20.4	28.0	28.3	34.6	24.7	27.5	23.3
Ab	56.9	53.6	54.1	47.4	57.8	61.6	51.5
An	22.7	18.4	17.6	18.0	17.5	10.9	25.2
D. I.	67.74	69.43	72.11	70.17	69.65	68.84	69.75

No.	22	376	19	51	87	9	203
Rock Name	Trachyte	Granodiorite	Quartz diorite	Trachy andesite	Porphyritic trachyte	Quartz diorite	Trachy andesite
Locality	1-d	4-h	1-d	2-b	2-g	1-b	6-b
SiO ₂	59.97	59.87	59.48	59.28	59.08	58.46	58.40
TiO ₂	1.02	0.86	0.81	0.99	0.94	0.63	0.96
Al ₂ O ₃	14.58	16.25	16.02	17.83	17.43	17.81	16.32
Fe ₂ O ₃	7.02	2.35	4.14	6.16	5.06	2.56	6.63
FeO	0.52	4.63	3.43	0.29	1.20	4.30	0.65
MnO	0.10	0.13	0.16	0.03	0.06	0.14	0.05
MgO	1.31	2.74	2.44	0.50	1.19	2.73	0.78
CaO	3.55	5.74	7.48	1.56	3.26	5.95	6.06
Na ₂ O	5.86	3.64	3.99	4.91	4.06	3.32	4.53
K ₂ O	3.58	2.26	1.31	4.66	3.71	1.73	2.72
P ₂ O ₅	0.42	0.11	0.14	0.15	0.21	0.21	0.28
H ₂ O (+)	0.82	1.55	0.44	2.02	1.47	1.29	1.51
H ₂ O (-)	1.24	0.02	0.13	0.80	1.93	0.39	0.41
Total	99.99	100.15	99.97	99.18	99.60	99.52	99.30
MgO	7.4	17.8	16.4	3.1	8.1	19.0	5.3
FeO	38.9	43.9	48.0	36.7	39.1	45.9	45.2
(Na,K) ₂ O	53.7	38.3	35.6	60.2	52.8	35.1	49.5
Q	6.36	12.90	14.28	9.54	13.26	13.80	10.92
C				2.96	1.22		
or	21.13	13.34	7.78	27.80	21.68	10.01	16.12
ab	49.78	30.92	33.54	41.40	34.06	28.30	38.25
an	2.78	21.13	21.96	4.73	15.29	28.63	16.12
le							
ne							
Sal. total	(80.05)	(78.29)	(77.56)	(86.43)	(85.51)	(80.74)	(81.41)
ac							
wo	4.41	2.74	6.03				4.76
en	3.30	6.90	6.10	1.30	3.00	6.80	2.00
fs		5.28	1.85			5.02	
fo							
fa							
mt		3.48	6.03		1.39	3.71	
lm	7.04			6.24	4.16		6.56
ll	1.22	1.67	1.52	0.61	1.82	1.23	1.52
ap	1.01	0.34	0.34	0.34	0.34	0.34	0.67
ti	0.98			1.57			0.39
Fem. total	(17.96)	(20.41)	(21.87)	(10.06)	(10.71)	(17.10)	(15.90)
Or	28.7	20.4	12.3	37.6	30.5	15.0	22.9
Ab	67.5	47.3	53.0	56.0	48.0	42.3	54.3
An	3.8	32.3	34.7	6.4	21.5	42.7	22.8
D. l.	77.27	57.16	55.60	78.74	69.00	52.11	65.29

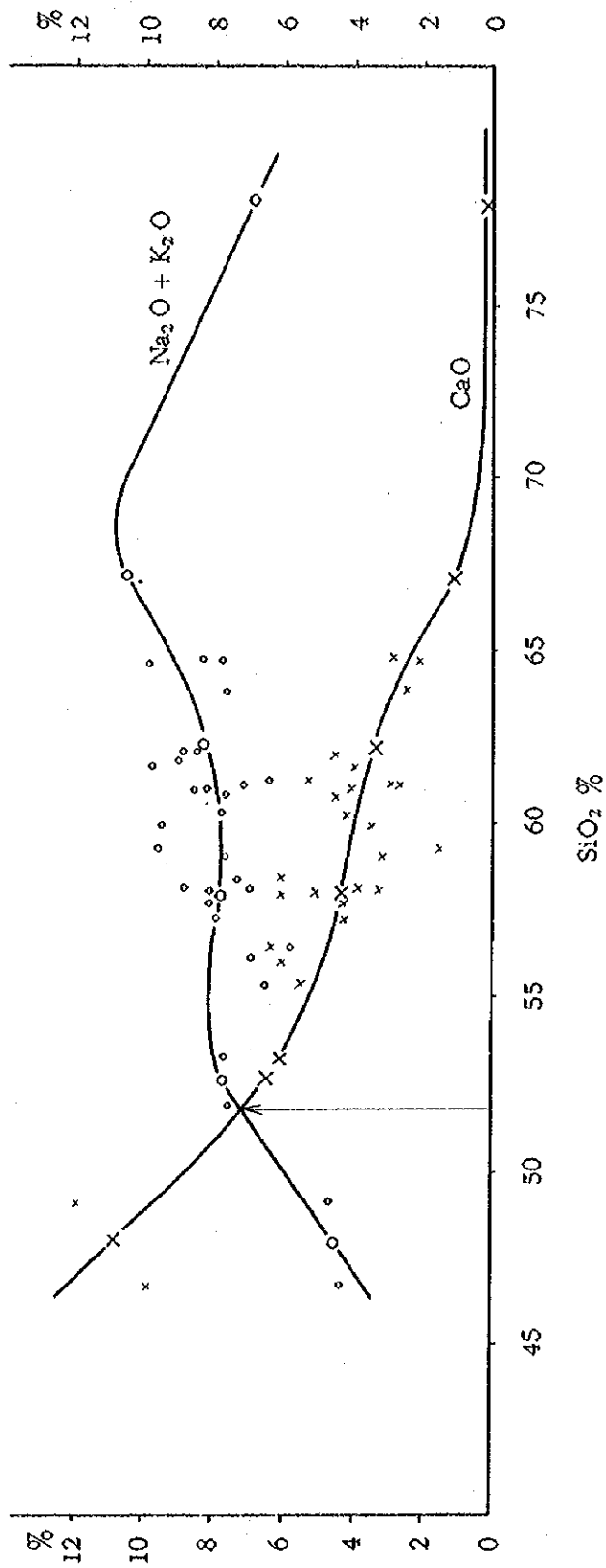
No.	253	287	72	66	293	328	351
Rock Name	Dacite	Trachy andesite	Trachy andesite	Trachy andesite	Trachy andesite	Trachy andesite	Microdiorite
Locality	7-c	1-g	2-d	2-d	1-h	2-h	3-h
SiO ₂	58.14	58.11	58.05	57.92	57.75	57.34	56.66
TiO ₂	1.03	1.08	1.20	1.30	1.25	1.10	0.70
Al ₂ O ₃	18.07	17.66	15.97	14.99	16.82	18.77	16.06
Fe ₂ O ₃	4.23	7.12	5.12	6.15	6.98	5.53	5.02
FeO	1.15	0.29	1.41	0.69	1.04	0.87	3.83
MnO	0.07	0.03	0.09	0.06	0.09	0.06	0.14
MgO	1.43	0.61	2.54	2.40	1.57	2.00	3.10
CaO	3.22	3.83	5.19	6.11	4.39	4.42	8.18
Na ₂ O	3.29	5.04	4.98	5.14	4.99	5.01	3.94
K ₂ O	3.59	3.79	3.10	2.54	3.05	2.91	0.90
P ₂ O ₅	0.20	0.17	0.61	0.68	0.49	0.50	0.15
H ₂ O (+)	3.68	1.28	0.72	1.10	1.00	0.96	0.41
H ₂ O (-)	1.51	1.12	0.72	0.63	0.11	0.64	0.11
Total	99.61	100.13	99.70	99.71	99.53	100.11	99.20
MgO	10.8	3.8	15.3	14.7	9.3	12.7	19.0
FeO	37.4	41.5	36.2	38.2	43.2	37.1	51.3
(Na,K) ₂ O	51.8	54.7	48.5	47.1	47.5	50.2	29.7
Q	16.62	6.66	6.12	6.96	7.86	6.18	10.86
C	3.16					0.71	
or	21.13	22.24	18.35	15.01	17.79	17.24	5.56
ab	27.77	42.44	41.92	43.49	41.92	42.44	33.54
an	15.29	14.46	12.23	10.29	14.73	18.07	23.07
lc							
ne							
Sal. total	(83.97)	(85.80)	(78.62)	(75.75)	(82.30)	(84.64)	(73.03)
ac							
wo		0.35	4.18	5.80	1.62		6.96
cn	3.60	1.50	6.40	6.00	3.90	5.00	7.80
fs							1.98
fo							
fa							
mt	0.93		1.39				7.19
hm	3.52	7.20	4.16	6.08	7.04	5.60	
il	1.98	0.61	2.28	1.67	2.28	1.98	1.37
ap	0.34	0.34	1.34	1.68	1.01	1.34	0.34
ti		1.96		0.98	0.20	0.20	
Fem. total	(10.37)	(11.96)	(19.75)	(22.21)	(16.05)	(14.12)	(25.64)
Or	32.9	28.1	25.3	21.8	23.9	22.2	8.9
Ab	43.3	53.6	57.8	63.2	56.3	54.6	54.0
An	23.8	18.3	16.9	15.0	19.8	23.2	37.1
D. I.	65.52	71.34	66.39	65.46	67.57	65.86	49.96

No.	4	442	344	296	34	75	354
Rock Name	Granodiorite	Basalt	Basalt	Altered basalt	Basalt	Trachy- basalt	Diorite porphyrite
Locality	1-b	7-h	3-h	1-h	2-1	2-d	3-h
SiO ₂	56.59	56.44	56.16	55.45	53.45	53.22	52.89
TiO ₂	0.75	1.30	1.69	1.33	1.56	1.71	0.91
Al ₂ O ₃	17.26	15.30	13.99	17.85	17.18	17.34	18.70
Fe ₂ O ₃	4.72	7.96	9.59	5.99	9.50	8.74	5.25
FeO	2.20	0.71	0.97	0.55	1.33	0.05	4.17
MnO	0.07	0.04	0.04	0.21	0.22	0.17	0.09
MgO	2.73	2.23	1.05	0.32	2.44	1.74	3.69
CaO	7.05	6.35	6.02	5.51	5.16	6.05	5.90
Na ₂ O	4.78	3.98	4.69	5.28	3.97	5.00	3.85
K ₂ O	0.45	1.74	2.15	1.20	1.82	2.72	2.10
P ₂ O ₅	0.12	0.16	0.14	0.75	1.80	0.45	0.11
H ₂ O (+)	2.20	1.77	1.29	5.05	1.03	1.93	1.24
H ₂ O (-)	0.24	1.22	1.50	0.46	0.22	0.45	0.35
Total	99.16	99.20	99.28	99.95	99.71	99.57	99.25
MgO	18.9	14.1	6.0	2.5	13.5	10.0	19.9
FeO	44.8	49.7	54.9	46.6	54.6	45.6	48.0
(Na,K) ₂ O	36.3	36.2	39.1	50.9	31.9	44.4	32.1
Q	10.38	12.60	10.38	10.32	9.66	1.50	4.20
C				0.20			
or	2.78	10.56	12.79	7.23	10.56	16.12	12.23
ab	40.35	33.54	39.82	44.54	33.54	42.44	32.49
an	24.19	18.63	10.56	20.85	23.63	16.68	27.52
tc							
ne							
Sal. total	(77.70)	(75.33)	(73.55)	(83.14)	(77.39)	(76.74)	(76.44)
ac							
wo	4.18	4.41	6.96		0.12	2.32	0.35
en	6.80	5.60	2.60	0.80	6.10	4.40	9.20
fs							1.98
fo							
fa							
mt	5.34				0.23		
hm	1.12	8.00	9.60	5.92	9.28	8.80	7.66
il	1.37	1.67	2.13	1.67	3.04	0.46	1.67
ap	0.34	0.34	0.34	1.68	0.67	1.01	0.34
tt		0.98	1.37	1.18		3.53	
Perm. total	(19.15)	(21.00)	(23.00)	(11.25)	(19.44)	(20.52)	(21.02)
Or	4.1	16.8	20.3	10.0	15.6	21.4	16.9
Ab	60.0	53.5	63.0	61.3	49.5	56.4	45.0
An	35.9	29.7	16.7	28.7	34.9	22.2	38.1
D. I.	53.51	56.70	62.99	62.09	53.76	60.06	48.92

No.	349	74	446	455	58		
Rock Name	Diorite	Trachy- basalt	Basalt	Gabbro	Basalt		
Locality	3-h	2-d	7-1	7-k	2-d		
SiO ₂	52.11	51.90	49.04	46.76	46.61		
TiO ₂	1.40	1.81	1.01	1.18	1.39		
Al ₂ O ₃	17.17	17.39	13.59	19.56	15.68		
Fe ₂ O ₃	2.83	7.15	2.25	5.18	9.74		
FeO	8.06	2.25	6.51	6.73	1.86		
MnO	0.19	0.12	0.17	0.16	0.19		
MgO	3.74	3.68	8.41	5.47	3.97		
CaO	7.69	6.83	11.92	10.42	9.90		
Na ₂ O	3.23	5.28	2.93	2.20	1.88		
K ₂ O	2.75	2.30	1.72	0.53	2.51		
P ₂ O ₅	0.31	0.37	0.14	0.22	0.19		
H ₂ O (+)	0.99	0.87	1.28	1.28	4.50		
H ₂ O (-)	0.02	0.36	0.22	0.19	2.30		
Total	100.49	100.31	99.19	99.88	100.72		
MgO	18.4	18.4	38.9	27.9	20.9		
FeO	52.2	43.6	39.6	58.2	56.0		
(Na,K) ₂ O	29.4	38.0	21.5	13.9	23.1		
Q				1.08	3.90		
C							
or	16.12	13.34	10.01	3.34	15.01		
ab	27.25	43.49	24.63	18.34	15.72		
an	23.84	16.96	18.90	41.98	26.97		
lc							
ne		0.57					
Sal. total	(67.21)	(74.36)	(53.54)	(64.74)	(61.60)		
ac							
wo	4.99	5.92	16.47	3.25	8.93		
en	8.60		2.20	13.70	9.90		
fs	9.50			6.34			
fo	0.56	6.49	13.25				
fa	0.82		6.73				
mt	4.18	2.32	3.25	7.42	2.78		
hm		5.60			7.84		
il	2.74	3.50	1.98	2.28	2.58		
ap	0.67	1.01	0.34	0.67	0.34		
ti							
Fem. total	(32.06)	(24.84)	(44.22)	(33.66)	(32.37)		
Or	24.0	18.1	18.7	5.3	26.0		
Ab	40.5	58.9	46.0	28.8	27.3		
An	35.5	23.0	35.3	65.9	46.7		
D. l.	43.37	57.40	34.64	22.76	34.63		

No.	414	415	450	Average of Perrobamba limestone	399	449	306
Rock Name	Limestone	Limestone	Limestone		Limestone	Calcarenite	Calcarenite
Locality	6-1	6-1	7-1		5-m	7-1	1-1
SiO ₂	4.04	1.13	2.25	2.47	1.11	4.22	26.62
TiO ₂	0.02	0.01	0.02	0.02	0.03	0.07	0.00 ₄
Al ₂ O ₃	0.32	0.14	0.45	0.30	0.21	1.76	0.21
Fe ₂ O ₃	0.14	0.18	0.82	0.38	0.19	0.49	0.13
MnO	0.01	0.01	0.01	0.01	0.02	0.03	0.01
MgO	0.03	0.09	0.04	0.05	0.02	0.04	0.01
CaO	0.05	0.10	0.01	0.05	0.05	0.06	0.09
Na ₂ O	0.14	0.00 ₄	0.00 ₄	0.05	0.01	0.12	0.01
K ₂ O	0.08	0.03	0.03	0.05	0.19	0.12	0.02
P ₂ O ₅	0.07	0.08	0.01	0.05	0.00 ₉	0.04	0.00 ₅
H ₂ O (-)	0.04	0.00	0.18	0.07	0.08	0.11	0.10
MnCO ₃	0.00	0.00	0.00	0.00	0.00	0.00	1.15
MgCO ₃	0.51	1.79	4.09	2.13	1.29	0.20	0.85
CaCO ₃	94.62	96.52	92.10	94.41	96.80	92.78	70.80
Total	100.07	100.08	100.01	100.04	100.00	100.04	100.00

Table I-11 Alkali-Lime Index of Volcanic Rocks from the Yauri Area

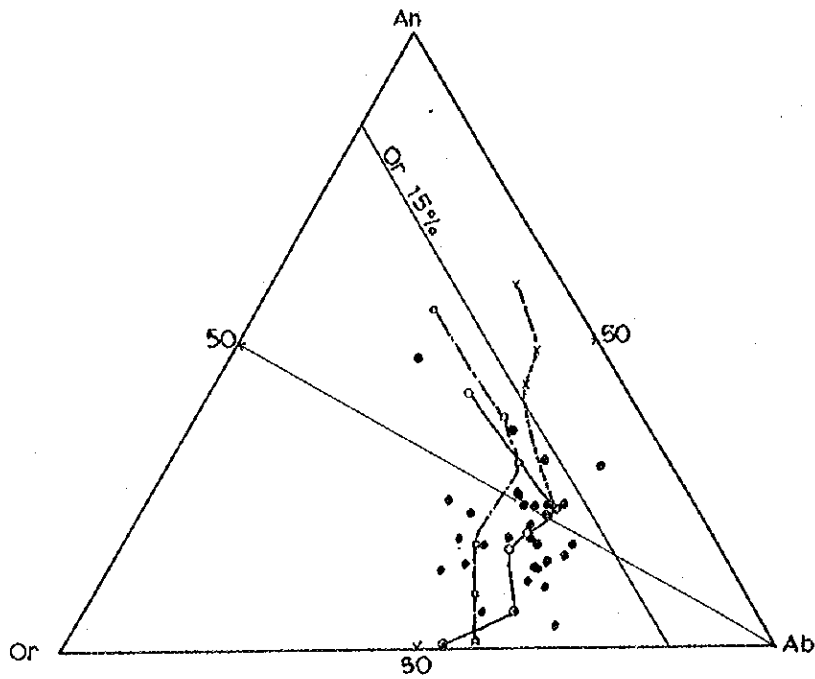


(1)	(2)	(3)	(4)
51	56	61	(SiO ₂ %)

Rock Series (after M. A. PEACOCK 1931)

(1) Alkalic (2) Alkali-Calcic (3) Calc-Alkalic (4) Calcic

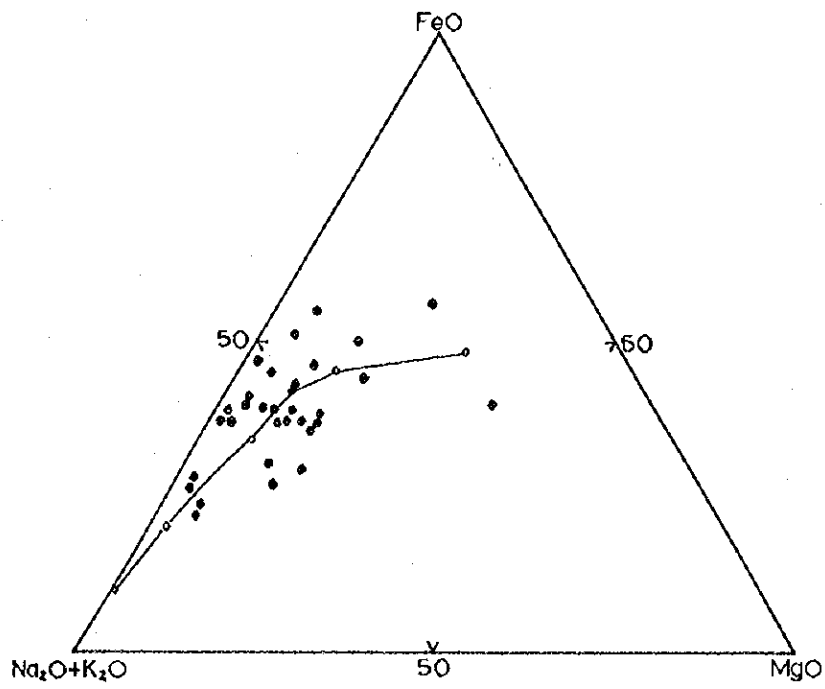
Table I-12 Triangular Diagram Showing the Ratio Normative Orthoclase (Or), Albite (Ab) and Anorthite (An) of Volcanic Rocks from the Yauri Area



LEGEND

- Average ratio of Yauri area
- x--- Izu-Hakone hypersthene rock series (Japan)
- Circum-Japan Sea alkali rock series (Japan)

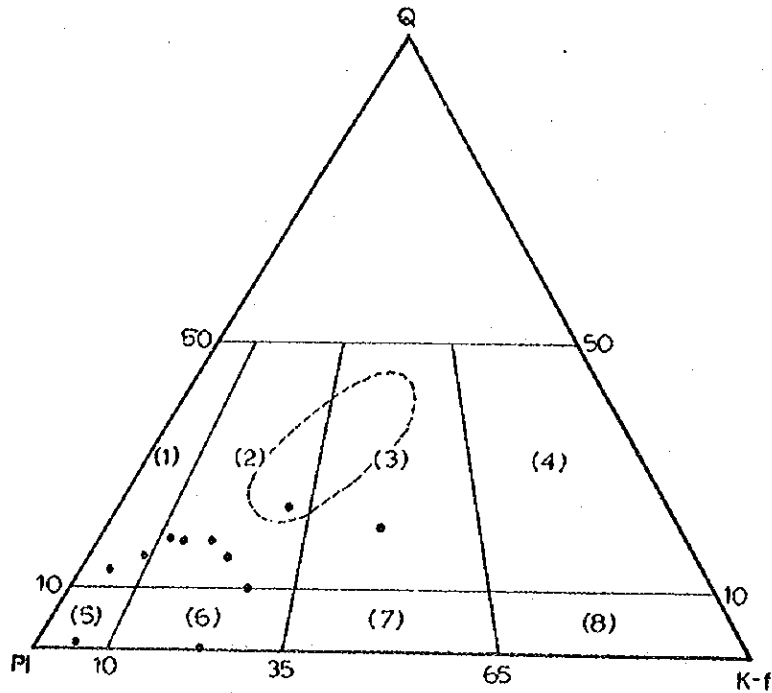
Table I-13 AFM Diagram of Volcanic Rocks from the Yauri Area



LEGEND

—○— Average ratio of Yauri area

Table I-14 Classification of Intrusive Rocks by Normative Quartz and Feldspars



LEGEND

- (1) Quartz diorite
- (2) Granodiorite
- (3) Quartz monzonite
- (4) Granite
- (5) Gabbro
- (6) Diorite
- (7) Monzonite
- (8) Syenite



Monzonitic rock of Southwestern U. S. A.

- Intrusives of Yauri Area

Table I-15 (1) Geochemical Analysis of Stream Sediments from the Yauri Quadrangle

Cu: ppm
Mo: ppm
N: Nil

Sample No.	Cu	Mo	Sample No.	Cu	Mo	Sample No.	Cu	Mo
1	20	N	39	25	N	77	5	N
2	25	N	40	35	N	78	10	N
3	30	N	41	20	N	79	8	N
4	30	N	42	20	N	80	-5	N
5	20	N	43	10	N	81	10	N
6	15	N	44	30	N	82	5	N
7	30	N	45	45	N	83	-5	N
8	20	N	46	30	N	84	40	N
9	15	N	47	20	N	85	30	N
10	15	N	48	15	N	86	30	N
11	20	N	49	25	N	87	25	N
12	20	N	50	35	N	88	20	N
13	20	N	51	10	N	89	50	N
14	30	N	52	20	N	90	30	N
15	20	N	53	20	N	91	10	N
16	25	N	54	10	N	92	5	N
17	10	N	55	20	N	93	30	N
18	15	N	56	30	N	94	80	N
19	30	N	57	30	N	95	20	N
20	20	N	58	30	N	96	20	N
21	15	N	59	30	N	97	20	N
22	30	N	60	8	N	98	20	N
23	20	N	61	20	N	99	10	N
24	15	N	62	20	N	100	10	N
25	20	N	63	20	N	101	75	N
26	20	N	64	10	N	102	60	N
27	30	N	65	10	N	103	30	N
28	20	N	66	10	N	104	30	N
29	40	N	67	15	N	105	30	N
30	40	N	68	20	N	106	30	N
31	30	N	69	30	N	107	20	N
32	30	N	70	30	N	108	15	N
33	30	N	71	-5	N	109	30	N
34	10	N	72	15	N	110	10	N
35	25	N	73	10	N	111	20	N
36	15	N	74	10	N	112	20	N
37	25	N	75	30	N	113	90	N
38	30	N	76	15	N	114	20	N

<u>Sample No.</u>	<u>Cu</u>	<u>Mo</u>	<u>Sample No.</u>	<u>Cu</u>	<u>Mo</u>	<u>Sample No.</u>	<u>Cu</u>	<u>Mo</u>
115	30	N	161	5	N	207	10	N
116	30	N	162	35	N	208	20	N
117	45	N	163	20	N	209	10	N
118	40	N	164	35	N	210	10	N
119	40	N	165	10	N	211	30	N
120	70	N	166	15	N	212	45	N
121	30	N	167	30	N	213	90	N
122	35	N	168	10	N	214	20	N
123	30	N	169	10	N	215	50	N
124	30	N	170	5	N	216	250	N
125	5	N	171	5	N	217	100	N
126	30	N	172	N	N	218	50	N
127	30	N	173	5	N	219	300	N
128	30	N	174	10	N	220	20	N
129	20	N	175	10	N	221	90	N
130	10	N	176	10	N	222	80	N
131	20	N	177	5	N	223	40	N
132	20	N	178	N	N	224	40	N
133	20	N	179	5	N	225	35	N
134	15	N	180	5	N	226	50	N
135	20	N	181	40	N	227	-5	N
136	15	N	182	30	N	228	45	N
137	20	N	183	30	N	229	45	N
138	40	N	184	8	N	230	600	N
139	30	N	185	30	N	231	60	N
140	40	N	186	45	N	232	45	N
141	25	N	187	45	N	233	15	N
142	40	N	188	15	N	234	20	N
143	15	N	189	35	N	235	600	N
144	35	N	190	20	N	236	200	N
145	30	N	191	30	N	237	30	N
146	10	N	192	40	N	238	45	N
147	15	N	193	20	N	239	50	N
148	20	N	194	10	N	240	95	N
149	30	N	195	20	N	241	150	N
150	25	N	196	25	N	242	250	N
151	30	N	197	30	N	243	50	N
152	10	N	198	20	N	244	30	N
153	30	N	199	5	N	245	75	N
154	30	N	200	5	N	246	60	N
155	30	N	201	15	N	247	180	N
156	35	N	202	35	N	248	550	N
157	30	N	203	25	N	249	35	N
158	30	N	204	5	N	250	30	N
159	30	N	205	15	N	251	30	N
160	30	N	206	20	N	252	20	N

Sample			Sample		
No.	Cu	Mo	No.	Cu	Mo
253	30	N	299	20	N
254	15	N	300	25	N
255	20	N	301	20	N
256	30	N	302	35	N
257	30	N	303	25	N
258	20	N	304	30	N
259	25	N	305	8	N
260	25	N	306	5	N
261	20	N	307	20	N
262	35	N	308	20	N
263	15	N	309	20	N
264	150	N	310	8	N
265	110	N	311	10	N
266	80	N	312	20	N
267	100	N	313	20	N
268	30	N	314	15	N
269	30	N	315	20	N
270	20	N	316	30	N
271	30	N	317	35	N
272	20	N	318	30	N
273	15	N	319	40	N
274	45	N			
275	40	N			
276	10	N			
277	30	N			
278	30	N			
279	30	N			
280	15	N			
281	15	N			
282	10	N			
283	20	N			
284	30	N			
285	20	N			
286	20	N			
287	30	N			
288	35	N			
289	25	N			
290	20	N			
291	20	N			
292	10	N			
293	40	N			
294	40	N			
295	20	N			
296	20	N			
297	8	N			
298	20	N			

Table I-15 (2) Geochemical Analysis of Stream Sediments from the Vellife Quadrangle

Sample No.	Cu	Mo	Sample No.	Cu	Mo	Sample No.	Cu	Mo
1	30	N	39	35	N	77	30	N
2	10	N	40	25	N	78	15	N
3	30	N	41	20	N	79	30	N
4	35	N	42	30	N	80	85	N
5	15	N	43	30	N	81	-5	N
6	20	N	44	20	N	82	-5	N
7	20	N	45	40	N	83	-5	N
8	30	N	46	10	N	84	20	N
9	40	N	47	20	N	85	8	N
10	45	N	48	30	N	86	-5	N
11	20	N	49	5	N	87	N	N
12	15	N	50	5	N	88	45	N
13	15	N	51	8	N	89	10	N
14	-5	N	52	8	N	90	15	N
15	45	N	53	5	N	91	5	N
16	30	N	54	30	N	92	10	N
17	25	N	55	20	N	93	-5	N
18	30	N	56	10	N	94	-5	N
19	20	N	57	10	N	95	10	N
20	50	N	58	10	N	96	25	N
21	20	N	59	25	N	97	20	N
22	10	N	60	30	N	98	5	N
23	10	N	61	40	N	99	8	N
24	30	N	62	N	N	100	5	N
25	20	N	63	5	N	101	8	N
26	20	N	64	50	N	102	15	N
27	20	N	65	20	N	103	10	N
28	30	N	66	25	N	104	15	N
29	15	N	67	25	N	105	5	N
30	30	N(+)	68	120	N	106	15	N
31	5	N	69	30	N	107	15	N
32	30	N(+)	70	30	N	108	10	N
33	10	N	71	40	N	109	25	N
34	20	N	72	30	N	110	25	N
35	30	N	73	100	N	111	15	N
36	30	N	74	35	N	112	15	N
37	10	N	75	80	N	113	10	N
38	10	N	76	5	N	114	15	N

<u>Sample No.</u>	<u>Cu</u>	<u>Mo</u>	<u>Sample No.</u>	<u>Cu</u>	<u>Mo</u>	<u>Sample No.</u>	<u>Cu</u>	<u>Mo</u>
115	10	N	161	10	N	207	25	N(+)
116	5	N	162	15	N	208	20	N(+)
117	10	N	163	10	N	209	10	N(+)
118	25	N	164	20	N	210	20	N(+)
119	10	N	165	10	N	211	20	N(+)
120	15	N	166	10	N	212	50	N(+)
121	10	N	167	30	N	213	20	N(+)
122	15	N	168	20	N	214	15	N(+)
123	20	N	169	40	N	215	25	N(+)
124	10	N	170	25	N	216	20	N
125	20	N	171	20	N	217	40	N(+)
126	30	N	172	20	N	218	25	N(+)
127	30	N	173	5	N	219	20	N(+)
128	20	N	174	15	N	220	10	N(+)
129	30	N	175	N	N	221	15	N(+)
130	20	N	176	15	N	222	10	N(+)
131	5	N	177	20	N	223	20	N(+)
132	20	N	178	15	N	224	10	N(+)
133	35	N	179	15	N	225	14	N
134	30	N	180	10	N	226	20	N
135	40	N	181	15	N	227	20	N(+)
136	20	N	182	25	N	228	15	N
137	40	N	183	25	N	229	15	N
138	40	N	184	20	N	230	15	N
139	-5	N	185	30	N	231	15	N
140	8	N	186	15	N	232	15	N
141	-5	N	187	10	N	233	10	N
142	10	N	188	15	N	234	5	N
143	20	N	189	25	N	235	5	N
144	20	N	190	-5	N	236	15	N(+)
145	30	N	191	-5	N	237	5	N
146	10	N	192	10	N	238	15	N
147	20	N	193	1000	N	239	20	N
148	20	N	194	20	N	240	15	N
149	15	N	195	10	N	241	5	N
150	10	N	196	25	N	242	5	N
151	10	N	197	5	N	243	15	N
152	20	N	198	25	N	244	15	N
153	15	N	199	10	N	245	20	N
154	15	N	200	15	N	246	15	N
155	25	N	201	20	N(+)	247	10	N
156	30	N	202	15	N(+)	248	15	N
157	15	N	203	8	N(+)	249	15	N
158	20	N	204	20	N(+)	250	100	N
159	15	N	205	15	N(+)	251	10	N
160	10	N	206	25	N(+)	252	10	N

<u>Sample No.</u>	<u>Cu</u>	<u>Mo</u>
253	5	N
254	20	N(+)
255	20	N(+)
256	10	N
257	100	N
258	5	N
259	10	N
260	45	N
261	10	N
262	N	N
263	15	N
264	-5	N
265	15	N
266	20	N
267	15	N(+)
268	15	N(+)
269	15	N
270	20	N(+)
271	5	N(+)
272	10	N(+)
273	10	N(+)
274	25	N(+)
275	15	N
276	10	N
277	15	N
278	50	N
279	25	N
280	10	N
281	5	N
282	N	N
283	35	N
284	15	N
285	-5	N
286	15	N
287	10	N
288	30	N
289	10	N

Table I-16. Chemical Analysis of Ores

Sample No.	Location	Total-Cu %	Soluble Cu %	Mo %	Au g/t	Ag g/t	S %	Pb %	Zn %	Sb %	Fe %
176	5 - f	2.62									
231	6 - f									Nil	
277	7 - g				Nil	342					
328	2 - h	0.02		0.004			14.2				
336	2 - i	0.11					4.40	tr	tr		57.4
338	2 - j	0.02		0.004			3.09				
356	3 - h	0.09		0.004							
378	4 - h	0.02		0.004	Nil						
388	4 - j	0.18		0.005							
454	7 - j	0.18		0.007							

Table I-17 Chart of X-ray Diffractive Analysis

